Gas Diffusion Layers Impregnated with Metal Oxide Decorated and Nitrogen-Doped Carbon Nanotube Catalysts for Electrically Rechargeable Zn-Air Batteries

by

Drew Aasen

A thesis submitted in partial fulfillment of the requirements for the degree of

Master of Science

in

Materials Engineering

Department of Chemical and Materials Engineering

University of Alberta

Abstract:

Secondary zinc-air batteries (ZABs) have garnered interest in recent years as a promising technology for energy storage due to their minimal safety concerns, low cost, and a high theoretical energy density. However, many issues still need to be resolved for commercialization of ZABs. Many of these issues are associated with the air electrode, such as the slow kinetics of the oxygen reduction and oxygen evolution reactions (ORR and OER, respectively) and poor cycle life. The former has been addressed previously through the use of noble metal catalysts such as Pt, Ru, and Ir, as well as their oxides. However, these catalysts are expensive and suffer from performance degradation during battery cycling. Additionally, the catalyst is often applied to the electrode as a layer on the surface which is susceptible to a phenomenon known as flooding. As the battery is cycled, electrolyte will flood the electrode and pass through the catalyst layer, resulting in performance losses. Therefore, development of low-cost catalysts and a simple electrode preparation technique to help mitigate the effects of flooding is desired.

This work focusses on the development of impregnated air electrodes using transition metal (Mn, Co, Fe, and Ni) oxide decorated, nitrogen-doped carbon nanotube (N-CNT) catalysts to improve the performance and cycling efficiency of ZABs. The effect of the impregnation technique as a form of electrode preparation was investigated through cross sectional scanning electron microscopy (SEM) and electrochemical tests such as galvanostatic charge and discharge rate tests (battery rate tests), as well as linear sweep voltammetry (LSV). The N-CNT supported catalysts were characterized using SEM, transmission electron microscopy (TEM), and X-ray photoelectron spectroscopy (XPS). The electrochemical performance of the catalysts was evaluated using cyclic voltammetry (CV), LSV, electrical impedance spectroscopy (EIS), and battery rate tests. The best performing samples were then selected for use in an electrically rechargeable ZAB.

The first study involved the impregnation and synthesis of air electrodes using Mn_3O_4 decorated N-CNT catalysts for ORR. The catalysts were prepared using a simple precipitation method. The air electrode was simultaneously impregnated with the catalysts during synthesis through soaking and vacuum filtration. The impregnated electrode showed superior performance to electrodes prepared by conventional spray coating. Furthermore, the Mn_3O_4/N-CNT impregnated electrodes

had superior ORR performance to other Mn_3O_4 catalysts from the literature, as well as similar ORR performance to commercially available Pt-Ru/C catalysts. The electrode was coupled with electrodeposited Co-Fe on Ni foam and was cycled in a tri-electrode cell. The tri-electrode cycling performance was comparable to that of Pt-Ru/C under the same tri-electrode cycling conditions.

The second study involved the preparation of bimetallic $(Co,Fe)_3O_4$ decorated N-CNTs as a bifunctional and highly stable catalyst for ZABs. The catalyst and electrode preparation were achieved again by simultaneous precipitation and impregnation. Characterization through TEM and XPS indicated mixed valence for both Co and Fe in a spinel oxide phase. Electrochemical testing of the $(Co,Fe)_3O_4$/N-CNT impregnated electrodes showed comparable ORR activity and superior OER activity to Pt-Ru/C at 20 mA cm^{-2}. Bifunctional cycling of $(Co,Fe)_3O_4$/N-CNT at a current density of 10 mA cm^{-2} exhibited exceptional stability with a discharge/charge efficiency of 58.5% after 200 cycles (100 h), which compared favorably with Pt-Ru/C under the same conditions (55.3% after 200 cycles).

The third study investigated the catalytic performance of transition metal based bimetallic and trimetallic oxides on N-CNTs for ZABs. Using the developed synthesis and impregnation technique, 6 bimetallic oxides (Mn-Co, Co-Fe, Mn-Fe, Ni-Co, Ni-Fe, Ni-Mn) and 3 trimetallic oxides (Ni-Co-Fe, Ni-Mn-Fe, Mn-Co-Fe) were synthesized on N-CNTs. All catalysts were characterized through TEM and SEM analysis. The trimetallic oxide catalysts were further characterized through XPS analysis and were determined to exist as various spinel phases. Ni-Mn oxide on N-CNTs ($NiMnO_x$/N-CNT) had the best ORR performance of the bimetallic oxides, while Ni-Fe oxide on N-CNTs ($NiFeO_x$/N-CNT) and $(Co,Fe)_3O_4$/N-CNT had the best OER performance and bifunctional performance, respectively. The trimetallic oxide systems were selected based on the battery rate test performance and discharge/charge efficiencies of the bimetallic oxide catalysts. Electrochemical testing of the trimetallic oxides on N-CNTs showed improved activity towards OER when compared with the bimetallic oxides. Furthermore, the trimetallic oxides had similar ORR performance to Pt-Ru/C and superior OER performance in battery rate tests. Bifunctional cycling of the trimetallic oxide catalysts showed good cycling stability and superior efficiencies to Pt-Ru/C after 200 cycles (100 h) at a current density of 10 mA cm^{-2}. Ni-Co-Fe oxide on N-CNTs (NCFO/N-CNTs) had the best cycling performance of the trimetallic oxide catalysts and the best OER activity of all 10 catalysts tested in the study.

Bifunctional cycling of NCFO/N-CNT at a current density of 20 mA cm^{-2} demonstrated better cycling efficiency than Pt-Ru/C after 100 cycles (53.2% vs 41.3%, respectively).

Preface:

This thesis focusses on the synthesis, electrode preparation, characterization, and electrochemical testing of air electrodes impregnated with metal oxide decorated and nitrogen doped carbon nanotubes for rechargeable Zn-air batteries. The research presented in Chapters 3, 4, and 5 along with their supporting information is my original work.

Chapters 3, 4, and 5 summarize work done in collaboration with Michael Clark (PhD student) in our group. Michael performed TEM analysis and contributed to many discussions regarding characterization and electrochemical testing. Optimization of synthesis parameters and electrode preparation, as well as electrochemical testing and SEM analysis, were conducted by myself. Manuscript preparation and conceptual development was accomplished with the help of Dr. Douglas Ivey, my supervisor. Dr. Ivey also assisted with the collection of TEM images and the analysis of the characterization techniques.

A version of Chapter 3 has been published as:

D. Aasen, M. P. Clark, D. G. Ivey, A Gas Diffusion Layer Impregnated with Mn_3O_4 Decorated, Nitrogen-Doped Carbon Nanotubes for the Oxygen Reduction Reaction in Zinc-Air Batteries, *Batteries & Supercaps*, **2019**, 2, 882-893.

(10.1002/batt.201900102)

Versions of Chapter 4 and Chapter 5 have been submitted for publication in Batteries & Supercaps and the Journal of the Electrochemical Society, respectively:

Chapter 4: D. Aasen, M. P. Clark, D. G. Ivey, $(Co,Fe)_3O_4$ Decorated Nitrogen-Doped Carbon Nanotubes in Nano-Composite Gas Diffusion Layers as Highly Stable Bifunctional Catalysts for Rechargeable Zinc-Air Batteries, *Batteries & Supercaps,* **2019** (Submitted August 16th, 2019)

Chapter 5: D. Aasen, M. P. Clark, D. G. Ivey, Investigation of Transition Metal-Based (Mn, Co, Ni, Fe) Trimetallic Oxide Nanoparticles on N-doped Carbon Nanotubes as Bifunctional Catalysts for Zn-Air Batteries, *J. Electrochem. Soc.,* **2019** (Submitted October 18th, 2019)

Acknowledgments:

I would like to thank my supervisor, Dr. Douglas G. Ivey for his support and guidance throughout my Master's program. His dedication to his students as well as his passion for materials science and engineering has continuously inspired me. Without his compassion and feedback, none of this would have been possible.

I would like to thank my group members for supporting and encouraging me. I am particularly grateful to Michael Clark, Arjun Dhiman, Wendy Tran, and Ming Xiong. Their insights allowed me to overcome many difficulties and gain new perspectives in my research. I would also like to thank Matthew Labbe for his assistance in the laboratory and valuable discussions.

I would like to thank Nathan Gerein (FESEM), Shihong Xu (SEM, XPS), and Danielle Covelli (XPS, University of Saskatchewan) for their technical knowledge and support.

Financial support from the Natural Sciences and Engineering Research Council of Canada (NSERC, RGPIN-2018-04488) the Faculty of Graduate Studies and Research (FGSR), the Graduate Student's Association (GSA) and the Future Energy Systems Project (FES, T06 P03) are gratefully acknowledged.

Table of Contents

List of Figures:

List of Tables:

1 Introduction

In recent years, initiatives to increase the use of renewable energy have been observed globally.[1] Renewable energy may represent a strategic path to mitigate climate change and create a sustainable future and has recently been reported to account for 24.5% of global electricity production.[2], [3] Furthermore, estimates suggest that renewable energy may provide up to 30% of global electricity by 2035.[2] However, development of renewable energy technologies alone cannot effectively meet global energy demands. Infrastructure and supporting technologies must, therefore, be developed in tandem with energy producing technologies in order to reduce energy costs and maintain energy supply. For instance, supply of electricity from solar panels is at a maximum during peak sunlight hours and a minimum overnight. However, the maximum production of electricity from solar does not reliably comply with peak demand. Thus, technology to regulate the production and supply of renewable energy is essential.

Due to the intermittent nature of renewable energy sources, there has been a subsequent increase in research for energy storage. The solution to energy storage should not only be cost effective and reliable but should have low environmental impact in order to be widely adopted. Traditional solutions rely heavily on local geographical and climate conditions which reduces the applicability of these technologies world-wide. As a result, there has been increased interest in various types of batteries and fuel cells as efficient and universal means to store energy. Currently, lithium ion is the most common battery technology for a wide variety of uses due to lithium's high energy density and good cyclability.[4], [5] However, lithium-based batteries are limited in size due to safety concerns.[4] Additionally, the cost of producing lithium-based batteries is difficult to minimize due to the cost of metallic Li (up to $180,000/ton, 2017).[1], [6] Therefore, lithium-based batteries are not ideal for energy storage and alternative technologies are preferred.

In this regard, alkaline metal-air batteries are promising due to their minimal safety risks, high energy density, and low environmental impact.[1] Furthermore, metal-air batteries offer the highest theoretical energy densities of most rechargeable battery types.[7] Of the aforementioned battery technology, zinc-air batteries (ZABs) are of great interest. Zinc is more stable than other metal-air compositions (such as Al and Mg) and has higher cell voltages than other stable batteries such as Fe-air.[1]. Although ZABs have lower energy densities than Li-air technologies, Li-air batteries are a concern because of the cost of Li and several safety issues.[6], [8] Additionally, Li-air batteries struggle with poor cyclability due to the reactivity of Li. For instance, Li_2O_2 is a common by-product during discharge of Li-air batteries and block the pores of the air-electrode and shorten the battery life.[6], [8] If the air electrode is carbon-based, Li_2O_2 may also decompose the carbon to form Li carbonates which further block the pores.[6] As a result, the low cost of Zn, in addition to its minimal safety concerns, allows ZABs to be a promising technology for energy storage.

Zn-air as a primary battery is an established technology with applications in hearing aids and other biomedical devices.[1] It is fundamentally based on the reduction of oxygen gas at the cathode and Zn oxidation at the anode. In terms of energy storage, a secondary (rechargeable) battery is desired and thus is dependent on the reversibility of the Zn oxidation reaction. Both oxygen and zinc redox reactions, as well as a simplified cell reaction, are expressed in Equations 1-3.

$$\mathrm{O_2} + 4e^- \rightarrow 4\mathrm{OH}^-,\ E^o = 0.40\ \mathrm{V\ vs\ SHE} \tag{1}$$

$$\mathrm{Zn} + 2\mathrm{OH}^- \rightarrow \mathrm{Zn(OH)_4}^{2-} + 2\mathrm{e}^-,\ E^o = -1.25\ \mathrm{V\ vs\ SHE} \tag{2}$$

$$2\ \mathrm{Zn} + \mathrm{O_2} \rightarrow 2\ \mathrm{ZnO},\ E^o = 1.65\ \mathrm{V\ vs\ SHE} \tag{3}$$

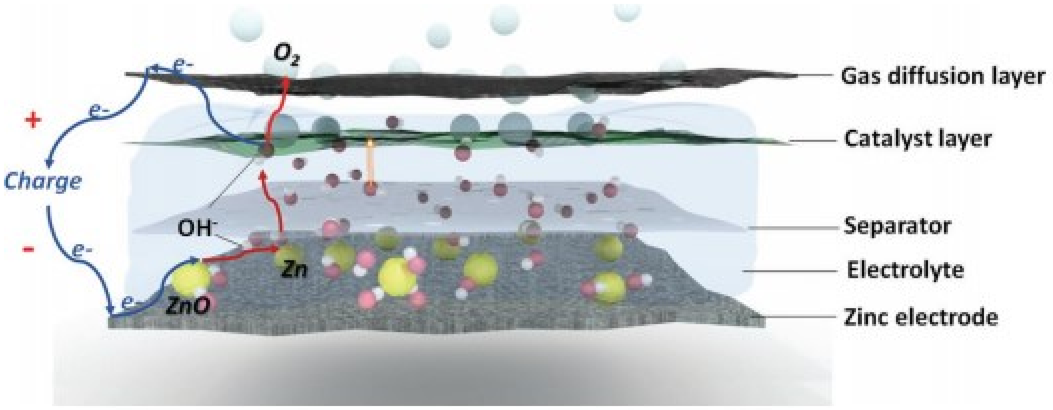

Figure 1.1 – Schematic representation of the structural components of a Zn-air battery.[1]

The structure of ZABs is demonstrated in Figure 1.1 and consists of a gas diffusion layer (GDL) for the oxygen reaction, a catalyst layer, an electrolyte, a separator, and the Zn anode. Although ZABs are considered to be one of the most feasible technologies for smart-grid energy storage, there are many issues that must be resolved.[1], [9] Particularly, ZABs suffer from low round-trip efficiency due to slow kinetics of the reactions at the air electrode. Therefore, electrocatalysts are needed at the GDL to improve the efficiency and power density of the cell.[5], [9] Noble metals (such as Pt, Ru, and Ir) are often considered as state-of-the-art catalysts for oxygen reduction and oxygen evolution reactions (ORR and OER, respectively).[10], [11] However, noble metals suffer from poor cyclability and high cost. In response, transition metals and their oxides have been used as low-cost alternatives as they show good stability in alkaline media and are more abundant than noble metals. Unfortunately, transition metal oxides suffer from poor conductivity and are often combined with conductive carbon materials which require complicated synthesis procedures.[9], [12]–[15] Thus, development of high-performing, commercially scalable, and cost-effective catalysts is essential to the development of ZABs.

This thesis aims to address several issues which ZABs currently face: poor kinetics of the oxygen reactions, loss of the three-phase boundary during cycling, poor cycle life, and complicated synthesis of catalyst materials. Preservation of the three-phase boundary and improvement of battery cycle life are achieved by impregnating the air electrode with nanocatalysts. Impregnation allows the catalyst to be distributed within the pores of the electrode as well as on the surface, creating a much larger active surface area while preserving the three-phase boundary during cycling. A simple precipitation process is proposed as an effective and versatile method in developing high performing nanocatalysts for the oxygen reactions. The precipitation process is combined with the impregnation method to allow for simultaneous synthesis and electrode preparation.

Chapter 2 provides a review of the literature and establishes the basis for Chapters 3 through 6. Chapter 3 explores the effect of impregnation as an electrode preparation technique and the resulting performance using Mn_3O_4 decorated, nitrogen-doped carbon nanotubes (N-CNT) as a catalyst. Chapter 4 discusses the development of $(Co,Fe)_3O_4$/N-CNT as a highly stable, bifunctional catalyst for ORR and OER; fabrication is again achieved through impregnation. Further investigation into bimetallic and trimetallic oxides anchored to N-CNTs as bifunctional catalysts for ORR and OER is discussed in Chapter 5. Finally, Chapter 6 provides a summary of the achievements from each study and provides perspectives and recommendations on the work going forward.

2 Literature Review

2.1 Zn-Air Batteries (ZABs)

As demonstrated in Figure 1.1, ZABs have multiple components. Each component faces its own challenges as the technology strives to grow and become more practical. The components may be set up in multiple types of battery configurations; conventional planar, flowing electrolyte, flexible, and multi cell batteries.[1] To maintain a focus on the application of ZABs for energy storage, the latter two configurations are mentioned but not explored.

Conventional planar configurations are common in primary ZABs and research applications as they are easy to set up and allow for maximum open air access.[1], [5] The configuration can be set up horizontally or vertically; the former allows for better current retention and the latter permits better electrolyte retention.[1] Flowing electrolyte configurations are characterized primarily by a mobile or flowing aqueous electrolyte which helps reduce problems that arise at both electrodes (such as GDL pore blockage and Zn electrode shape change).[1] However, flowing electrolyte configurations often struggle with low energy efficiency and increased complexity of the cell design.[1], [9] In this section, a brief overview of the battery components and their issues will be discussed.

2.1.1 Electrodes

ZABs function based on the redox reactions of oxygen and zinc. From Equations 1 – 3 the cell potential has a theoretical value of approximately 1.65 V. However, depending on the applied current density, the voltage can drop to <1.4 V.[5] Furthermore, the voltage may drop over the cycle-life of the cell due to challenges at each electrode.

Zn Electrode

The Zn electrode is often made from Zn foil for research endeavors. At the electrode, four main performance limiting mechanisms are observed. The first is dendrite formation, which occurs during the charge cycle of the battery. Dendrites negatively affect performance as their morphology makes them susceptible to fracture, resulting in capacity loss and possible tearing of the separator.[1] The second is shape change, which occurs during discharge of the cell. Shape change is due to area-selective oxidation of the anode, which can eventually result in anode failure.[1], [9] The third is passivation and increased resistance at the anode, which is caused by the cell reaction during discharge. The production of ZnO from the oxidation by-products (Equation 4a and 4b), during saturation conditions, results in a passive layer forming on the Zn electrode, as seen in Equation 4c. The ZnO layer increases the resistance of the anode as well as limits the active surface area, thus preventing further discharge.[1] Finally, the hydrogen evolution reaction (HER) is the fourth challenge at the Zn electrode. During charging conditions, HER is more thermodynamically favourable than the Zn reaction (Equation 5).[9] Therefore, a phenomenon known as "self-discharge" is observed at rest as the Zn electrode is corroded (Equation 6), which reduces the charging efficiency of the cell.[1]

$$\mathrm{Zn} + 2\mathrm{OH}^- \rightarrow \mathrm{Zn(OH)_2} + 2\ \mathrm{e}^- \quad (4a)$$

$$\mathrm{Zn(OH)_2} + 2\mathrm{OH}^- \rightarrow \mathrm{Zn(OH)_4^{2-}} \quad (4b)$$

$$\mathrm{Zn(OH)_4^{2-}} \rightarrow \mathrm{ZnO} + 2\mathrm{OH}^- + \mathrm{H_2O} \quad (4c)$$

$$2\ \mathrm{H_2O} + 2\mathrm{e}^- \rightarrow 2\mathrm{OH}^- + \mathrm{H_2} \quad (5)$$

$$\mathrm{Zn} + \mathrm{H_2O} \rightarrow \mathrm{ZnO} + \mathrm{H_2} \quad (6)$$

Strategies to limit the presence of all four of the mentioned challenges are currently being studied. A summary created by Fu et al. is reported in Table 2.1.

Table 2.1 - Strategies for Improving Zn Electrode Performance[1]

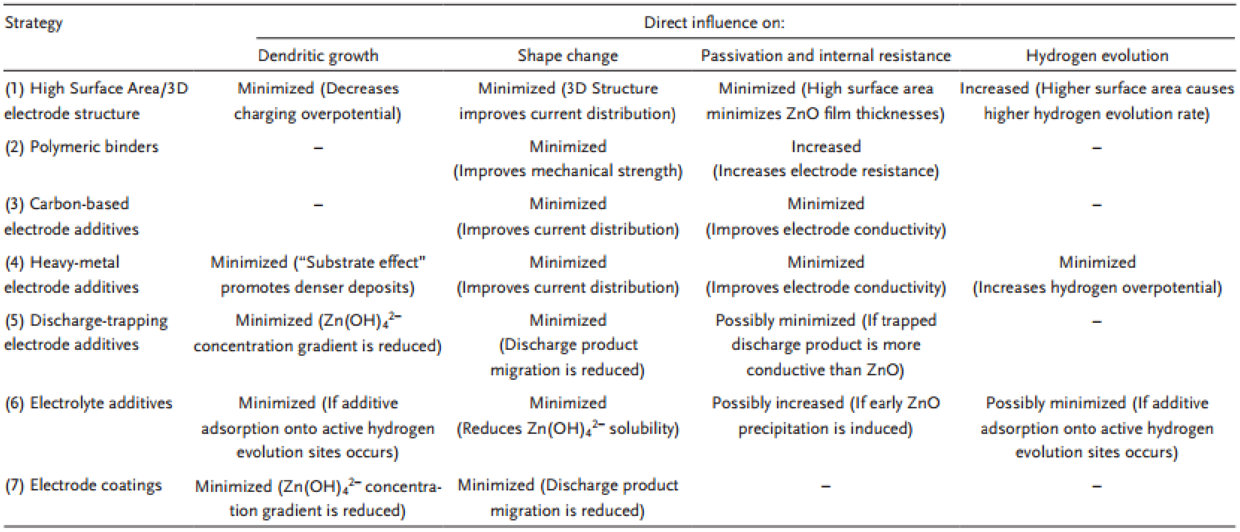

Strategy	Direct influence on:			
	Dendritic growth	Shape change	Passivation and internal resistance	Hydrogen evolution
(1) High Surface Area/3D electrode structure	Minimized (Decreases charging overpotential)	Minimized (3D Structure improves current distribution)	Minimized (High surface area minimizes ZnO film thicknesses)	Increased (Higher surface area causes higher hydrogen evolution rate)
(2) Polymeric binders	–	Minimized (Improves mechanical strength)	Increased (Increases electrode resistance)	–
(3) Carbon-based electrode additives	–	Minimized (Improves current distribution)	Minimized (Improves electrode conductivity)	–
(4) Heavy-metal electrode additives	Minimized ("Substrate effect" promotes denser deposits)	Minimized (Improves current distribution)	Minimized (Improves electrode conductivity)	Minimized (Increases hydrogen overpotential)
(5) Discharge-trapping electrode additives	Minimized ($Zn(OH)_4^{2-}$ concentration gradient is reduced)	Minimized (Discharge product migration is reduced)	Possibly minimized (If trapped discharge product is more conductive than ZnO)	–
(6) Electrolyte additives	Minimized (If additive adsorption onto active hydrogen evolution sites occurs)	Minimized (Reduces $Zn(OH)_4^{2-}$ solubility)	Possibly increased (If early ZnO precipitation is induced)	Possibly minimized (If additive adsorption onto active hydrogen evolution sites occurs)
(7) Electrode coatings	Minimized ($Zn(OH)_4^{2-}$ concentration gradient is reduced)	Minimized (Discharge product migration is reduced)	–	–

Air Electrode

The GDL acts as an interface between air and the catalysts, and allows for the electrolyte to be directed towards active sites.[5], [16] This interaction between liquid electrolyte, solid catalyst, and gas is referred to as the three-phase reaction zone or as the three-phase boundary. The GDL is often a bilayer structure formed with a macro-porous layer and a microporous layer. The porous layers are often carbon-based with varying amounts of a polytetrafluoroethylene (PTFE) binder to increase hydrophobicity and reduce flooding of the GDL.[5] Flooding occurs as the electrolyte passes the catalyst layer and permeates farther into the GDL, which may result in the loss of the three-phase boundary or leakage of the electrolyte from the cell. The microporous layer is exposed to the electrolyte while the macro-porous layer is exposed to air.[17] The microporous layer is often coated with a catalyst layer and plays host to the three-phase boundary. Several techniques have been used to apply the catalyst layer to the surface of the microporous layer, such as spray coating, applied catalyst paste, electrodeposition, and application of catalyst-dipped carbon materials (such as carbon cloth).[15], [17]–[19]

Since the oxygen reactions consume oxygen present in air, the source of oxygen at the air electrode is essentially inexhaustible.[5] However, the air electrode faces many challenges such as flooding, slow reaction kinetics, and relatively poor electrode stability.[5], [17], [18] Poor electrode stability can be caused by a variety of issues, such as catalyst loss, oxidation of the electrode, carbonate formation, and damage during charging conditions.[17] CO_2 in the air can enter the cell and react and form carbonates. Additionally, carbon present in PTFE and the carbon GDL can oxidize under operating conditions, leading to further formation of carbonates.[1], [5], [9] These carbonates then block the pores of the GDL and reduce the ability of the air to reach the three-phase boundary.[20] Performance of the cell is reduced as a result of limited interaction.[1], [5]

Strategies to reduce carbonate build up in the GDL include using flowing electrolyte configurations to "rinse" off carbonates and remove air bubbles, fabrication of more evenly dispersed microporous layers, nanostructured air electrodes, and creating binder-free GDLs (such as metal-mesh GDLs).[5], [21], [22] Furthermore, carbonates may be reduced if the charging potential can be decreased. Thus, better OER catalysts are desired.[17], [18]The traditional GDL made of porous carbon paper and PTFE is often loaded with catalyst on its microporous surface. Alternatively, an aerogel electrode may be fabricated to satisfy the design parameters of the GDL (porosity for oxygen diffusion, high active surface area, conductivity, and hydrophobicity) while simultaneously achieving certain desired characteristics such as good activity towards the oxygen reactions.[23], [24]

Although limited work has been done with respect to ZABs, graphene based composites and aerogels have been used in Li ion, Na ion, Li-air, and Li-S batteries, as well as methanol fuel cells.[23]–[26] Aerogels are good candidates as alternative GDL materials, as they can be synthesized with a high level of control, resulting in tunable pore size, surface area, and other properties.[24] Furthermore, aerogel electrodes may be doped during synthesis with metals and other heteroatoms (such as nitrogen) to be catalytically active towards ORR and/or OER.[24], [26] Kwok et al. fabricated a graphene-carbon nanotube (CNT) composite aerogel loaded with Pt/Ru particles, which displayed good ORR performance in a methanol fuel cell.[25] The CNTs improved the activity of the aerogel electrode for ORR, since the CNTs increase the conductivity of the aerogel.[25] The use of graphene and CNTs also produce a more stable catalyst support due to the sp^2 carbon-carbon bonds, resulting in a more durable electrode.[15], [25] Additionally, work by Baskakov et al. reports a nitrogen doped graphene oxide (N-GO) aerogel electrode for use in Li batteries, fuel cells, and other energy storage applications.[26] The aerogel displayed a 90 mV reduction in onset potential for ORR when compared with a glassy carbon electrode (GCE).[26] These findings suggest that aerogel electrodes are suitable alternatives to traditional GDL, and more research should be done to assess their suitability for use in metal-air batteries.

2.1.2 Electrolytes

Alkaline Electrolytes

Electrolytes in ZABs have historically been aqueous and highly alkaline, with the most common electrolyte being KOH due to its high ionic conductivity (0.6 S cm^{-1}, at 30 wt %).[1], [5] The benefits of using alkaline electrolytes include increased corrosion resistance for the Zn electrode and better kinetics for the oxygen reactions.[1] Upon reaction with air, the carbonate product of KOH Equation (7) is also more soluble than the carbonate products for other common alkaline electrolytes, such as NaOH.[5], [27] As mentioned in Section 2.1.1, carbonate formation is detrimental to the air electrode. Although the solubility of K_2CO_3 is higher than for other alkaline electrolytes, precipitation on the pores of the GDL may still occur.

$$2\mathrm{KOH} + \mathrm{CO_2} \rightarrow \mathrm{K_2CO_3} + \mathrm{H_2O} \qquad (7)$$

The second issue that arises with alkaline electrolytes is a high sensitivity to temperature and humidity.[5], [27] This sensitivity can result in evaporation of the electrolyte during long term cycling operations, limiting the performance of the cell.[1] To circumvent the two common issues of alkaline electrolytes, alternative electrolytes have been researched. Additives to alkaline electrolytes have been reported (such as Li-Na-K-CO_3 compositions) with some success.[28] However, there is limited research on the effects of additives at this time.[5] Three common alternatives to aqueous electrolytes have been discussed in the recent literature: solid-state electrolytes, alkaline gel electrolytes (AGEs), and ionic liquid electrolytes.[1], [5], [27]

Solid State Electrolytes

Solid-state electrolytes and AGEs have better mechanical properties and lower sensitivity to air, temperature, and humidity relative to aqueous alkaline electrolytes.[1] These improved qualities are beneficial for flexible battery configurations.[1], [5], [27] Solid-state electrolytes can have good ionic conductivity, but current densities tend to be lower due to a restriction in the number of the aforementioned three phase reaction zones, which is visualized in Figure 2.1.[1], [27] AGEs are typically an alkaline electrolyte suspended in a polymer gel, which often results in poor contact at the AGE-electrode interface.[1] Poor contact increases the resistance of the cell and, consequently, limits the cell performance.

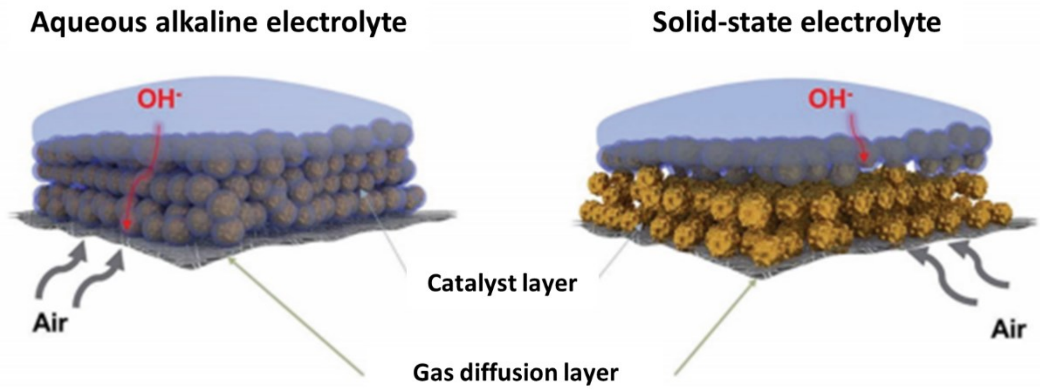

Figure 2.1 - Three phase boundary comparison of aqueous alkaline and solid-state electrolytes.[1]

2.1.3 Separators

Separators are porous structures that allow the transport of ionic species to both electrodes while preventing the electrodes from contacting one another.[1] They are typically made of non-woven polymers, such as polyethylene (PE) and polypropylene (PP).[5] Specifically in ZABs, the separator plays an important role in limiting dendrite growth.[5] Recent ZABs have been designed using Celgard©, which is a tri-layered separator (PP/PE/PP).[1], [5] The issue with conventional Celgard© separators is polarization of the air electrode. Polarization occurs if the Zn ion species reach the air electrode.[1], [5] Although limiting Zn ions through the separator is important, OH^- ions still need to be able to reach the Zn electrode for the cell reaction to be complete.[5] Thus, the separator must have selective permeability.

To achieve the desired selective permeability, several approaches have been investigated. These strategies include selection of different materials (such as cationic polysulfonium), coating in an ionic liquid, coating with an insoluble organic layer, and sulfonating the separator.[1], [5], [9] These approaches have shown promising results, such as increased lifetime, increased conductivity, and lower sensitivity of the cell to operating conditions.[5]

2.1.4 Catalysts

The oxygen reaction at the cathode is kinetically slow, though thermodynamically spontaneous. Therefore, overcoming the slow kinetics is crucial in developing an efficient, rechargeable ZAB. To increase the kinetics of the reaction in both directions (charging and discharging), a bifunctional catalyst structure is often desired.[1], [5] The catalyst types that have received the most attention are noble metal and alloys, transition metals, transition metal oxides, and carbon-based catalysts.[5], [15] More discussion on the various catalysts can be found in Section 2.2.

Noble Metals and Alloys

Noble metals such as Pt, Ir, and Ru are commonly used as catalysts for the oxygen reactions at the air electrode due to their good performance, good stability in alkaline and acidic solutions, and low overpotentials.[5], [15], [17] ORR and OER bifunctional electrodes are achieved through the use of a combination of noble metals.[1] In terms of ORR activity, Pt supported on carbon (Pt/C) has the greatest activity and lowest overpotential of the noble metals.[11] As a result, Pt/C (20 wt% Pt) is the most used ORR catalyst and is available commercially.[5], [11] It is for this reason that the development of any new ORR catalysts should be compared with Pt/C. Density functional theory (DFT) calculations and further studies suggest that Ir and Ru oxides are the most suitable noble metal catalysts for OER.[10] The activity of bulk noble metals towards OER follows the trend of Ru > Ir > Pt and can be visualized in Figure 2.2.[10] New OER catalysts are compared with Ru and/or Ir oxides when evaluating their activity. The performance of noble metal catalysts has been shown to further increase through alloying with various transition metals.[11], [10]

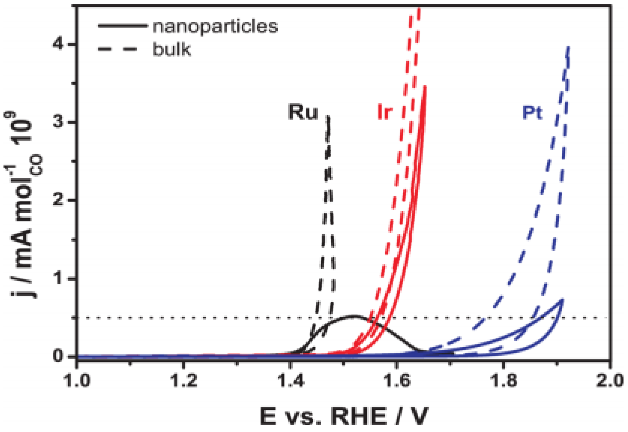

Figure 2.2 – Comparison of OER polarization curves for Ru, Ir, and Pt.[10]

Although noble metals are common catalysts for the desired oxygen reactions, their cost and scarcity is not ideal when creating an affordable and efficient ZAB.[5], [9] In an attempt to reduce cost, investigation into various nanoparticles of noble metals is currently being done.[5], [10] The higher surface area of nanoparticles increases their activity towards the oxygen reactions and reduces the amount of material necessary.[10] However, the higher performance and relatively lower cost of the nanoparticle approach can reduce the stability and lifetime of certain noble metals (Pt and Ru), as shown by the solid lines in Figure 2.2.[10] Alternatively, Ag catalysts have been studied, since their cost is ~1% that of Pt.[5] Ag catalyst structures have also been coupled with CNTs and certain Mn oxides, but they are still fairly remain expensive.[29]

Transition Metals

Transition metals (such as Mn, Co, Fe, and Ni) and transition metal oxides are also commonly used catalyst materials in industry and for various synthesis operations.[1], [5], [30] They are significantly cheaper and more abundant than noble metal catalysts, making them much more desirable for Zn-air applications.[5], [13], [31] Transition metal oxides can be further subdivided into a number of groups depending on the oxidation levels of the oxides.[5] Transition metals operate similarly to their oxide counterparts, but are often supported by carbon-based structures for enhanced stability and conductivity.[1], [13] The largest drawback to both transition metal-type catalysts is the slow process in determining the best candidates, since as their performance varies widely depending on their oxidation state, electrolyte composition, and operating conditions.[1], [5], [9] Furthermore, the catalytic mechanisms governing ORR and OER are not completely understood, making it difficult to predict the behaviour of the metals or metal oxides as catalysts.[13]

Although transition metal and transition metal oxides are cheaper and more abundant than noble metal catalysts, there remain a few challenges limiting their usage. Metal oxides tend to have low conductivity and low stability during operating conditions, low electroactive surface areas, and limited catalyst active sites.[13] As a result, a number of methods to overcome these challenges have been investigated and are shown in Figure 2.3. Nano-structuring of the catalysts has been performed with some success to increase both surface area and the number of active sites.[13], [15] To improve stability and conductivity, hybridizing the catalysts with some sort of support (metal or carbon) has also been done.[13], [15], [31], [32] Further discussion on carbon supported catalysts is found in Section 2.2.2.

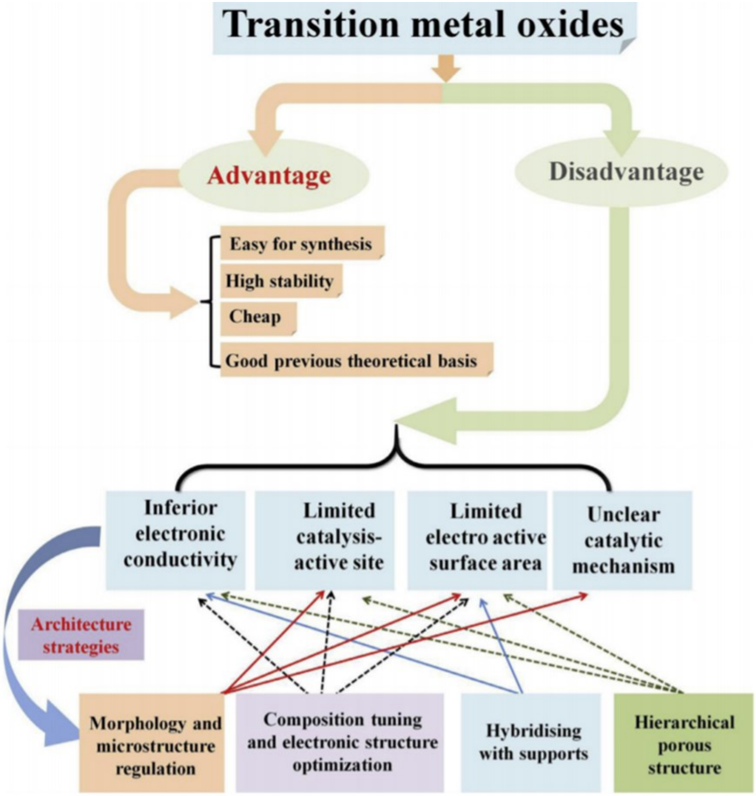

Figure 2.3 – Advantages and disadvantages of transition metal oxides. Common issues with transition metal oxides are noted under Disadvantage, in the blue boxes. Strategies to overcome the various challenges are addressed in the bottom boxes, and arrows are used to relate the strategy to the challenges they address.[13]

Carbon-Based Catalysts

Carbon-based catalysts (such as mesoporous/microporous carbons, CNTs, graphene, and carbon black) have received a lot of recent attention due to their abundance, high surface area, and relatively low production costs.[5], [15] Furthermore, nano-carbon structures have good stability during charge-discharge cycling, which results from their electrical and mechanical properties.[5], [15], [33] For instance, the high conductivity of nano-carbon structures may facilitate electron transfer while the sp^2 hybridization of the C bonds is thought to provide better stability of the structures during OER.[15] Different approaches in terms of synthesis and dopants have been explored in an attempt to reach performance levels that can compete with Pt/Ru, and Pt/Ir bifunctional catalyst structures.[15], [34], [35] More information on carbon-based catalysts is provided in Section 2.2.2.

2.2 Electrocatalysts

In Section 2.1.4, various catalysts used to improve the kinetics of the oxygen reactions were briefly discussed. Among the alternatives for noble metal catalysts, various transition metals and metal oxides as well as nano-carbon structures have achieved moderate success.[15], [36] Additionally, the combination of these metals and the nano-carbons have good synergy, improving activity towards ORR and OER and exhibiting good cyclability.[15] Based on these findings, various metals/metal oxides (particularly Mn, Fe, Ni, and Co, and their oxides), carbon-based catalysts, and combinations thereof are the focus of this section.

2.2.1 Transition Metals and Transition Metal Oxides

Transition metal and transition metal oxide catalysts have been frequently studied as cheap and effective alternatives to noble metal catalysts, both for ORR and OER. Manganese oxides (MnO_x), in particular, have received significant interest for use as electrocatalysts in ZABs because of their good stability in alkaline electrolytes.[5], [15], [19] The many multivalent polymorphs of MnO_x enable a variety of active sites which may favour either ORR or OER.[15] These polymorphs can be seen in Figure 2.4. The tunnel structures and electrical conductivity of MnO_2 polymorphs show strong ORR activity in alkaline solutions, following the trend of α-MnO_2 > β-MnO_2 > γ-MnO_2. In terms of OER, Mn^{3+} structures show better activity when compared with Mn^{4+} due to the more flexible Mn-O bonds in Mn^{3+} being more attractive to OH^-, so that MnOOH structures more easily form.[5], [15], [17] However, the stability of bifunctional MnO_x catalysts under OER conditions remains a challenge, particularly for $\alpha\text{-MnO}_2$.[5], [15] Therefore, MnO_x are often preferred as the ORR catalyst.

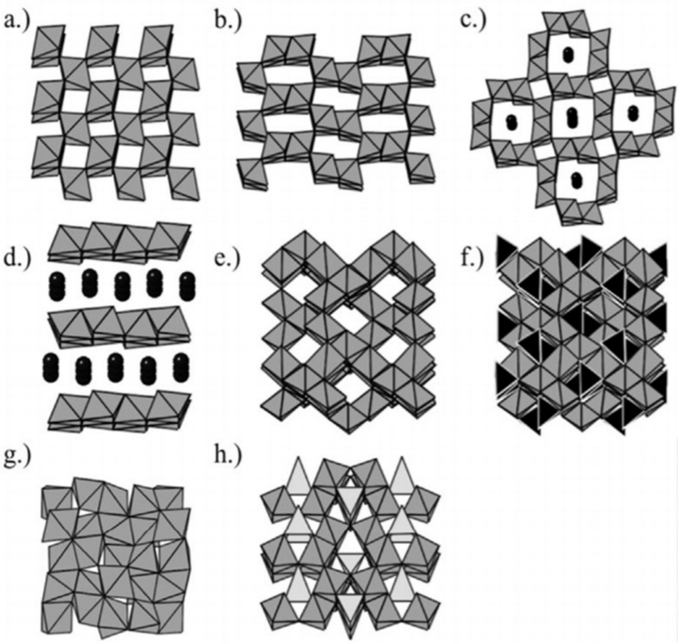

Figure 2.4 – Polyhedral structures of various MnO_x materials. a) β-MnO_2, b) R-MnO_2, c) α-MnO_2, d) δ-MnO_2, e) λ-MnO_2, f) $LiMn_2O_4$, g) Mn_2O_3, and h) Mn_3O_4.[15]

Co-based electrocatalysts have also received attention as OER and bifunctional catalysts for metal air batteries.[31] The spinel structures of many Co oxides allows for the use of Co in different oxidation states within the same structure.[13], [15], [31] Similar to Mn based catalysts, the activity of Co catalysts depends on its oxidation state. For instance, Co^{3+} and Co^{4+} favour OER activity while Co^{2+} favours ORR activity.[31] The activity towards OER or ORR may be explained by the tendency of the Co oxidation state to attract OH^- and O_2 molecules, respectively.[31] In terms of OER activity, Co^{3+} was observed to convert to Co^{4+} just prior to the onset of the OER, suggesting that higher amounts of Co^{4+} will increase OER activity.[15] As a result, the ratio of oxidation states for Co is an important parameter in determining catalytic activity towards the oxygen reactions.[31] Furthermore, the surface and shape of the Co catalyst also has an effect on activity, controlling which oxidation state is exposed.[15] Generally, surfaces exposing more Co^{2+} are more favourable for ORR, since Co^{2+} can attract O_2, donate an electron, and oxidize to Co^{3+}.[15]

Fe and FeO_x catalysts are not widely used for ORR or OER as they are inferior catalysts to Co, Ni, and Mn (and their oxides).[13], [31], [37], [38] However, combining Fe with other transition metals to form bimetallic or tri-metallic oxides has shown promising results.[37], [39]–[41] A study by Rodney et al. on the effects of stoichiometric ratio of Ni, Co, and Fe in individual, bimetallic, and ternary oxide systems found that 20-40 at% of Fe in a bimetallic or ternary oxide system resulted in the lowest overpotential for OER.[38] The study also found that the bimetallic oxides containing Fe compared favourably with their monometallic counterparts. Furthermore, other reports in the literature have shown good activity and stability of $CoFe_2O_4$ spinel towards ORR and OER when supported by various carbon materials (Figure 2.5).[39], [40], [42]

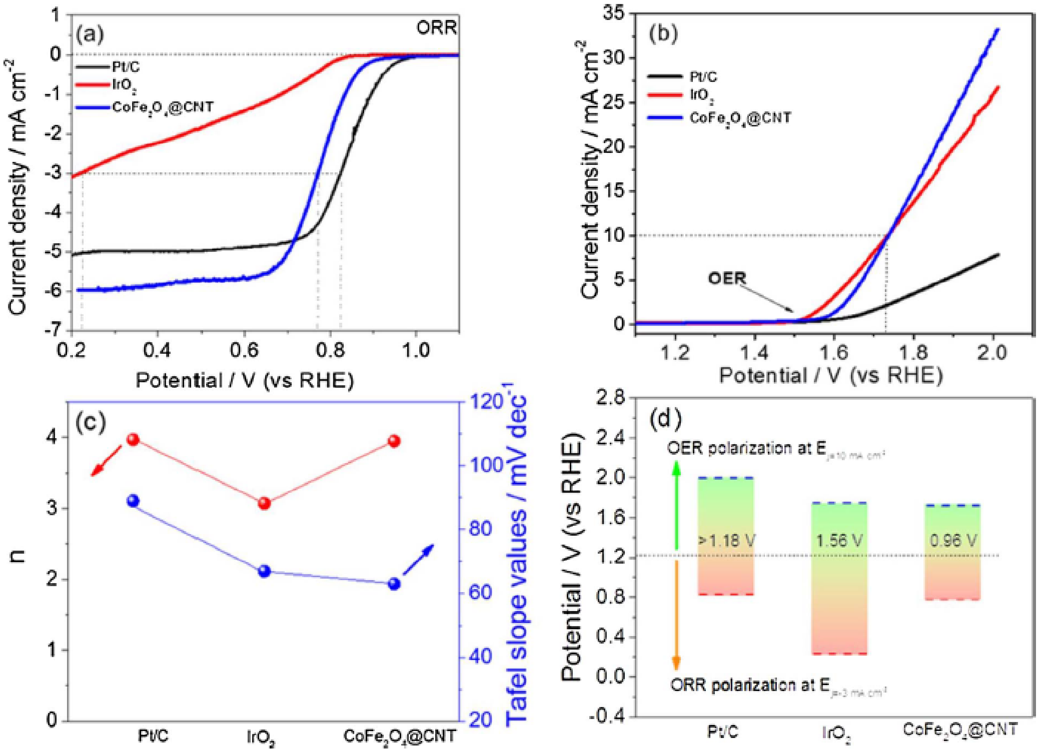

Figure 2.5 - Electrochemical performance of $CoFe_2O_4$@CNT: a) ORR LSV curves, b) OER LSV curves, c) Tafel slope values and electron transfer numbers (n) comparison, and d) charge-discharge potential difference in 0.1 M KOH.[39]

The synergistic effect of Fe and other transition metals (namely Co and Ni) has been reported with two recurring explanations. First, it is proposed that Fe facilitates higher oxidation states of the other transition metals after the initial oxidation event, resulting in better catalytic performance (e.g., Co^{3+} oxidizes to Co^{4+} giving improved OER activity).[38], [43], [44] Second, Fe improves the stability of the metal oxide nanoparticles due to an enhanced electron transport pathway, especially when combined with a carbon support.[43], [44] Despite the promising results reported for Fe-containing, mixed spinel oxides, little research has been conducted on applications for ZABs.

2.2.2 Carbon-Based Catalysts

Carbon-based materials have gained popularity for application in ZAB air electrodes, due to their good stability as both a catalyst and a catalyst support, and their good conductivities and relatively low cost. Two primary types of carbon catalysts are of interest in the current review: meso/microporous nano-carbons and graphene/CNT-metal composites.

Meso/microporous carbons have high surface areas, favourable physicochemical properties, and a large number of active sites for mass transport during cycling.[5], [33] A study by Hadidi et al. synthesized N-doped mesoporous carbon nanoparticles, achieving a discharge voltage of 1.24 V (vs Zn/Zn^{2+}) during galvanostatic cycling at 2 mA cm^{-2}.[33] The catalysts also exhibited good cyclability compared with Pt/C at a current density of 1 mA cm^{-2}.[33] These results suggest significant potential for mesoporous carbons as bifunctional catalysts for ZABs as longer cycle life is currently desired.

Similarly, graphene, carbon black, and CNTs are of interest because of their good stability and electrical properties.[5], [15] These materials display good stability during cycling with minimal catalyst loss in comparison with Pt/C structures.[15], [45] Recent efforts have doped carbon black, CNTs,and graphene structures with nitrogen to improve the number of active sites in the catalyst, in an attempt to increase oxygen adsorption.[1], [5], [45] The increase in the number of active sites is due to the pyrrolic, pyridinic, and graphitic C-N bonds that are formed.[5], [46] Furthermore, N reduces the band gap of the carbon material and reduces the work function at the solid-liquid interface, resulting in decent performance as a catalyst for both ORR and OER.[15], [33], [46] Similarly, S and N, as well as P and N, doped porous carbon structures have been developed with promising bifunctionality. [24], [49], [48]

Fe and Co derived N-doped carbon structures have been studied in efforts to further increase activity for ORR and OER.[15], [50] Metal (M) and N-doped carbons (M-N-C) display an increase in active sites due to the synergistic behaviour between the metals and N, as well as good stability of the active sites and can be applied to both mesoporous nano-carbons and graphene or CNTs.[51] This synergy between the metal, N, and C results in superior performance compared with M-C structures without the presence of nitrogen.[51]–[54] Fe, Mn, and Co M-N-Cs, in particular, provide good ORR and OER performance.[32], [51] A study by Wang et al. synthesized

$Fe_3C/Co(Fe)O_x$-N-CNTs for use as a bifunctional catalyst in ZABs and observed exceptional results.[52] The catalytic activity during ORR and OER in 0.1 M KOH was reported to be superior to Pt/C and IrO_2, respectively. Furthermore, the cycle life of the $Fe_3C/Co(Fe)O_x$-N-CNTs was shown to outperform Pt/C.[52] Polarization curves and a cycle life comparison are shown in Figure 2.6. Generally, ORR performance of M-N-Cs, where M = Co, Fe, Mn, Ni, follows the trend of Mn > Co > Fe and Ni.[32], [51] Metal nitride doped carbons have also been explored due to similar mechanisms to M-N-Cs. The combination of metal nitride active sites for ORR with N-C and M-N-C active centres is also believed to provide superior ORR activity.[51] Additionally, nitrides such as MnN_x and MoN_x, provide a direct 4 electron pathway resulting in greater ORR activity.[17], [51]

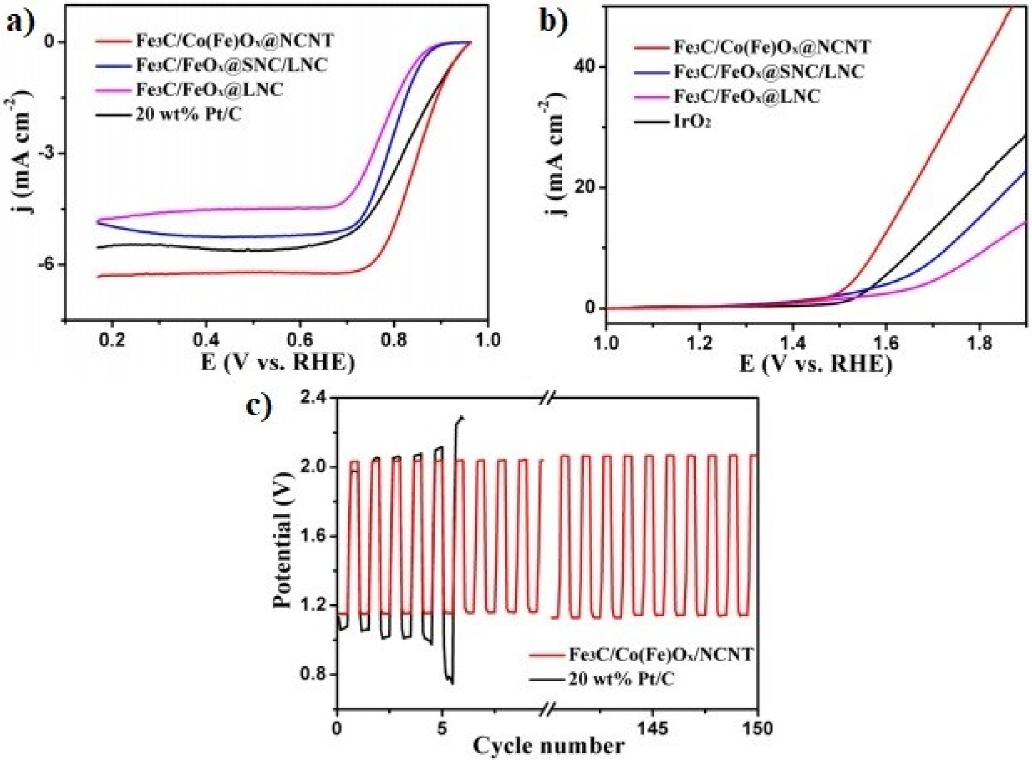

Figure 2.6 - Performance comparison of $Fe_3C/Co(Fe)O_x$-NCNT with Pt/C and IrO_2. (a) ORR comparison, (b) OER comparison, (c) cycle life comparison vs Pt/C at 10 mA cm^{-2}.[52]

Metal-organic frameworks have also shown promising results as precursors for bifunctional catalysts due to their controllable pore size and ultra-high surface area.[15], [47], [48] Alternatively, nano-carbon materials doped with B, N, S, and/or P and co-doped with certain transition metals have exhibited good electrical and mechanical properties, as well as large surface areas and increased numbers of active sites (particularly for ORR).[15], [47], [48] The drawback to organic-derived electrocatalysts is that further doping or addition of foreign atoms into the carbon base often alters the structure, which potentially hinders durability during OER conditions.[15] This challenge stems from the different active sites required to increase the kinetics of both ORR and OER, which often leads to the necessity of two non-metal dopants as well as a transition metal/metal oxide co-dopant.[15] Therefore, work into new synthesis methods has been conducted by multiple research groups.[5], [15]

2.2.3 Doping of Nano-Carbons

Because of the morphologies of commonly used graphene (two-dimensional) and CNTs (quasi one-dimensional) as nano-carbons for electrocatalysis, doping of these materials differs slightly from the conventional definition. Traditional doping refers to substitutional or interstitial addition of foreign atoms into the host material in order to alter its electrical properties; however, the definition is often extended to any substitution, physisorption, or chemisorption.[55] Alternatively, addition of atoms for the purpose of altering chemical reactivity is considered functionalization, and particle formation on nano-carbons is considered synthesis of composite materials.[55]

The addition or adsorption of foreign atoms will result in changes in the Fermi level and band gap, while also affecting catalytic activity.[55], [56] Dopants which increase the number of electron donors are referred to as n-type dopants and those which increase the number of electron acceptors are referred to as p-type dopants. Specifically for CNTs, doping can be organized into three categories: endohedral, exohedral, and substitutional doping, as shown in Figure 2.7.[55] Endohedral doping – or amphoteric doping – refers to atoms, ions, or molecules which are trapped within the walls of the CNTs. Encapsulating the dopants, although challenging, enables good stability to air and the environment, meaning reactions between the dopant and oxygen from air are not expected.[55].Therefore, endohedral doping is not ideal for ZABs.

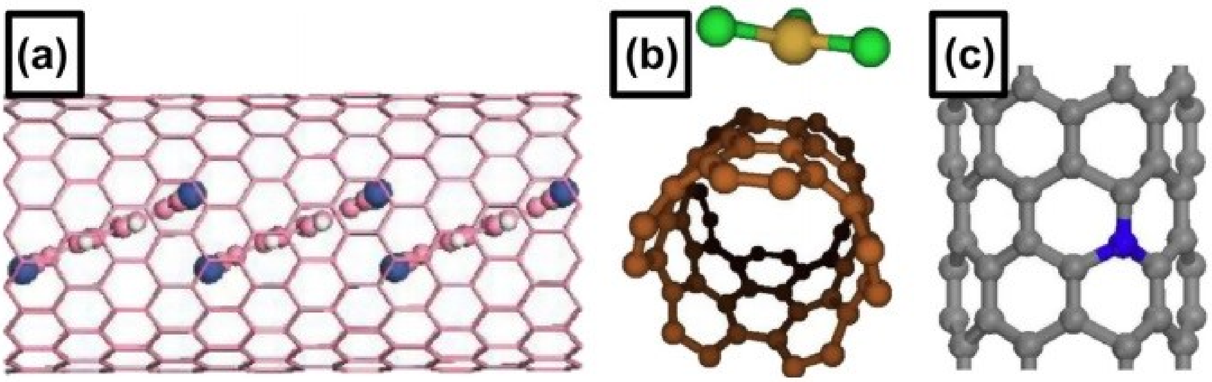

Figure 2.7 – Visual representations of a) endohedral doping, b) exohedral doping, and c) subsitutional doping of CNTs.[55]

Exohedral doping often refers to coordination of the dopant to the outer CNT surface through π-stacking or non-covalent functionalization.[55] Exohedral doping is the simplest and most common method of doping CNTs and depends heavily on the physical characteristics of the CNTs.[55] Some physical properties that are related to the affinity of the dopant to coordinate to the CNT are defects and stereochemistry of the nanotube. Additionally, the diameter of the CNT affects the affinity of the dopant to coordinate. P-type exohedral dopants are more stable than n-type in terms of reactivity with air, which may provide insight into the design of carbon-based catalysts for ORR and OER.[55]

Finally, substitutional doping of CNTs is congruent with the conventional doping definition. Carbon atoms within the CNT structure are replaced by dopant atoms, resulting in a large activation energy.[55] Therefore, substitutional doping is often achieved during the CNT synthesis or under harsh conditions.[55], [57], [58] Since functionalization is achieved through substitution or creation of defects in the CNT, it also relies on harsh conditions in order to break the C-C bonds.[55] Substitutional dopants are most commonly N, B, P, and/or S, with N and B being the most suitable.[34], [48], [55], [59] Nitrogen in particular has attracted a lot of attention in energy storage, fuel cell, and battery applications due to its effect on active sites towards ORR.[36], [45], [59] Nitrogen can be either n-type or p-type depending on the post-doping geometry within the CNT.[55] If the hexagonal structure of the C bonds is not disrupted by N, it becomes an n-type dopant, while alterations resulting in pyridine geometries can result in either n or p-type behaviour.[55] Furthermore, N doping may change the electronic properties of the CNT to a quasi-metallic state and preserve the sp^2-sp^2 structure of the CNT.[55] The latter, as previously discussed, results in better cycle-life of the catalysts in ZABs.[36], [51] Substitutional doping with transition metals results in dislocation towards the inner or outer side of the CNT and can be categorized as endo or exo-substitution, as shown in Figure 2.8.[55] These structural alterations cause delocalized electron density and further alter the electrical properties of the nanotube.[55] Transition metals and non-metallic dopants have been co-doped through the combined use of exohedral and substitutional doping, resulting in the aforementioned M-N-C and other metal-non-metal carbon structures.[32], [36], [51], [55] The combination of substitutional and exohedral dopants increases the amount of chemisorbed molecules as they coordinate to the substitutional dopants as a result of delocalization of electron density.[55], [60] The synergy between exohedral metal dopants and substituted N dopants further increases capacity as well as cycle life because of the strong binding of the metal/metal oxide to the N sites during cycling.[60] Studies of NiO_3-N-CNT for use in Li ion batteries have reported cycle lifetimes of over 10,000 cycles with minimal loss in capacity.[60]

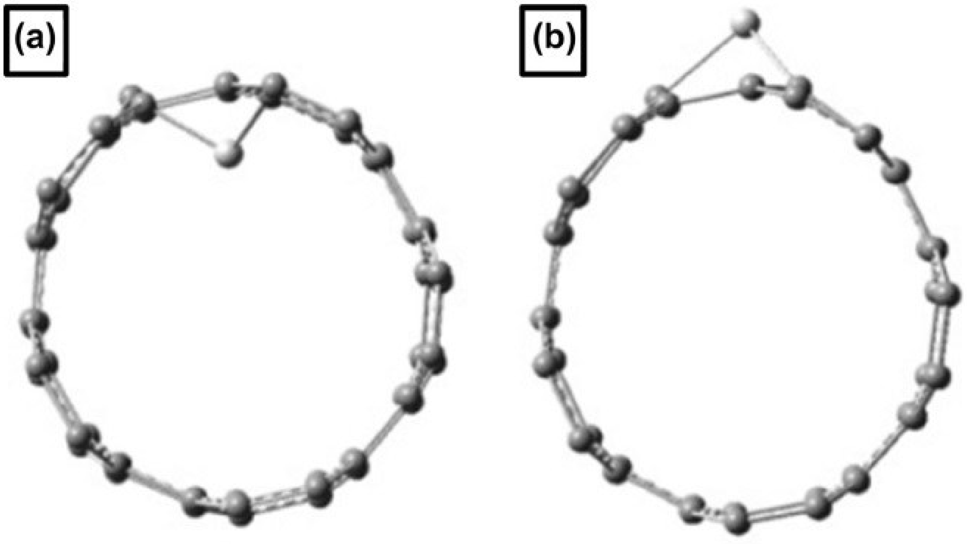

Figure 2.8 – Representation of a) endo-substitutional doping of CNTs and b) exo-substitutional doping of CNTs.[55]

Evaluation of CNT doping depends again on the physical properties. Single-walled carbon nanotubes (SWCNTs) can be evaluated based on diameter changes, certain physical characteristics (such as a "bamboo" structure caused by N doping), and Raman spectroscopy (RS).[55], [61], [62] Multiwalled carbon nanotubes (MWCNTs) are more complicated to evaluate as the number of walls and diameters of the nanotubes are increased. Since the diameter of MWCNTs is too large for RS, doping evaluation is often limited to characterization techniques performed on the nanotube bundles.[55] X-ray diffraction (XRD), x-ray photoelectron spectroscopy (XPS), and various imaging techniques are most commonly used to evaluate the extent of MWCNT doping, although they may be inconclusive in terms of post-doping (doping after CNT synthesis).[55] Alternatively, post-doping and functionalization may be evaluated by measuring changes in the electrochemical characteristics of the nanotubes.[55] Since CNTs are piezo-resistive and have high conductivity, the difference in electrochemical testing results for as-synthesized CNTs and doped CNTs allows for identification of doping.[55], [60], [63] However, electrochemical testing does not quantify the amount of doping or yield information regarding specific changes in CNT structure.

2.2.4 Synthesis Methods

Preparation of nano-carbon supported catalysts varies widely depending on the type of hetero-atoms being used.[19], [35], [45], [48], [52], [53], [64]–[67] Typically, CNT doping is achieved during synthesis or as a post-synthesis treatment.[55], [68] For instance, N doped CNTs are often successfully synthesized through preparation of catalyst islands (ferrocene or Ni) under a nitrogen atmosphere, followed by introduction of a carbon containing gas (CH_4, C_2H_2, etc.).[55], [60], [68] Post-doping of CNTs often requires a treatment of the CNTs to increase the affinity of the dopant to substitute for carbon atoms.[55] CNT post-doping preparations include acid treatments (commonly HNO_3) or the creation of defects within the nanotube through a mechanical process to lower the energy required to break the C-C bonds.[59], [68], [69] After treatment, CNTs and dopant precursors are often mixed in solution, dried and washed, and then carburized at temperatures between 600 and 1000ºC in an inert atmosphere to yield the final product.[57], [59], [68] Other methods of doping using polymers and various novel techniques have also been reported.[32], [70], [71] Transition metal co-doping has also been achieved through both two-step and one-step processes.[32], [66], [72] Most often, transition metal or metal oxide growth on the nanotube walls is achieved through a post-CNT-synthesis hydrothermal method, in which metal substitution or encapsulation occurs during a synthesis method similar to that mentioned above.[32], [72], [73] Various catalysts and their respective synthesis procedures are summarized in Table 2.2.

Table 2.2 - Synthesis Methods of Some CNT Based Catalysts

Final Product	Precursors		CNTs	Synthesis Technique	Half-Cell Performance	Ref.
	Metal	Non-Metal				
M-N-CNTs, M=Co, Fe, Ni	Metal salts/metal salt hydrates (e.g., $CoCl_2$*6H_2O)	Cyanamide (N precursor)	MWCNT, Purchased (Sigma Aldrich)	Mix precursors with ultra pure water @ 80°C, dried then heated to 500C to form graphitic carbon nitride, H_2SO_4 + heating to 700°C in Ar	Co-N-CNT was best. E_{onset} ORR: 0.84 V vs RHE E_{onset} OER: 1.62 V vs RHE	[73]
Fe_3C/Co(Fe)Ox-N-CNT	Ppy-Fe, Co-Zn complex	Ppy-Fe (N and carbon)	Synthesized during process	Ppy-Fe and Co-Zn mixed in MeOH, 900°C in Ar	E_{onset} ORR: 0.86 V vs RHE E_{onset} OER: 1.58 V vs RHE	[52]
M-N-CNTs, M=Mn, Co, Fe, Ni	Metal salts	Dopamine hydrochloride (N precursor), N_2 gas	MWCNT, purchased (Times Nano)	DA HCL with metal salts (1:1 molar ratio, M:DA) in deionized water, CNTs added, Tris added (pH 8.5), centrifuge + wash (DIW + etOH), 800°C for 2h (N_2)	ORR activity follows trend Mn > Co > Fe > Ni; E_{onset} for Mn-N-CNT was -0.1 V vs Ag/AgCl	[32]
Mn_3O_4-O-CNTs	$Mn(CH_3COO)_2$	Oxygen Plasma (O precursor)	MWCNT, purchased (NanoLab Inc.)	CNTs, Mn precursor mixed with LiOH in ethanol, ultrasonicated 5 h, washed & dried, calcined @ 300°C (air), O_2 plasma treatment (700 Torr, 20 min)	E_{onset} ORR: 0.92 V vs RHE E_{onset} OER: 1.64 V vs RHE	[19]
Co-N-S-CNT	$Co(CH_3COO)_2$	Thiourea (C, S, & N precursor), N_2 gas	MWCNT, synthesized, purchased (Alfa Aesar)	Thiourea, Co acetate mixed in pure $H_2$0, dried to make powder, 180°C (N_2) @ 0.5 h, 800°C (N_2) @ 2 h (tube furnace)	E_{onset} ORR: -0.047 V vs Ag/AgCl (i = 0.1 mA cm^{-2})	[34]
MnOx-CNT	$MnSO_4$	N/A	MWCNT, purchased	CNT modified GC electrode put into solution of $MnSO_4$ and Na_2SO_4, voltage of +1.7 V vs SHE + stirring, electrodeposition of MnOx into CNTs	E_{onset} ORR: -0.19 V vs Ag/AgCl (i = 0.1 mA cm^{-2})	[54]
MnO_2-N-CNT	$KMnO_4$	Ppy (C & N precursor)	Functionalized MWCNT, purchased (Sinopharm Chemical Reagent Co. Ltd.)	Ppy, HCL, CNTs mixed, $FeCl_3$ added and stirred 24 h, washed, heated to 900°C (N_2) 4h. N-CNTs, $KMnO_4$, HCL mixed, SDS added, 180°C for 10 h, washed and dried	Not used for ZABs	[66]
MnO_2/CNT-OH	$KMnO_4$	N/A	OH-MWCNT, purchased (Jinyang Nanometer Mat. Co.)	CNTs mixed with $KMnO_4$ for 0.5 h, $MnSO_4$ and H_2SO_4 solution drops added for 0.5 h, dried 60°C, powder heated to 200°C, 400°C, 600°C; 400°C is best	E_{onset} ORR: 0.91 V vs RHE	[53]
$NiCoO_2$/CNT	Ni/Co nitrate hydrates	N/A	Sulfunated polysterene-CNTs, pre-prepared	CNTs mixed with nitrates hexamethylenetetramine and citric acid trisodium salts, 90°C @ 6 h, centrifuged 3 min (7000 rpm), dried 60°C, calcined 450°C @ 2 h (N_2)	E_{onset} ORR: 0.91 V vs RHE E_{onset} OER: 1.48 V vs RHE	[74]
NiO-Fe_2O_3/CNT	Fe/Ni nitrate hydrates	N/A	MWCNT, purchased (Nanjing XF Nano Corp.)	CNTs are acid treated and washed, CNTs and nitrates mixed with NH_4F and urea in DIW, autoclave 120°C @ 6 h, 300°C 2 h (N_2)	E_{onset} ORR: -0.22 V vs Ag/AgCl E_{onset} OER: 0.65 V vs Ag/AgCl	[65]

2.3 Electrode Preparation

Catalyst loading on the air electrode is achieved during electrode preparation. Spray coating and pasting mixtures of synthesized catalysts onto the air electrode are two of the most common practices in the current literature.[15], [18], [31], [34] Additionally, electrodeposition techniques have been tried to deposit transition metals and metal oxides onto the GDL.[64], [75], [76] Each technique suffers from its own challenges; however, in all cases catalyst loading in limited to the surface of the electrode. The various electrode preparation methods are discussed in this section.

2.3.1 Spray Coating and Pasting

Currently, the air electrode is most often prepared by drop casting, spray coating or applying a catalyst paste to the surface of the air electrode.[1], [77] For spray coating and drop casting, a catalyst ink is prepared by mixing the catalyst material with a conductive agent (such as acetylene black or carbon black) and a binder material (such as PTFE or Nafion) in solution.[1], [5], [45] Once the ink has been prepared, it is then applied to the GDL by the respective method. The inconsistency in mass deposited and coverage of the GDL with both spray coating and drop casting are major drawbacks to the techniques and can cause significant variability between samples. Catalyst pastes are made in a method similar to the inks used for spray coating. The catalyst is mixed with conductive and binding agents and stirred to form a slurry.[18], [66], [78] The slurry is then pasted onto the GDL surface. This method can also result in variability on the mass deposited among samples, as with spray coating.

Although the three described methods are common in the literature, they all suffer from similar issues.[1] The binding materials may degrade at the higher charging potentials, causing delamination of the catalysts from the electrode surface.[1], [20], [77] Furthermore, as the electrolyte floods the electrode, the catalyst layer is no longer in contact with both the electrolyte and air.[1], [18], [20] Both key issues result in a decrease in the cell performance and are obstacles that need to be overcome.

2.3.2 Impregnation of Air Electrode

Impregnation is a technique by which the catalyst ink infiltrates the pores of the air electrode and enables catalyst distribution throughout the GDL structure. This technique may hold several advantages, such as simplicity, higher active surface area, preservation of the three-phase region, and improved cyclability of the battery. Despite these apparent benefits, there has been very limited study of impregnation for air electrode fabrication in the literature.

Impregnation of the air electrode may be achieved by soaking the air electrode in the catalyst ink or by directly precipitating catalyst into the electrode through a direct growth mechanism. Soaking the electrode is quite simple and can be used to adjust mass loading by altering the soaking time. Li et al. soaked carbon cloth in a catalyst ink consisting of Mn_3O_4 particles anchored on O-CNTs and achieved a mass loading of 0.5 mg cm^{-2}.[19] The impregnated carbon cloth was then applied to the surface of the GDL; it was used simply as the catalyst layer and not a catalyst impregnated electrode. Similarly, Wei et al. soaked Ni foam in a catalyst ink of bimetallic oxide graphene particles and then pressed two pieces of impregnated Ni foam together to form a plate to be used as the air electrode.[43] The prepared electrode displayed good performance and better bi-functional cyclability than Pt and IrO_2 on carbon at 25 mA cm^{-2}.[43]

Alternatively, Sumboja et al. directly deposited MnO_2 catalysts into porous carbon paper by immersing the paper in the catalyst precursor solution.[79] The directly grown catalyst was reported to increase the active surface area without blocking the pores of the air electrode and showed good activity towards ORR. The directly grown catalyst had superior cycling stability when compared with both powdered MnO_2 and Pt/C (20 wt%).[79] Sumboja et al. proposed that the directly grown catalyst preserved the three-phase boundary during cycling and had improved contact to the air electrode which facilitated charge transfer. Both effects resulted in improved battery performance. However, no other reports highlighting the benefits of impregnation-type electrode preparation have been reported despite the promising results and simplicity of the techniques.

2.3.3 Electrodeposition

Electrodeposition (ED) is an electrochemical technique which enables the fabrication of films and coatings with tunable properties on various substrates.[80], [81] The technique is not limited by the shape of the substrate and can be performed at low temperatures.[80] Commonly, the technique is used for the synthesis of nanostructured or nanocrystalline coatings, but is not limited to the deposition of metals.[80], [81] Due to the high level of control over the deposition process and the simplicity of the technique, ED is promising as a method of preparation for the air electrode in ZABs, allowing for the deposition of a wide range of ORR and OER catalysts.

Deposition is achieved by passing electric current between electrodes through the electrolyte and relies on Faradaic (reduction and oxidation) behaviour and charge transfer to electrodeposit the desired material.[82] Precursors (often metal salts) are dissolved into the electrolyte and their respective ions are then reduced onto the electrode surface to form a solid coating.[80]–[82] Therefore, the process relies on ions and electron transfer.[81]

In order to control the deposition process, several parameters, such as choice of electrode, the type of cell, the electrolyte composition and concentration, the temperature, the pH, and the applied current or voltage, need to be controlled.[81], [82] The working electrode or substrate must be electrically conductive for successful deposition, since conductivity correlates to the kinetics of the deposition.[81] The working electrode is often placed between a counter electrode and a reference electrode in order to control the relative charge of the substrate.[82] Alternatively, the working electrode may be the cathode or anode in an electrolytic cell, where no reference electrode is necessary.[81] The bath conditions (electrolyte composition, pH, temperature, etc.) and applied current/voltage are important parameters and depend on the species to be deposited.[80]

During deposition, the activity of the precursor in solution decreases.[82] The decrease in activity can be compensated by modifying the current density or applied voltage. Thus, two types of ED processes are possible: galvanostatic ED and potentiostatic ED. Galvanostatic ED refers to controlling the current density and allows for greater control over the rate of deposition and typically results in good adhesion of the product.[82] However, controlling the current density allows the potential to drift and may also result in a multiplicity of products, depending on the precursor material.[82] Potentiostatic ED refers to controlling the potential by using a reference electrode and results in a more pure product.[82] The potential can be determined through the combined use of linear sweep voltammetry of the electrolyte and referencing the Pourbaix diagram of the system.[81], [82] The drawback, however, is that the current density and activity of the reactant will decay as the reaction proceeds.[82] Pulsed ED is another technique that may be utilized, where the current or potential are pulsed on and off. Pulsing is often used to create nanotubes/nano-rods or porous coatings.[81]

The deposition of metallic species relies heavily on nucleation and growth mechanisms.[81] Nucleation of the metallic film occurs preferentially on defects (such as imperfections and grain boundaries), holes, inclusions, adsorbed molecules, and certain oxide layers.[81] Therefore, it is important to select an appropriate substrate and cleaning procedure before deposition.[80]–[82] Table 2.3 lists a number common substrates. Once deposition of the metallic film is complete, metal oxide coatings can be achieved by applying oxidizing currents through the coating or annealing the substrate.[81], [82]

Table 2.3 - List of Common Working Electrodes[81]

Common Working Electrodes
Pt
Au
Cu
Stainless Steel
Vitreous (Glassy) Carbon
Indium Tin Oxide (ITO)
Fluorine Doped Tin Oxide (FTO)

Co-deposition during ED can be performed in several ways. Metallic co-deposition has been achieved by using baths with different compositions in sequence or by using mixed precursors in a single bath.[41], [76], [80]–[82] Using several electrolyte baths in sequence enables co-deposition of metals in layers, while using mixed precursors in a single electrolyte bath can deposit alloys or layers by varying the applied potential. Alternatively, co-deposition of metals and ceramic materials has been achieved by suspending ceramic particles in the electrolyte and using the motion of the metal ions to deposit a composite film.[81], [83], [84] In order to deposit ceramics and other non-metals through electrochemical processes, an alternative method to traditional ED must be applied. Electrophoretic deposition (EPD) functions on similar mechanisms to traditional ED, but uses net particle charge to attract non-metallic materials (ceramics/metal oxides and organics) to the substrate instead of relying on ions and charge transfer.[85] EPD typically utilizes an electrolytic cell (negative cathode and positive anode) and suspended non-metal particles in a liquid medium.[85] As a result, positively charged particles will deposit on the cathode, while negatively charged particles will deposit on the anode A variety of parameters need to be controlled to optimize the deposit and product characteristics. These parameters may be divided into two categories: suspension parameters and process parameters.[85]

Like the bath parameters of ED, suspension parameters for EPD refer to the characteristics of the liquid medium. In particular, these parameters refer to the zeta potential of the particles, the dielectric constant of the solution, the conductivity of the solution, and the viscosity of the solution.[85] Generally, low viscosity, a dielectric constant typically between 12 and 25, and relatively low conductivity of the solution are preferred, although the parameters may change depending on the desired product.[85] The zeta potential is a key factor in EPD, as it influences the stability of the suspension (interaction between particles), the direction and velocity of the particles, and the density of the deposit.[85] The zeta potential is not easily measured and is dependent on the solvent, temperature, and pH.[85] Therefore, optimizing the solvent, temperature, and pH is required for EPD.

The process parameters of EPD are also similar to those of ED, and include the applied voltage, deposition time, and concentration of precursor.[85] Higher applied voltages generally result in larger deposit mass, but may lower the deposit quality.[85] Deposition time has a logarithmic relationship with the deposit mass. Lower deposition times correlate linearly with mass, while longer deposition times reach a plateau or limit to the mass deposited. The relationship between time and mass is a consequence of the formation of an insulating layer on the electrode surface, which occurs at longer deposition times.[85] It should be noted that deposition time is being discussed in a relative sense and it will vary based on the particles being deposited.

Although ED and EPD are techniques commonly used to prepare films and coatings in a variety of applications, limited work has been done using these techniques as an electrode preparation method for ZABs. However, electrodeposition of Mn and Co in ZABs would create better contact and adhesion between the catalysts and the electrode surface in addition to reducing the need for binders (such as PTFE and Nafion).[41], [80] Deposition conditions for both Mn and Co oxides vary widely depending on the desired phase and application. For instance, anodic deposition is more common for MnO_x, and uses Mn^{2+} ions in the deposition solution.[86], [87] However, cathodic deposition of Mn^{7+} has also been reported for the deposition of MnO_2.[76], [86], [87] One of the challenges faced by the ED of Co is HER. HER happens in parallel to the Co deposition reaction and has a significant effect on the properties of the deposited film due to fluctuations in the pH.[88] Similar to MnO_x, the film's properties may influence capacitance, surface area, durability, and conductivity, and thus fine tuning of ED parameters is necessary to improve the OER performance for ZABs.[75], [87], [88] For instance, addition of Fe to Co deposits has been observed to improve the catalytic activity of the cobalt deposit.[41], [75]

Many nano-carbon based materials and composites have been investigated as catalysts for ZABs. Though most nano-carbon materials are applied to the electrode in a paste like that described for Mn and MnOx, ED is an attractive alternative due to its relative simplicity and tunable properties. ED of graphene and CNTs has been scarcely reported in literature without the addition of some co-deposition material. However, there is evidence that such nano-carbons may be deposited potentiostatically. Jiang et al. reported deposition of a N-doped graphene-CNT composite material by potentiostatic deposition at 1.7 V in double distilled water and 0.1 M KCl solution.[89] More commonly, CNT and graphene-based materials have been deposited through electrophoretic processes. As mentioned, EPD is effective for depositing ceramic and other particles in suspension and is therefore an effective means for depositing nano-carbons.[90] Successful EPD of graphene-based materials has been reported in literature through several methods, but very limited work has been conducted for the applications in ZABs.[72], [83], [91], [92]

2.4 Microstructural Characterization Techniques

Evaluating and understanding the mechanisms and challenges associated with each component of the battery is essential to the progress in ZAB development. To achieve these goals, various characterization techniques are used in tandem with battery testing methods. This section focuses on the characterization techniques that are commonly used for ZABs and employed in this thesis.

2.4.1 Scanning Electron Microscopy and Energy Dispersive X-ray Spectroscopy

Although some characterization can be achieved through general observation and optical microscopy, electron microscopy enable the evaluation of topography and morphology at a much higher resolution.[93] Many of the challenges faced by ZABs require this resolution. For instance, the microsize and nanosize pores of the GDL, ZnO deposition on the Zn electrode, the nanoscale nature of the catalyst structures, and the oxidation of the GDL all require better resolution than that provided by optical microscopy. As such, scanning electron microscopy (SEM), coupled with energy dispersive X-ray (EDX) spectroscopy, is widely used for battery component microstructural characterization.[93]–[95]

SEM and EDX use a finely focused electron beam which is scanned over the surface of the sample, and creates secondary electrons, backscattered electrons, and characteristic X-rays.[93] These signals are then received by respective detectors to achieve images (through SEM) and compositional analysis (through EDX).[93], [94] Secondary and backscattered electrons both generate images, but provide different types of information. Secondary electrons (SE) are low energy valence electrons (typically less than 25 eV) ejected from the near surface region of the sample and provide information about the topography of the sample.[93], [95] SEs receive their kinetic energy from the incident electron beam and result from several inelastic scattering mechanisms.[93] Many SEs are reabsorbed by the material during scattering, so only those emitted near the specimen surface (depth of <20 nm) are detected.[95] Backscattered electrons (BSE) are the incident energy electrons that have been scattered by the sample at angles high enough for them to leave the sample surface (90° – 180°); they have much higher energies than SE, in some cases with energies approaching the energy of the incident electron beam.[93], [95] BSE provide atomic number contrast, since backscattered yield increases with increase sample atomic number.

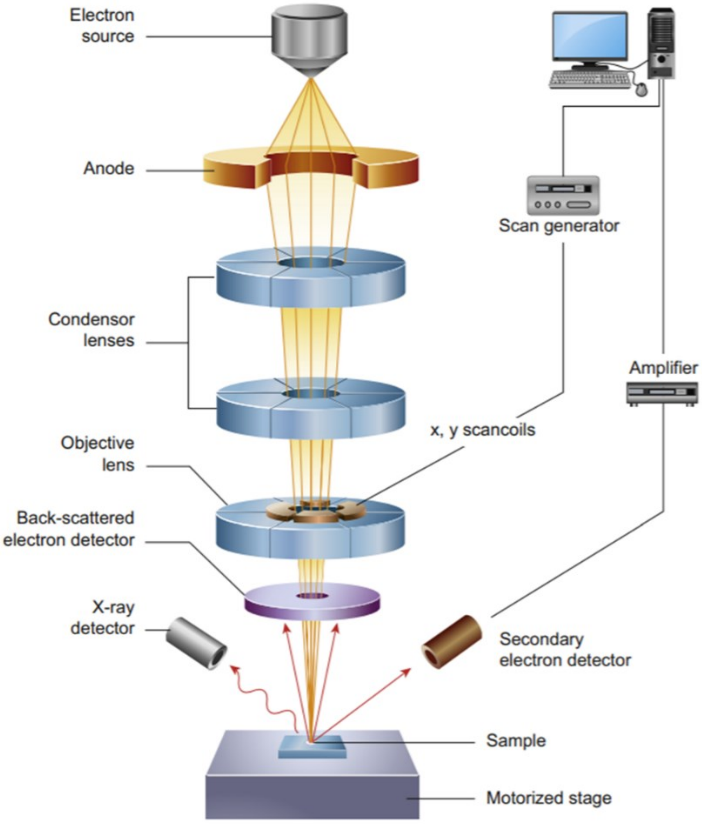

Figure 2.9 – Schematic representation of a conventional SEM.[95]

SEM instruments may have thermionic emission (TE or TESEM) or field emission (FE or FESEM) electron sources. A schematic of a conventional SEM instrument is shown in Figure 2.9. TESEM instruments will use either a tungsten filament or solid-state LaB_6 crystal as the electron source.[93] In TESEM, the electron source is heated resistively to produce the electron beam. The best imaging resolution of TESEM is ~5 nm.[96] FESEM instruments generate finer electron beams and produce images with better resolution than TESEMs.[93] The electron source for FESEM instruments is a field emission gun which often uses a single crystal tungsten filament with a sharp tip. The electron beam is produced by using a high electric field to extract electrons.[93], [95] As a result, the imaging resolution of FESEM is approximately 1.5 nm.[96] Depth resolution of the specimen surface can be further improved by lowering the accelerating voltage.[93], [96] EDX analysis is used to determine the composition of the electrodes and catalysts through the detection of characteristic X-rays.[15], [17], [93] However, EDX detection is limited to elements whose atomic number is greater than that of boron and the spatial resolution is ~1 μm.[93], [95] As mentioned, upon interaction with the incident beam three signals are emitted from the specimen; SEs, BSEs and X-rays. X-rays are generated through inelastic scattering mechanisms similar to SEs. As the incident electrons interact with the atoms of the specimen, electrons can be excited and ejected from the nucleus. An electron from the outer shell of the atom will replace the ejected electron and emit an X-ray.[93], [95], [96] These X-rays can be detected and used for chemical analysis of the specimen, since each element has a unique X-ray spectrum.[95] An EDX detector collects the characteristic X-ray signals and plots the intensities as a function of energy. The resulting EDX spectrum can be used to determine chemical composition of the specimen.[93] Other common techniques used to determine composition include Raman spectroscopy, X-ray photoelectron spectroscopy (XPS), secondary ion mass spectroscopy (SIMS), among others.[1], [94], [97]

2.4.2 Transmission Electron Microscopy

As previously mentioned, many of the electrode components in ZABs are nanoscale in nature, particularly the catalysts which are often nanoparticles, nanorods, thin films, or nanotubes. Transmission electron microscopy (TEM) uses an electron beam, which passes through a thin sample. The scattered and/or unscattered electrons are used to form images with better resolution than an SEM. Therefore, TEM is a powerful technique for characterizing the catalysts used in ZABs.[1], [18], [95] A conventional TEM instrument is shown in Figure 2.10.

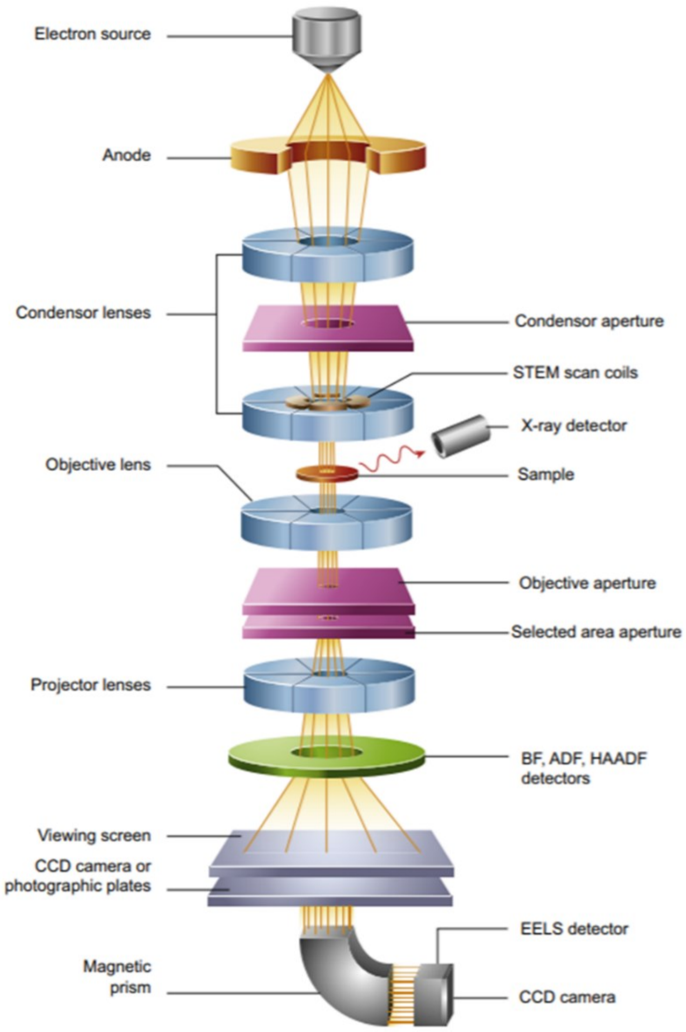

Figure 2.10 – Schematic representation of a conventional TEM instrument.[95]

Similar to SEM, TEM instruments form images based on the interaction between an electron beam and the sample. In TEM, the electron beam is produced by an electron gun at accelerating voltages up to 300 kV.[95] However, unlike SEM, conventional TEM images are produced using the transmitted electrons which require electron transparent specimen. Therefore, the material imaged in TEM must be thin (up to ~200 nm thick).[95], [96] Additionally, TEM instruments have more electromagnetic lenses than SEM instruments, enabling a more focussed electron beam and better resolution (best resolution is 0.05 nm).[95], [96]

Interaction between the electron beam and the specimen produces multiple signals. These signals include unscattered electrons, scattered electrons (elastic and inelastic) and X-rays and are formed by the same mechanisms explained in Section 2.4.1.[95] As elastically scattered electrons pass through the sample, their wavelength does not change but they may change direction. Interference between scattered electrons generates strong beams of transmitted electrons at specific angles.[95], [96] These angles are determined by the crystal structure of the specimen material and are analogous to x-ray diffraction.[96] As the diffracted electrons are collected by the detector, an electron diffraction pattern is formed. Use of this technique over a specific area is called selected area diffraction (SAD).[95], [96] If the material is a single crystal, a spot pattern is formed, while polycrystalline materials will form ring patterns resulting, with each ring correspond to a set of Miller Indices.[96] The radius of these rings is measured and is related to the inverse of the interplanar spacing.[95], [96] The spatial resolution for electron diffraction can be <10 nm.

Bright-field (BF) images may be generated by blocking the scattered electrons with the objective aperture.[95] Areas of the specimen with significant amounts of scattering will appear as dark regions in the BF image; e.g., grain boundaries and dislocations.[95], [96] BF images are useful for analyzing surface characteristics and defects within the specimen. If the specimen is thin enough (<100 nm), then high resolution TEM (HRTEM) images may be achieved. HRTEM images are produced due to interference of elastically scattered electrons to form complex patterns.[96] Some interference patterns may correspond to atom positions and yield information regarding sample crystallinity.[95], [96] HRTEM and SAD are useful tools in determining phase and crystallinity of nanocatalysts used in ZABs. Alternatively, the objective aperture can be used to block the unscattered electrons to generate a dark field (DF) image. The contrast produced in the image is complementary to that in a BF image.

A TEM can also be coupled with scanning coils (similar to an SEM) to give a hybrid TEM/STEM (scanning transmission electron microscope). Images can also be generated in STEM mode; e.g., BF images where only the unscattered electrons are collected to form images or annular dark field (ADF) images where the scattered electrons are collected to form images.[95], [96] ADF images provide chemical information since scattering of electrons increases as the atomic number (Z) of the sample increases.[95], [96] Areas with higher Z elements will appear bright in ADF images.

Chemical analysis, using characteristic X-rays may be achieved using either TEM or STEM modes. The basic principles for generating and detecting X-rays is the same as for SEM. The main difference is the improved spatial resolution for TEM/STEM versus SEM. Because thin samples are used for TEM analysis, the interaction volumes are much smaller than for SEM, which provides spatial resolution better than 10 nm.[95], [96]

2.4.3 X-ray Photoelectron Spectroscopy

X-ray photoelectron spectroscopy (XPS) can yield surface layer elemental and chemical bonding information.[98], [99] The technique measures the kinetic energy distribution of photoelectrons emitted from core levels of elements within a solid by irradiating the sample with X-rays and has an average depth resolution of approximately 5 nm.[98], [100] XPS can detect all elements except H and He.[98] An XPS system typically consists of an X-ray source (either Al-K_α or Mg-K_α), a photoelectron detector, and an electron energy analyser operated under ultrahigh vacuum.[98]–[100] Upon interaction with the sample, the X-rays excite and eject core level electrons.[98]–[100] These electrons have various energies which are characteristic to the atom from which they were ejected. The electrons are detected, counted, and then plotted as a function of the kinetic or binding energies.[98], [99]

$$h\nu = E_K + E_B + \phi, \tag{8}$$

Elements can be identified by the core electron binding energy (E_B), which is related to the incident X-ray energy ($h\nu$), kinetic energy (E_K), and work function (ϕ).[99], [100] Upon the release of the photoelectron, a vacancy is left in the atom core. This vacancy is replaced by an electron from the outer shell and an Auger electron or a characteristic X-ray are emitted. An example of an XPS survey spectrum for N-CNTs on GDL is shown in Figure 2.11, which is a plot of signal intensity versus the binding energy; the energy resolution is 0.1 eV. XPS detects both photoelectrons and Auger electrons, which can yield more insight into sample composition.[98] The area under a given peak is directly proportional to the concentration of the respective element and can be used to determine the relative concentration of that element within the surface of the sample.[98], [99] Since peak intensity and position can change based on sample surface area, surface contaminants, and various measuring conditions, it is difficult to determine absolute concentrations within the sample.[98], [99] For calculation of the relative concentrations of each element, the respective spectra must be calibrated and must have their backgrounds removed.[99] Calibration of the instrument is often achieved using the C 1s peak (binding energy of ~285 eV); however, other material standards can also be used for calibration in instances where the C 1s is not appropriate (such as the Au $4f_{7/2}$ peak).[98], [99], [101]

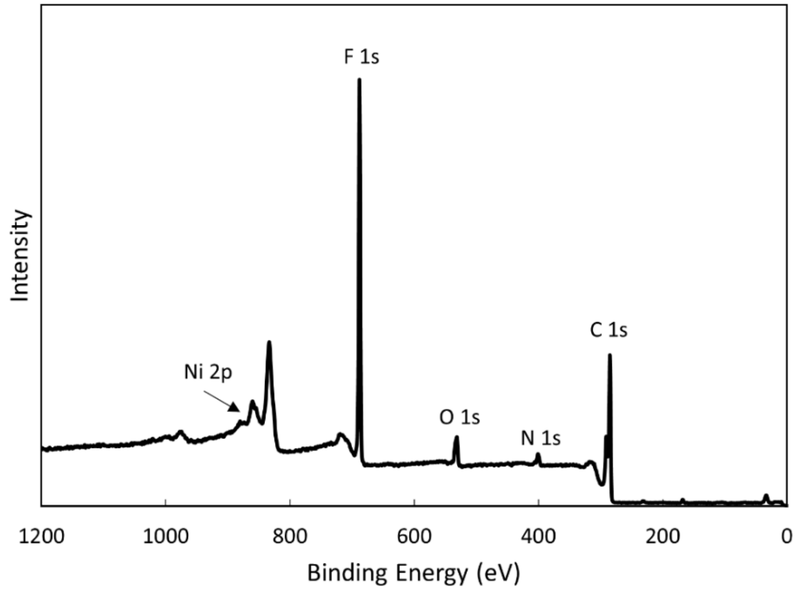

Figure 2.11 – XPS survey spectrum of N-CNTs on GDL.

Chemical bonding information can also be determined from XPS results. Bonding information of a given element is reflected in the XPS spectrum in various ways. For instance, the peak position (chemical shift), Auger parameter (sum of photoelectron binding energy and Auger electron kinetic energy), satellite structure, and multiplet splitting can all be used.[98], [99] The chemical shift depends on the chemical environment (bonding) as well as the oxidation state of the element in question.[98], [99], [102] Generally, a lower oxidation state (lower electron density) results in peak positions at lower binding energies.[98], [99] As a result, the spectrum of a given element may be deconvoluted into a number of components related to various chemical bonds. An example is the O 1s spectrum,[99] which is often deconvoluted into a variety of components that correspond to different oxygen bonds (e.g., O-C, O-H, O-Metal, etc.).[103], [104] These differences arise from the different bonding energies of various chemical bonds. However, the accuracy of the fitted components varies due to inevitable fluctuations in peak position and requires careful interpretation.[99] Experimental XPS spectra are generally compared with spectra from standards to aid in interpretation of the data.

The XPS photoelectron spectra of metals and metal oxides are often more complex due to plasmon losses, mixed oxide, and hydroxide structures, and their ability to form high-spin or low-spin compounds. As a result, multiplet splitting of the metal's 2p spectrum is useful in determining the oxidation state of the material. Multiplet splitting occurs in high-spin metal compounds due to unpaired electrons. Photoionization causes a core electron vacancy in the metal atom, leaving an unpaired core electron. As a result, coupling between the unpaired core electron and an unpaired outer-shell electron may occur and causes multiplet peaks in the XPS spectrum.[99], [102], [105] Multiplet splitting of the 2p peaks enables more reliable chemical analysis by constraining the components (position, full-width-half-max, and areas) relative to one another for a given oxidation state.[99], [102], [105], [106] An example of multiplet peaks for the Fe^{2+} and Fe^{3+} species in Fe_3O_4 is shown in Figure 2.12. Multiplet splitting is a useful tool in interpreting XPS data of transition metal oxide catalysts, which are commonly utilized in ZABs.

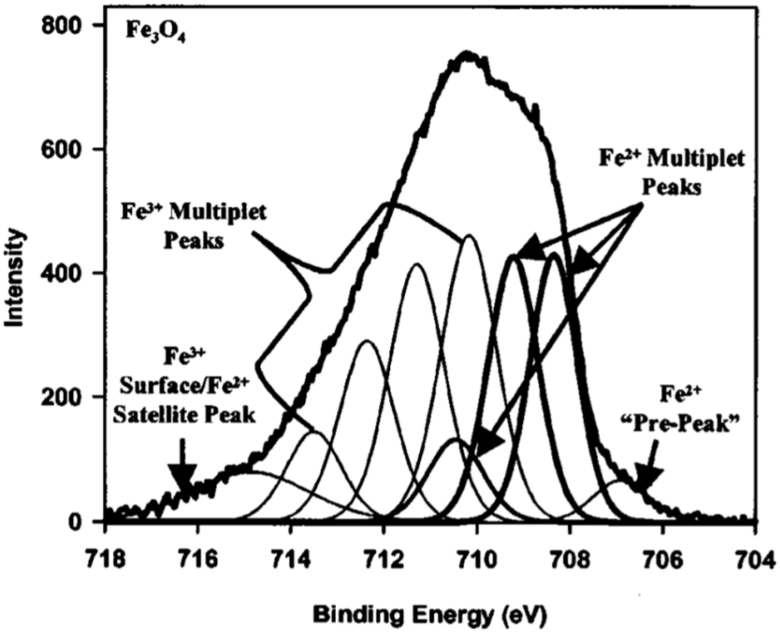

Figure 2.12 – XPS spectrum showing Fe 2p multiplet splitting for Fe^{2+} and Fe^{3+} species in Fe_3O_4.[102]

2.4.4 X-ray Diffraction

X-ray diffraction (XRD) is another useful technique for the characterization of materials. XRD analysis is achieved by irradiating a sample with X-rays of a given energy.[107] Unlike EDX, XRD measures X-rays diffracted by the atoms rather than those produced by electron excitation and ejection.

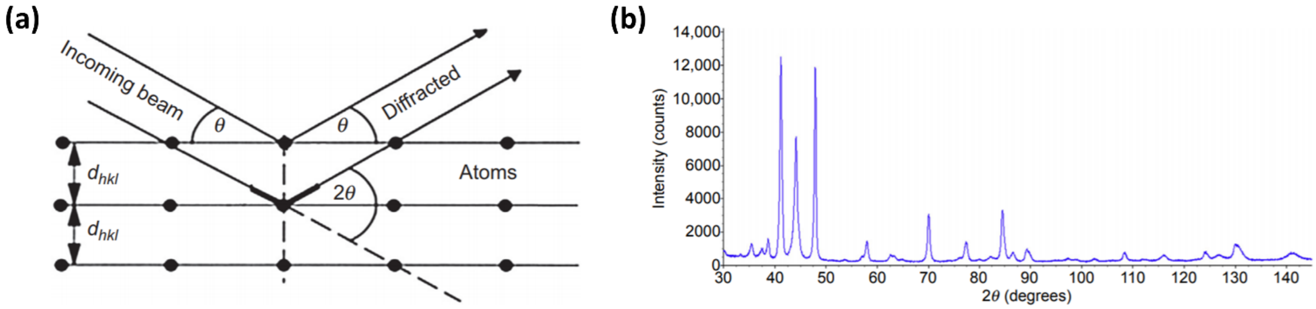

Figure 2.13 – a) Schematic representation of incident and diffracted X-rays in XRD analysis related to Bragg's Law (Equation 9) and b) an example of an XRD pattern for nitirided tool steel X40CrMo V5-1.[107]

As the incident X-rays interact with the sample, they scatter elastically in all directions and maintain the same energy as the incident beam (Raleigh scattering).[107], [108] Materials with a periodic atomic structure (such as crystalline materials) cause constructive and destructive interference of the scattered X-rays.[107] This interference leads to characteristic diffraction phenomena and allows for the identification of crystal structure. The diffraction phenomena are related geometrically to Bragg's Law (Equation 9, Figure 2.13a), where n is the order of diffraction, λ is the X-ray wavelength (nm), d_{hkl} is the lattice spacing (nm), and θ is the angle of the diffracted X-ray in degrees.[107], [108] The detected X-rays and their intensities are represented graphically as a function of 2θ (Figure 2.13b).[107]

$$n\lambda = 2d_{\text{hkl}} \sin\theta \tag{9}$$

The peak positions and lattice spacings can be compared to standards and results from XRD databases to identify crystal structure and phase.[107], [108] However, the peak width and intensity can be affected by several factors, such as instrument broadening, composition homogeneity, crystallite size, defects, and inhomogeneous strains.[107] XRD is often used for characterization of the ZAB air-electrode; e.g., crystallite size and composition effects. As crystallite size decreases, XRD peaks will broaden which may make identification more difficult.[108] Therefore, thin film XRD techniques are often implored to accurately characterize catalyst structures.[107], [108]

2.5 Electrochemical Testing Methods

There are several testing methods which are used to evaluate ZABs in terms of the individual components (half-cell testing) or as a full battery cell (full-cell testing). Half-cell testing provides information on the function-specific performance of a component, while full-cell testing provides information of the combined performance of multiple components. Some of the important parameters include open-circuit voltage (OCV), discharge voltage or operating voltage, power density, energy efficiency, and cyclic stability.[1] In this section, both half-cell and full-cell testing methods are discussed.

2.5.1 Electrochemical Impedance Spectroscopy

Electrochemical impedance spectroscopy (EIS) is used to determine resistances and capacitances within the cell through interpretation of Nyquist plots.[1], [109] EIS measurements are achieved by a superimposed sinusoidal voltage to the electrode at a frequency (ω) which generates a current response. Using Ohm's Law ($I = V R^{-1}$), impedance can be calculated. The technique is conducted at different frequencies to achieve an impedance spectrum, which is represented in a Nyquist plot (Figure 2.14).

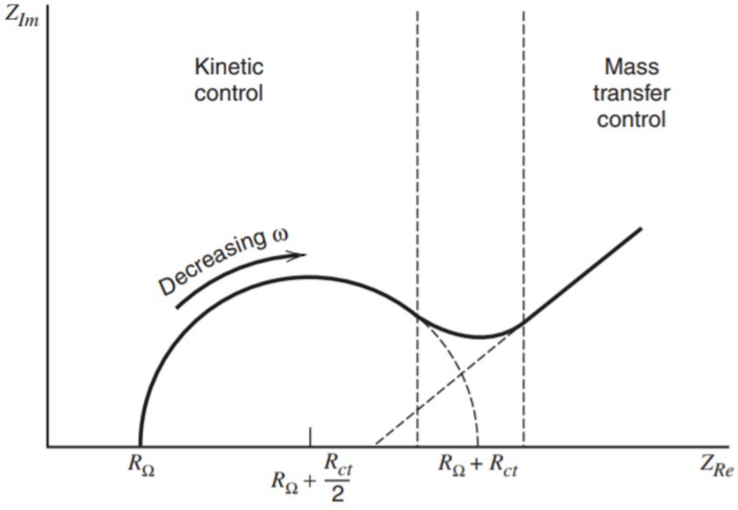

Figure 2.14 – Representation of EIS measurements graphically in a Nyquist plot.[97]

The Nyquist plot shows two regions of interest: the high frequency region and low frequency region. In the high frequency region, the solution (contact) resistance is determined where impedance is zero (intercept of the x axis).[97], [109], [110] Meanwhile, charge transfer resistance can be determined from the size of the semi-circular region. Specifically, the diameter of the semi-circle is interpreted as the charge transfer resistance.[97] The low frequency region is often diffusion controlled. This region gives information about the Warburg impedance, which is the impedance resulting from mass transport limitations by diffusion.[109]–[111] Warburg impedance can be determined from the Nyquist plot by a positive slope in the low frequency region next to the semi-circle and can be used to calculate the diffusion coefficient of the reaction.[97], [109] In instances where both kinetic and diffusion behaviours are observed (Figure 2.14), modelling may be necessary to appropriately determine the values of charge-transfer resistance and Warburg impedance.[97]

Often EIS is performed for ZABs to confirm proposed resistances in the cell (interface and electrolyte) and to compare activity of catalysts for the oxygen reactions.[1] Therefore, the high frequency region of the Nyquist plot is of interest. Moreover, since the oxygen reactions are kinetically limited, Warburg impedance is sometimes not observed. The cell resistances can be confirmed by the x-intercept of the Nyquist plot, while the catalyst activity can be compared from the charge-transfer resistance. In short, a smaller semi-circular behaviour in the Nyquist plots suggests promising catalyst materials.

2.5.2 Cyclic Voltammetry and Linear Sweep Voltammetry

Cyclic voltammetry (CV) and linear sweep voltammetry (LSV) are electrochemical techniques that measure the current response as a function of applied voltage. [97], [110], [112] Both techniques rely on a potential sweep at a given scan rate (v) between two potential limits (E_1 and E_2). LSV is the simpler of the two techniques as the technique is terminated once the potential reaches E_2.[112] For CV, the sweep is reversed once E_2 is reached and can be cycled between E_1 and E_2 to observe the change in behaviour of the current response.[97], [110], [112] As a result, CV can provide more information regarding the roles of absorption, diffusion, and chemical reactions while LSV can provide insight into reaction kinetics.[112]

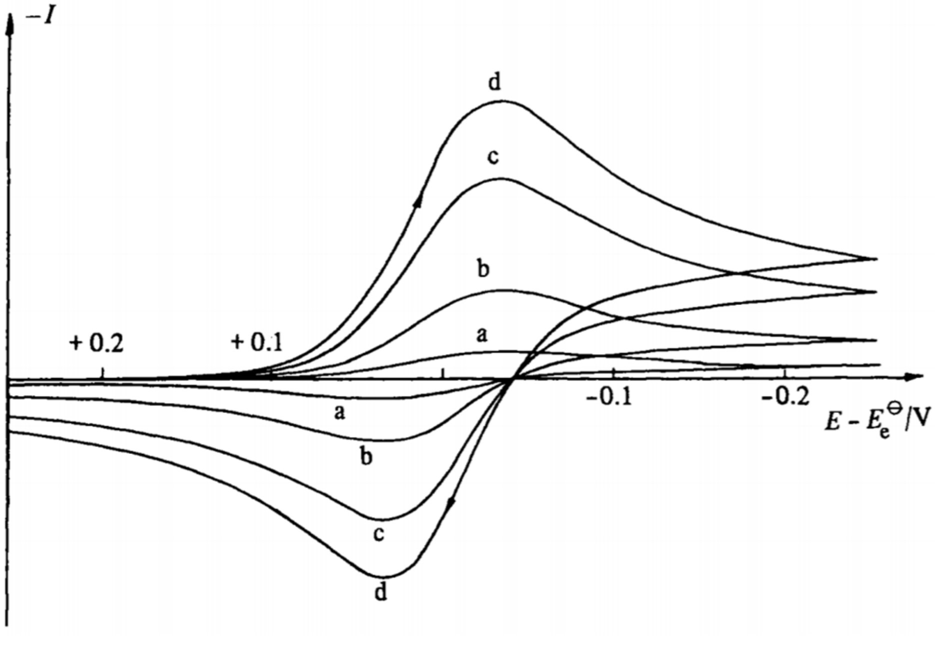

Figure 2.15 – CV curves of a reversible reaction at various scan rates: (a) v, (b) 10 v, (c) 50 v, and (d) 100 v.[112]

Typical CV curves for a reversible process at different values for v are shown in Figure 2.15. Peaks form in the CV curve as a result of chemical reactions occurring at the electrode surface. If v is low, the reactions occur at steady state and the peaks are very shallow as there is enough time for the diffusion layer to reach equilibrium.[97], [110], [112] At higher v, the diffusion layer has insufficient time to reach equilibrium which results in increased current (larger peaks).[112] The combination of forward and backward sweeps results in reaction couples of opposite current signs. It should be noted that the peak positions do not change with *v* for reversible reactions. Quasi-reversible reactions, however, exhibit shifts in peak position due to the relationship between electron transfer and mass transfer.[97], [110], [112] At low scan rates, electron transfer may be faster than mass transfer, which can cause the CV curves to resemble those of reversible processes.[112] At higher scan rates, mass transfer can become faster than electron transfer which results in peak separation.[97], [112] Completely irreversible processes will only show a peak in one sweep direction.[97]

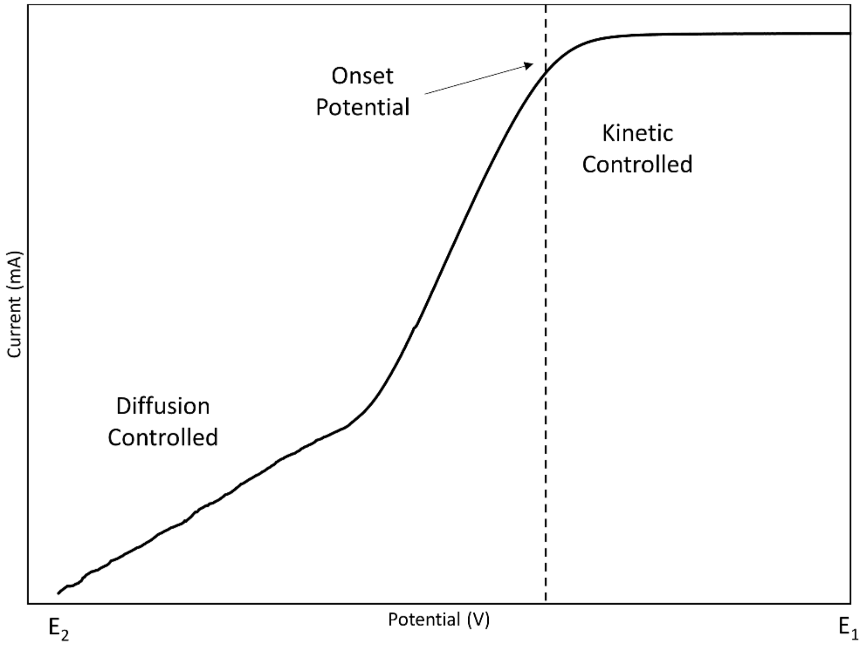

Figure 2.16 – A sample LSV curve showing kinetic and diffusion behaviours. The onset potential is shown by the dashed vertical line.

A typical LSV curve for ORR is shown in Figure 2.16. As the potential is swept from E_1 to E_2, a change in the slope of the LSV plot can be observed. This region is due to the kinetics of any reaction that is taking place and the potential at which the behaviour changes is known as the onset potential for the given reaction. For instance, the onset potential for ORR is identified using the dashed line in Figure 2.16. As the reaction event occurs, the concentration of ions at the electrode surface is decreased and the absolute value of the current increases. As the potential approaches E_2, the reaction is dominated by diffusion and a different behaviour is observed.[1], [97] This diffusion behaviour is a result of depletion effects after the mass transfer has reached a maximum.[97] The kinetic and diffusion behaviours are best observed using rotating disc electrode (RDE) measurements. RDE applies the LSV technique to a disc electrode which rotates at a set speed. The electrode material for RDE is often glassy carbon, which contributes minimally to many electrochemical reactions and enables more reliable analysis of the applied material.[113] Therefore, the onset potential can be reliably determined using RDE. Different rotation speeds will alter the currents observed during the depletion effect (limiting currents) in the diffusion-controlled region of the LSV plot.[97], [113] The limiting current values can be used to calculate the electron transfer number of the material coated on the electrode for a given reaction.[113]

Both CV and LSV are useful techniques for the electrochemical characterization of the catalysts used in ZABs. Due to the slow kinetics of ORR and OER, LSV and RDE are often used to evaluate changes in onset potentials of the reactions.[1] Furthermore, RDE measurements enable the determination of the electron transfer number for the given catalysts.[113] Moreover, CV of catalyst-coated electrodes can provide insights into any additional reactions occurring besides ORR and OER.

2.5.3 Chronopotentiometry

Chronopotentiometry (CP) is a measure of the potential as a response to altering the charge or discharge current.[109] As current is applied to the electrode, a gradient of ions is created near the electrode surface which elicits a change in potential.[109] CP curves can show changes in potential behaviour which can result from depletion of the primary electron transfer species or changes to the electrode surface (such as passivation).[97], [109], [110] Changing the current can be accomplished in a number of ways. One way is by altering the current in a step-wise fashion and holding the current for a determined amount of time. A second method is linearly increasing the current until a set current limit. The former is often referred to as charge or discharge rate tests, which show the potential stability at a given current for a window of time, while the latter is often recognized as galvanodynamic polarization (Figure 2.17).[1], [97], [109] For polarization, the potentials measured are redox potentials and thus follow the Nernst equation. Since the concentration of charged species follows a decreasing profile as the distance from the electrode surface increases, the polarization curve behaviour is very linear.[1], [109] Other types of CP consist of current reversal and cyclical changes in current, which yield information on the capacitance and cycling stability, respectively.[109]

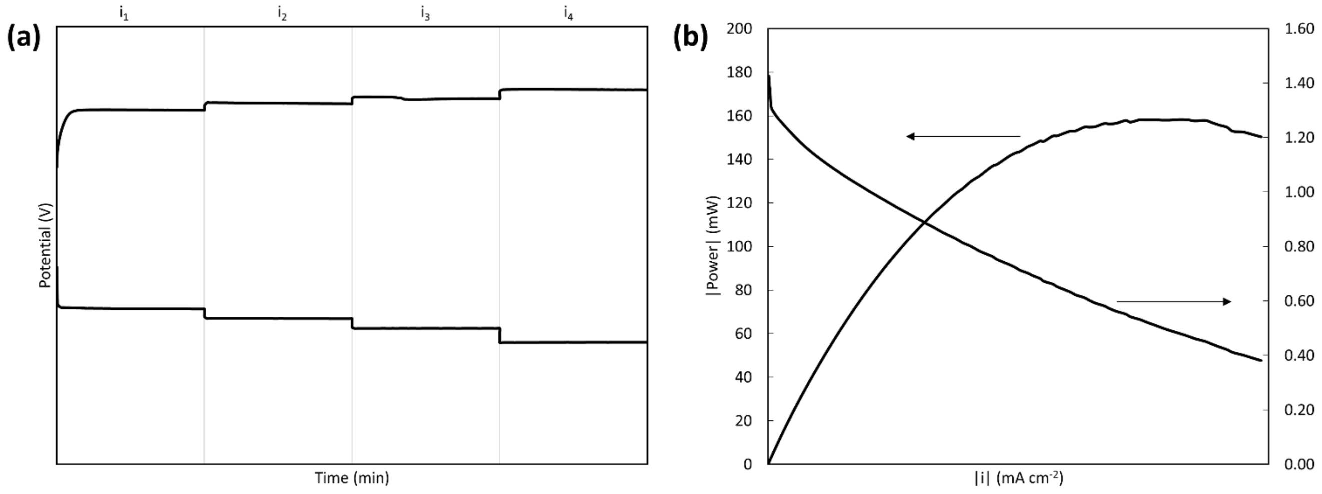

Figure 2.17 – Sample CP curves: a) Battery rate tests at varying currents, i_x and b) polarization and power as a function of current.

In terms of ZABs, polarization and charge/discharge rate tests are often measured through use of a full cell or complete battery configuration and the battery's response to changing currents is measured. Polarization is a measure of voltage losses relative to the cell's open circuit voltage (OCV). The variation between the operating voltage and the OCV represents the losses due to activity and ohmic resistances in the cell.[1] For ZABs, the losses are primarily due to the slow kinetics of the oxygen reactions.[1], [5] As the magnitude of current increases, the losses become largely dominated by the Ohmic resistances in the cell such as interfacial resistances and the internal resistance of the electrolyte.[1] By multiplying the potential by the applied current density, a power curve as a function of applied current can be obtained, the maximum value of which is considered the maximum power output of the cell.[1], [109] Rate tests in ZABs are useful in comparing battery performance at different current densities. By dividing the discharge potential by the charge potential, efficiencies can be calculated for a given current density. Furthermore, the tests can show relative stability of the electrodes at a given current. Galvanostatic CP (constant current) can be useful for conducting stability measurements on the electrodes.[109], [110] Therefore, CP is a useful electrochemical testing method for the evaluation of battery performance for ZABs.

2.5.4 Galvanostatic Charge and Discharge

Galvanostatic charge/discharge (GCD) is achieved using a variation of cycling current CP methods, and is used to determine cycling stability of the ZAB.[1], [5], [97], [109], [110] Often referred to as battery galvanostatic cycling, the measurements are achieved by alternating the current between positive and negative values of the same magnitude (charging and discharging potentials, respectively).[1] An example of galvanostatic cycling is shown in Figure 2.18. There are a number of parameters to be determined for this test, such as the number of cycles, the length of time per cycle, whether or not the cell will return to OCV between charging and discharging, and the magnitude of current density applied.[1], [109] The efficiency of the battery can be calculated by dividing the discharge potential by the charge potential for a given cycle, and the stability of the battery can thus be determined by observing the changes in efficiency over a set number of cycles.[1], [109] However, there are no current standards by which cycling tests are conducted, and thus it becomes difficult to compare batteries which are tested under different conditions. As a result, Pt/C and Pt-Ru/C are often used as reference catalysts for the cycling tests.[1], [5], [22] Alternatively, the potential difference between charge and discharge can also be used as a metric for comparison, so long as the cells are tested at similar current densities.[114]

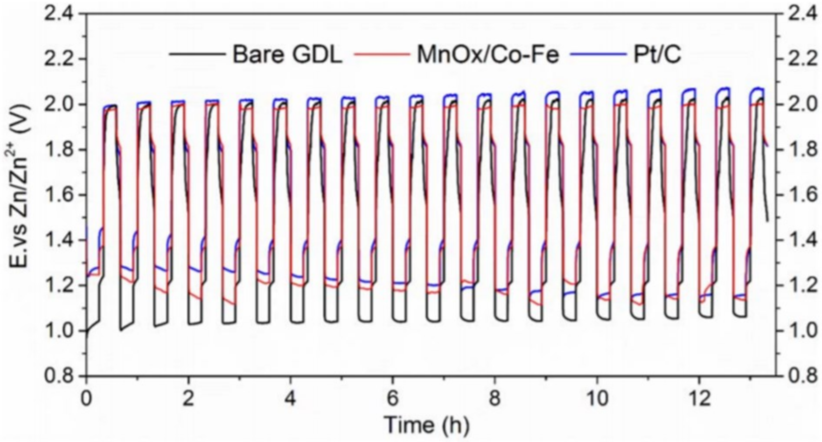

Figure 2.18 – Comparison of GCD (cycling) curves for different catalysts in ZABs at a current density of 5 mA cm^{-2}.[76]

2.6 Summary

Because of the increased drive for energy storage, Zn-air batteries (ZABs) are a promising technology due to their minimal safety concerns and relatively high energy densities. The main challenge, as noted in this review, is the low cycle life of ZABs relative to Li ion batteries, as well as the performance limiting phenomena observed in the components of the cell. For ZABs to become an efficient solution to energy storage, improvements to the cell technology are essential. Although many strategies presented in this review yield promising results, the improvements to ZAB performance are still not at the level needed for efficient storage. Not only do the challenges associated with ZAB need to be overcome, but the solutions to these challenges must be developed in a way that improves battery performance and scalability to produce batteries on an industrial scale. In this regard, further research into optimizing production as well as performance is necessary.

3 A Gas Diffusion Layer Impregnated with Mn_3O_4 Decorated, Nitrogen-Doped Carbon Nanotubes for the Oxygen Reduction Reaction in Zinc-Air Batteries

A version of this chapter has been published in Batteries & Supercaps:

D. Aasen, M. P. Clark, D. G. Ivey, A Gas Diffusion Layer Impregnated with Mn_3O_4 Decorated, Nitrogen-Doped Carbon Nanotubes for the Oxygen Reduction Reaction in Zinc-Air Batteries, *Batteries & Supercaps*, **2019**, 2, 882-893

(10.1002/batt.201900102)

3.1. Introduction

Extensive work has been conducted in developing transition metals and their oxides into effective catalysts for ORR and OER.[18], [31], [115] Various manganese oxides (MnO_x) in particular have attracted a great deal of interest as cost effective catalysts for ORR due to the abundance of Mn and Mn oxide's stability in alkaline solutions.[5], [15] However, their use in ZABs has been limited due to their poor electrical conductivity and poor stability during the harsh oxidizing conditions of OER.[15], [21], [76] Additionally, the electro-active surface area and number of catalytically active sites of MnO_x are relatively low.[13] A number of strategies have been applied to combat these issues, namely using carbon based supports as well as various nanocarbons such as carbon nanotubes (CNTs), graphene, and carbon black to make composite catalyst materials.[9], [15] The use of non-metal (B, S, N, O, P), doped nanocarbons has been shown to increase the number of active sites in the catalyst material when compared with un-doped nanocarbon catalysts.[49], [51], [116] Nitrogen is the most common non-metal dopant in nanocarbon structures due to the similarity in atomic size of N and C, coupled with an increase in activity towards ORR.[55], [62] By combining N-doped nanocarbons and metals/metal oxides, the catalyst performance can be greatly enhanced due to nitrogen-carbon-metal (N-C-M) synergistic effects.[9], [32] For instance, Mn_3O_4 quantum dots were anchored to partially exfoliated, N-doped multiwalled CNTs by Huang et al., showing good activity towards ORR and good stability in a mechanically rechargeable Zn-air battery.[117] Similarly, Mn_3O_4 particles were synthesized onto CNTs and were treated with oxygen plasma to achieve Mn_3O_4/O-CNTs and were shown to have good stability during cycling.[19] Thus, combining MnO_x and N-CNTs is predicted to have high performance towards ORR and better stability than MnO_x alone. However, synthesis of metal oxides supported on doped nano-carbon materials is often quite complex and may require acid or mechanical treatments to functionalize the carbon materials prior to doping and synthesis.[19], [55], [58], [117]. Chemical vapour deposition and hydrothermal methods, among various other techniques, are commonly employed to achieve the desired catalysts.[55], [59], [118]

Many strategies have improved the intrinsic activity of the catalysts; however, an issue is still faced during electrode preparation. Poor adherence of the catalyst layer to the gas diffusion layer (GDL) greatly increases the contact resistance and results in reduced electrochemical performance of the battery.[1], [5], [77] Often, the electrode is prepared by spraying a catalyst ink onto the GDL surface or mixing catalyst powders into a slurry and applying the slurry onto the GDL.[18], [45], [77] Binders, such as Nafion and PTFE, are added to the ink/slurry to improve adhesion to the electrode and minimize delamination, although many binders are not stable in the operating conditions of the battery.[1], [5], [77] Electrodeposition has been explored as a binder-free solution to this issue and provides better adherence to the electrode.[75], [76], [86] All three methods still struggle with the issue of flooding as performance is lost once the electrolyte passes through the surface-bound catalyst layer.[1], [5] To mitigate the issue of flooding and preserve the interface between the air, electrolyte, and catalysts, a composite air electrode with catalysts dispersed through its porosity is ideal. Furthermore, achieving such an electrode by relatively simple means while maintaining competitive electrochemical performance is desired. Impregnating the microporous layer of the GDL with nano-sized catalysts is a logical answer to this proposition, as it is a potentially simple and cost-effective method to fabricate a composite electrode without the need for excessive materials or expensive equipment. Moreover, impregnating the microporous layer of the GDL would increase the exposed and active surface areas of the electrode, thus improving battery performance. For instance, MnO_2 was grown directly on carbon paper by Sumboja et al. via an immersion process followed by heat treatment for 24 h.[79] The direct-growth of MnO_2 showed superior performance to an applied MnO_2 powder due to better adhesion, a maintained three-phase boundary, and better contact with the electrode which facilitated charge transfer.[79] Similarly, Li et al. soaked carbon cloth in an ink consisting of Mn_3O_4/O-CNTs.[19] However, the carbon cloth was then applied to the surface of the GDL to be used as the air electrode resulting in a surface-bound catalyst layer. To the best of our knowledge, impregnation has not otherwise been explored as a means of electrode preparation for ZABs, specifically with regards to CNT supported catalysts.

In the current study, nanoparticle Mn_3O_4-decorated N-CNTs are synthesized and impregnated into the GDL simultaneously in a simple, one-pot synthesis process using only the catalyst precursor solution and a piece of GDL. Mn_3O_4 decorated N-CNTs enter the microporous layer of the GDL, allowing continuous contact between the air and electrolyte as the electrolyte begins to enter the electrode. Additionally, the high surface areas of the Mn_3O_4 nanoparticles, coupled with the increased active sites, electrical conductivity, and surface area of the N-CNTs, can provide performance superior to Mn_3O_4/N-CNT catalysts previously reported in the literature, particularly for ORR. The synthesis and electrode preparation processes are done together and may be repeated to fabricate multiple air electrodes from a single solution. The result is a simple and cost-effective method of preparing a high performing air electrode for ZABs.

3.2 Experimental

3.2.1 Material Synthesis and Electrode Preparation

Using a synthesis procedure similar to that described by Li et al.[19], 50 mg of multi-walled N-CNTs (30-50 nm OD and 1-2 μm length, purchased from MK Nano), 250 mg of $Mn(CH_3COO)_2 \cdot 4H_2O$, and 80 mg of NaOH were mixed with 10 mL of ethanol in a 30 mL glass flask under vigorous stirring at 800 RPM for 10 min. The suspension was then sonicated for 5 h, with 15 mL of ethanol and 1 mL of 5% Nafion added to the suspension at 4.5 h. Teflon coated porous carbon paper, sectioned into circular pieces 4.5 cm in diameter, was used as the GDL substrate and was soaked in the catalyst-precursor suspension for 20 minutes under sonication. The impregnated GDL substrates were removed and dried in air for 15 min. Once dry, 3 mL of the suspension was passed through each impregnated GDL piece by vacuum filtration (BOLA vacuum filter funnel, Finemech Inc.). The impregnated GDL pieces were then removed from the filter and annealed for 0.5 h at 300°C, achieving composite GDL substrates impregnated with Mn_3O_4 decorated N-CNTs (denoted as Mn_3O_4/N-CNT/GDL) with a mass loading of approximately 2 mg cm^{-2}. The Mn oxide was identified as Mn_3O_4 through the characterization work, present in the Results and Discussion section. Composite GDL pieces impregnated with only Mn_3O_4 particles were also synthesized for comparison via the same procedure without the addition of N-CNTs (denoted Mn_3O_4/GDL).

To compare the effects of the impregnation techniques, GDL samples loaded with as-purchased N-CNTs (N-CNT/GDL) were prepared by spray coating, soaking for 30 min, and vacuum filtration. Spray coating of N-CNT/GDL samples was achieved by using an ink consisting of 50 mg N-CNTs, 1 mL DIW, 2 mL ethanol, and 0.1 mL 5% Nafion. Soaked and vacuum filtered samples were prepared separately in a process similar to that described for Mn_3O_4/N-CNT/GDL samples. Pt-RuO_2 samples (Pt-Ru/GDL) were also prepared, for baseline comparison, by spray coating GDL pieces with an identical ink made with 50 mg Pt-RuO_2/C powder (nominally 30% Pt and 15% RuO_2 on carbon black, purchased from Alfa Aesar) instead of N-CNTs.

3.2.2 Materials Characterization

The composition and morphology of the samples were characterized using scanning electron microscopy (Tescan VEGA3 and Zeiss SEMs operated at 5-20 kV), transmission electron microscopy (JEOL JEM-ARM200CF TEM/STEM), and x-ray photoelectron spectroscopy (Krato AXIS Supra XPS, using a monochromatic Al-K_α X-ray source and a pass energy of 20 eV). Both SEM and TEM instruments were equipped with energy dispersive X-ray (EDX) spectrometers for composition analysis. SEM samples were prepared by attaching the composite GDL pieces to an Al stub using carbon tape. Cross-sectional SEM samples were prepared by freezing pieces of the impregnated or spray coated GDL in liquid N_2 followed by fracturing through the sample centre. The samples were then mounted using carbon tape onto an angled Al stub for imaging. For TEM samples, catalyst material was scraped off the surface of the GDL composite and dispersed in 1 mL of ethanol. The suspension was then dropped by pipette three times onto the carbon grids and left to dry in air. XPS samples were prepared by cutting the composite GDL into small pieces. No sputter clean was used during XPS due to the size of the expected Mn oxide particles. XPS spectra were calibrated using the C 1s peak at 284.4 eV.

3.2.3 Electrochemical Measurements

Electrochemical measurements were achieved using linear sweep voltammetry (LSV), cyclic voltammetry (CV), and electrical impedance spectroscopy (EIS). The techniques were conducted in 1 M oxygen saturated KOH using various potentiostats (Biologic SP300 and VSP-100) with a three-electrode configuration. The impregnated or spray coated GDL samples, Pt wire, and Hg/HgO (0.098 V vs. SHE) were used as the working electrode, counter electrode, and reference electrode, respectively. Pt-Ru/GDL was also used as the working electrode as a baseline material for comparison. The electrolyte was purged with pure O_2 gas and agitated by magnetic stirring. The reported current densities were normalized to the exposed surface area of the working electrode. The reported potentials were IR compensated ($R_u = 2\text{-}4\ \Omega$).

3.2.4 Battery Testing

Zn-air battery testing was conducted in both vertical and horizontal home-made cells using 6 M KOH mixed with 0.25 M ZnO as the electrolyte (Figure S3.9). The vertical cell had a two electrode configuration while the horizontal cell had a three electrode (tri-electrode) configuration with decoupled ORR and OER electrodes, as described in previous work [114]. The vertical cell consisted of an anode made from Zn sheet metal and catalyst loaded GDL (Mn_3O_4/N-CNT/GDL or N-CNT/GDL) as the air electrode. The horizontal cell utilized Zn sheet metal, Mn_3O_4/N-CNT impregnated GDL and electrodeposited Co-Fe on GDL as the anode, ORR electrode, and OER electrode, respectively. For comparison, Pt-Ru/GDL samples were also used as the air electrode for the vertical cell, and as both ORR and OER electrodes for the horizontal cell. Discharge and charge cycling were conducted at 10 mA cm^{-2} in the vertical cell and 20 mA cm^{-2} in the horizontal cell.

3.3 Results and Discussion

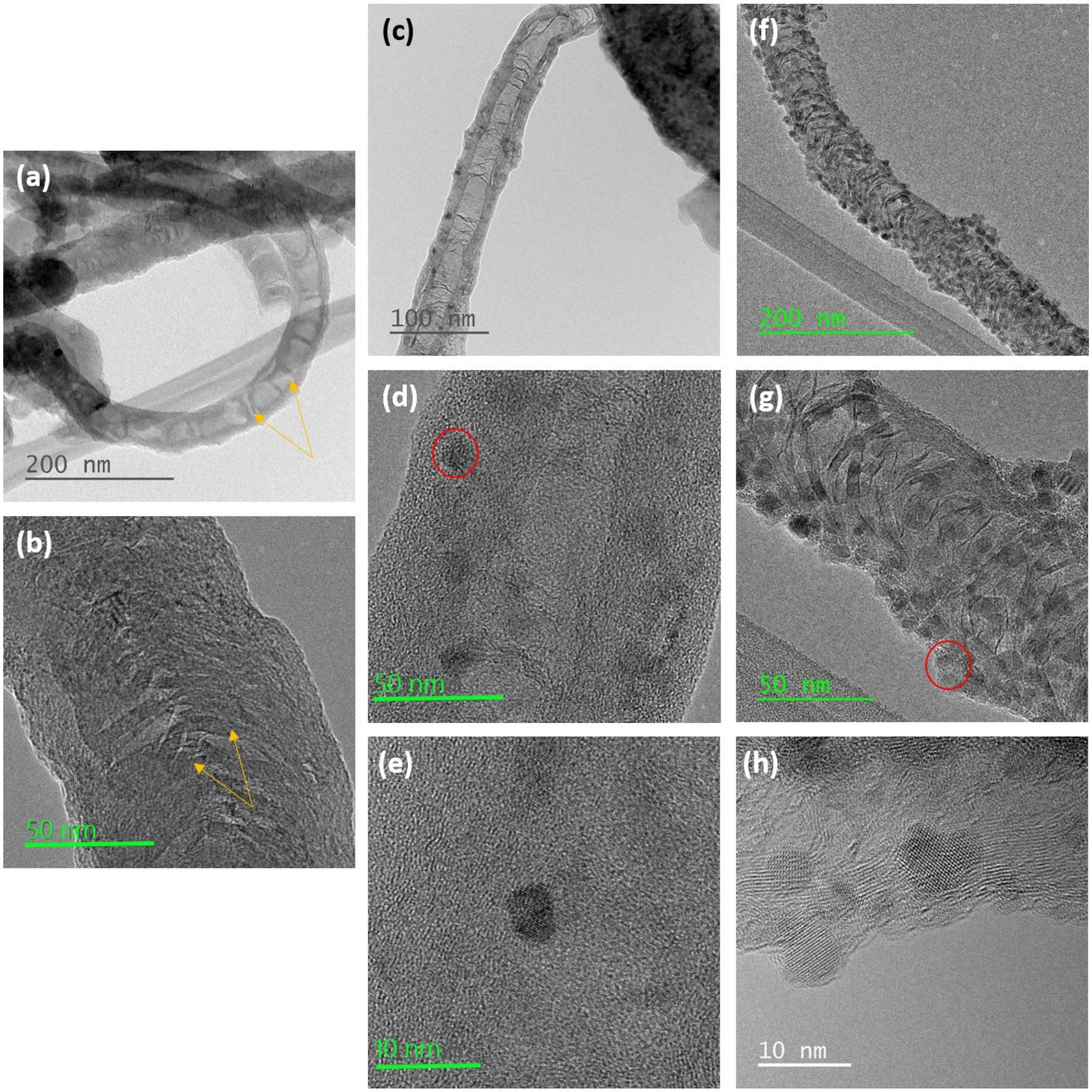

Figure 3.1 - TEM bright field (BF) micrographs of a), b) N-CNTs; c)-e) as prepared Mn_3O_4/N-CNT/GDL, and f)-h) annealed Mn_3O_4/N-CNT/GDL. Arrows mark nitrogen induced defects in the CNT walls and circles highlight Mn oxide particles in the Mn_3O_4/N-CNT/GDL samples.

Figure 3.1 shows TEM images of N-CNTs and synthesized Mn oxide decorated N-CNTs (Mn_3O_4/N-CNT/GDL samples) in both the as prepared (Figure 3.1c-3.1e) and annealed (Figure 3.1f-3.1g) conditions. The N-CNTs clearly show the bamboo-like structure expected from the nitrogen doping (Figure 3.1a and 3.1b).[55] Comparison of the N-CNTs with the Mn_3O_4/N-CNTs shows that Mn oxide particles preferentially nucleate along the nitrogen induced defects within the CNT walls. TEM analysis of Mn_3O_4/CNT samples (no nitrogen doping) confirms the importance of nitrogen for Mn oxide particle attachment to the nanotubes (Figure S3.10). Clusters of nanoparticles (10-20 nm in size) form and intertwine with the undoped CNTs; however, HRTEM imaging of the CNTs shows no evidence of MnO_x particles on the surface (Figure S3.10a – S3.10c; also confirmed by EDX mapping). Therefore, Mn oxide particles do not decorate the CNTs without N doping. Nucleation of the Mn oxide particles on N-CNTs occurs during the mixing process (as indicated by the particles in Figure 3.1c-3.1h), where the Mn^{2+} ions are attracted to the negative dipole created by the slight difference in electronegativity caused by the nitrogen heteroatoms.[55] Additionally, the Mn oxide particles nucleate on the defects in order to reduce the overall energy of the material, resulting in two driving forces for the formation of the Mn oxide particles. Examination of the particles, both as fabricated and annealed, at higher magnification (Figure 3.1e and 3.1h) shows that they are clearly crystalline and ~5-10 nm in size.

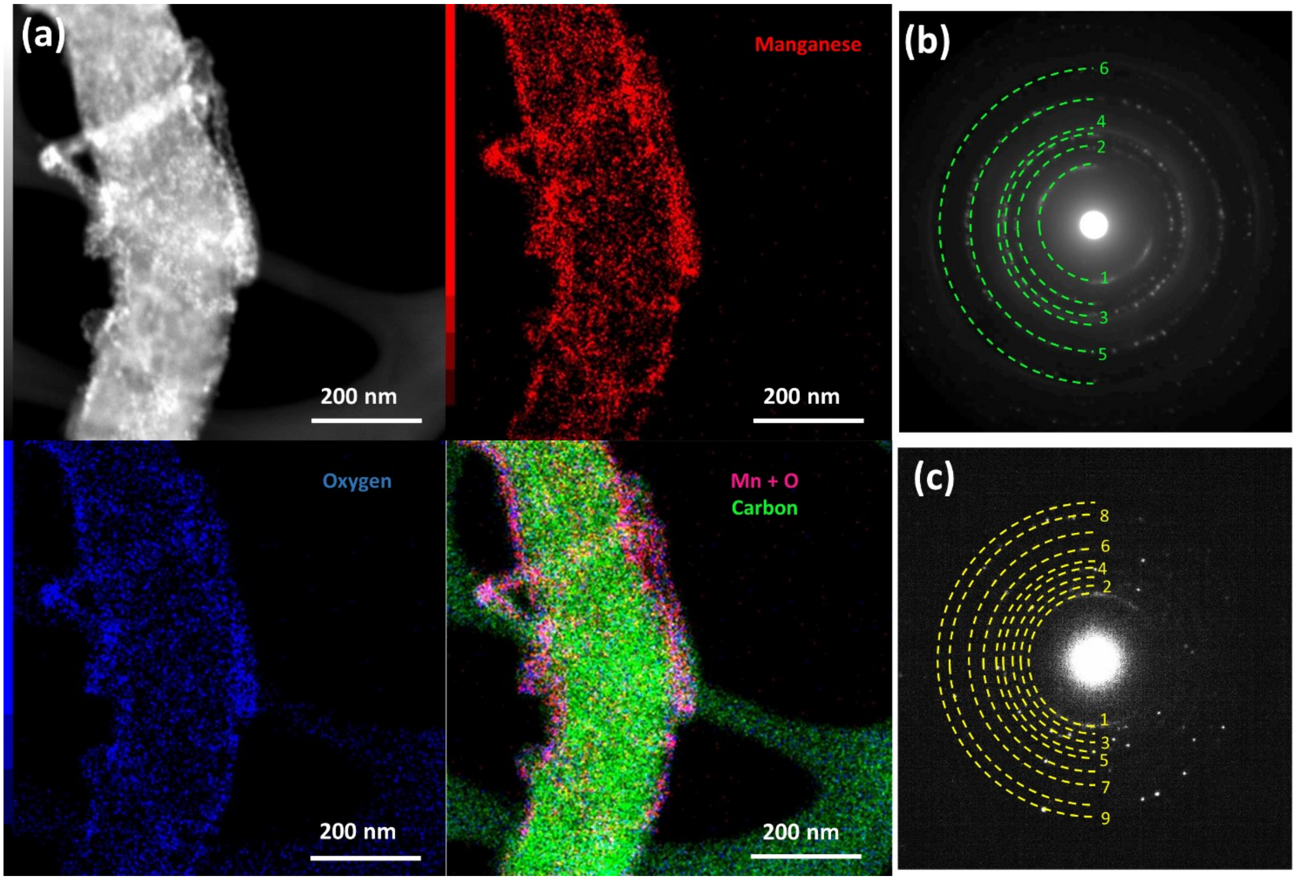

Figure 3.2 – a) STEM high angle annular dark field (HAADF) micrograph, EDX elemental maps, and EDX map overlay for Mn_3O_4/N-CNT/GDL in the annealed condition. In the EDX map overlay, the combined Mn (red) and O (blue) signals generate a pink color. b) SAD pattern obtained from as fabricated Mn_3O_4/N-CNT/GDL. c) SAD pattern obtained from annealed Mn_3O_4/N-CNT/GDL. Coloured and dashed lines are used to illustrate the rings on the diffraction patterns, while numbers are used to label each ring (b, c). Associated crystal structure information is presented in Table 3.1.

EDX maps from one of the nanotubes decorated with Mn oxide (annealed condition) are shown in Figure 3.2a. The O and Mn signals overlap, which clearly indicates the Mn particles are oxidized. EDX maps taken from the as fabricated sample (not shown here) are similar, which means that Mn oxide forms prior to annealing. EDX maps from the Mn_3O_4/CNT samples also show overlap between the Mn and O signals (Figure S3.10f). However, Mn and O signals are only observed over the particle clusters and not on the CNTs. Nickel particles were also detected through EDX analysis and these are remnants of the synthesis of CNTs and N-CNTs, during which Ni acts as a catalyst.[55], [62] Selected area diffraction (SAD) patterns of the Mn oxide decorated N-CNTs are shown in Figure 3.2b (as fabricated) and 3.2c (annealed), and are evaluated in Table 3.1. The pattern in Figure 3.2b shows 2 sets of rings; the faint, continuous rings are from carbon (N-CNTs), while the spotty, discontinuous rings are from the Mn oxide. The Mn oxide rings for the as fabricated sample can be indexed to Mn_3O_4, to both the cubic spinel (a = 0.842 nm – PDF #13-

0162) and tetragonal spinel (hausmannite, with a = 0.5762 nm and c = 0.947 nm – PDF #01-071-6262) structures. The SAD pattern from the annealed sample (Figure 3.2c) also shows two sets of rings, corresponding to carbon from the N-CNTs and Mn oxide. The Mn oxide pattern can also be indexed to both cubic and tetragonal Mn_3O_4. Similarly, the Mn oxide in the undoped CNT samples was also identified as Mn_3O_4 (SAD pattern in Figure S3.2d). Based on the TEM diffraction data, conclusive identification of the form of Mn_3O_4 was not possible.

Table 3.1 - SAD Pattern d-Spacings and Miller Indices for As-Fabricated and Annealed Mn_3O_4/N-CNT/GDL

As-Fabricated SAD (Figure 3.2b)				Annealed SAD (Figure 3.2c)			
Ring Number	d Spacing (Å)	Cubic (h k l)	Tetragonal (h k l)	Ring Number	d Spacing (Å)	Cubic (h k l)	Tetragonal (h k l)
1	3.36*	-	-	1	3.38*	-	-
-	-	-	-	2	2.77	(2 2 0)	(1 0 3)
2	2.49	(3 1 1)	(2 1 1)	3	2.45	(2 2 2)	(2 0 2)
3	2.15	(4 0 0)	-	-	-	-	-
4	2.05*	-	-	4	2.03*	-	(2 2 0)
				5	2.01	-	(2 1 3)
-	-	-	-	6	1.77	(4 2 2)	(1 0 5)
-	-	-	-	7	1.74*	-	-
5	1.53	(4 4 0)	(2 2 4)	8	1.54	(4 4 0)	(2 2 4)
6	1.25	(5 3 3)	(4 2 2)	9	1.17	(4 4 4)	(0 0 8)

* Indicates carbon ring.

The as fabricated samples are coated with an organic film which contains Na, from the NaOH added during the mixing step. This layer makes imaging and EDX analysis in the TEM problematic, as a contamination layer builds up on the surface during exposure to the electron beam (Figure S3.11). The Na-containing film burns off during annealing, leaving the N-CNTs with embedded Mn_3O_4. Therefore, the main effect of annealing the sample is the removal of the Na-containing film and excess water.

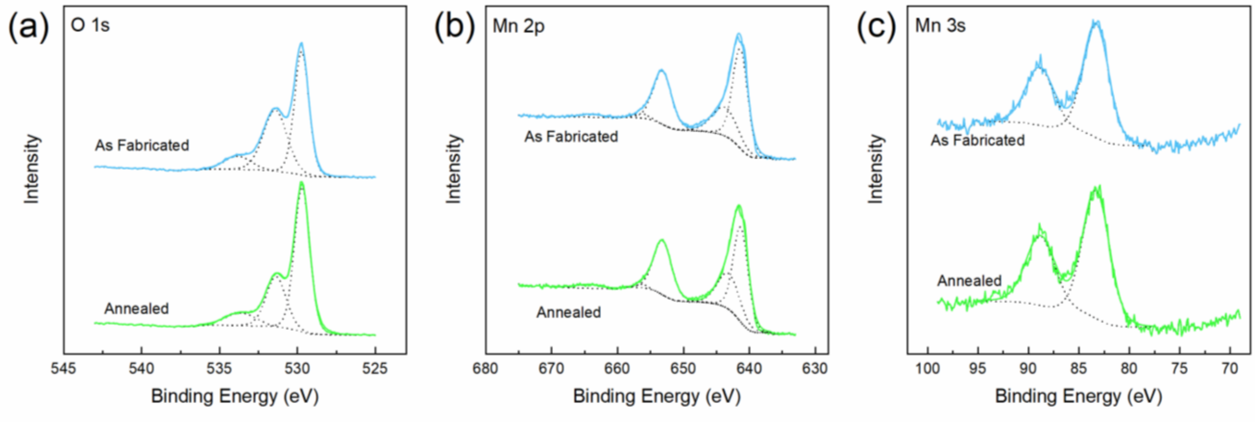

Figure 3.3 - XPS results for the as-fabricated and annealed Mn_3O_4/N-CNT/GDL samples. a) O 1s spectra, b) Mn 2p spectra, and c) Mn 3s spectra. Deconvolution of the peaks is represented by dashed lines.

The formation of Mn_3O_4 was confirmed using XPS (Figure 3.3 and Table 3.2). The valence of Mn is estimated using the Mn 2p and 3s peaks and the O 1s peak. Deconvolution of the O 1s peak (Figure 3.3a) yields three peaks which correspond to Mn-O-Mn bonds (529.3-530.0 eV), Mn-O-H bonds (530.5-531.5 eV), and H-O-H bonds (531.8-532.8 eV), respectively. The spectra are comparable to reports in literature for various Mn oxides.[119] The difference in the Mn-O-H and H-O-H peaks between the as-fabricated and annealed samples is a result of the annealing process where excess water is evaporated. The Mn 2p peak (Figure 3.3b) for the as-fabricated and annealed samples can be deconvoluted into 2 major components which correspond to the Mn $2p_{1/2}$ and Mn $2p_{3/2}$ with positions at approximately 653 eV and 641 eV, respectively. Three minor components are also present in the Mn 2p data. These components correspond to Mn^{2+} and Mn^{3+} components which have been reported for MnO and Mn_2O_3 XPS data in the literature.[120] Using the areas under the peaks corresponding to Mn^{2+} and Mn^{3+}, the Mn valence of the samples can be estimated by use of a weighted average (Table 3.2).[103] The separation between the Mn-O-Mn component of the O 1s peak and the Mn $2p_{3/2}$ component from the deconvoluted Mn 2p peak has also been reported as a tool for determining Mn valence (Δ2p-1s).[119] Additionally, Mn 3s peak separation (Figure 3.3c) is often used as a factor in determining Mn valence.[104], [119], [120] The 3s peak splitting is a result of an exchange interaction between the 3s and 3d orbitals upon photoelectron ejection.[119] Therefore, wider peak splitting is observed for lower valence. From the Mn 3s splitting, Mn 2p data, and Δ2p-1s results, it can be confirmed that Mn_3O_4 is formed in both as-fabricated and annealed Mn_3O_4/N-CNT/GDL, since the estimated valence is close to the 2.67 value expected for Mn_3O_4 (Table 3.2).[104], [119], [120] These results corroborate the TEM diffraction results discussed above.

Table 3.2 - XPS Data and Mn Valence Using Mn 2p, Mn 3s, and O1s Peaks

XPS Sample	Mn 2p		Mn 3s			Mn Valence (2p)	Mn Valence (3s)	Δ2p-1s (eV)
	2+ Peak (eV)	3+ Peak (eV)	Peak 1 (eV)	Peak 2 (eV)	Δ3s (eV)			
As-Fabricated	656.32	664.28	88.855	83.295	5.56	2.50	2.47	111.7
Annealed	656.25	664.48	88.787	83.294	5.49	2.64	2.58	111.6
Reference Mn_3O_4 [119]	-	-	88.30 - 88.86	83.00 - 83.36	~5.5	~2.67		111.5 - 111.8

Mn_3O_4/GDL samples (no CNTs) were compared with Mn_3O_4/N-CNT/GDL samples (Figure 3.4). A dense Mn oxide film is visible in Figure 3.4a and 3.4b for the sample without CNTs, which suggests that individual nanoparticles are not achieved without the presence of N-CNTs. This is confirmed by the compositions obtained through EDX analysis (Table 3.3) and the lack of Mn on the GDL within the cracks of the Mn oxide film (Figure 3.4c). Cracking of the Mn oxide film is likely due to drying of the film during the annealing step. By contrast, Mn_3O_4 particles are visible on the N-CNTs for the Mn_3O_4/N-CNT/GDL sample in Figure 3.4f and no continuous Mn oxide film is visible in the lower magnification images (Figure 3.4d and 3.4e). Furthermore, Figure 4 shows Mn_3O_4/N-CNTs wrapped around GDL particles and present within the GDL pores.

Table 3.3 - EDX Point Analysis Data for Mn_3O_4/GDL and Mn_3O_4/N-CNT/GDL Samples Presented in Figure 3.4

Spectrum	Sample	C (wt%)	O (wt%)	F (wt%)	Ni (wt%)	Mn (wt%)	Figure
1	Mn_3O_4/GDL	90.8	1.9	7.3			3.4b
2	Mn_3O_4/GDL	12.9	26.1	19.7		40.4	3.4b
3	Mn_3O_4/N-CNT/GDL	33.8	17.9	13.3	4.7	30.3	3.4f

To evaluate the success of GDL impregnation, cross sectional SEM images were obtained as well as EDX line scans (Figure 3.5). Mn_3O_4/N-CNTs are present both at the surface (Figure 3.5b) and ~100 µm (Figure 3.5c) into the microporous layer. As expected, there is a higher concentration of nanotubes present on the surface than deeper into the interior. Mn_3O_4 particles on the N-CNTs were used to track the relative amount of catalyst throughout the microporous layer via SEM EDX line scans. An example of a line scan is presented in Figure 3.5d and confirms that there are significant amounts of catalyst up to 35 μm from the surface of the GDL, after which the catalyst amount is significantly reduced.

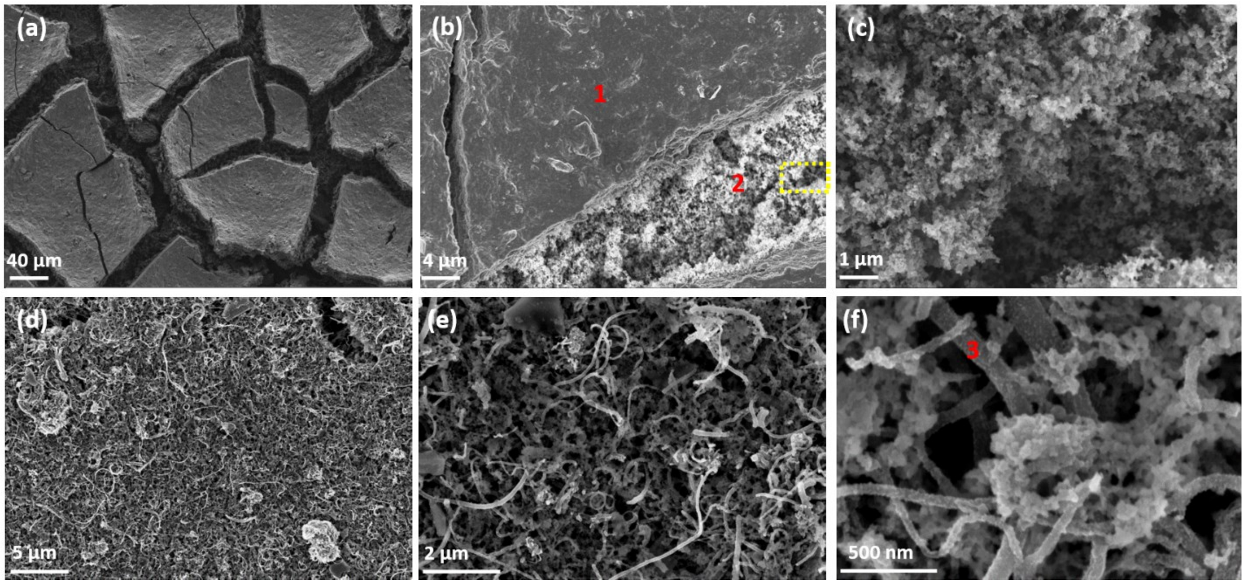

Figure 3.4 - SEM secondary electron (SE) micrographs of the Mn_3O_4/GDL (a-c) and Mn_3O_4/N-CNT/GDL (d-f) sample surfaces. The Mn oxide film and GDL for Mn_3O_4/GDL can be seen in a) and b), while c) shows the GDL carbon particles from the region (yellow box) indicated in b) at higher magnification. The low magnification view of Mn_3O_4/N-CNT/GDL in d) shows catalysts across the GDL surface, while e) shows dispersion of Mn_3O_4/N-CNTs on and within GDL pores. The image in f) shows a high magnification view of Mn_3O_4/N-CNTs with visible Mn oxide particles on the nanotubes. Points used for EDX analysis are indicated by red numbers (b and f). Results for EDX point analysis are presented in Table 3.3.

Since impregnation of Mn_3O_4/N-CNT into the GDL occurs simultaneously with synthesis, the effect of electrode preparation was investigated electrochemically using as-purchased N-CNTs. Three preparation techniques were compared: spray coating, soaking, and vacuum filtration. The techniques were compared using half-cell LSV as well as full-cell discharge rate tests (Figure S3.12). For consistency, the catalyst loading was about the same for all N-CNT electrode samples (~1 ± 0.4 mg cm^{-2}). From Figure S3.12a, it is apparent that there is no significant difference between soaking and vacuum filtration techniques, while spray coating has the largest current at higher overpotentials. Furthermore, the spray coated sample has a relatively lower onset potential than the impregnated samples which is considered to be a result of higher accumulation of N-CNTs on the GDL surface. The lack of significant variation in the half-cell results can be attributed to oxygen saturation of the electrolyte. Since oxygen does not have to diffuse through the GDL and electrolyte to gain access to the catalysts, the half-cell performance is more dependent on surface catalyst loading.

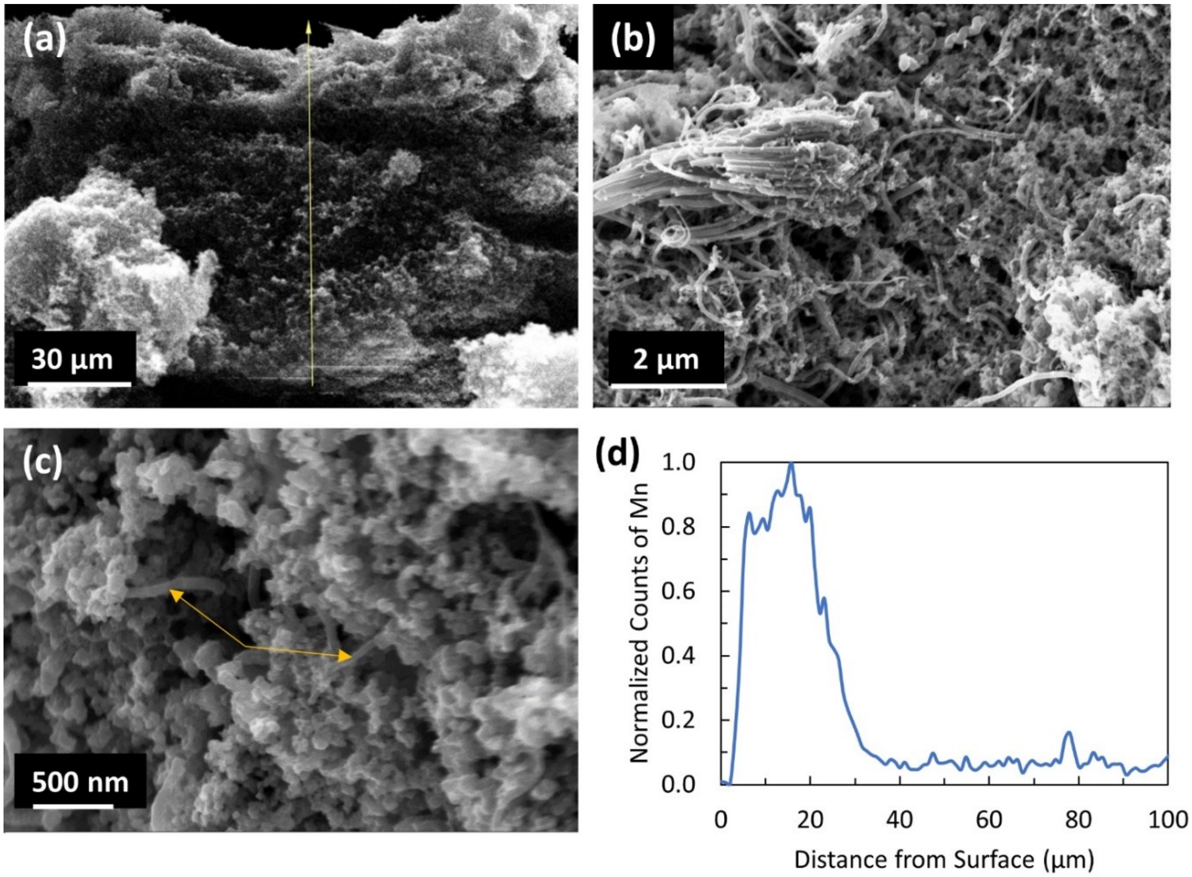

Figure 3.5 - a) SEM SE micrograph from a cross section of the microporous layer used for EDX line scan in (d). b) SEM SE micrograph of Mn_3O_4/N-CNT/GDL sample surface. c) SEM SE micrograph of Mn_3O_4/N-CNT/GDL sample at a depth of ~100 µm into the GDL with arrows indicating the presence of nanotubes. d) Normalized Mn composition throughout the microporous layer from EDX line scan data. The Mn amount shown is relative to the maximum number of Mn counts obtained. Imaged samples were prepared by combined soaking and vacuum filtration.

The spray coating technique deposits more catalyst on the surface of the GDL than the other two techniques; compare Figure S3.13a and S3.13b (spray coated GDL samples) with S3.13c and S3.13d (soaked GDL samples). Infiltration, through either soaking or vacuum filtration, is expected to have a greater effect in full cell testing since oxygen needs to diffuse through the GDL layer to access the catalysts. This expectation is confirmed for soaked samples in Figure S3.13b. As the discharge current density is increased, the soaked sample experiences smaller decreases in discharge potential compared with the spray coated and vacuum filtered samples. Conversely, vacuum filtration appears to improve the performance at lower current densities, which suggests a higher accumulation of catalyst near the surface of the GDL. The difference between soaking and vacuum filtration is likely a result of the physical differences between the impregnation techniques. Soaking the GDL in the suspension during sonication allows catalysts to impregnate the GDL from both the surface (microporous layer) and back (macroporous layer), while vacuum filtration is directional and pulls the catalyst suspension from the microporous surface inwards. Therefore, there is a greater chance of the impregnated catalysts accumulating closer to the surface when using vacuum filtration. These tests were repeated for 10 soaked samples and 6 vacuum filtered samples, and the results were reproducible.

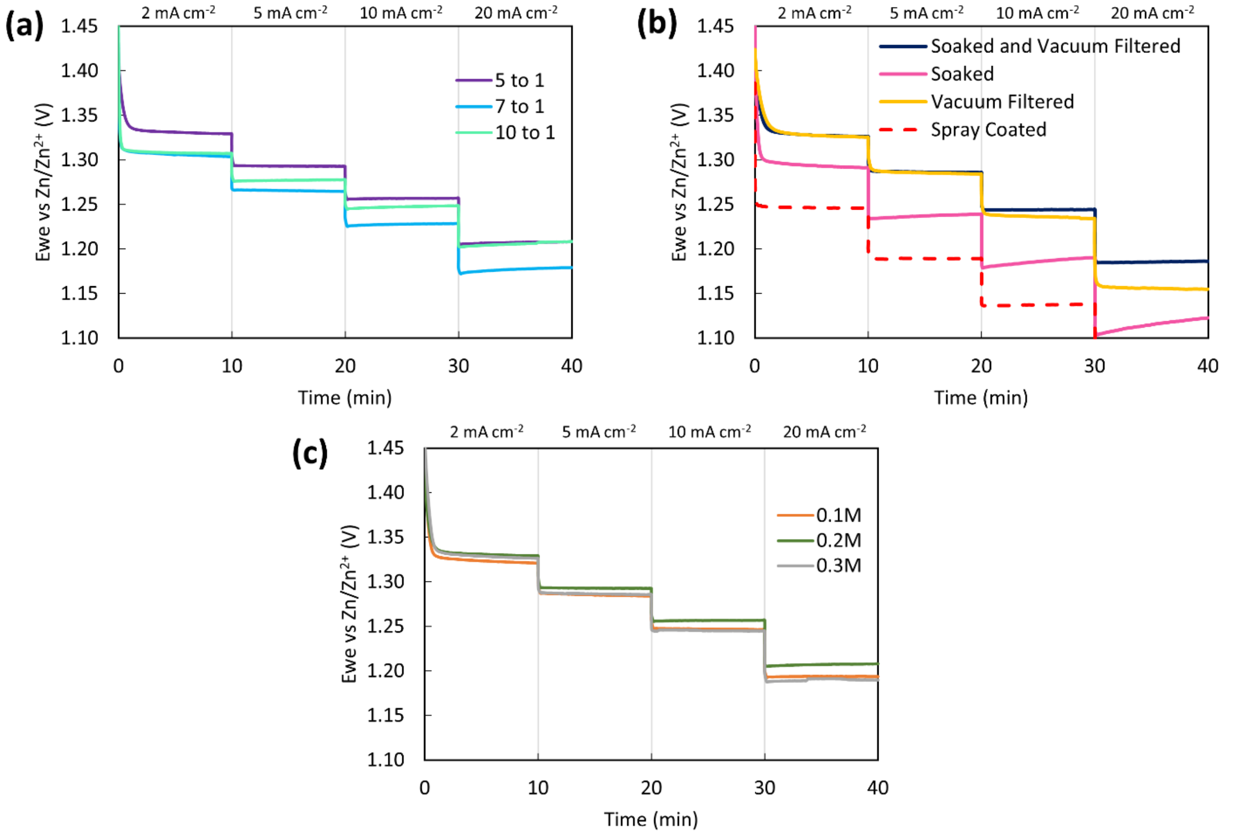

Figure 3.6 – Full cell CV testing. a) Discharge rate comparison of different Mn:N-CNT ratios; b) discharge rate comparison of the different impregnation techniques for Mn_3O_4/N-CNT/GDL; c) discharge rate comparison of varying OH^- concentration in the catalyst precursor suspension.

The preparation comparison of the N-CNT electrodes was used as a foundation for the work done with Mn_3O_4/N-CNT/GDL samples. To optimize the performance of the catalyst, a series of experiments was conducted to discover the effects of the concentration of hydroxide, the cation in the hydroxide used, the mass ratio of Mn to N-CNT, and the preparation method. Since the performance of the impregnated samples was best evaluated using full cell tests, battery discharge potentials were used to compare the effects of each variable and are shown in Figure

3.6. Figure 3.6a compares the Mn:N-CNT mass ratios in the suspensions (5:1, 7:1, 10:1). Although both the 5:1 and 10:1 samples reach a discharge potential of 1.21 V at 20 mA cm^{-2}, the 5:1 mass ratio was chosen as the better sample due to its relatively higher discharge potentials at lower current densities.

The morphologies of the 5:1 and 10:1 samples are shown in Figure A6. The surface of the electrode is comparable for both samples, showing many nanotubes with no distinct differences (Figure S3.14a and S3.14c). Higher magnification images (Figure S3.14b and S3.14d) show some N-CNTs decorated with larger particles for the 10:1 sample, while the 5:1 sample has many fine particles on virtually all N-CNTs. SEM EDX analysis confirms that the amount of Mn is higher for the 10:1 ratio sample; note the larger Mn:C ratio for the 10:1 sample in Table S3.5. Therefore, the slight differences in performance between samples with varying Mn:N-CNT ratios in suspension is thought to be related to the average Mn oxide particle size on the N-CNTs.

Figure 3.6b compares the preparation techniques in terms of discharge rate. In addition to comparing the vacuum filtration and soaking methods of impregnation, a combined soaking and vacuum filtration method was explored. The soaked samples were prepared by soaking the GDL for 0.5 h to achieve a mass loading comparable to vacuum filtration. Soaked and vacuum filtered samples were prepared by 20 min of GDL soaking followed by 3 mL of suspension vacuum filtered through the GDL in order to maintain a comparable mass loading. All samples are also compared with spray coated Mn_3O_4/N-CNTs on GDL, which have the lowest discharge potentials (Figure 3.6b). Soaking, combined with vacuum filtering of the GDL with catalyst, improved the performance at higher current densities when compared with soaking or vacuum filtration alone. Moreover, soaking and vacuum filtration shows significant improvement when compared with conventional spray coating. This corroborates the results observed for N-CNTs. Using soaking and vacuum filtration together combines the benefits of the respective techniques. Vacuum filtration provides an adequate surface layer of the catalyst while better dispersion of the catalyst within the porosity of the GDL is achieved through soaking. As such, combined soaking and vacuum filtration was chosen as the optimal preparation method for impregnation.

Figure 3.6c compares the effect of OH^- concentration. Three concentrations of NaOH were investigated: 0.1 M, 0.2 M, and 0.3 M. There is very little difference in performance as the OH^- concentration is varied, with the samples prepared with 0.2 M NaOH exhibiting slightly superior discharge potential at 20 mA cm^{-2}. 22 samples were synthesised using either NaOH or KOH. Table 3.4 shows the mean discharge potential and standard deviation (at 20 mA cm^{-2}) for the 22 samples prepared using both hydroxides. NaOH synthesized samples have slightly higher discharge potentials, with less variation between samples, for a lower average mass loading. The optimal fabrication process then includes a solution with 0.2 M NaOH and a 5:1 mass ratio of Mn to N-CNT, with 20 min of GDL soaking in the suspension followed by vacuum filtration with 3 mL of the suspension.

Table 3.4 - Comparison of Hydroxide Cation Used for Mn_3O_4/N-CNT/GDL Synthesis

	Mean Performance at 20 mA cm^{-2} (V)	Standard Deviation (V)	Average Mass Loading (mg cm^{-2})
NaOH	1.19	0.019	1.89
KOH	1.15	0.039	2.75

Using the optimized methodology, Mn_3O_4/N-CNT/GDL samples were prepared for half-cell and full-cell comparisons (Figure 3.7). Figure 3.7a shows that the ORR activity of the Mn_3O_4/N-CNT/GDL sample is superior to both N-CNT/GDL and Mn_3O_4/GDL which can be explained by the synergistic effect between Mn, N, and C. The addition of Mn_3O_4 active sites to the N active sites already present in the N-CNTs leads to higher catalytic activity; the N-CNTs also reduce the electronic resistance of the composite material.[15], [36], [55] The onset potential for ORR in this work is defined as the measured potential at 10 mA cm^{-2}. The Mn_3O_4/N-CNT sample compares favourably with Pt-Ru (0.849 V vs RHE) with an onset potential of 0.854 V vs RHE. The competitive onset potential suggests strong ORR activity of the synthesized catalyst; however, Pt-Ru/GDL shows larger current at higher overpotentials. Mn_3O_4/N-CNT/GDL is primarily considered as an ORR catalyst in this work; however, its capability as an OER catalyst has been evaluated through LSV measurements (Figure S3.15). Clearly, the OER activity of Mn_3O_4/N-CNT is poor compared with Pt-Ru/GDL. The slight improvement in OER activity relative to Mn_3O_4/GDL is attributed to the presence of N-CNTs.

In full-cell battery discharge rate tests (Figure 3.7b), Mn_3O_4/N-CNT/GDL samples have discharge potentials greater than Pt-Ru at lower current densities and the same discharge potential of 1.21 V at 20 mA cm^{-2}, which essentially corroborates the LSV results in Figure 3.7a. The discharge rate results show better performance when compared with Mn_3O_4 particles on doped

CNTs reported previously in the literature.[19], [117] For instance, Li et al. reported a discharge potential of 1.20 at 2 mA cm^{-2} for Mn_3O_4/O-CNTs which is 140 mV lower than that of Mn_3O_4/N-CNT/GDL at the same current density (1.34 V).[19] Similarly, Mn_3O_4/N-CNT/GDL shows a superior discharge potentials to Mn_3O_4 quantum dots supported on partially exfoliated N-CNTs at both 10 and 20 mA cm^{-2} (1.25 V and 1.21 V vs 1.21 V and 1.11 V).[117] The low electrical resistance of Mn_3O_4/N-CNT/GDL is confirmed by the EIS measurements (Figure 3.7c). Interfacial resistance can be estimated by the intercept of the Nyquist plot with the horizontal axis.[97], [110] The similarity in interfacial resistance between the Mn_3O_4/N-CNT/GDL sample and the N-CNT/GDL sample confirms that the good conductivity of N-CNTs plays a significant role in reducing interfacial resistance. Charge transfer resistance can be used as a metric for catalytic activity and is evaluated by the size of the semi-circular region of the EIS Nyquist plot.[97], [110] Mn_3O_4/N-CNT/GDL has the lowest charge transfer resistance when compared with both N-CNT/GDL and Pt-Ru/GDL. The Mn_3O_4/N-CNT/GDL sample achieves a maximum power of 133 mW cm^{-2} (Figure 3.7d). Pt-Ru still boasts a higher maximum power of approximately 150 mW cm^{-2}, although the Mn_3O_4/N-CNT/GDL samples have improved power compared with N-CNTs alone. From the polarization curves in Figure 3.7d, it is apparent that the performance of Mn_3O_4/N-CNT/GDL remains comparable to Pt-Ru until approximately 50 mA cm^{-2}. Therefore, the data suggests that improving the active surface area may not alter the behaviour of the electrochemical curves, but instead slightly shifts the power and polarization curves upwards. These results confirm that the higher active surface area achieved by impregnation improves the battery performance, although it may not directly affect the catalytic activity of Mn_3O_4/N-CNT/GDL.

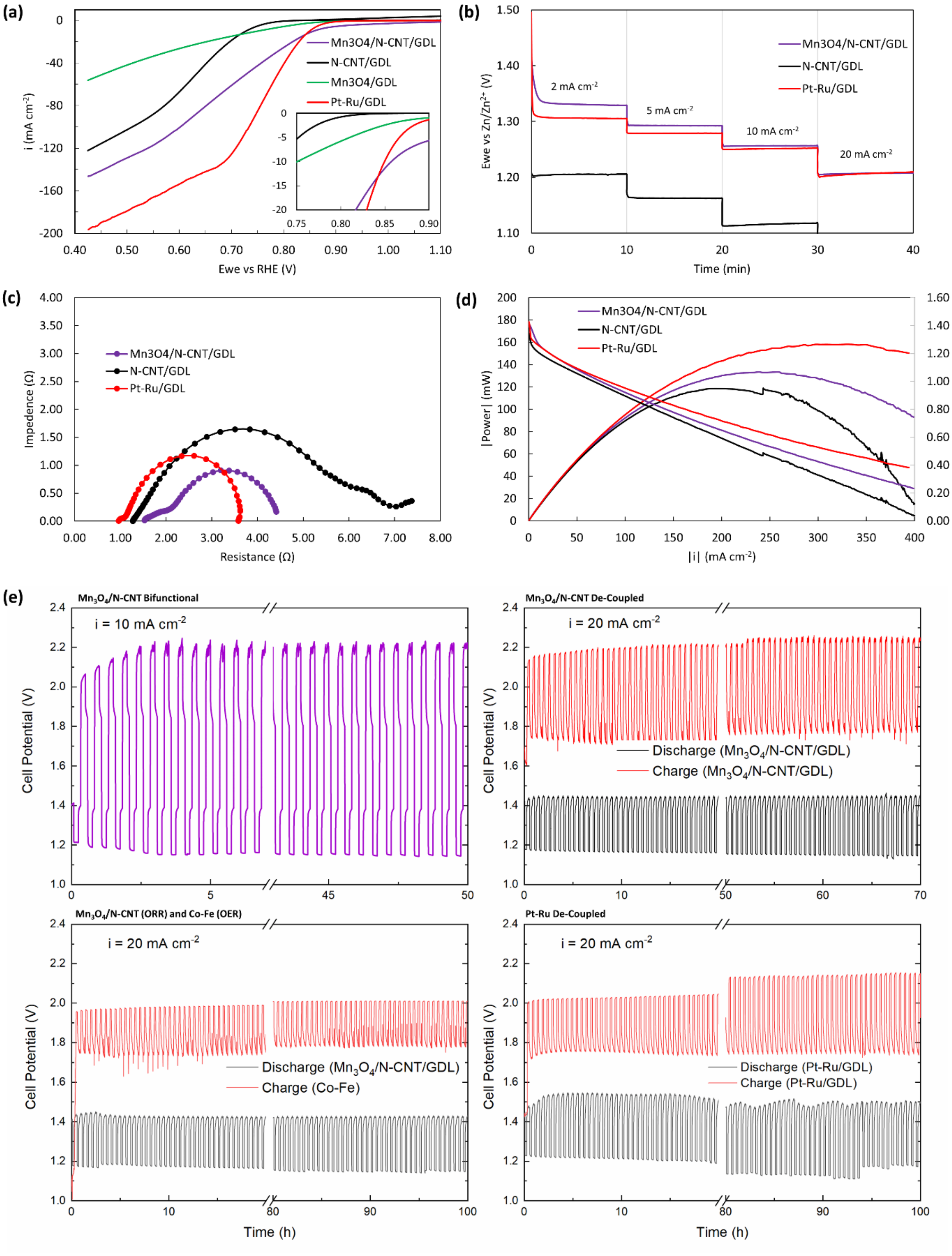
(a)
i (mA cm^{-2})
Ewe vs RHE (V)
Mn3O4/N-CNT/GDL
N-CNT/GDL
Mn3O4/GDL
Pt-Ru/GDL
(b)
Ewe vs Zn/Zn^{2+} (V)
Time (min)
2 mA cm^{-2}
5 mA cm^{-2}
10 mA cm^{-2}
20 mA cm^{-2}
Mn3O4/N-CNT/GDL
N-CNT/GDL
Pt-Ru/GDL
(c)
Impedence (Ω)
Resistance (Ω)
Mn3O4/N-CNT/GDL
N-CNT/GDL
Pt-Ru/GDL
(d)
|Power| (mW)
Ewe vs Zn/Zn^{2+} (V)
|i| (mA cm^{-2})
Mn3O4/N-CNT/GDL
N-CNT/GDL
Pt-Ru/GDL
(e)
Mn_3O_4/N-CNT Bifunctional
i = 10 mA cm^{-2}
Mn_3O_4/N-CNT De-Coupled
i = 20 mA cm^{-2}
Discharge (Mn_3O_4/N-CNT/GDL)
Charge (Mn_3O_4/N-CNT/GDL)
Mn_3O_4/N-CNT (ORR) and Co-Fe (OER)
i = 20 mA cm^{-2}
Discharge (Mn_3O_4/N-CNT/GDL)
Charge (Co-Fe)
Pt-Ru De-Coupled
i = 20 mA cm^{-2}
Discharge (Pt-Ru/GDL)
Charge (Pt-Ru/GDL)
Cell Potential (V)
Time (h)

Figure 3.7 – Electrochemical and battery performance of Mn_3O_4/N-CNT/GDL: a) half-cell LSV comparison of various catalysts with Mn_3O_4/N-CNT/GDL; b) battery discharge rate comparison with Mn_3O_4/N-CNT/GDL; c) battery EIS spectra comparison with Mn_3O_4/N-CNT/GDL; d) power comparison with Mn_3O_4/N-CNT/GDL; e) bifunctional and de-coupled (tri-electrode) battery cycling in 6 M KOH + 0.25 M ZnO. Bifunctional cycling of Mn_3O_4/N-CNT/GDL was done at 10 mA cm^{-2} (100 cycles or 50 h). De-coupled cycling of Mn_3O_4/N-CNT/GDL as both ORR and OER electrodes (145 cycles or 72.5 h), de-coupled cycling of Mn_3O_4/N-CNT/GDL and Co-Fe on Ni foam as the ORR and OER electrodes, respectively (200 cycles or 100 h), and de-coupled cycling of Pt-Ru/GDL as both ORR and OER electrodes (200 cycles or 100 h) were conducted at 20 mA cm^{-2} in 6 M KOH + 0.25 M ZnO.

Battery cycling tests were conducted in bifunctional (two-electrode) and de-coupled (tri-electrode with separate ORR and OER electrodes) configurations at 10 mA cm^{-2} and 20 mA cm^{-2}, respectively (Figure 3.7e). Bifunctional cycling of Mn_3O_4/N-CNT/GDL shows degradation of the catalyst under OER conditions, which was most significant during the first 5 cycles. The damage accumulated during the OER conditions over 100 cycles, leading to a reduction in the discharge potential by approximately 50 mV (Figure 3.7e). It should be noted that the discharge potential decreases the most during the first 10 cycles, after which the potential is relatively stable. The initial efficiency was 60.1% and dropped to 51.7% after 100 cycles. Tri-electrode cycling with Mn_3O_4/N-CNT/GDL as both ORR and OER electrodes (de-coupled Mn_3O_4/N-CNT/GDL – Figure 3.7e) was conducted in order to confirm that degradation is due to the harsh oxidizing conditions during OER. Degradation was observed primarily for the OER electrode, while the ORR electrode was stable over 145 cycles with a decrease of less than 30 mV in discharge potential. Similar to the bifunctional cycling, the OER electrode was relatively stable after the initial degradation. An increase in charge potential was observed after 47 h due to O_2 bubble accumulation on the OER electrode surface. The bubbles increase the interfacial resistance at the electrode surface resulting in an increase in the potential. A similar phenomenon is observed for the ORR electrode during cycling of Pt-Ru/GDL (de-coupled Pt-Ru – Figure 3.7e). Oxygen bubbles accumulate on the ORR electrode surface which gradually increases the potential; the potential resets once the bubbles are expelled.

The stability during discharge is attributed to catalyst impregnation of the microporous layer. Once the electrolyte begins to flood the GDL during cycling, oxygen diffusing through the GDL maintains access to the catalysts as they are present throughout the microporous layer; as such, the three-phase boundary is preserved. In a typical GDL prepared by surface loading techniques, flooding of the electrode will result in a loss of the three-phase boundary as the solid catalyst is no longer readily accessible to oxygen. Oxygen is then forced to diffuse through the electrolyte to reach the catalyst layer which slows the oxygen reactions and decreases performance of the cell.[1], [5]

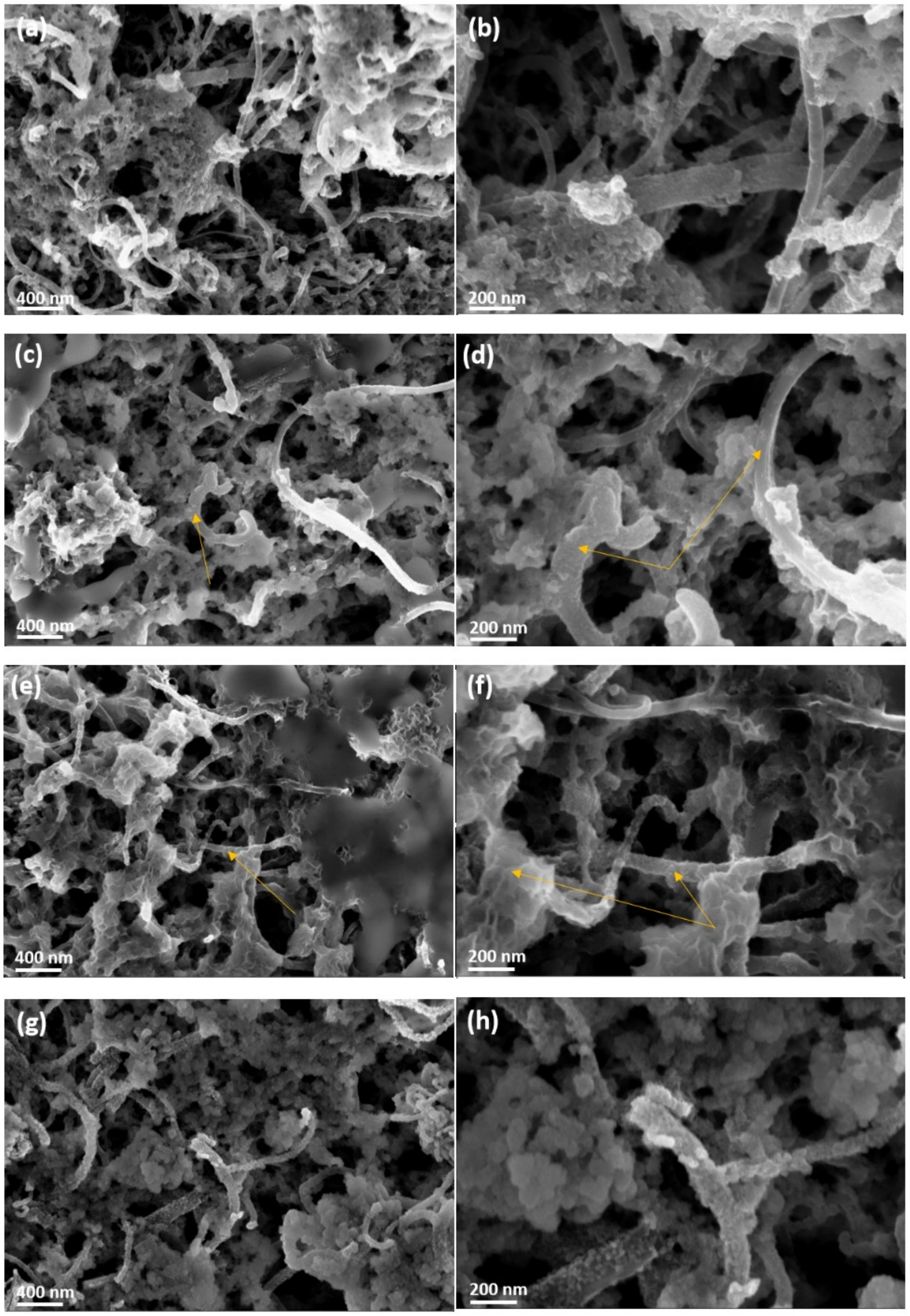

Figure 3.8 - SEM SE micrographs of Mn_3O_4/N-CNT/GDL electrodes a), b) before battery cycling; c), d) after OER cycling; e), f) after ORR cycling; g), h) after bifunctional cycling. Arrows are used to indicate regions of interest in d) and f) where Mn oxide deposition or dissolution are observed, respectively.

The degradation of the air electrode during charging is believed to be due to Mn_3O_4 dissolution and re-deposition onto the electrode surface during cycling (Figure 3.8). Before cycling (Figure 3.8a and 3.8b), the nanotubes are clearly distributed across the surface of the GDL particles and in the pores of the microporous layer and Mn_3O_4 particles on the N-CNTs cause the surface of the nanotubes to appear rough. After OER cycling (Figure 3.8c and 3.8d), the nanotubes appear much smoother which is likely due to Mn_3O_4 loss. Since the ORR and OER electrodes of the tri-electrode configuration are submerged in the same electrolyte, Mn may dissolve from the OER electrode during charging and re-deposit on both the ORR and OER electrodes during discharging. Re-deposition on the electrode during ORR cycling is confirmed in Figure 3.8e and 3.8f, as Mn oxide sheets are visible on the GDL and around the Mn_3O_4/N-CNTs. Unlike the OER electrode, Mn_3O_4 particles are visible on the N-CNTs of the ORR electrode, indicated by the rougher nanotube surface. New deposits on the ORR electrode surface have little effect on discharge performance as the ORR reaction is not limited to the electrode surface due to impregnation of the GDL. Conversely, the OER reaction primarily occurs on the electrode surface and would be expected to suffer greater performance loss due to surface changes and the loss of Mn_3O_4 particles on the N-CNTs. New Mn oxide deposits and Mn dissolution limit the availability of surface Mn_3O_4/N-CNT catalysts for the OH^- ions, thus slowing the kinetics of oxygen evolution.

The performance loss is more significant for the bifunctional electrode since it is exposed to both ORR and OER conditions (Figure 3.8g and 3.8h) and undergoes both Mn_3O_4 dissolution (charging) and re-deposition (discharging). Thus, the visible changes to the bifunctional electrode are less severe in comparison to the OER and ORR electrodes. However, the morphology of the particles on the N-CNT surface is altered when compared with the as-deposited sample (Figure 3.8a). Furthermore, thin Mn oxide sheets are visible on the GDL carbon particles after bifunctional cycling (Figure S3.16a and S3.16b), which confirms re-deposition similar to that of the ORR-exclusive electrode. Degradation of the Mn_3O_4 nanoparticles on the N-CNT surface reduces the activity of the catalyst towards both ORR and OER, while uncontrolled re-deposition of Mn_3O_4 onto the surface alters the active surface area for OER. Subjecting Mn_3O_4/N-CNT/GDL samples to both ORR and OER conditions will inevitably increase the rate at which the performance of the battery is lost. These findings agree with previous reports in the literature comparing two electrode and three electrode battery configurations.[1], [114] To achieve higher battery efficiency, tri-electrode cycling was conducted with Mn_3O_4/N-CNT/GDL and Co-Fe electrodeposited onto Ni-foam as the ORR and OER electrodes, respectively (Mn_3O_4/N-CNT/GDL and Co-Fe – Figure 3.7e). Electrodeposited Co-Fe was chosen as the OER electrode as it was shown in previous work to have good OER activity and durability during cycling.[75] The initial efficiency of the combined Mn_3O_4/N-CNT/GDL and Co-Fe tri-electrode battery was 61% when cycled at 20 mA cm^{-2}. After 200 cycles (100 h), the efficiency dropped only to 59%, boasting higher stability and cyclability than Mn_3O_4/N-CNT/GDL utilized as both de-coupled electrodes (51% efficiency after 150 cycles). A sudden jump in the ORR potential for the Mn_3O_4/N-CNT/GDL and Co-Fe battery was observed at 70 h and is due to accumulation and release of air bubbles under the horizontally positioned ORR electrode. Again, the ORR potential only decreases by 30 mV over 200 cycles, while the Co-Fe OER electrode potential increases by only 50 mV over 200 cycles. Additionally, the performance is superior to that of Pt-Ru/GDL tested in the same tri-electrode configuration (de-coupled Pt-Ru – Figure 3.7e). The ORR and OER electrodes both have superior durability after 200 cycles when compared with Pt-Ru, and the discharge-charge efficiency after cycling (59%) is 4% higher than that of Pt-Ru (55%). Battery discharge rate and battery cycling results also compare favourably with other transition metal and carbon based ORR catalysts reported under similar testing conditions, particularly Mn_3O_4 catalysts supported on other CNT frameworks (Table S3.6).[1], [19], [77], [117], [121]

3.4 Summary

In summary, an ORR-active nanocomposite air electrode was synthesized in a one-pot process using Mn_3O_4 decorated N-CNTs and a simple impregnation method. The novel impregnation technique showed superior performance to other electrode preparation techniques in battery testing as a result of higher active surface area. The nanocomposite electrode displayed comparable performance to commercially used Pt-Ru catalysts and even superior performance to other Mn oxide catalysts supported on nano-carbon frameworks in terms of discharge potential and cyclability, while mitigating some of the adverse effects of flooding during cycling. The electrode also proved to be durable through battery cycling when used exclusively as an ORR electrode. Combining the impregnated electrode with a suitable OER-active catalyst (i.e Co-Fe on

Ni foam) in a physically decoupled tri-electrode battery configuration provided discharge-charge efficiencies superior to Pt-Ru. These results indicate that simple impregnation of appropriate nano-catalysts into the GDL may be a cost effective and reproducible means to preserve the three-phase boundary during flooding, while simultaneously providing good ORR performance and cycling of electrically rechargeable Zn-air batteries.

3.5 Supporting Information

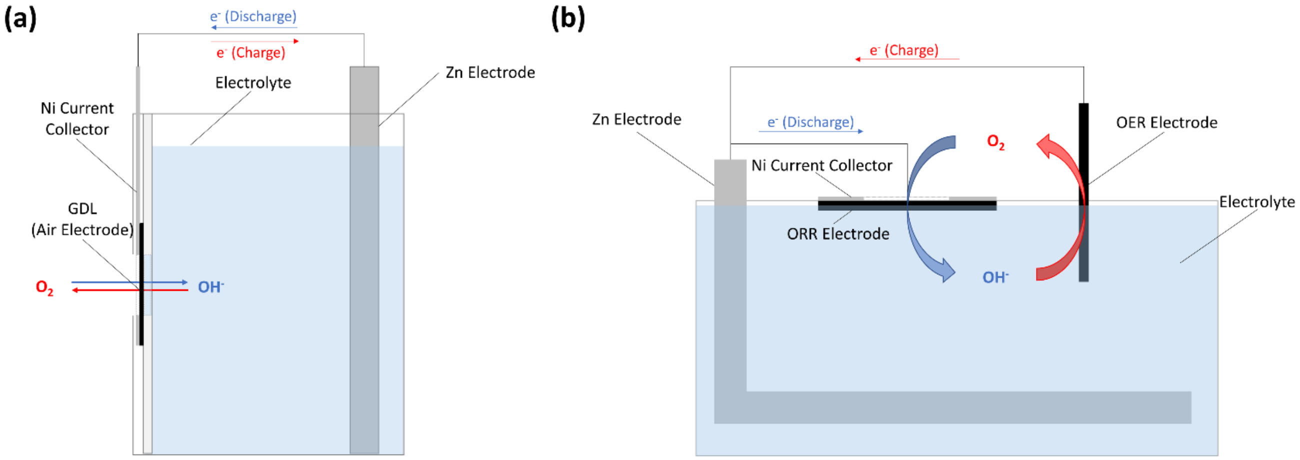

Figure S3.9 – Schematic representation of homemade Zn-air batteries: a) a vertical, 2 electrode configuration and b) a horizontal tri-electrode configuration with decoupled air electrodes

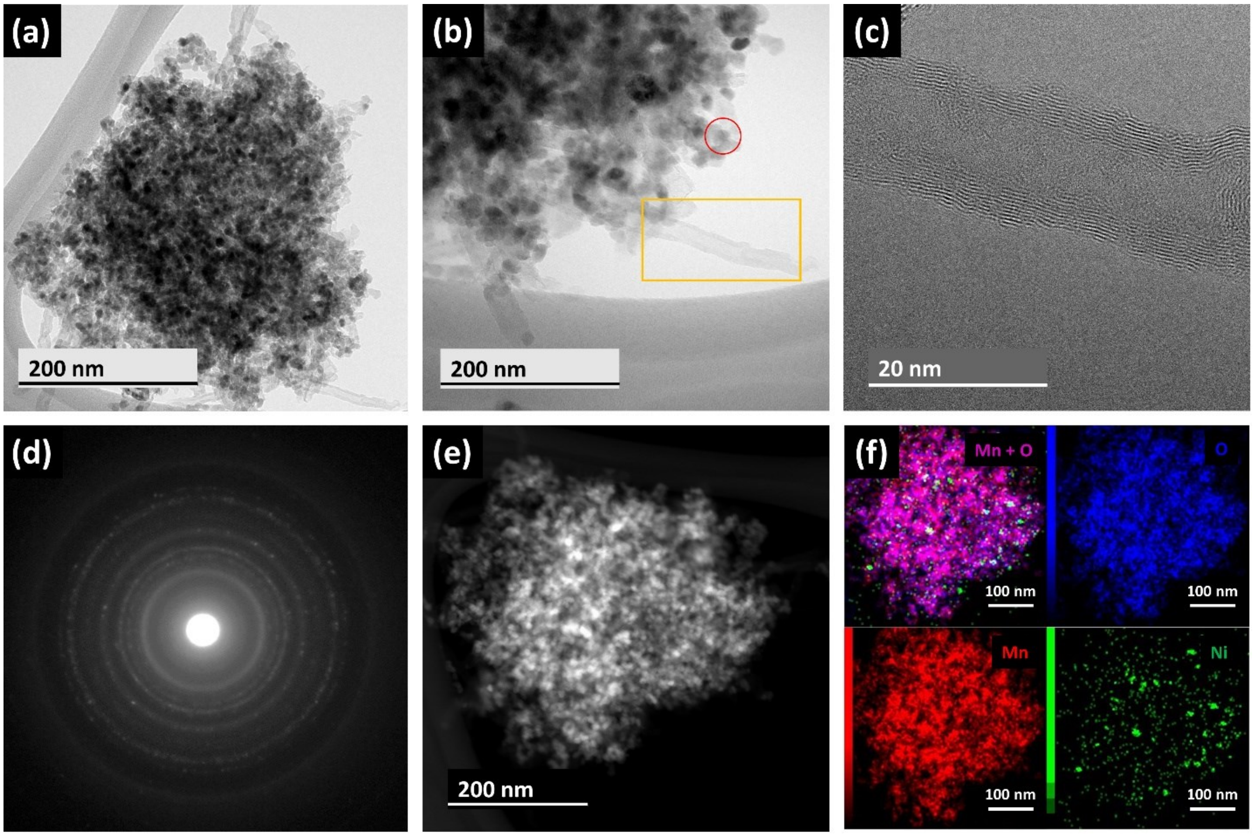

Figure S3.10 - TEM analysis of Mn_3O_4/CNT samples. a-b) TEM BF micrographs, c) HRTEM micrograph of an un-doped CNT, d) SAD pattern of the Mn_3O_4 cluster, e) STEM HAADF image and f) resulting STEM EDX elemental maps. A red circle is used to identify a Mn oxide particle, while a yellow box shows the un-doped CNT selected for high resolution imaging. Mn oxide was identified as Mn_3O_4 from the SAD pattern.

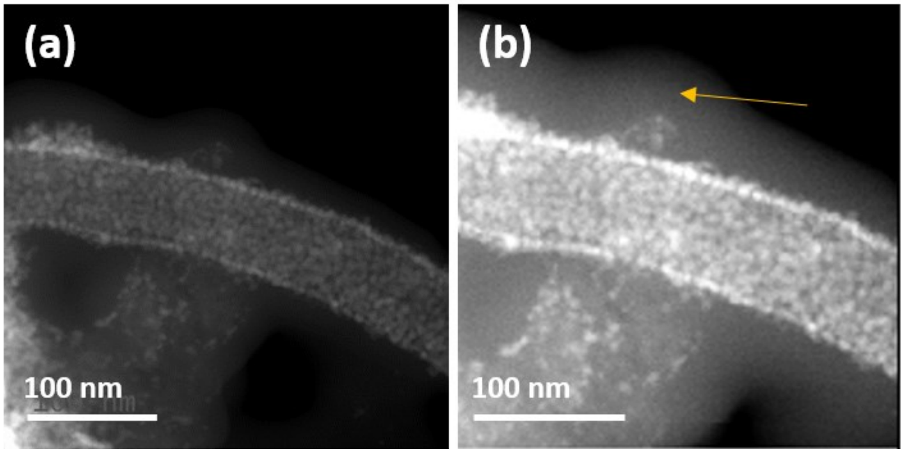

Figure S3.11 – STEM HAADF micrographs of as-fabricated Mn_3O_4/N-CNT/GDL a) before and b) after STEM EDX analysis. An arrow is used to highlight the contamination layer which developed during exposure to the electron beam (b).

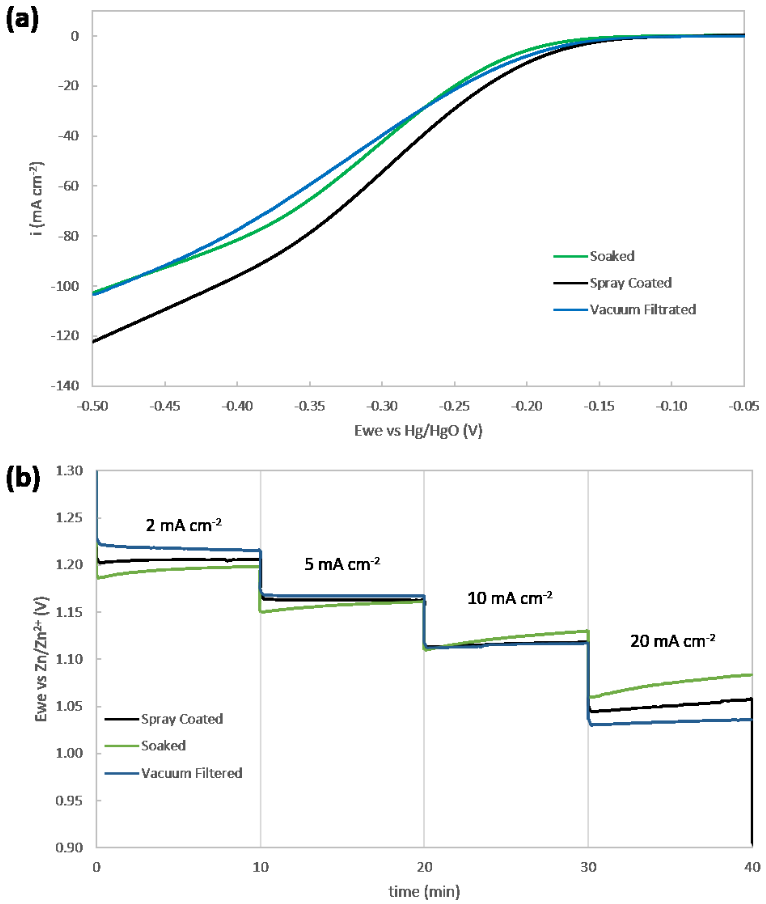

Figure S3.12 - a) Average half-cell LSV results for N-CNT prepared GDL samples in oxygen saturated 1 M KOH and b) average full cell discharge rate tests on N-CNT prepared GDL samples in 6 M KOH.

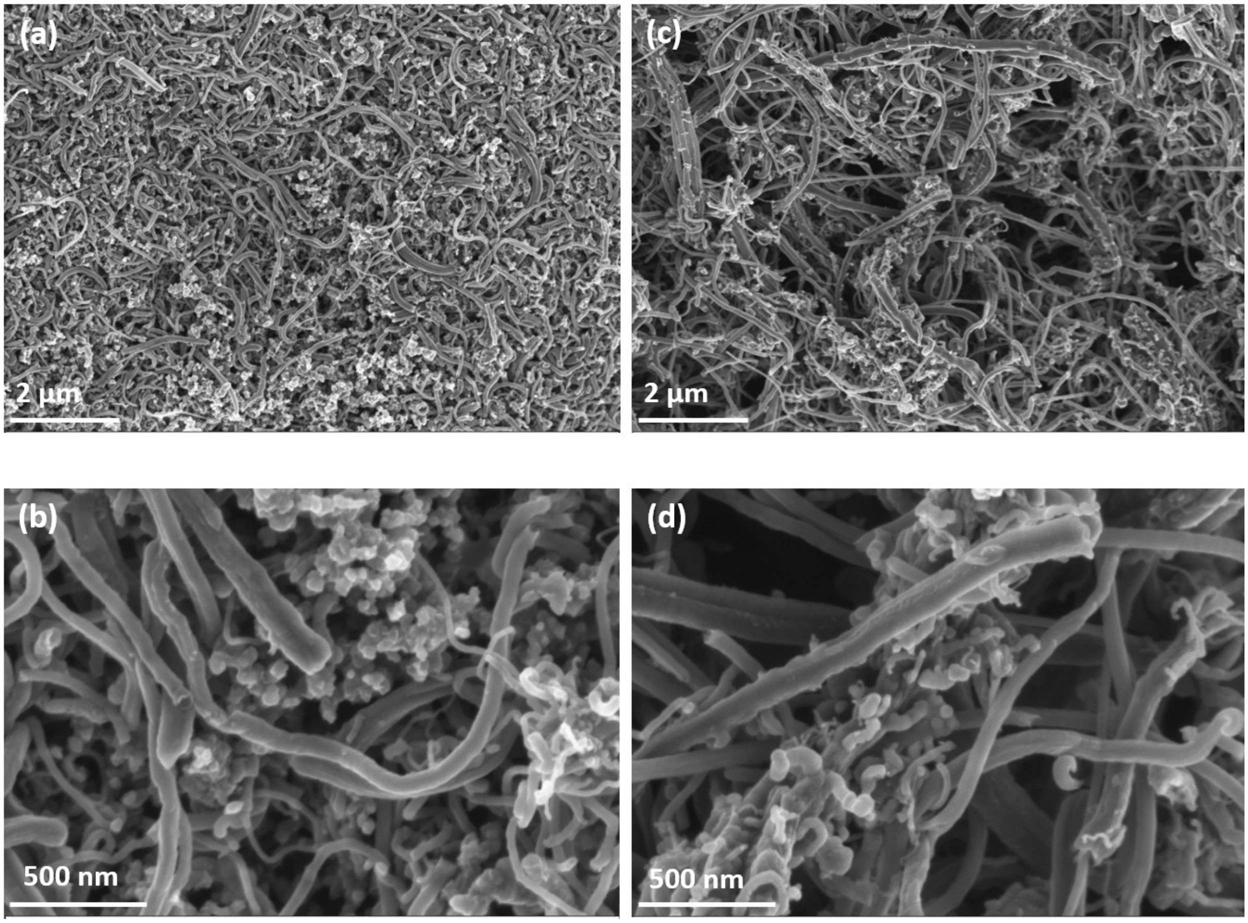

Figure S3.13 - SEM SE micrographs of a), b) spray coated N-CNTs on the GDL surface and c), d) soaked N-CNTs on the GDL surface.

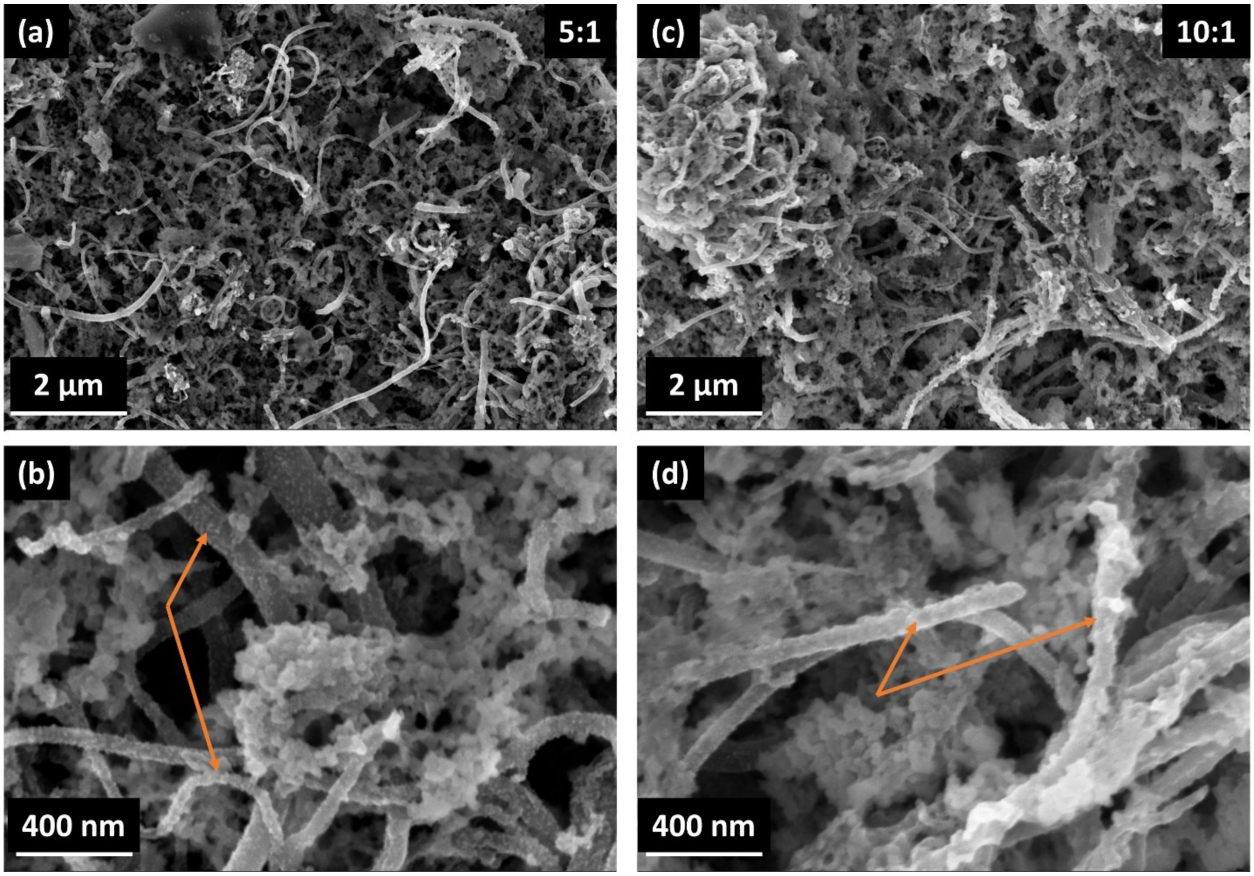

Figure S3.14 – SEM SE micrographs of the GDL surface for Mn3O4/N-CNT/GDL samples prepared with Mn to N-CNT ratios of a-b) 5:1 and c-d) 10:1. Arrows are used to show particles on the N-CNT surface for both samples.

Table S3.5 – Comparison of Mn to C Ratios from SEM EDX Analysis

$Mn(CH_3COO)_2$ to N-CNT Ratio (Synthesis, by Mass)	Average Ratio of Mn to C (SEM EDX)
5:1	1.13
10:1	1.36

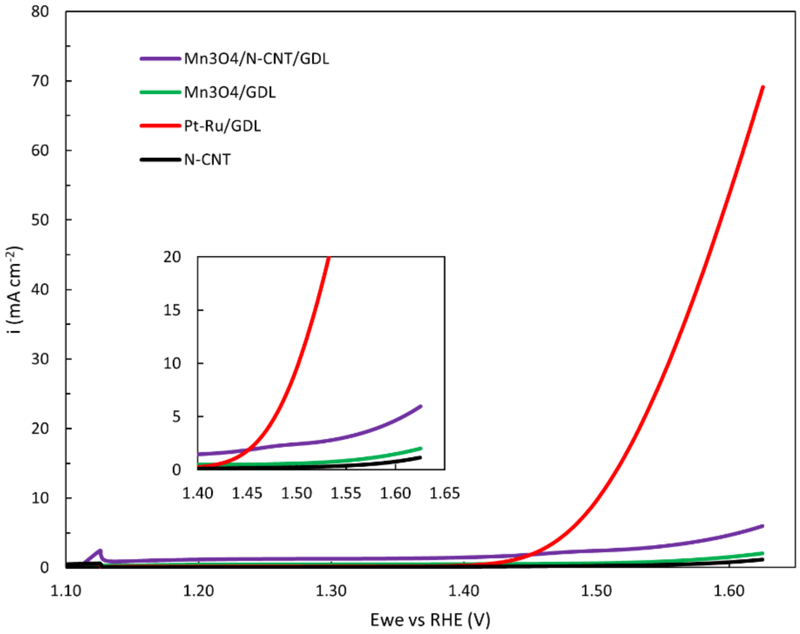

Figure S3.15 – OER LSV comparison of Mn_3O_4/N-CNT/GDL, N-CNT, Mn_3O_4/GDL and Pt-Ru/GDL catalysts. The insert is used to show more clearly the behaviour near 10 mA cm^{-2} to evaluate the onset of OER.

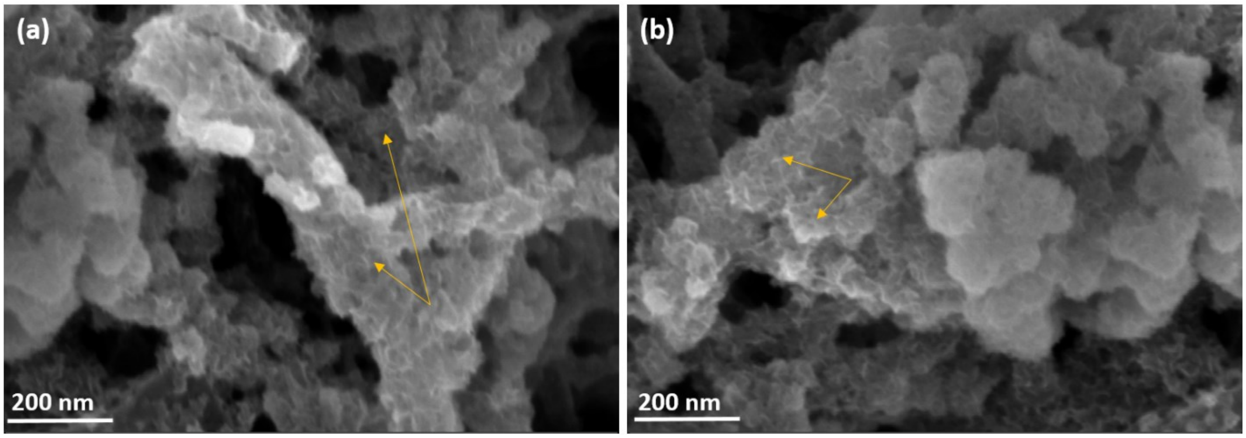

Figure S3.16 – SEM SE micrographs of Mn_3O_4/N-CNT/GDL after 100 cycles as a bifunctional catalyst showing a) Mn oxide re-deposition on the N-CNTs and b) Mn oxide deposits on the GDL carbon particles. Mn oxide deposits are indicated by arrows in both a) and b).

Table S3.6 compares Mn_3O_4/N-CNT/GDL (this work) with ZAB catalysts from the literature. Only catalysts tested in a battery configuration with aqueous electrolyte under ambient air conditions were included for comparison. Mn_3O_4/N-CNT/GDL boasts a better discharge potential than most transition metal-based catalysts presented, with comparable stability.

Table S3.6 – Performance Comparison of Mn_3O_4/N-CNT/GDL with Other ZAB Catalysts from the Literature

Notable Catalysts from Literature	**Catalyst Type**	**Preparation Method (Synthesis, Electrode Preparation)**	**Electrolyte**	**Discharge Potential (V) @ i (mA cm^{-2})**	**Cyclability**	**Ref***
Mn_3O_4/N-CNT/GDL	Transition Metal Oxide and Carbon Support	Impregnation (Soaking and Filtration)	6M KOH + 0.25M ZnO	1.21 @ 20	100 mV drop, 100 cycles, 10 mA cm^{-2}	This Work
Mn_3O_4/O-CNT	Transition Metal Oxide and Carbon Support	Mixing + Annealing and Oxygen Plasma Treatment, Soaked Carbon Cloth (CC)	6M KOH + 0.2M $ZnCl_2$	~1.20 @ 10	Stable, 150 cycles, 2 mA cm^{-2}	[19]
Mn_3O_4 QD/N-p-MCNT	Transition Metal Oxide and Carbon Support	Exfoliation of MWCNT, mixing and annealing, Paste Spread on Hydrophobic CC	6M KOH + 0.2M $Zn(CH_3COO)_2$	~1.1 @ 20	Stable (mechanically recharged), 100 h, 20 mA cm^{-2}	[117]
MnO_2/Co_3O_4	Transition Metal Oxide	Hydrothermal Synthesis, Spray Coated onto GDL	6M KOH	~1.15 @ 15	13% drop. 60 cycles, 15 mA cm^{-2}	[122]
Co_3O_4/N-CNT on Stainless Steel Mesh	Transition Metal Oxide and Carbon Support	CVD of CNTs, Electrodeposition	Cellulose Gelled w/ 6M KOH	1.20 @ 25	Stable, 60 cycles, 25 mA cm^{-2}	[123]
$Fe_{0.5}Co_{0.5}O_x$/N-rGO	Transition Metal Oxide and Carbon Support	Hummers Method and Chemical Reaction + Annealing, Drop Coating on Ni Foam Plates	6M KOH + 0.2M $ZnCl_2$	1.21 @ 10	50 mV drop, 60 cycles, 10 mA cm^{-2}	[43]
Fe-N-CNN	Metal Organic Framework	Hydrothermal Synthesis, Spray Coated onto GDL	6M KOH	1.27 @ 20	N/A - Not cycled	[124]
$MnCo_2O_4$/CNT	Transition Metal Oxide and Carbon Support	Hydrothermal Method, Slurry Applied to GDL	25 mL Aqueous Electrolyte (30 wt% KOH + 20g L^{-1} $ZnCl_2$)	1.20 @ 10	200 mV drop in potential, 70 cycles, 10 mA cm^{-2}	[125]
MnO_2 on Carbon Paper	Transition Metal Oxide and Carbon Support	Immersion/Direct Growth	6M KOH + 20g L^{-1} $ZnCl_2$	1.20 @ 15	20 mV drop in potential, 350 cycles, 15 mA cm^{-2}	[79]
Co_4N/CNW/CC	Transition Metal Nitride and Carbon Support	Electrodeposition and Pyrolysis	6M KOH + 0.2M Zn Acetate	~1.15 @ 10	Stable over 400 cycles	[126]
Fe@N-C	N-C Encapsulated Transition Metal	Pyrolysis, Slurry Applied to GDL	6M KOH + 0.2M Zn Acetate	1.25 @ 10	125 mV drop in potential, 200 cycles, 10 mA cm^{-2}	[127]

4 $(Co,Fe)_3O_4$ Decorated Nitrogen-Doped Carbon Nanotubes in Nano-Composite Gas Diffusion Layers as Highly Stable Bifunctional Catalysts for Rechargeable Zinc-Air Batteries

A version of this chapter has been accepted for publication in Batteries & Supercaps as of November 4th, 2019:

D. Aasen, M. P. Clark, D. G. Ivey, $(Co,Fe)_3O_4$ Decorated Nitrogen-Doped Carbon Nanotubes in Nano-Composite Gas Diffusion Layers as Highly Stable Bifunctional Catalysts for Rechargeable Zinc-Air Batteries, *Batteries & Supercaps,* **2019** (Accepted November 4th, 2019)

4.1 Introduction

Transition metals (Mn, Co, Ni, Fe, etc.) and their oxides have been extensively researched as replacements for precious metal catalysts because of their lower costs and higher abundance.[15] Mn and Co, in particular, have multiple valence states and various phases which may act as active sites for ORR and/or OER.[1], [13], [15] Since metal oxide catalysts suffer from poor conductivity, they are often coupled with nano-carbon supports such as carbon black, graphene, or carbon nanotubes (CNTs).[1], [15], [17] The carbon supports offer high conductivity and large surface area which help to improve catalytic activity when combined with the various transition metal oxides. Furthermore, the use of heteroatom doping within the carbon structure with non-metal atoms (N, O, S, B, P, and others) has been reported to increase the number of active sites for catalysis.[15], [36], [55] Nitrogen is the most common dopant reported for nano-carbon structures and shows good synergy with various metal and metal oxide catalysts through metal-N-C active sites.[15], [36], [45], [59], [62] Synthesis of transition metal oxides supported by doped nano-carbon structures is often achieved through complex means such as chemical vapour deposition, atomic layer deposition, pyrolysis, or various hydrothermal methods, which limit scalability and increase cost.[1], [15], [36], [58], [75] Bimetallic oxides have recently been explored as bifunctional or OER exclusive catalysts with promising results.[1], [15], [43] Bimetallic oxides with a spinel structure are of particular interest due to their mixed valence, low toxicity, and good redox stability.[128], [129] Spinel oxides also have been reported to show improved O_2 adsorption due to electrons hopping between the metals of different valence states, which may increase their activity towards ORR and OER.[130] Zhang et al. prepared $MnCo_2O_4$ on 3D graphene as a catalyst for ORR and reported good ORR stability and more positive half-wave potentials than Pt/C.[131] The combination of the catalytically active and stable spinel oxide with the high surface area and conductivity of the 3D graphene enabled the improved ORR activity of the catalyst. However, the use of Fe as a monometallic or bimetallic oxide has been scarcely reported for metal-air batteries.[39], [42] For instance, Wei et al. reported that various bimetallic oxides consisting of Ni, Co, and/or Fe can be used as OER catalysts for the electrolysis of water and that certain amounts of Fe in bimetallic and trimetallic oxides improved the onset potential for OER.[43] Wei et al. and Smith et al. both proposed that Fe facilitates higher oxidation states of other metals within the oxide, which may favour OER.[38], [43] Despite their findings, the use of Fe-Co oxides as catalysts for ZABs remains under-explored. Similar findings were reported by Bian et al, who synthesized $CoFe_2O_4$ on graphene as a bifunctional catalyst for ORR and OER for applications in fuel cells and metal-air batteries.[40] The synergy between Fe and Co was reported as being responsible for similar performance to commercially used Pt/C for ORR and superior performance to Pt/C for OER, based on results achieved through linear sweep voltammetry (LSV) measurements in 0.1 M KOH. However, no battery cycling was conducted. Xu et al. synthesized $CoFe_2O_4$ spinel particles on CNTs and reported good stability of the catalyst during cycling in a homemade ZAB at 5 mA cm^{-2} for 1500 cycles, with an efficiency of approximately 50%.[39] Although the $CoFe_2O_4$/CNTs showed similar OER performance to IrO_2, the ORR performance was improved.[39] Other reports of Co-Fe spinel oxides anchored to nitrogen-doped nanocarbons have shown excellent bifunctional activity through fundamental electrochemical measurements.[128], [129], [132], [133] However, many of these catalysts have not been studied with direct application to ZABs and have not been cycled in a battery configuration as a bifunctional catalyst. Thus, the results currently reported in literature suggest that Fe-Co spinel oxides show promise as bifunctional catalysts for ZABs and deserve further investigation.

Application of transition metal oxide-based catalysts onto the air electrode is often achieved through spray coating or application of a paste, resulting in a surface bound catalyst layer.

Spraying or application of the paste generally requires the use of binding agents to improve adhesion.[1] Electrodeposition has been explored as a binder-free alternative method to apply catalysts to the air electrode, but is still limited by the catalyst layer forming mostly on the electrode surface.[1], [5], [41], [75] Therefore, the issues related to flooding of the air electrode remain largely unsolved, as the electrolyte will eventually pass through the catalyst layer during cycling. Fabrication of an air electrode with catalyst throughout the depth of porosity in the electrode may yield two main advantages: preservation of the three phase boundary during cycling which will mitigate the effects of flooding and an increase in catalyst surface area which may improve battery performance at higher current densities.[79], [103] For instance, Sumboja et al. directly grew MnO_2 onto carbon paper in an immersion process and reported lower charge transfer resistance and superior performance compared with MnO_2 applied to the carbon paper by conventional means.[79] The findings were attributed to the larger three phase boundary area which resulted from deposition of MnO_2 throughout the porosity of the carbon paper and better contact of the catalyst with the air electrode. There are, however, no other reports in the recent literature discussing an impregnation-like technique for electrode preparation.

Our previous work reported excellent ORR performance for a gas diffusion layer (GDL) impregnated with Mn_3O_4 decorated N-CNTs.[134] The catalyst was loaded into the GDL by a simple soaking and filtering process, where the GDL was used in place of filter paper. The results were in good agreement with the work of Sumboja et al., as the impregnated electrode showed superior performance to electrodes prepared by conventional spray coating. However, performance of the Mn_3O_4/N-CNTs decreased during bifunctional cycling due to the instability of Mn_3O_4 in the harsh OER conditions. The current work aims to address the issues of oxygen reaction kinetics, flooding, bifunctional cyclability, and scalability through an air electrode impregnated by $(Co,Fe)_3O_4$ decorated nitrogen-doped CNTs (N-CNTs). The nomenclature $(Co,Fe)_3O_4$ is used throughout this paper (not $CoFe_2O_4$), since the Fe:Co ratio is variable with an average value in excess of 2. Coupling of $(Co,Fe)_3O_4$ with nitrogen doped nanocarbons may yield improvements in activity towards ORR due to metal-N-C sites, while maintaining the good OER performance and stability that has been previously reported for Co-Fe oxides. To the best of our knowledge, $(Co,Fe)_3O_4$ has yet to be synthesized on N-CNTs for application in ZABs. $(Co,Fe)_3O_4$ attached to N-CNTs may provide superior performance to that of $CoFe_2O_4$ anchored on N-doped carbon nanofibers (CNFs) reported by Li et al., due to the higher surface area of CNTs vs CNFs [129]. Similarly, $(Co,Fe)_3O_4$

attached to N-CNTs may yield superior ORR performance and a simpler synthesis method to that of $CoFe_2O_4$ on CNTs reported by Xu et al.[39], due to the increase in ORR active sites resulting from N-doping and impregnation, respectively. The catalyst and air electrode are prepared simultaneously in a simple one-pot process at room temperature. The proposed preparation of the air electrode is a low-cost procedure which yields a large catalyst surface area to increase the cell performance while preserving the three phase boundary during cycling.

4.2 Experimental

4.2.1 Material Synthesis and Electrode Preparation

Similar to the synthesis described in our previous work[134], 50 mg N-CNT (30-50 nm diameter, 1-2 µm length, ~3 wt% N, purchased from MK Nano), 175 mg of $FeSO_4{\cdot}7H_2O$, 35 mg of $Co(CH_3COO)_2{\cdot}4H_2O$, and 80 mg of NaOH were mixed in 10 mL of ethanol in a 30 mL glass beaker by vigorous stirring at 800 RPM for 10 min. The suspension was sonicated for 5 h, then 1 mL of Nafion 5% and an additional 15 mL of ethanol were added to the catalyst suspension. To prepare the air electrodes, PTFE coated porous carbon paper (purchased from the Fuel Cell Store, 5 wt% PTFE) was sectioned into circles, 4.5 cm in diameter, to be used as the gas diffusion layer (GDL) substrates. The substrates were soaked in the catalyst suspension for 20 min under sonication, then removed and dried in air for 10 min. Once dry, 5 mL of the catalyst suspension was passed through each substrate by vacuum filtration (BOLA vacuum filter funnel, Finemech Inc.). The GDL pieces were annealed for 0.5 h at 300°C resulting in a GDL impregnated with Co-Fe oxide decorated N-CNTs (denoted as $(Co,Fe)_3O_4$/N-CNT/GDL, since the Co-Fe oxide is identified later in the paper as $(Co,Fe)_3O_4$) with a mass loading of approximately 2.5 mg cm^{-2}. Identification of $(Co,Fe)_3O_4$ was achieved through various characterization techniques which are discussed in the following sections.

For comparison, GDL samples impregnated exclusively by N-CNTs (N-CNT/GDL) and samples impregnated by $(Co,Fe)_3O_4$ without N-CNTs ($(Co,Fe)_3O_4$/GDL) were prepared by the same procedure, while Pt-RuO_2 samples (referred to as Pt-Ru/GDL) were prepared by spray coating. For spray coating, 50 mg of Pt-RuO_2 powder (nominally 30 wt% Pt and 15 wt% RuO_2 on carbon black, purchased from Alfa Aesar) was mixed with 2 mL of deionized water (DIW), 1 mL of ethanol, and 0.1 mL Nafion 5% to form a catalyst ink which was sprayed onto the GDL.

4.2.2 Material Characterization

Scanning electron microscopy (SEM) imaging was conducted at an accelerating voltage of 5 kV and SEM energy dispersive X-ray (EDX) spectroscopy was done at an accelerating voltage of 20 kV (Zeiss Sigma Field Emission SEM). SEM samples were prepared by sectioning the prepared GDL into small pieces. The GDL pieces were then attached to an Al stub with carbon tape for analysis. Cross-sectional SEM samples were prepared by first freezing the GDL piece in liquid nitrogen for 60 s, cleaving the sample, and mounting it to a cross-sectional Al stub with carbon tape. Transmission electron microscopy (TEM) and EDX were performed at an accelerating voltage of 200 kV (JEOL JEM-ARM200CF TEM). To prepare TEM samples, catalyst material was scraped off the prepared GDL and dispersed in 1 mL of ethanol under sonication. The suspension was dropped by pipette onto holey carbon grids. X-ray photoelectron spectroscopy (XPS) analysis was conducted using a monochromatic Al-K_α X-ray source and a pass energy of 20 eV (Kratos AXIS Supra XPS Instrument). XPS sprecta were calibrated using the C 1s peak located at a binding energy of 285 eV. XPS samples were prepared by sectioning the prepared air electrode into 1 cm x 1 cm pieces.

4.2.3 Electrochemical Measurements and Battery Testing

Electrochemical measurements were performed using Biologic SP 300 and VSP-100 potentiostats in oxygen saturated 1 M KOH. A Pt coil and an Hg/HgO electrode (0.098 V vs SHE) were used as the counter and reference electrodes, respectively. The prepared GDL samples were utilized as the working electrodes with an exposed area of 1 cm^2. All electrochemical measurements were IR-corrected using the Hg/HgO reference electrode. Battery testing was done using a home-made Zn-air battery in 6 M KOH + 0.25 M ZnO under ambient air conditions. A Zn electrode was made from a 2 cm x 6 cm piece of Zn sheet metal (0.51 mm thick), while the prepared

GDL samples were used as the air electrode with an exposed area of 1 cm^2. Photographs of the half-cell and Zn-air battery configurations are shown in Figure S4.9.

4.3 Results and Discussion

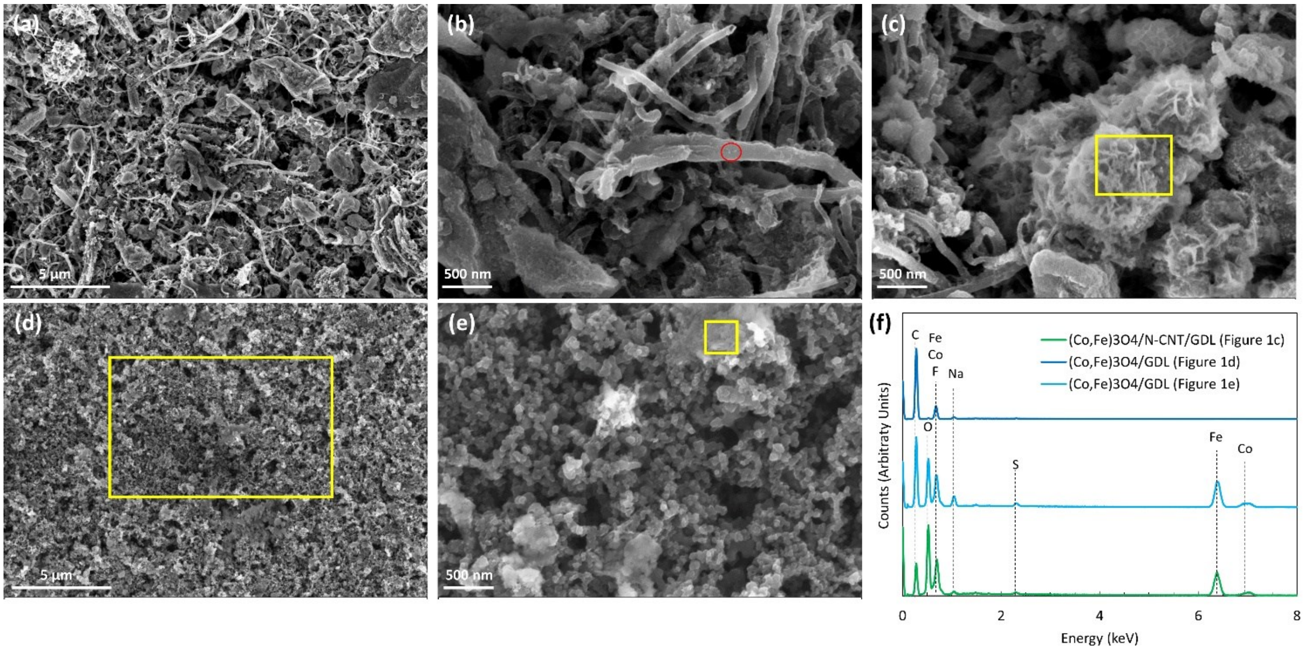

Figure 4.1 - SEM secondary electron (SE) micrographs of a) the GDL surface of $(Co,Fe)_3O_4$/N-CNT/GDL samples, b) $(Co,Fe)_3O_4$ decorated N-CNTs from a $(Co,Fe)_3O_4$/N-CNT/GDL sample at higher magnification, c) a $FeCoO_x$ precipitate on the surface of $(Co,Fe)_3O_4$/N-CNT/GDL at higher magnification, d) the GDL surface of a $(Co,Fe)_3O_4$/GDL sample, e) GDL pores and $FeCoO_x$ precipitates on the $(Co,Fe)_3O_4$/GDL surface at higher magnification, and f) EDX spectra acquired from $(Co,Fe)_3O_4$/N-CNT/GDL and $(Co,Fe)_3O_4$/GDL samples. Yellow boxes in (c)-(e) indicate regions used for EDX analysis. The red circle in (b) is used to highlight nanoparticles on the N-CNT surface.

SEM secondary electron (SE) micrographs are presented in Figure 4.1. Micrographs of the GDL surface for $(Co,Fe)_3O_4$/N-CNT/GDL samples (Figure 4.1a) show an abundance of nanotubes in addition to larger particles. EDX analysis (Figure 4.1f) of the large particles confirms that they are an Fe-Co oxide and are Fe-rich. A higher magnification image of the sample shows Fe-Co oxide nanoparticles along the N-CNTs (Figure 4.1b) as well as a sheet-like morphology of the Fe-Co oxide precipitates (Figure 4.1c). Contrary to expectation, synthesis without N-CNTs ($(Co,Fe)_3O_4$/GDL, Figure 4.1d and 4.1e) showed only a few precipitates on the surface of the GDL. EDX point analysis of $(Co,Fe)_3O_4$/GDL samples indicates that the particles are also an Fe-Co oxide (Figure 4.1e and 4.1f); however, EDX area analysis of the GDL surface shows no significant amounts of Fe or Co (Figure 4.1d and 4.1f). Additionally, higher magnification imaging of (Co,Fe)$_3$O$_4$/GDL samples shows no evidence of Fe-Co oxide nanoparticles or any Fe-Co oxide film on the GDL structure (Figure 4.1e). Therefore, it appears that Fe-Co oxide nanoparticles are only synthesized with the presence of the N-CNTs.

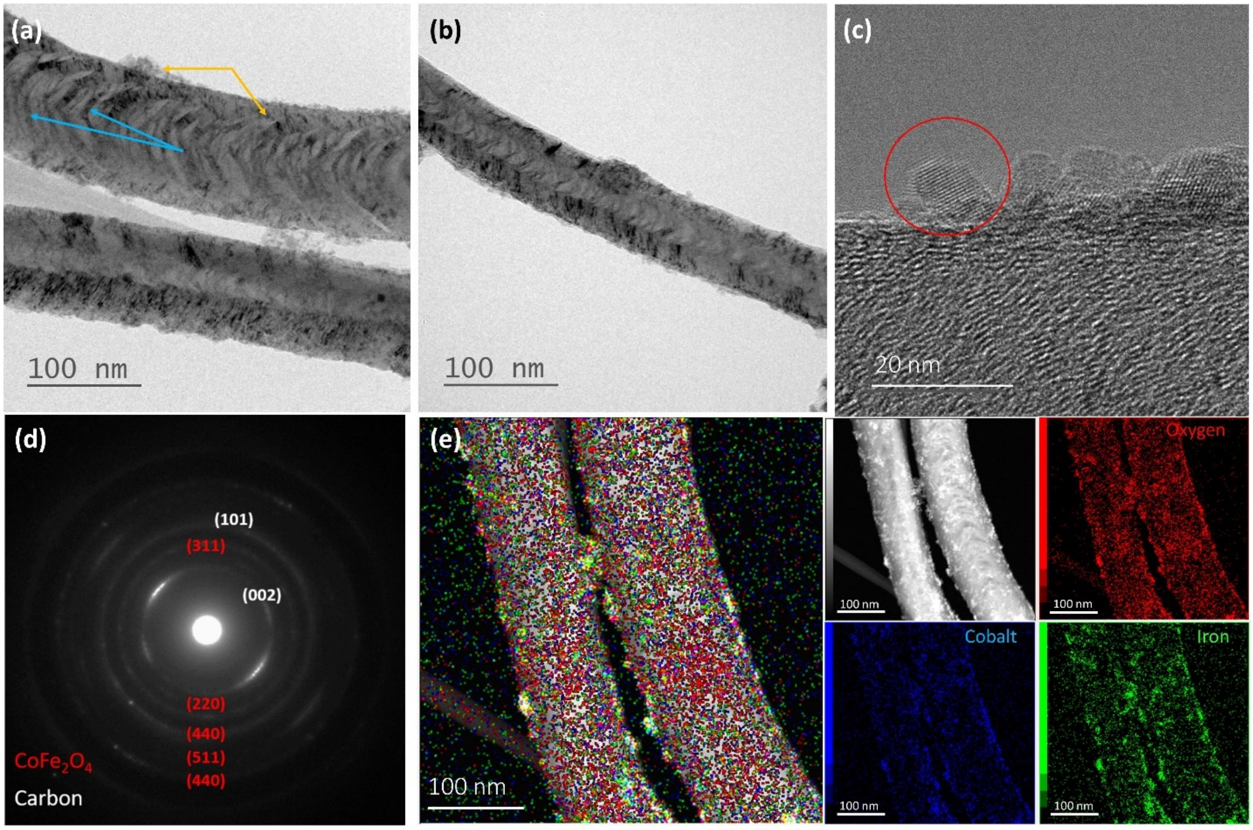

Figure 4.2 - TEM micrographs of (Co,Fe)$_3$O$_4$/N-CNTs: a) annealed (Co,Fe)$_3$O$_4$/N-CNTs, b) as-deposited (Co,Fe)$_3$O$_4$/N-CNT, c) high resolution TEM (HRTEM) micrograph of (Co,Fe)$_3$O$_4$ nanoparticles on the N-CNT surface, d) SAD pattern acquired from (Co,Fe)$_3$O$_4$ particles and CNTs, e) STEM EDX elemental maps of (Co,Fe)$_3$O$_4$/N-CNTs. Yellow arrows in (a) are used to highlight nanoparticles on the N-CNT surface, while blue arrows in (a) are used to indicate the N defects in the CNT wall. The red circle in (c) is used to highlight one of the (Co,Fe)$_3$O$_4$ nanoparticles.

TEM micrographs, a selected area diffraction (SAD) pattern, and STEM EDX elemental maps of (Co,Fe)$_3$O$_4$/N-CNT/GDL are shown in Figure 4.2. The as-purchased N-CNTs were also investigated for comparison using the same techniques (Figure S4.10). The bamboo structure of the CNTs due to N-doping can be clearly observed in Figure 4.2a.[55], [62] These defects are also clearly visible in the as-purchased N-CNTs (Figure S4.10a and S4.10b). Along the nitrogen induced defects in the CNT walls, numerous Fe-Co oxide particles, approximately 5-10 nm in size, are visible in both the annealed and as-deposited samples (Figure 4.2a-4.2c). The nitrogen defects increase the free energy of the system, resulting in preferential nucleation sites for the Fe-Co oxide particles. Fe-Co oxide particles are nanocrystalline as indicated by the lattice fringes in the high resolution TEM (HRTEM) image (Figure 4.2c). A sample SAD pattern taken from multiple Fe-Co oxide particles is presented in Figure 4.2d and can be used to identify the particles as a spinel phase (PDF #22-1086; $CoFe_2O_4$ with a = 0.8392 nm). The two diffuse rings in the SAD pattern correspond to the carbon (101) and (002) planes, which was confirmed based on the SAD pattern for the as-purchased N-CNTs (Figure S4.10c). It should be noted that the particles are denoted as $(Co,Fe)_3O_4$, instead of $CoFe_2O_4$, because SEM/TEM EDX analysis shows that the Fe:Co ratio is variable and exceeds 2.0. In addition, the XPS data (next paragraph) indicates that both Fe and Co have multiple valence states of 2+ and 3+. The crystal structure was the same for both annealed and as-deposited samples, suggesting that annealing has no significant role in the synthesis of the catalyst aside from removing excess H_2O and contaminants from the GDL. These results corroborate the EDX elemental maps (Figure 4.2e) which show that the Fe, Co, and O locations overlap over the N-CNT surface.

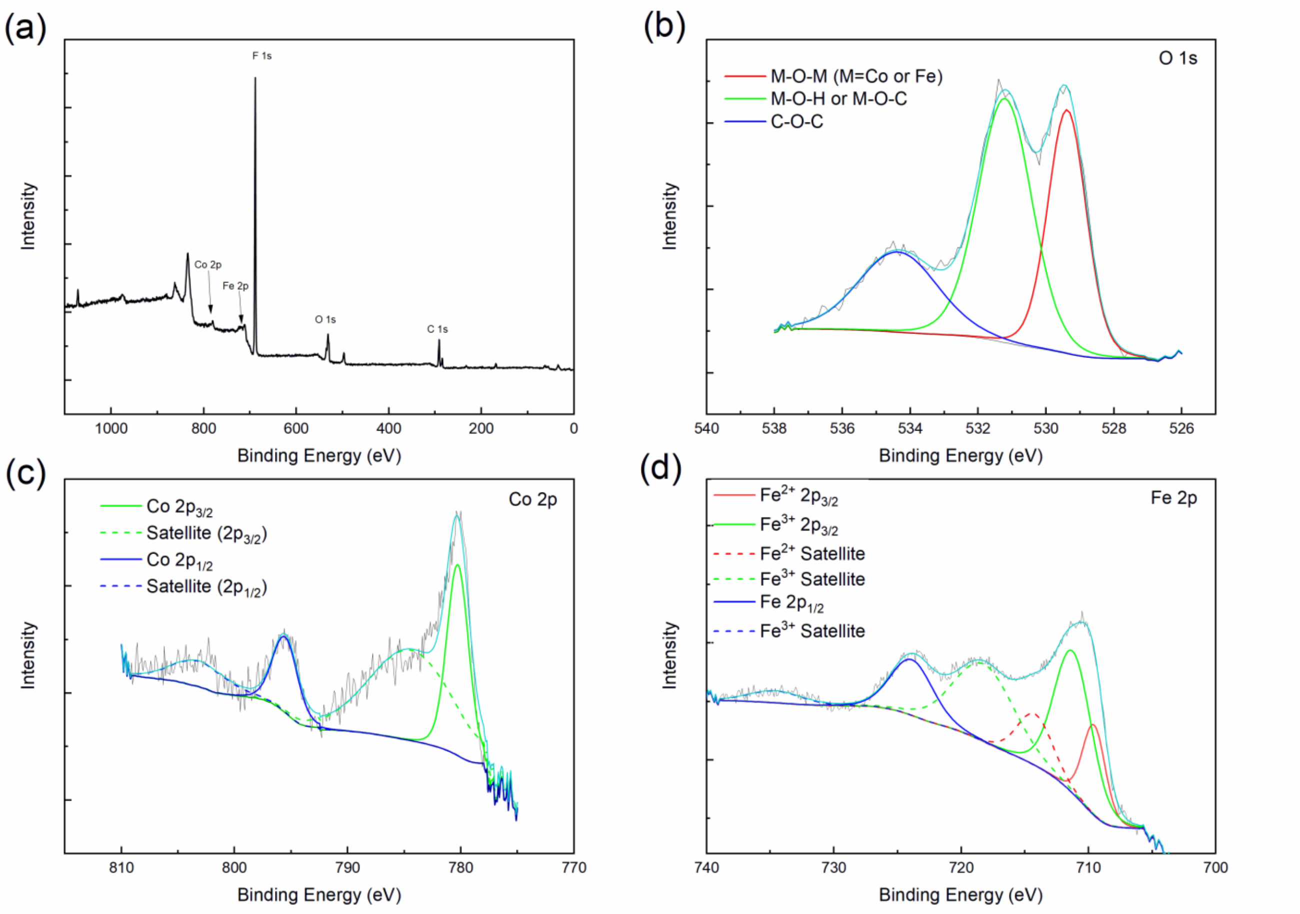

Figure 4.3 - XPS results for annealed $(Co,Fe)_3O_4$/N-CNT/GDL samples: a) survey spectrum, b) de-convolution of the O 1s spectrum, c) de-convolution of the Co 2p spectrum, and d) de-convolution of the Fe 2p spectrum.

The identification of $(Co,Fe)_3O_4$ was further confirmed through XPS analysis (Figure 4.3). Figure 4.3a shows the survey spectrum for $(Co,Fe)_3O_4$/N-CNT/GDL. The N, O, Co, and Fe peaks in the survey spectrum are from the $(Co,Fe)_3O_4$/N-CNTs while the F peak is from the PTFE in the GDL. Carbon is from both the CNTs and the GDL. The peaks from the catalyst material are relatively weak, particularly the N signal, which is due to the small amount of catalyst relative to the GDL substrate. De-convolution of the O 1s spectrum results in three main components at 529.4 eV, 531.2 eV, and 534.4 eV (Figure 4.3b). The binding energy of 529.4 eV corresponds to M-O-M (M = Co, Fe) bonds, while the binding energy of 531.2 eV may correspond to M-O-H bonds and M-O-C bonds.[40], [119], [129], [135], [136] The peak at a binding energy of 534.4 eV can be attributed to C-O-C bonds in the N-CNTs, PTFE, and/or GDL.[136] The O 1s spectrum confirms the presence of metal oxide bonds and is in good agreement with the literature.

De-convolution of the Co 2p spectrum yields 4 components (Figure 4.3c). The peaks at binding energies of 780.3 eV and 795.5 eV correspond to Co $2p_{3/2}$ and Co $2p_{1/2}$ peaks, respectively [40], [129], [132], [137]. Co valence can be estimated from the binding energy of the $2p_{3/2}$ and $2p_{1/2}$ shake-up satellite peaks [40], [129]. Satellite peak positions are at 784.4 eV and 803.2 eV, respectively, which suggests the presence of Co^{2+} and Co^{3+} in $(Co,Fe)_3O_4$/N-CNT/GDL.[40], [105], [129], [137] The presence of Co^{3+} corroborates the influence of Fe on preserving higher oxidation states in bimetallic oxides.[38], [43] Figure 4.3d shows the de-convolution of the Fe 2p spectrum. A number of peaks are fit to the 2p spectrum suggesting the presence of both Fe^{2+} and Fe^{3+} in the sample.[102], [105], [138] There are Fe^{3+} peaks at 711.3 eV and 723.9 eV, corresponding to $2p_{3/2}$ and $2p_{/1/2}$, respectively.[102], [105], [129], [138] Similarly, an Fe^{2+} peak at 709.6 eV corresponds to $2p_{3/2}$.[102], [138] Various shake-up satellite peaks for both Fe^{3+} and Fe^{2+} are also observed. The respective intensities of the Fe^{3+} and Fe^{2+} peaks suggest that Fe exists mostly as Fe^{3+} within the $(Co,Fe)_3O_4$/N-CNT/GDL sample.

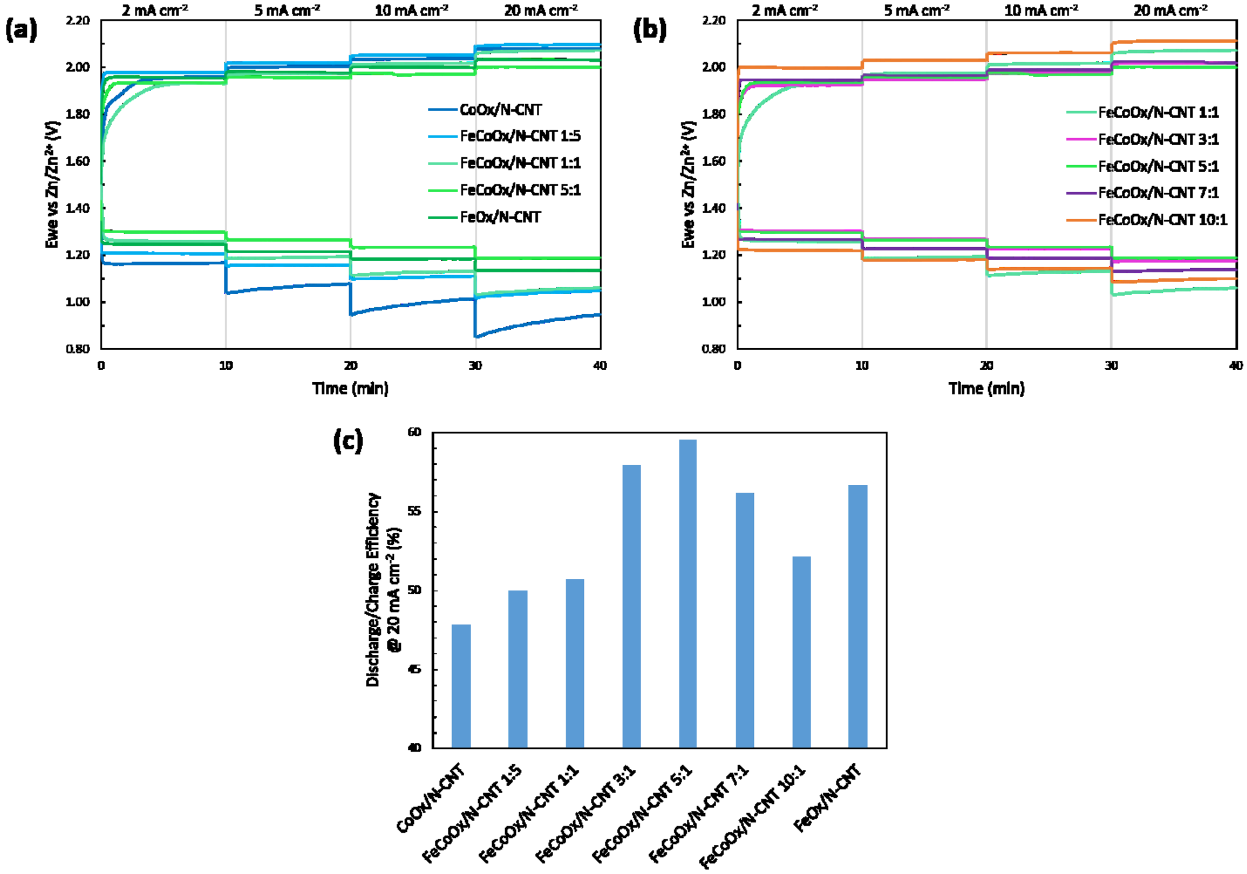

Figure 4.4 - a) Battery discharge and charge rate data comparison of FeCoOx/N-CNT (with varying Fe to Co ratios (Fe:Co) in the deposition solution), CoOx/N-CNT, and FeOx/N-CNT samples. b) Discharge and charge rate data for FeCoOx/N-CNTs with additional Fe:Co ratios. c) Discharge/charge efficiencies at 20 mA cm^{-2} for FeCoOx//N-CNT samples with varying Fe:Co ratios.

To optimize the synthesis and performance of $(Co,Fe)_3O_4$/N-CNT/GDL catalysts, samples using various ratios of $Fe(SO_4)\cdot 7H_2O$ and $Co(CH_3COO)_2\cdot 4H_2O$ in the deposition solution (expressed as FeCoOx/N-CNT Fe:Co, where Fe:Co denotes the Fe to Co ratio in solution) were synthesized and tested in a home-made ZAB (Figure 4.4). Fe oxide and Co oxide samples coupled with N-CNTs were also synthesized via the same procedure and were tested for comparison (denoted as FeO_x/N-CNT and CoO_x/N-CNT, respectively). Battery discharge and charge rate tests (Figure 4.4a and 4.4b) were conducted in place of half-cell (three electrode) LSV tests, due to discrepancies between half-cell performance and battery performance. Half-cell LSV testing was found to be unreliable in predicting battery performance at higher current densities. This observation is presumed to be due to oxygen saturation of the electrolyte in half-cell tests, meaning oxygen is not required to diffuse through the GDL to reach a three-phase boundary. Therefore, the catalyst layer on the surface maintains immediate contact with the O_2 molecules resulting in less contribution from the catalysts within the GDL porosity. In a battery configuration, however, air must pass through the GDL to reach the catalyst and electrolyte. In this scenario, catalysts throughout the GDL porosity shorten the oxygen diffusion pathway and create a larger three phase boundary area [79]. Thus, battery tests were determined to be more suitable for comparison based on the desired application. The combination of Co and Fe shows significant improvement in comparison with both CoO_x/N-CNT and FeO_x/N-CNT samples (Figure 4.4a). Further testing was done on other Fe and Co ratios in the catalyst suspension (Figure 4.4b). The efficiencies for each sample were calculated by dividing the discharge potential by the charge potential at a common current density of 20 mA cm^{-2} and are compared in Figure 4.4c. An Fe:Co ratio of 5:1 provided the best performance for both ORR and OER, with an efficiency of 59.7% (Figure 4.4b and 4.4c). All subsequent electrochemical testing for $(Co,Fe)_3O_4$/N-CNT/GDL is reported for the optimized composition (Fe:Co ratio = 5:1).

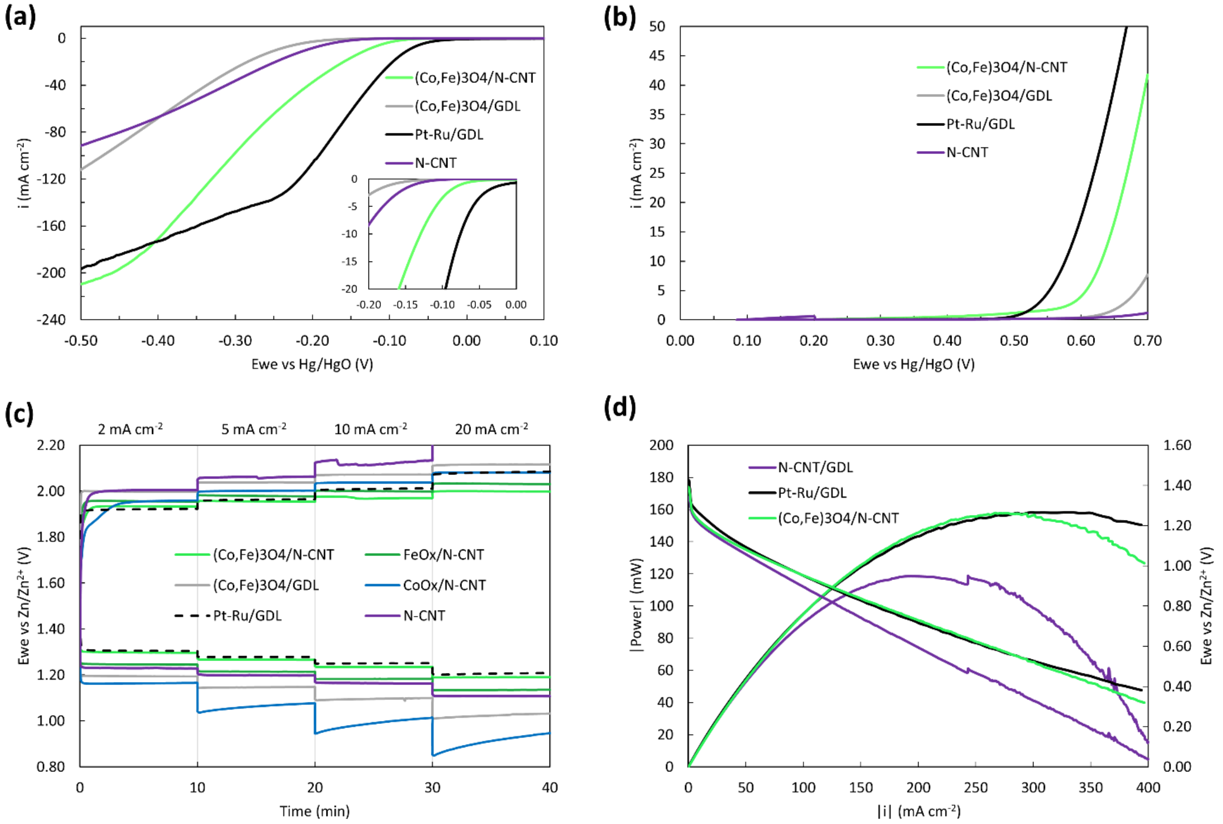

Figure 4.5 - a) LSV curves showing ORR catalyst activity in O_2-saturated 1 M KOH. b) LSV curves showing OER catalyst activity in O_2-saturated 1 M KOH. d) Catalyst discharge and charge rates in a Zn-air battery configuration at varying current densities. d) Polarization and power curve comparison of catalysts.

$(Co,Fe)_3O_4$/N-CNT/GDL was then compared electrochemically with $(Co,Fe)_3O_4$/GDL, N-CNT/GDL, and the baseline Pt-Ru/GDL catalyst (Figure 4.5). Half-cell LSV results for ORR and OER are presented in Figure 4.5a and 4.5b, respectively. For comparison purposes, the ORR and OER onset potentials were defined as the potential reached at 10 mA cm^{-2} for the respective reaction. $(Co,Fe)_3O_4$/N-CNT/GDL shows significant improvement in activity towards both oxygen reactions when compared with $(Co,Fe)_3O_4$/GDL samples. The improvement in activity confirms that the combination of $(Co,Fe)_3O_4$ particles and N-CNTs increases the active sites for both reactions. It is presumed that the number of active sites for both reactions is increased due to the higher valence state of Co facilitated by the Fe, in addition to the metal-N-C centres. $(Co,Fe)_3O_4$/N-CNT/GDL shows an onset potential of approximately -0.13 V vs Hg/HgO for ORR, which is only ~55 mV worse than that of Pt-Ru (-0.075 V vs Hg/HgO). The same trend is observed for OER LSV results (Figure 4.5b). $(Co,Fe)_3O_4$/N-CNT/GDL shows increased activity toward oxygen evolution relative to $(Co,Fe)_3O_4$/GDL. The onset potential for OER is only ~53 mV worse than that of Pt-Ru (0.628 V and 0.575 V vs Hg/HgO, respectively). Despite appearing to be inferior to Pt-Ru in LSV testing, battery discharge and charge rate tests suggest that $(Co,Fe)_3O_4$/N-CNT/GDL is the superior catalyst, particularly at high current densities and for OER (Figure 4.5c). Again, a significant performance improvement for both ORR and OER is observed when compared with $(Co,Fe)_3O_4$/GDL. It can, therefore, be concluded that the contribution to catalysis of the isolated precipitate regions on the GDL surface observed in Figure 4.3 is not significant. The discharge potential of $(Co,Fe)_3O_4$/N-CNT/GDL is 1.19 V at 20 mA cm^{-2}, which is only 20 mV lower than that of Pt-Ru (1.21 V at 20 mA cm^{-2}). Moreover, the charge potential of $(Co,Fe)_3O_4$/N-CNT/GDL is 1.99 V at 20 mA cm^{-2}, which compares favourably with that of Pt-Ru (2.07 V at 20 mA cm^{-2}). The overall discharge/charge efficiency calculated from the battery rate tests of $(Co,Fe)_3O_4$/N-CNT/GDL at 20 mA cm^{-2} is superior to that for Pt-Ru (59.7% vs. 58.5%, respectively). A power curve comparison of $(Co,Fe)_3O_4$/N-CNT/GDL, N-CNT/GDL, and Pt-Ru/GDL is presented in Figure 4.5d. The power curve of $(Co,Fe)_3O_4$/N-CNT/GDL reaches a maximum of 158 mW cm^{-2} at 278 mA cm^{-2}, matching that of Pt-Ru.

The discrepancies between half-cell LSV measurements and battery rate tests were also observed in our previous work.[134] Half-cell LSV measurements were insensitive to electrode preparation methods due to the presence of O_2 in the electrolyte. Battery performance, on the other hand, was much more sensitive to the electrode preparation method, which influenced the distribution and active surface area of the catalysts. The superior performance of the catalyst in battery rate tests is attributed to the benefits provided by the impregnation technique (such as higher active surface area, shorter oxygen diffusion pathway, and larger three-phase boundary area).[134]

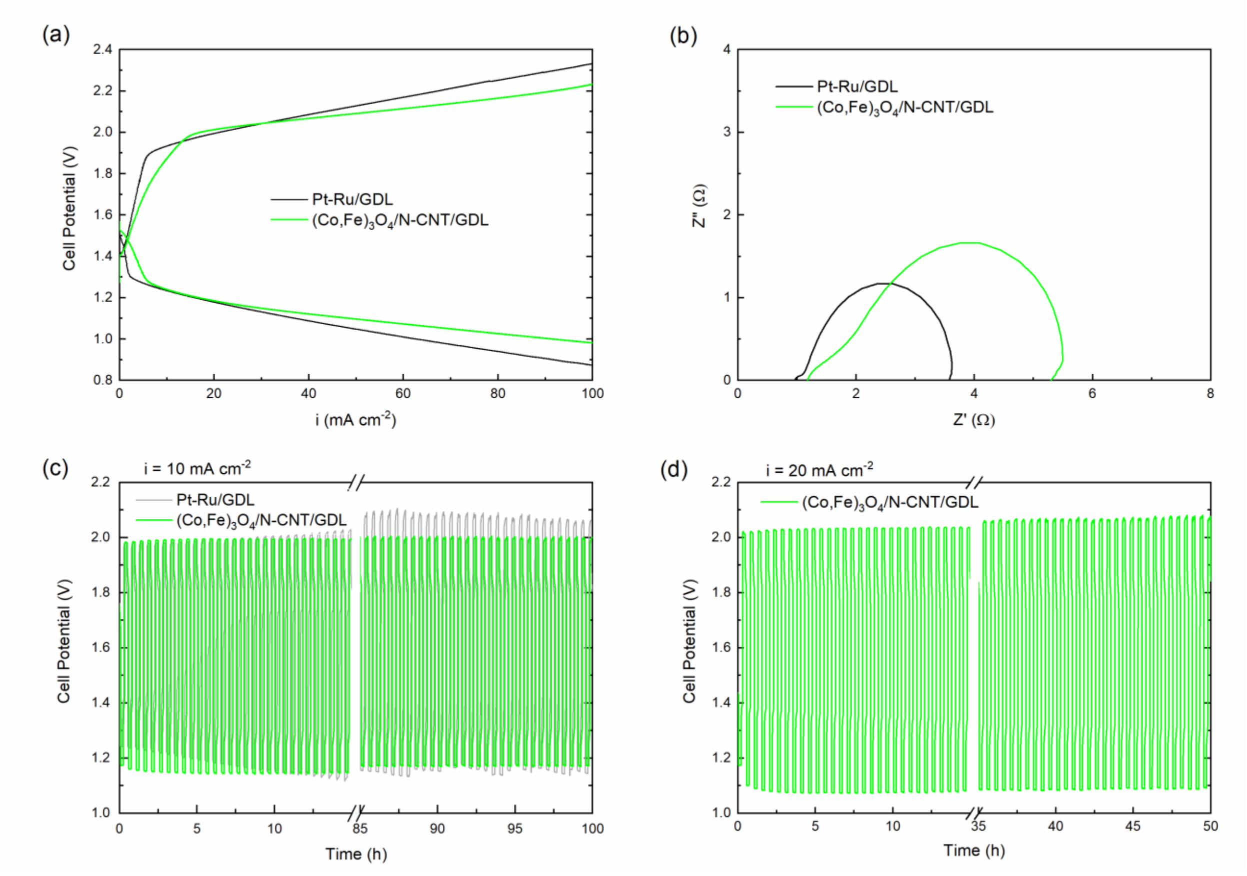

Figure 4.6 - a) Zn-air battery polarization curves for (Co,Fe)$_3$O$_4$/N-CNT/GDL and Pt-Ru/GDL samples. b) EIS Nyquist plot comparison of (Co,Fe)$_3$O$_4$/N-CNT/GDL and Pt-Ru/GDL. c) Cycling comparison of Pt-Ru/GDL and (Co,Fe)$_3$O$_4$/N-CNT/GDL at 10 mA cm^{-2}. d) Cycling results for (Co,Fe)$_3$O$_4$/N-CNT/GDL at 20 mA cm^{-2}. Cycling tests were conducted in 6 M KOH at 30 min per cycle.

(Co,Fe)$_3$O$_4$/N-CNT/GDL polarization curves, EIS analysis, and cycling results are presented in Figure 4.6. ORR and OER polarization curves for (Co,Fe)$_3$O$_4$/N-CNT/GDL are comparable to those for Pt-Ru/GDL (Figure 4.6a). (Co,Fe)$_3$O$_4$/N-CNT/GDL performs better for both charging and discharging (lower OER and higher OER potentials) at current densities in excess of 30 mA cm^{-2}, which can be attributed to the higher surface area achieved due to the N-CNTs and impregnation.[79], [103] Charge transfer resistance can be estimated from the size of the semi-circular region of the Nyquist plot in Figure 4.6b.[97], [110] (Co,Fe)$_3$O$_4$/N-CNT/GDL samples have a slightly higher charge transfer resistance when compared with Pt-Ru/GDL samples, despite comparable polarization performance. This corroborates the results of the LSV curves where Pt-Ru/GDL shows better catalytic activity. Therefore, the Nyquist plot suggests that the battery performance of $(Co,Fe)_3O_4$/N-CNT/GDL is enhanced due to the impregnation technique and agrees with results from our previous work.[134]

Bifunctional cycling results for $(Co,Fe)_3O_4$/N-CNT/GDL at 10 mA cm^{-2} (Figure 4.6c) show excellent stability of the catalyst over 200 cycles. A slight drop of 30 mV in ORR potential occurs for the first 10 cycles, due to the hydrophobicity of the PTFE within the GDL. During cycling, $(Co,Fe)_3O_4$/N-CNT/GDL recovers its initial potential, which is attributed to better wetting of the GDL providing better electrolyte contact with the catalyst surface. After recovery, the discharge potential is stable for the remaining cycles. The OER potential for $(Co,Fe)_3O_4$/N-CNT/GDL increases by only 30 mV over the 200-cycle period. The increase in OER potential is attributed to the formation and accumulation of O_2 bubbles within the pores of the GDL during cycling. As the electrolyte infiltrates the electrode, bubbles are no longer formed exclusively on its surface. Bubbles trapped within the porosity of the electrode limit the available surface area for OER leading to the slight increase in potential. The discharge/charge efficiency decreases by only 0.6% during cycling (Table 4.1). The results compare favourably with Pt-Ru/GDL cycling behavior (Figure 4.6c). Initially, Pt-Ru/GDL shows similar charge potentials and superior discharge potentials to those of $(Co,Fe)_3O_4$/N-CNT/GDL. The performance of Pt-Ru/GDL worsens over cycling with a 7.3% drop in efficiency over the cycling period (Table 4.1) and becomes worse than $(Co,Fe)_3O_4$/N-CNT/GDL after approximately 22 cycles. The fluctuation in discharge potential for Pt-Ru/GDL is due to accumulation of O_2 bubbles on the GDL surface. As the bubbles accumulate, the relative current increases resulting in a potential drop. Once the bubbles are removed, the potential recovers.

Because of the exceptional performance of the catalyst at 10 mA cm^{-2}, $(Co,Fe)_3O_4$/N-CNT/GDL samples were also tested at 20 mA cm^{-2} for 100 cycles. Similar behaviour to that at 10 mA cm^{-2} was observed, although the effects are more pronounced. The discharge potential drops significantly over the first few cycles (100 mV drop). As cycling continues, the discharge potential gradually recovers, almost reaching the initial discharge potential, and becomes stable for the remainder of the test. The gradual 40 mV increase in OER potential is again attributed to O_2 bubbles trapped within the GDL. Despite the adverse effects at higher current densities, the loss in efficiency during cycling at 20 mA cm^{-2} is only 5.2% (58.7% to 53.5%). These results compare very favourably to Pt-Ru/GDL cycled under the same conditions (Figure S4.11, Table 4.1); Pt-Ru/GDL undergoes more degradation during cycling, particularly at 20 mA cm^{-2}.

The durability of $(Co,Fe)_3O_4$/N-CNT/GDL was further investigated through half-cell chronopotentiometry (CP). The change in potential was measured at current densities of -10 mA cm^{-2} and 10 mA cm^{-2} for ORR and OER, respectively (Figure 4.7a). CP results show excellent stability of the catalyst for both reactions, particularly for OER. The difference between ORR and OER potentials (ΔE) increased only 60 mV over 48 h which results in a ΔE retention of 93.4%. The long-term durability of $(Co,Fe)_3O_4$/N-CNT/GDL was also tested through cycling at 10 mA cm^{-2} for 250 h (500 cycles, Figure 4.7b). The cycling test showed good stability of the catalyst even after 500 cycles with similar ORR and OER behaviour to that for the 100 h cycling test. The ORR potential stabilizes after 50 h, then decreases slowly after 150 h reaching a final potential of ~1.16 V after 500 cycles. The OER potential increases slowly due to O_2 bubble accumulation within the GDL and reaches a final potential of ~2.01 V. The final efficiency after 500 cycles is 57.8% (ΔE = 0.85 V) which is only 1.3% lower than the initial efficiency (59.1%, ΔE = 0.81 V).

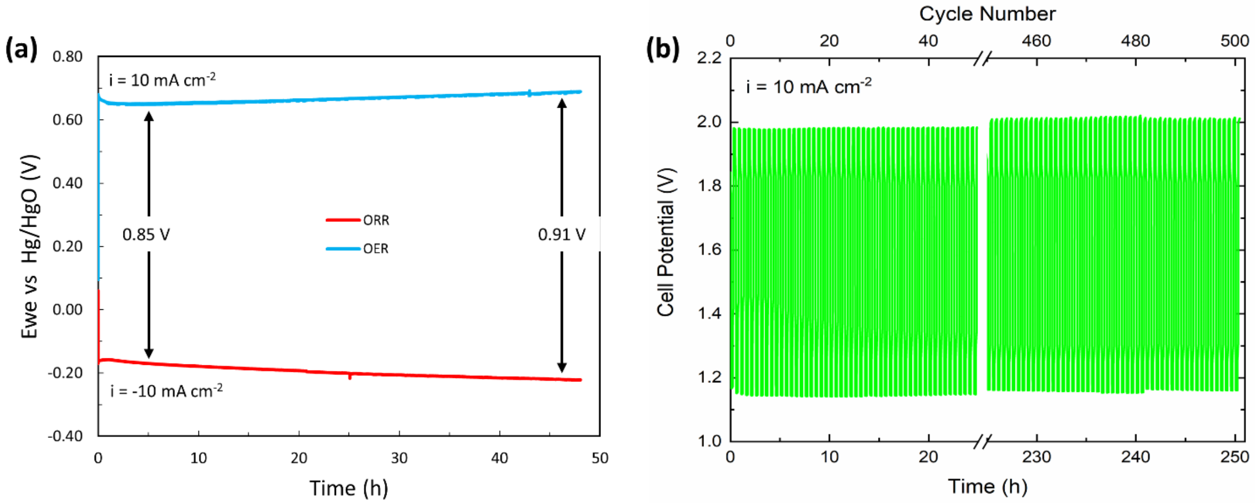

Figure 4.7 – Long-term durability analysis of $(Co,Fe)_3O_4$/N-CNT/GDL; a) ORR and OER CP measurements at -10 mA cm^{-2} and 10 mA cm^{-2}, respectively, and b) long-term bifunctional cycling at 10 mA cm^{-2} for 250 h (500 cycles) in 6 M KOH + 0.25 M ZnO.

It is apparent for cycling at both 10 mA cm^{-2} and 20 mA cm^{-2} that $(Co,Fe)_3O_4$/N-CNT is very stable as a bifunctional catalyst. Furthermore, the performance of $(Co,Fe)_3O_4$/N-CNT/GDL is superior to that of other bifunctional Co-Fe based catalysts reported in the literature (Table 4.2). $(Co,Fe)_3O_4$/N-CNT/GDL also compares favourably to the ZAB performance other spinel and metal-N-C catalysts in literature. For instance, $NiCo_2O_{4s}$ catalysts on a Ni-based GDL were prepared by Cano et al. and were cycled in a ZAB (6 M KOH) at 10 mA cm^{-2}.[139] However, significant performance losses were reported after 50 h (~55.6% efficiency at 50 h). Performance declined more rapidly until 100 h with a final discharge potential of ~0.1 V. 3D Fe/N co-doped graphene (Fe/N-G) was developed by Wang et al. and showed superior stability and efficiency to Pt/C when cycled in a ZAB (6 M KOH + 0.2 M Zn acetate) at 20 mA cm^{-2} for 60 h.[140] However, the discharge/charge efficiency of Fe/N-G was ~44% after 50 h. In both cases, the $(Co,Fe)_3O_4$/N-CNT catalyst from this work had superior performance under similar cycling conditions.

Table 4.1 - Bifunctional Battery Cycling Results for $(Co,Fe)_3O_4$/N-CNT/GDL and Pt-Ru/GDL Air Electrodes

Tested Electrode		**Cycling at 10 mA cm^{-2} (100 hours, 200 Cycles)**				**Cycling at 20 mA cm^{-2} (50 hours, 100 Cycles)**			
		E_{ORR} (V)	E_{OER} (V)	ΔE (V)	Efficiency* (%)	E_{ORR} (V)	E_{OER} (V)	ΔE (V)	Efficiency* (%)
$(Co,Fe)_3O_4$/N-CNT/GDL	Initial:	1.17	1.98	0.81	59.1	1.18	2.01	0.83	58.7
	Final:	1.17	2.00	0.83	58.5	1.10	2.06	0.95	53.5
Pt-Ru/GDL	Initial:	1.24	1.98	0.72	62.6	1.18	2.06	0.88	57.3
	Final:	1.15	2.08	0.95	55.3	0.95	2.30	1.35	41.3

* Efficiencies are calculated using an average of the first and last 10 cycles.

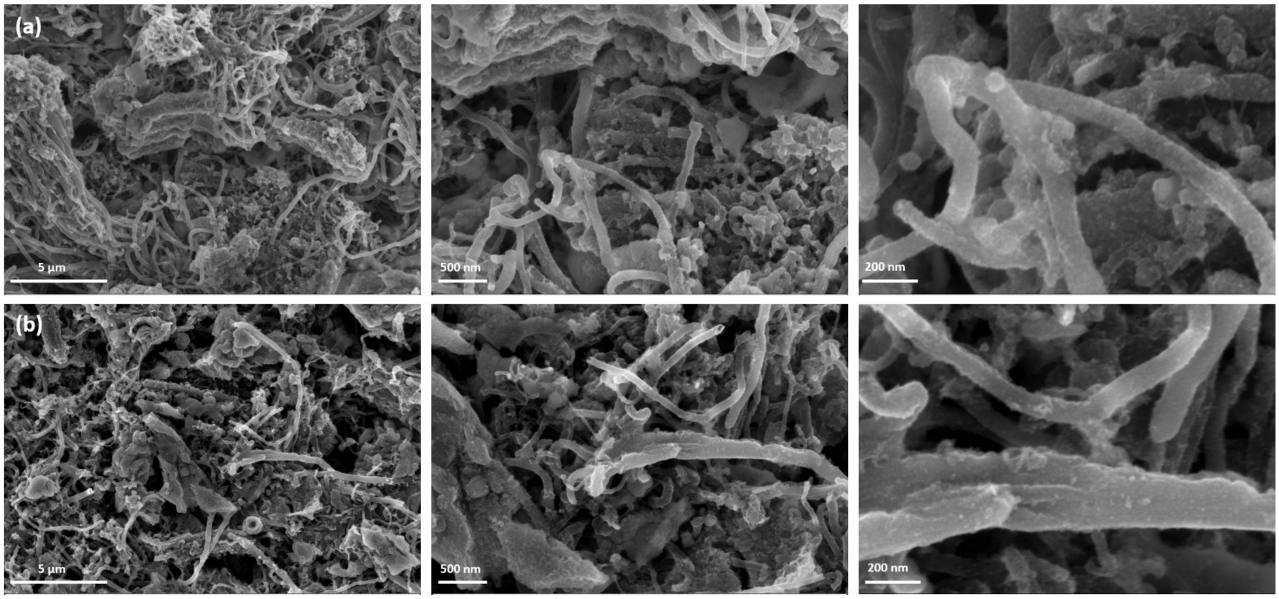

Figure 4.8 - SEM SE micrographs at various magnifications of $(Co,Fe)_3O_4$/N-CNT/GDL samples before (a) and after (b) cycling at 10 mA cm^{-2}.

SEM SE micrographs of $(Co,Fe)_3O_4$/N-CNT/GDL samples before and after cycling are presented in Figure 4.8. The GDL surface remains virtually the same before (Figure 4.8a) and after cycling (Figure 4.8b). The Fe-Co oxide precipitates are still visible on the electrode surface at lower magnification and $(Co,Fe)_3O_4$ particles are still observable on the nanotube surface at higher magnification. The similarities between as-deposited and cycled samples confirm the excellent stability of the $(Co,Fe)_3O_4$/N-CNT/GDL electrode in both ORR and OER conditions. The negligible changes in morphology of the GDL and N-CNT surfaces corroborate the assumption that the slight performance loss in OER during cycling is due primarily to the formation and trapping of O_2 bubbles and is not a result of catalyst degradation.

Table 4.2 - Comparison of Co-Fe Catalysts Recently Reported in the Literature

Catalyst	Synthesis, Electrode Preparation	Battery/Cell Characteristics	E_{ORR} (V) @ i (mA cm^{-2})	E_{OER} (V) @ i (mA cm^{-2})	Cycling Parameters	Cycling Results (Efficiency % @ i mA cm^{-2})	Ref.
$(Co,Fe)_3O_4$/N-CNT/GDL	Impregnation (Soaking + Vacuum Filtration)	6 M KOH + 0.25 M ZnO, Ambient Air	1.19 @ 20	1.99 @ 20	10 mA cm^{-2} and 20 mA cm^{-2} bifunctional cycling for 200 cycles (100 h)	58.7% @ 10, 53.5% @ 20	This Work
$CoFe_2O_4$ decorated CNTs	Hydrothermal Method, Spray Coating	6 M KOH, Ambient Air	1.10 @ 20	2.00 @ 5	5 mA cm^{-2} bifunctional cycling for 1200 cycles (200 h)	60% (Initial) to 50% (Final)@ 5	[39]
Co-Fe	Electrodeposition	6 M KOH + 0.25 M ZnO, Ambient Air	1.10 @ 10	1.95 @ 10	5 mA cm^{-2} bifunctional cycling for 20 cycles (20 h)	~60% @ 5	[75]
Other Results (Not Cycled):							
$CoFe_2O_4$/rGO	Hydrothermal Method, Drop Cast onto Glassy Carbon Electrode (GCE)	Rotating Disk Electrode (RDE) testing for ORR, LSV for OER, 0.1 M KOH	0.862 vs RHE*	1.60 vs RHE @ 5	Not Cycled	N/A	[40]
$CoFe_2O_4$/CNT Hybrid	Solvothermal Method, Drop Cast onto GCE	RDE testing, 0.1 M KOH	0.85 vs RHE*	1.58 vs RHE*	Not Cycled	N/A	[137]
$CoFe_2O_4$/3DG (3D graphene)	Calcination and Hydrothermal Method, Drop Cast onto GCE	RDE Testing, 0.1 M KOH	0.92 vs RHE*	1.63 vs RHE @ 10	Not Cycled	N/A	[135]
$FeCo_2O_4$/hollow graphene spheres	Hydrothermal-Assisted Electrostatic Assembly Method, Drop Cast onto GCE	RDE testing for ORR, LSV for OER, 0.1 M KOH	0.91 V vs RHE*	1.66 vs RHE @ 5	Not Cycled	N/A	[42]
$CoFe_2O_4$/N-CNF	Electrospinning and Calcination, Drop Cast onto GCE	RDE testing for OER, 0.1 M KOH	Not Tested	1.57 vs RHE @ 10	Not Cycled	N/A	[129]
Co-$CoFe_2O_4$/N-rGO	Polymerization and Pyrolysis, Drop Cast onto GCE	RDE testing, 0.1 M KOH	0.77 vs RHE*	1.62 vs RHE @ 10	Not Cycled	N/A	[128]
$CoFe_2O_4$	Selective Dealloying and Annealing, Mixed with XC-72, Drop Cast onto GCE	RDE testing, 0.1 M KOH	0.85 vs RHE*	1.57 vs RHE*	Not Cycled	N/A	[130]

* Indicates onset potential results obtained from RDE testing. Potentials are vs Zn/Zn^{2+} unless otherwise stated.

4.4 Summary

A highly stable and efficient $(Co,Fe)_3O_4$/N-CNT catalyst was synthesized and impregnated simultaneously into the GDL in a simple one-pot process. The combination of Fe and Co in a spinel oxide yielded higher Co oxidation states which increase the activity towards OER. Anchoring the oxide particles onto N-CNTs increased the number of active sites towards ORR through the formation of metal-N-C centres. Several Fe:Co composition ratios in the deposition solution were studied, with a ratio of 5:1 providing the best performance. The discharge potential of $(Co,Fe)_3O_4$/N-CNT/GDL (optimal composition) was 1.19 V at 20 mA cm^{-2} which is only 20 mV lower than that for Pt-Ru, while the charge potential at the same current density was superior to that of Pt-Ru/GDL (2.00 V vs 2.06 V, respectively); the efficiency was 59.7%. In battery cycling tests, $(Co,Fe)_3O_4$/N-CNT/GDL was very stable at both 10 mA cm^{-2} and 20 mA cm^{-2} with final efficiencies of 58.5% and 53.5%, respectively. The cycling stability of the catalyst was also superior to that of Pt-Ru/GDL which showed final efficiencies of 55.3% and 43.1% at 10 mA cm^{-2} and 20 mA cm^{-2}, respectively. The excellent battery performance is proposed to be a result of the inherent bifunctional activity of the $(Co,Fe)_3O_4$/N-CNTs combined with the benefits achieved through impregnation of the GDL. The benefits offered by impregnation include: intimate contact between the catalyst and electrode which facilitates charge transfer, higher active surface area due to catalyst dispersion within the porosity of the GDL, and preservation of the three-phase boundary during cycling. Minimal performance losses during cycling highlight the effectiveness of impregnation to address the issues associated with flooding of the air electrode. The simultaneous synthesis and electrode preparation technique is a low-cost and effective means to prepare high performing air electrodes for ZABs without the need for complex processes or facilities.

4.5 Supporting Information

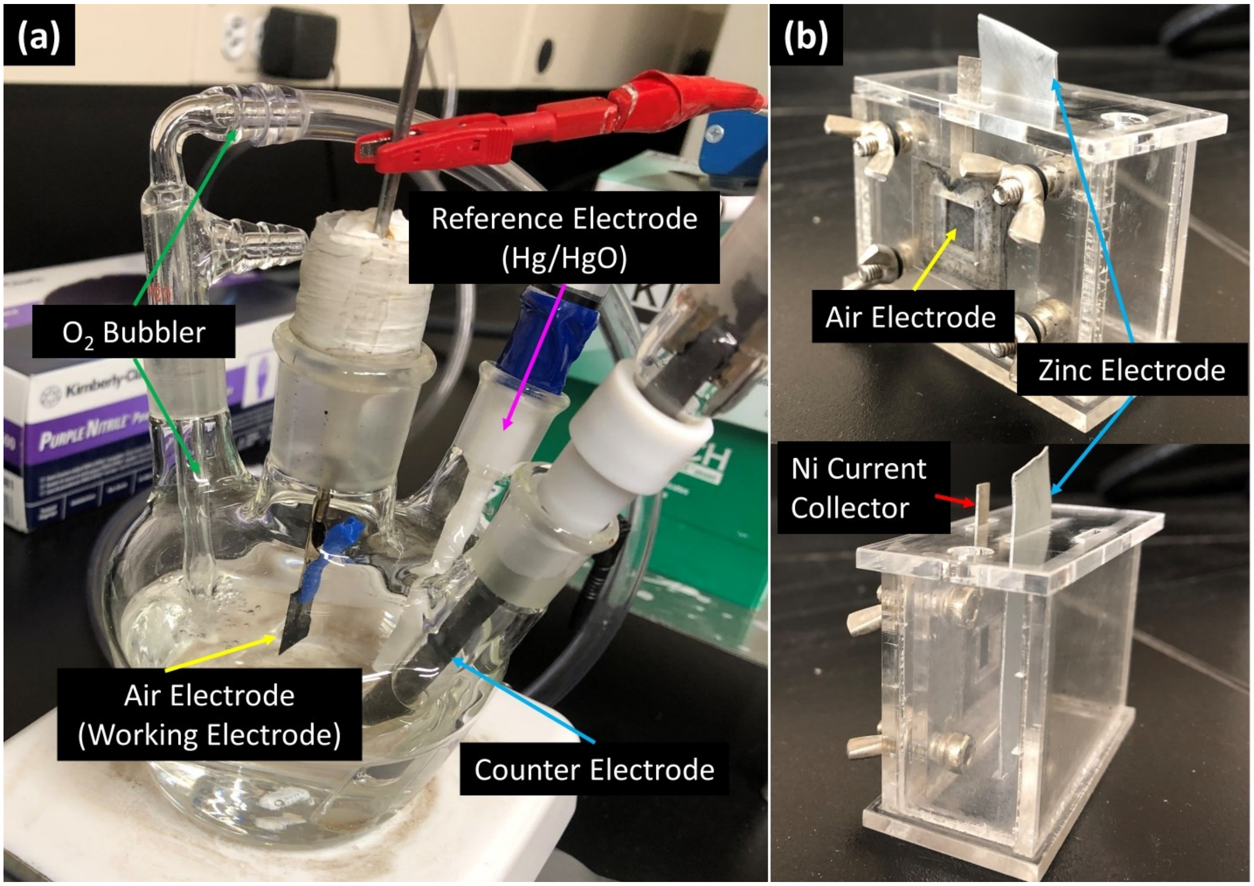

Figure S4.9 – Images of the electrochemical and battery test configurations. a) Three electrode configuration in a pine cell for half-cell measurements and b) a Zn-air battery in a vertical configuration (two electrode cell). Arrows and labels are shown to identify the cell components.

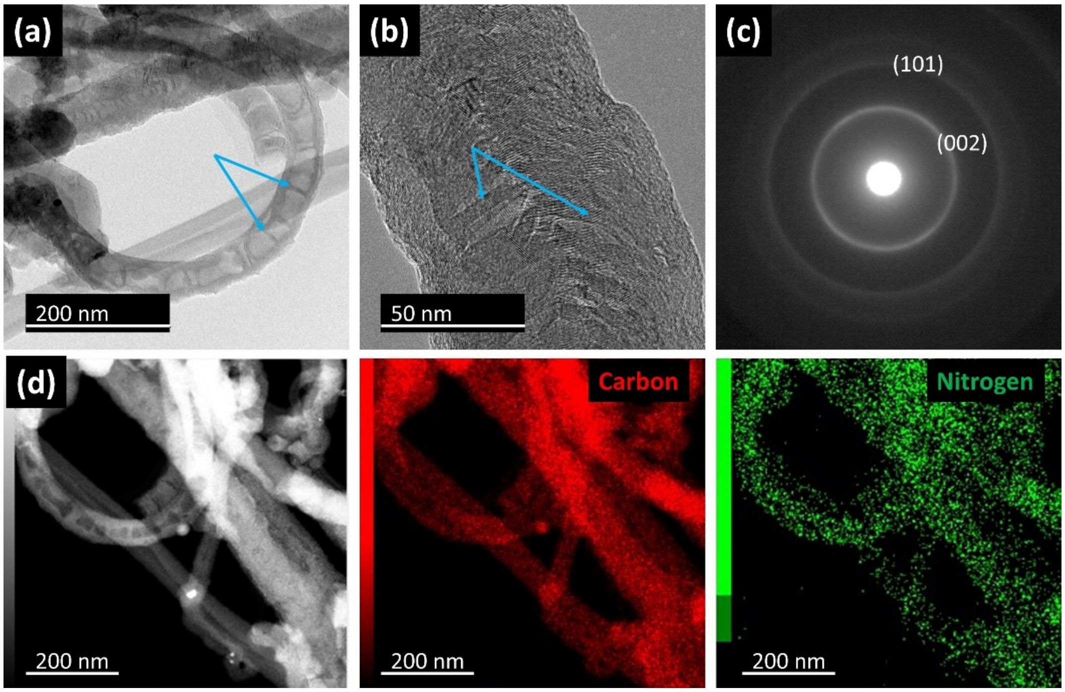

Figure S4.10 – TEM analysis of as-purchased N-CNTs: a) TEM BF image of N-CNTs, b) HRTEM micrograph showing N defects in the nanotube wall, c) SAD pattern from several CNTs with diffraction rings indexed to carbon. d) STEM ADF image and EDX elemental maps for C and N. The arrows in a) and b) highlight the N defects.

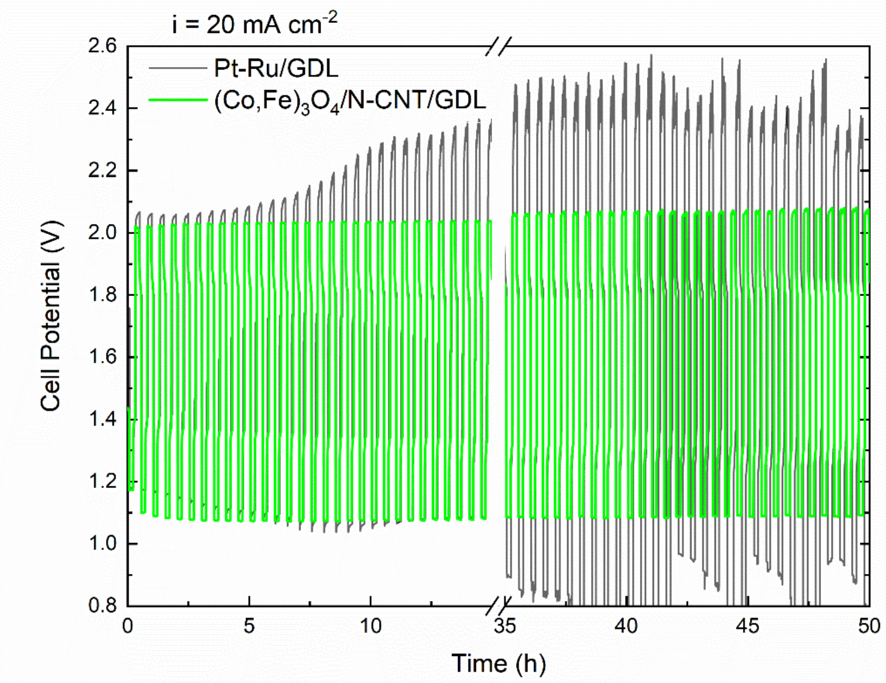

Figure S4.11 - Battery cycling comparison of $(Co,Fe)_3O_4$/N-CNT and Pt-Ru/C at a current density of 20 mA cm^{-2}. The batteries were cycled for 50 hours (30 min/cycle) in 6 M KOH + 0.25 M ZnO.

5 Investigation of Transition Metal-Based (Mn, Co, Ni, Fe) Trimetallic Oxide Nanoparticles on N-doped Carbon Nanotubes as Bifunctional Catalysts for Zn-Air Batteries

A version of this chapter has been submitted to the Journal of the Electrochemical Society on October 18th, 2019 and is under peer review:

D. Aasen, M. P. Clark, D. G. Ivey, Investigation of Transition Metal-Based (Mn, Co, Ni, Fe) Trimetallic Oxide Nanoparticles on N-doped Carbon Nanotubes as Bifunctional Catalysts for Zn-Air Batteries, *J. Electrochem. Soc.,* **2019** (Submitted October 18th, 2019)

5.1 Introduction

Oxygen reduction and oxygen evolution reactions (ORR and OER) play a critical role in many energy storage applications.[1], [77] For instance, electrically rechargeable Zn-air batteries (ZABs) are thought to be a low-cost solution to energy storage, but are hindered by the slow kinetics of the oxygen reactions.[1], [5], [77] Therefore, development of catalysts for ORR and OER are desired for the development of ZABs. Recently, several transition metal oxide catalysts have shown promise as low-cost alternatives to precious metal catalysts.[32], [40], [52], [65], [117], [134], [141] For instance, Mn oxides (MnO_x) have been widely studied as catalysts for ORR in alkaline media. Mn_3O_4 spinel has been particularly popular due to the mixed valence states of Mn within the oxide, which provide active sites for ORR.[19], [117], [134] However, MnO_x suffers from poor stability during the harsh oxidizing conditions of OER.[5], [15] Bimetallic spinel structures and layered double hydroxides (LDH) have shown promise as bifunctional catalysts due to their superior stability in alkaline media.[17], [37], [38], [43], [135], [141]–[143] Ni, Fe, and Co based bimetallic oxides with varying compositions were synthesized by Smith et al. to evaluate activity towards OER.[38] The results suggested that Fe facilitated higher oxidation states of other metals and improved the activity towards OER.[38] Furthermore, Davari et al. synthesized a Mn-Co mixed oxide film which exhibited improved activity as a bifunctional catalyst for ORR and OER.[141] The mixed oxide film demonstrated better cycling performance when compared with Pt-Ru/C at 5 mA cm^{-2} for 60 cycles.[141]

To combat the poor conductivity of transition metal oxides, nanocarbon materials such as carbon nanotubes (CNTs), graphene, reduced graphene oxide (rGO), and carbon black have been used as supports for the metal oxides to form nano-composite catalysts.[15], [36], [40], [67], [118], [128] Furthermore, these nanocarbons may yield additional active sites for ORR or OER through doping of the carbon material. For instance, N-doped rGO and CNTs (N-rGO and N-CNTs) showed improved activity towards ORR while O-functionalized CNTs (O-CNTs) exhibited improved activity towards OER.[19], [43], [45], [117], [144] Mn_3O_4 quantum dots were synthesized on partially exfoliated N-CNTs by Huang et al. and showed improved performance towards ORR.[117] Similar improvements were observed by Li et al., who synthesized Mn_3O_4 nanoparticles onto O-CNTs.[19] The oxygen groups on the CNTs facilitated synthesis of the Mn_3O_4 and improved bifunctional activity of the catalyst. Coupling $CoFe_2O_4$ and N-graphene by Niu et al. provided excellent bifunctional activity.[128] The catalysts showed ORR activity only slightly worse than Pt/C while exhibiting superior OER activity to that of RuO_2. These results suggest a strong synergy between doped nanocarbons and various transition metal oxides.

In attempt to lower the cost of precious metal catalysts some reports have alloyed precious metals with cheaper transition metals. For example, PtFeNi trimetallic alloy nanoparticles were synthesized to catalyze ORR by Li et Al.[145] The nanoparticles were created using a FeNi alloy template in order to significantly lower the Pt loading in proton exchange membrane fuel cells.[145] Although this approach does improve the practicality of precious metal oxides, the cost of catalysts could be further decreased by replacing Pt completely in a trimetallic alloy, oxide, or LDH.[38], [143], [146] The trimetallic strategy could also be used to reduce the loading of relatively more costly transition metals (such as Co). For instance, Smith et al. synthesized a NiCoFe oxide film which had a better OER onset when compared with NiFe, NiCo, and CoFe oxides.[38] NiCoFe oxide catalysts ($Fe_{33}Co_{33}Ni_{33}O_x$) achieved through photochemical synthesis by R. Smith et al also exhibited good OER activity for water oxidation.[147] Similarly, improved bifunctional catalyst performance was reported by Jia et al. for NiCoMn LDH on N-rGO relative to common NiFe LDH catalysts.[148] Furthermore, ternary LDH on N-rGO had improved bifunctional activity compared with Pt/C and RuO_2. NiFeMn systems also demonstrated good OER activity as both oxides and LDHs in alkaline media, although the ORR activity was not investigated.[143], [146]

Recently, Wu et al. synthesized trimetallic nitrides on N-CNTs, which exhibited good bifunctional performance with a long cycle life in ZABs.[149] The nitride was identified as Fe_2Ni_2N with partial Ni substitution by Co atoms. The decorated N-CNTs had comparable ORR activity to Pt/C, with superior OER activity to RuO_2. The trimetallic nitride catalyst was quite stable for 850 h and 570 h of cycling at 5 mA cm^{-2} and 20 mA cm^{-2}, respectively, with a charge/discharge time of 30 min.[149] Several ternary spinel oxides with the structure $M_{0.1}Ni_{0.9}Co_2O_4$ (M = Mn, Fe, Cu, Zn) were synthesized by Lu et al. for use in ZABs.[150] Of the ternary spinel oxides tested, $Fe_{0.1}Ni_{0.9}Co_2O_4$ (FNCO) had the best performance for ORR and OER. Cycling of FNCO at 10 mA cm^{-2} showed good stability over 98 cycles, with discharge and charge potentials of approximately 1.18 V and 2.03 V, respectively. Trimetallic based catalysts, thus, are promising as bifunctional catalysts for ORR and OER and should be further explored. Initial reports of Ni-Co-Fe oxides indicate good cycling stability and promise as a bifunctional catalyst for ZABs. However, to the best of our knowledge, the combination of trimetallic oxides and N-CNTs has yet to be used for direct application in ZABs and no information regarding their cyclability has been reported.

Our previous works have reported a simple and unique method, involving impregnation, for preparing high performing air electrodes for ZABs.[134], [151] The combined synthesis and electrode preparation process successfully prepared mono-metallic Mn_3O_4 nanoparticles on N-CNTs as well as bimetallic $(Co,Fe)_3O_4$ on N-CNTs, which exhibited good performance as ORR and bifunctional catalysts, respectively. The impregnation process enables good distribution of catalysts throughout the porosity of the gas diffusion layer (GDL), which increases the active surface area. Additionally, better catalyst distribution is thought to preserve the three-phase boundary between oxygen, catalyst, and the electrolyte over cycling. Herein, several transition metal-based bimetallic and trimetallic oxides (using Ni, Co, Mn, and Fe) supported on N-CNTs are investigated as bifunctional catalysts for ZABs. The catalysts are synthesized using the aforementioned impregnation technique and are compared based on activity for ORR and OER, as well as bifunctional efficiency. Trimetallic combinations are based on the results of the best performing bimetallic oxide/N-CNTs. The use of trimetallic oxides and N-CNTs can yield improved bifunctional performance due to the synergy associated with the metals in the oxides as well as the synergy between the N-CNTs and the metal oxides themselves. Furthermore, the N-CNTs may help improve the conductivity of the nano-composite catalysts which could enhance electron transfer and catalytic activity. The combination of trimetallic oxides and N-CNTs has not been explored with respect to ZABs and would enable valuable insight into the design of bifunctional catalysts for the oxygen reactions. Coupled with the impregnation method, the resulting air electrodes may enable high performance of ZABs via a simple low-cost and highly scalable process.

5.2 Experimental

5.2.1 Synthesis of Electrocatalysts and Electrode Preparation

Bimetallic Oxides on N-CNTs:

The synthesis method was based on the procedure outlined in our previous works; i.e., 50 mg of N-CNTs (MK Nano, 30-50 nm OD, 1-2 μm length) were mixed with 210 mg of the metal salt mixture (combination of $Mn(CH_3COO)_2{\cdot}4H_2O$, $Co(CH_3COO)_2{\cdot}4H_2O$, $FeSO_4{\cdot}7H_2O$, and/or $NiSO_4{\cdot}6H_2O$), 80 mg of NaOH and 10 mL of ethanol in a glass beaker.[134], [151] The ratio of metal salts (A:B) within the mixture was varied based on the bimetallic oxide as follows: 5:1 Fe salt to Co salt for $(Co,Fe)_3O_4$, 5:1 Ni to Fe for $NiFeO_x$, 1:1 Mn to Fe for $MnFeO_x$, 5:1 Ni to Co for $NiCoO_x$, 1:1 Mn to Co for $MnCoO_x$, and 1:7 Ni to Mn for $NiMnO_x$. It should be noted that the ratios of metal salts do not reflect the final atomic or mass ratios of metals within the prepared catalyst. The mixtures were mixed under vigorous stirring at 800 rpm for 5 min and then were transferred to a bath sonicator where they were sonicated for 5 h. Teflon coated porous carbon paper was sectioned into circles, 4.5 cm in diameter, to be used as the GDL. After sonication, 15 mL of ethanol and 1 mL Nafion 5% were added to the mixtures in addition to the sectioned GDL pieces. The GDL was soaked in the catalyst solution for 20 min under bath sonication and then removed to dry in air for 5 min. Next, the GDL was essentially used as filter paper in which 3-5 mL of catalyst solution was passed through in a vacuum filtration process (BOLA vacuum filter funnel, Finemech Inc.). The catalyst-impregnated GDL was removed from the filtration funnel and used as the air electrode with a mass loading of ~2 mg cm^{-2}. The catalysts are denoted ABO_x/N-

CNT, where 'A' and 'B' are transition metals. $(Co,Fe)_3O_4$ was identified as the spinel phase ($CoFe_2O_4$) in our previous work through selected area electron diffraction and x-ray photoelectron spectroscopy (XPS).[151] Annealing of selected bimetallic oxides ($MnFeO_x$/N-CNT, $NiMnO_x$/N-CNT and $MnCoO_x$/N-CNT) was conducted in air at 300°C for 0.5 h to optimize electrochemical performance.

Trimetallic Oxides on N-CNTs;

Impregnation of GDL pieces with tri-metallic oxides on N-CNTs was done in a process akin to that described for bimetallic oxides, with the exception of the metal salt mixture. The mixture of metal salts for tri-metallic oxides on N-CNTs contained three metal salts, as opposed to two, while maintaining a total mass of 210 mg. The optimal ratios of metal salts were selected based on the results of battery rate testing. These ratios for the metal salts (A:B:C) for different tri-metallic combinations are as follows: 3:1:5 (Ni:Co:Fe) for $NiCoFeO_x$/N-CNT (denoted as NCFO/N-CNT), 3:5:1 (Ni:Mn:Fe) for $NiMnFeO_x$/N-CNT (denoted as NMFO/N-CNT), and 1:1:1 (Mn:Co:Fe) for $MnCoFeO_x$/N-CNT (denoted as MCFO/N-CNT). Annealing of NMFO/N-CNT and MCFO/N-CNT impregnated samples was performed at 300°C in air for 0.5 h in order to optimize electrochemical performance of the electrode. However, NCFO/N-CNT samples were not annealed, since they had better electrochemical performance in the as-deposited condition compared with the annealed condition. Mass loading of GDL pieces impregnated with trimetallic oxides on N-CNTs was approximately 2.8 mg cm^{-2}.

Pt-Ru/C was prepared as a baseline for comparison using a spray coating method. 50 mg of Pt-RuO_2/C (30% Pt and 15% RuO_2 on carbon black, purchased from Alfa Aesar) was mixed with 2 mL DIW, 1 mL ethanol, and 0.1 mL of Nafion 5% under sonication for 10 min. The ink was then sprayed onto the GDL.

5.2.2 Characterization

Scanning electron microscopy (SEM) and energy dispersive X-ray (EDX) spectroscopy were conducted at acceleration voltages of 5 kV and 20 kV, respectively (Zeiss Sigma Field

Emission SEM). Sample preparation for SEM analysis required sectioning of prepared electrodes into 1 cm x 1 cm pieces which were then mounted on Al stubs using double-sided carbon tape. Transmission/scanning transmission electron microscopy (TEM/STEM, JEOL JEM-ARM200CF TEM) and EDX analysis were done at an accelerating voltage of 200 kV. TEM samples were prepared through drop casting. Catalyst was scraped off the surface of the prepared GDL electrodes and dispersed in 2 mL of ethanol. The suspension was drop cast onto a carbon grid and dried in air prior to imaging. X-ray photoelectron spectroscopy (XPS, Kratos AXIS Supra XPS Instrument) was conducted with a mono-chromated Al K_α X-ray source and a pass energy of 20 eV. Catalyst-impregnated electrodes were sectioned into 1 cm x 1 cm pieces; resulting spectra were calibrated using the C 1s peak at a binding energy of 285 eV.

5.2.3 Electrochemical and Battery Testing

Electrochemical testing was performed using a potentiostat (Biologic VSP 100) and a three-electrode cell in oxygen saturated 0.1 M KOH. The catalyst-impregnated electrode, a Pt coil and Hg/HgO were used as the working, counter, and reference electrodes, respectively. Catalyst-impregnated electrodes were prepared with an exposed area of 1 cm^2. Linear sweep voltammetry (LSV) was done at a scan rate of 5 mV s^{-1}, while cyclic voltammetry (CV) was done at a scan rate of 20 mV s^{-1}. All electrochemical measurements were IR compensated using the Hg/HgO reference electrode. Battery testing was conducted in a homemade ZAB (both horizontal and vertical configurations) with 6 M KOH + 0.25 M ZnO as the electrolyte and the ZAB was operated in ambient air conditions. Zn sheet-metal with dimensions of 2 cm x 6 cm was used as the Zn electrode, while catalyst-impregnated GDL sectioned into a 2 cm x 2 cm square was used as the air electrode with an electrolyte exposed area of 1 cm^2.

5.3 Results and Discussion

5.3.1 Bimetallic Oxides on N-CNTs

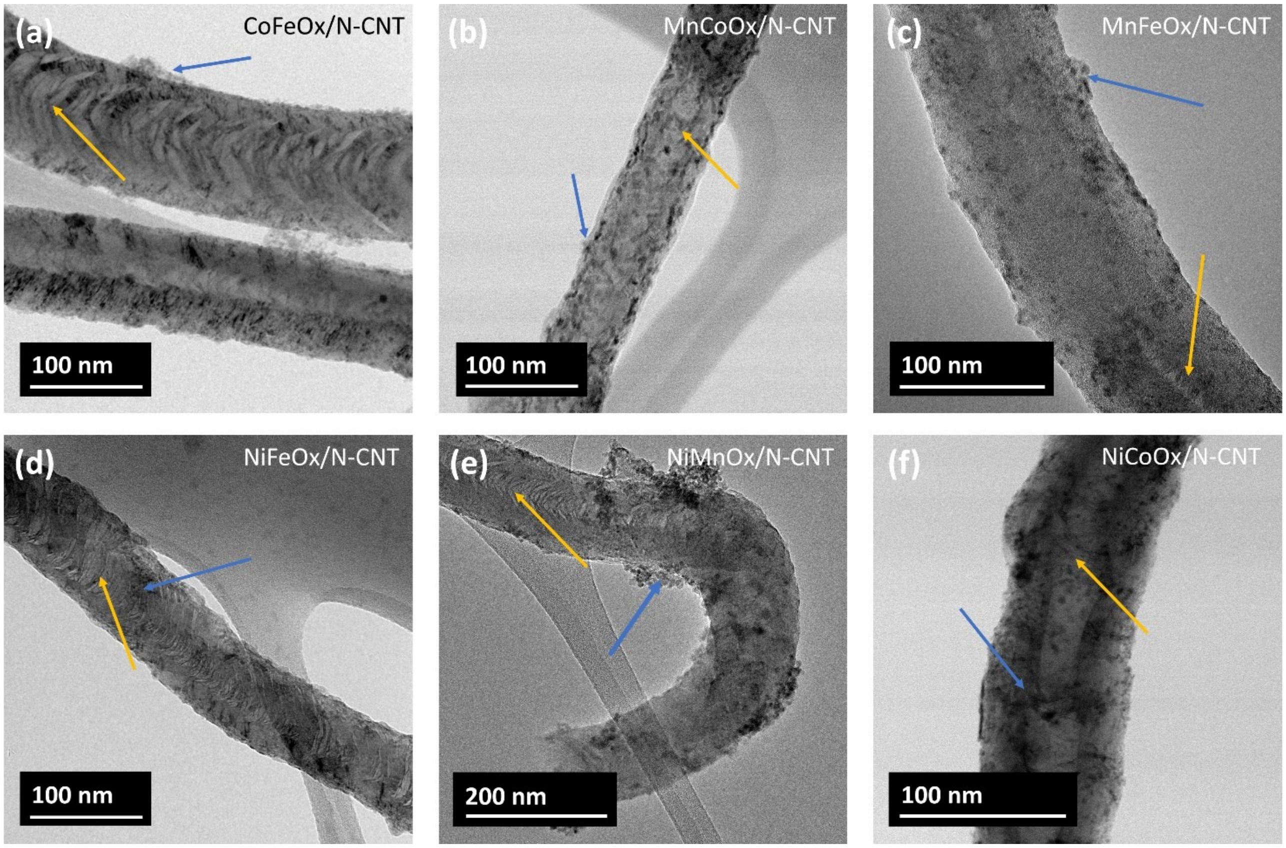

Figure 5.1 - TEM bright field (BF) images of a) $(Co,Fe)_3O_4$/N-CNT, b) $MnCoO_x$/N-CNT, c) $MnFeO_x$/N-CNT, d) $NiFeO_x$/N-CNT, e) $NiMnO_x$/N-CNT, and f) $NiCoO_x$/N-CNT samples. Yellow arrows are used to highlight the bamboo-like structure caused by the N-defects in the N-CNTs. Blue arrows are used to identify nanoparticles on the N-CNT surface.

Bimetallic oxides on N-CNTs were examined in order to develop a foundation for the investigation of trimetallic oxides on N-CNTs for ZABs. TEM images of the bimetallic oxides on N-CNTs are shown in Figure 5.1. Similar morphology for the catalysts is observed for most bimetallic species as nanoparticles 5–10 nm in size decorate the surface of the N-CNTs. Defects due to N-doping in the CNTs are apparent as striations and the bamboo-like structure. It is also noted that the nanoparticles form primarily around the N-defects in the nanotube wall, especially in $(Co,Fe)_3O_4$/N-CNT, $MnCoO_x$/N-CNT, and $MnFeO_x$/N-CNT samples (Figure 5.1a-5.1c). N substitution in the CNT matrix attracts metal ions as N increases the local electronegativity.[55] Furthermore, the defects result in favorable nucleation conditions due to a reduction in free energy.[55], [152] The growth of nanoparticles along N-defects is in good agreement with our previous results. The presence of Ni in the bimetallic oxide appears to promote agglomeration of the nanoparticles (Figure 5.1d-5.1f). This observation is most apparent in the $NiMnO_x$/N-CNT samples (Figure 5.1e), as larger clusters of particles are formed. Clustering of particles on $NiFeO_x$/N-CNT and $NiCoO_x$/N-CNT samples is less pronounced than for $NiMnO_x$/N-CNT samples (Figure 5.1d and 5.1f).

STEM elemental mapping of the bimetallic oxides confirms the presence of bimetallic particles on the N-CNTs (Figure 5.2). For all samples, there is clear overlap between both metals and oxygen within the maps, confirming that the nanoparticles are bimetallic oxides. It should be noted that for $NiFeO_x$/N-CNT, $NiMnO_x$/N-CNT, and $NiCoO_x$/N-CNT catalysts, Ni is observed all along the N-CNT surfaces as well as within the bimetallic oxide particles (Figure 5.2d-5.2f). X-ray mapping of the non-Ni containing bimetallic catalysts also showed Ni along the N-CNT surfaces (not shown here), suggesting that Ni may have been present on the as-purchased N-CNTs. STEM imaging and EDX analysis of as-purchased N-CNT confirmed the presence of Ni on the CNT surfaces (Figure S5.14a). Ni particles are used as catalysts for CVD of CNTs and N-CNTs and individual catalyst particles are observed in the STEM ADF images (Figure S5.14a). Interestingly, elemental maps of pristine CNTs (no N-doping) do not show Ni along the CNT surfaces; Ni is only present as isolated catalyst particles (Figure S5.14b). Therefore, the presence of the Ni coating on N-CNT surfaces must be related to the N-doping of the CNTs, while the Ni present within the oxide nanoparticles is due to the Ni salt added during the air electrode fabrication process. Clustering of oxide nanoparticles is only observed in Ni-based oxides, while more even distributions of particles on the N-CNTs occurs for $(Co,Fe)_3O_4$/N-CNT, $MnCoO_x$/N-CNT, and $MnFeO_x$/N-CNT. Clustering may be related to the Ni present on the surface of the as purchased N-CNTs.

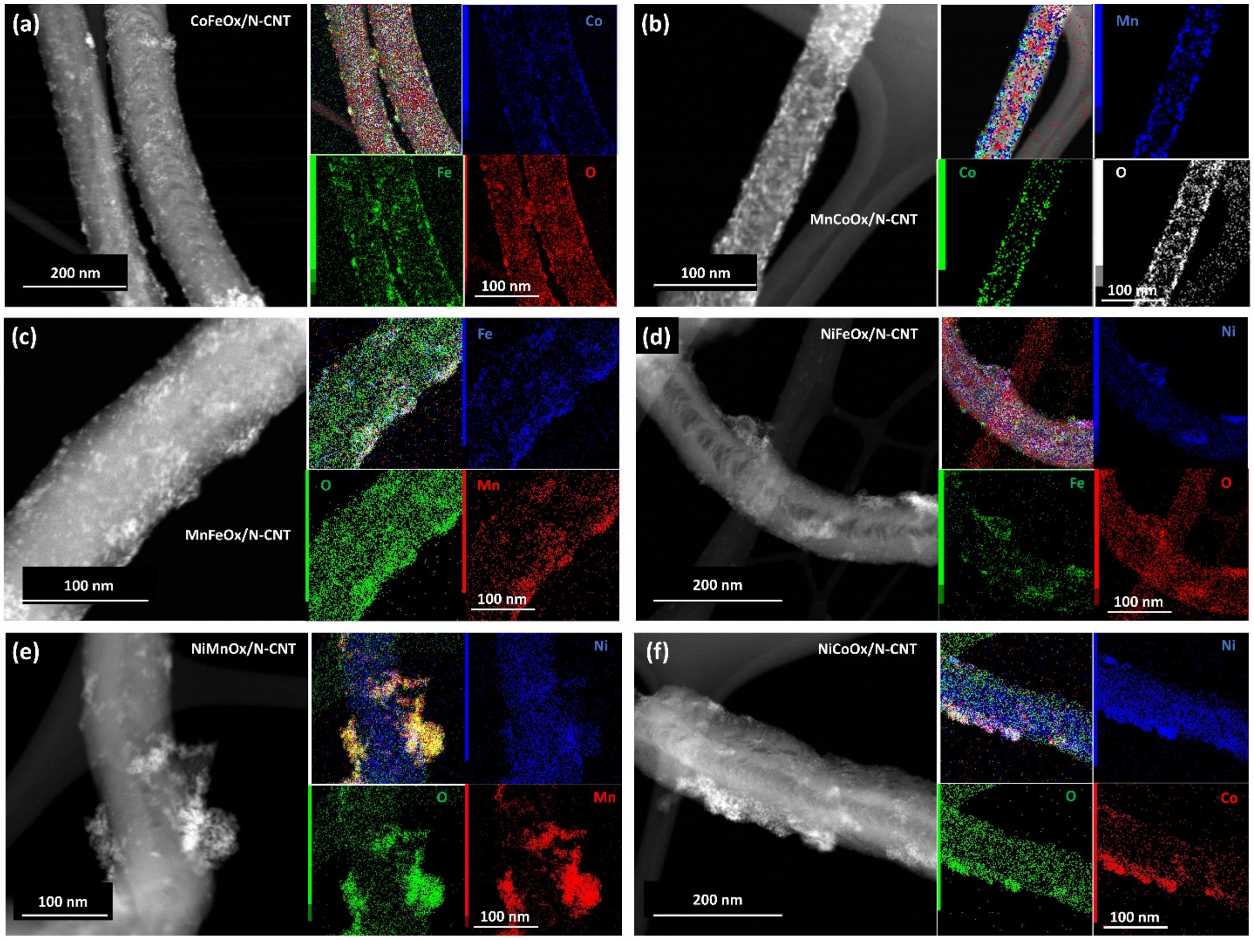

Figure 5.2 - STEM annular dark field (ADF) images and STEM EDX elemental mapping of a) $(Co,Fe)_3O_4$/N-CNT, b) $MnCoO_x$/N-CNT, c) $MnFeO_x$/N-CNT, d) $NiFeO_x$/N-CNT, e) $NiMnO_x$/N-CNT, and f) $NiCoO_x$/N-CNT samples.

SEM secondary electron (SE) images of the impregnated GDL surface show further similarities among bimetallic oxides on N-CNTs (Figure S5.15). $NiCoO_x$/N-CNT is used as a representative bimetallic oxide/N-CNT sample in Figure S5.15. Several nanotubes are visible along the surface of the electrode as well as nanotube bundles and metal oxide precipitate clusters (Figure S5.15a and S5.15b). EDX analysis of the precipitate clusters is shown in Figure S5.15c and confirms the presence of Ni, Co, and O. The Ni and Co peaks for the precipitate spectrum are more intense than those from the nanotube spectrum. The difference in intensity is due to the size of the $NiCoO_x$ precipitates. The large precipitate clusters contain Ni and Co compared with the $NiCoO_x$ nanoparticles that decorate the N-CNTs. SEM imaging and EDX analyses indicate that both $NiCoO_x$ precipitates and $NiCoO_x$/N-CNT catalysts are visible on the electrode surface. Surface morphology and EDX results for other bimetallic samples are similar to those for $NiCoO_x$/N-CNT.

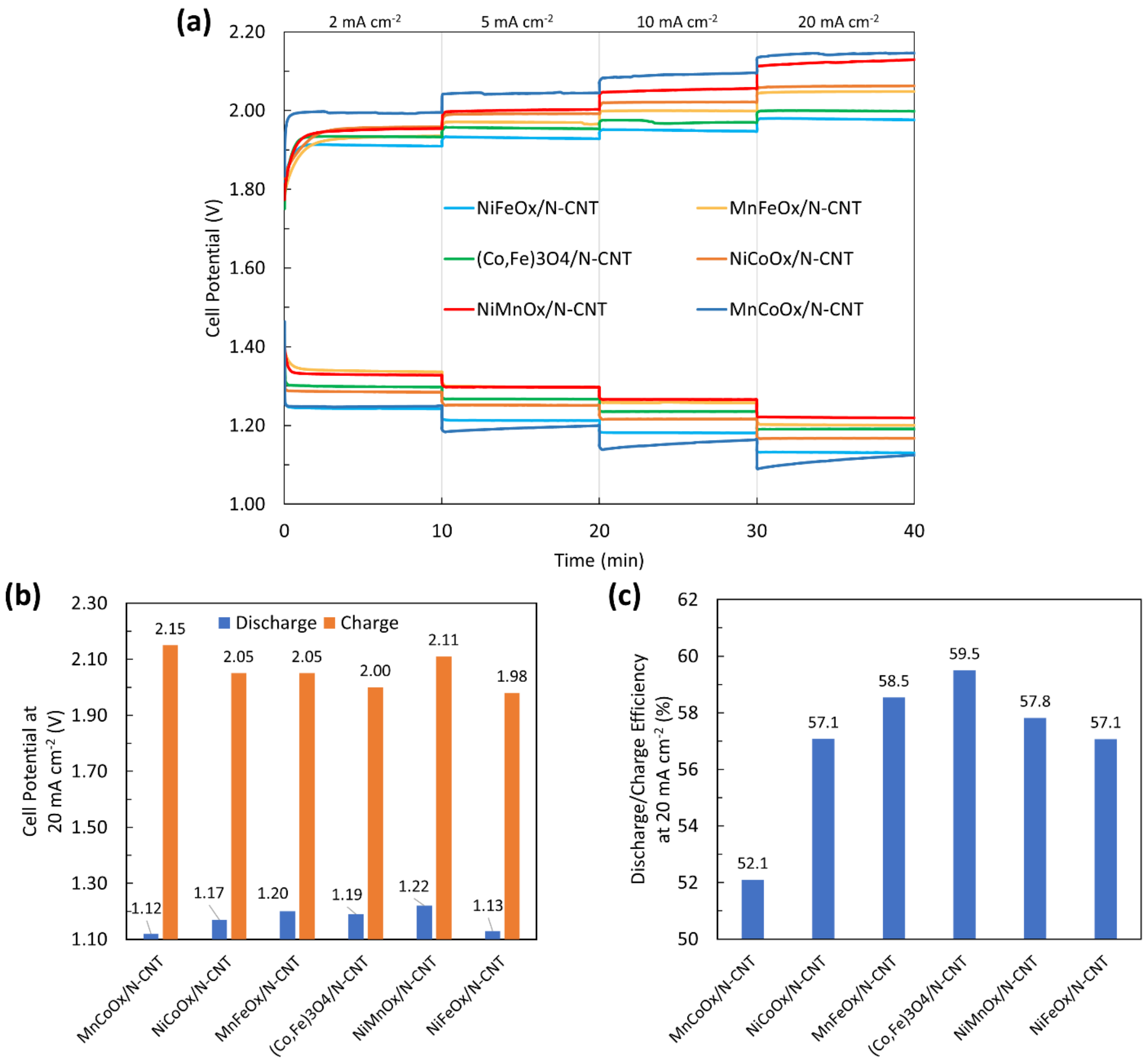

Figure 5.3 - Battery performance comparisons of GDL samples impregnated with bimetallic oxides on N-CNTs. a) Battery rate test results of the catalysts, b) discharge and charge potential comparisons of catalysts at 20 mA cm^{-2}, and c) discharge/charge efficiency comparison of catalysts at 20 mA cm^{-2}.

Prior to investigating trimetallic oxide catalysts on N-CNTs, battery performance tests were conducted for the electrodes impregnated with bimetallic oxides on N-CNTs (Figure 5.3). Half-cell results are discussed in the following section. At lower current densities, the charge performance of all catalysts is somewhat comparable, while differences in discharge performance are more apparent. Therefore, the selection of trimetallic combinations was determined by the battery performance of the bimetallic catalysts at higher current densities (10 mA cm^{-2} and 20 mA cm^{-2}). Similarly, optimal synthesis parameters for the bimetallic oxide on N-CNT samples (sonication time, effect of metal-to-N-CNT ratio and the effect of metal-to-metal ratio) were determined using battery rate test performances at 20 mA cm^{-2} (not shown here). Only the optimal synthesis conditions and corresponding performance of each bimetallic catalyst are presented. Figure 5.3a compares the battery discharge and charge rates of all six bimetallic oxide catalysts. $NiMnO_x$/N-CNT electrodes exhibited the highest discharge potential at 20 mA cm^{-2} with a cell potential of 1.22 V followed by $MnFeO_x$/N-CNT with a cell potential of 1.20 V (Figure 5.3a and 5.3b). Similarly, $NiFeO_x$/N-CNT had superior charge performance in comparison to the other catalysts with a cell potential of 1.97 V at 20 mA cm^{-2} (Figure 5.3a and 5.3b). In order to strategically select combinations of trimetallic oxides for use as bifunctional catalysts, discharge/charge efficiency was an important consideration (Figure 5.3c). $(Co,Fe)_3O_4$/N-CNT samples had the highest efficiency at 20 mA cm^{-2} (59.5%) with discharge and charge potentials of 1.19 V and 2.00 V, respectively.[151] Based on the bimetallic oxide on N-CNT results, $NiFeO_x$/N-CNT, $NiMnO_x$/N-CNT, and $(Co,Fe)_3O_4$/N-CNT samples were selected as the basis for the development of trimetallic oxide catalysts. Thus, the trimetallic systems were chosen as Ni-Co-Fe, Ni-Mn-Fe, and Mn-Co-Fe.

5.3.2 Trimetallic Oxides on N-CNTs

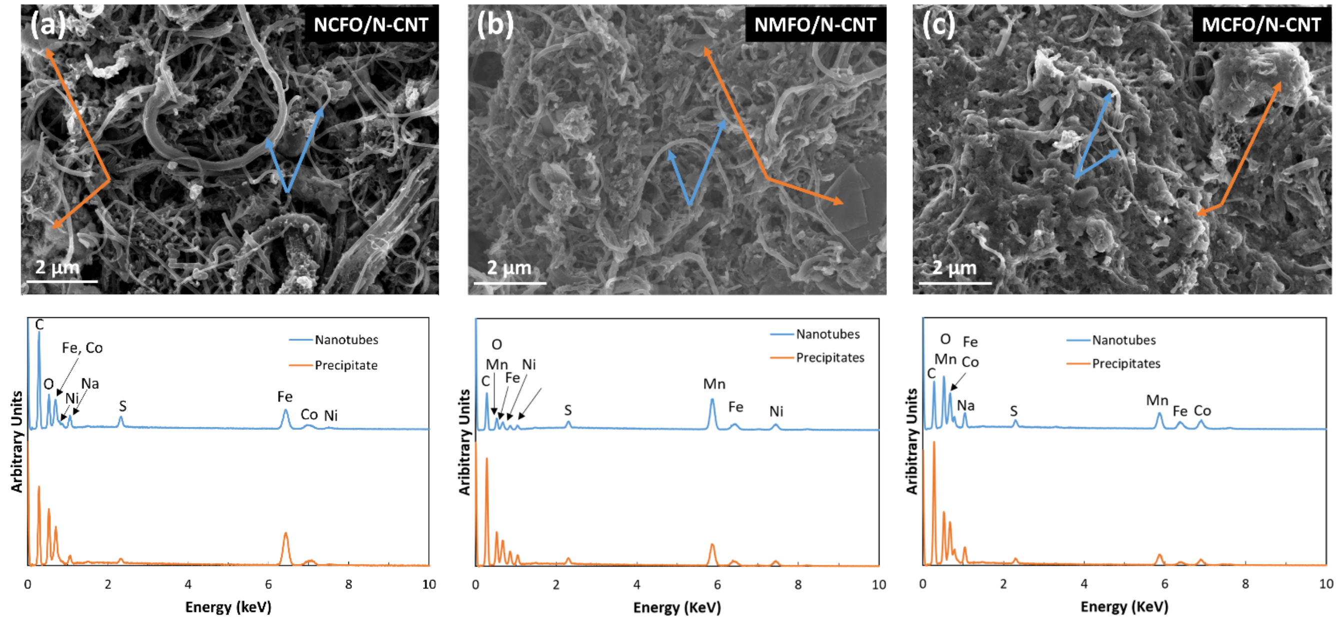

Figure 5.4 – SEM SE images and EDX analysis for GDLs impregnated with a) NCFO/N-CNT, b) NMFO/N-CNT, and c) MCFO/N-CNT. Blue arrows are used to highlight the oxide decorated nanotubes, while orange arrows indicate precipitate clusters found on the electrode surface.

SEM imaging and corresponding EDX analysis for the electrodes impregnated with the trimetallic oxides on N-CNTs are shown in Figure 5.4. The surface morphology is very similar to that observed for bimetallic oxide samples. The surface shows a matrix of nanotubes in addition to several precipitate clusters and nanotube bundles for all trimetallic oxide samples (Figure 5.4a, 5.4b, and 5.4c). However, the MCFO/N-CNT electrodes also have a film-like morphology between the nanotube catalysts, bundles and precipitates. The similarities between bimetallic and trimetallic samples are attributed to the consistency of the electrode preparation technique. EDX analysis was performed on the precipitates as well as the nanotube catalysts. Analysis of the NCFO/N-CNT GDL samples confirm the presence of Ni, Co, Fe, and O on both the nanotube surfaces and in precipitate clusters, suggesting the oxides are likely the same in both cases (Figure 5.4a). The trimetallic oxide particles in the NCFO/N-CNT sample are Fe-rich.

SEM EDX analysis of NMFO/N-CNT electrodes show the presence of Ni, Mn, Fe, and O both on the nanotubes and in precipitate clusters (Figure 5.4b). Once again, the oxide present in the precipitates/bundles is the same as that formed on the N-CNTs, since the ratio between Ni, Mn and Fe peaks is comparable. This oxide is Mn-rich with lower amounts of Ni and Fe. Similarly, analysis of MCFO/N-CNT electrodes show comparable metal and O compositions for the nanotubes and precipitate clusters (Figure 5.4c). Mn peaks for both the nanotubes and precipitates are more intense than those for Co and Fe, indicating that the oxides are Mn-rich. There are small Na and S peaks in all trimetallic oxide spectra; these are remnants from the synthesis. Na likely comes from NaOH, while S is from the metal salts.

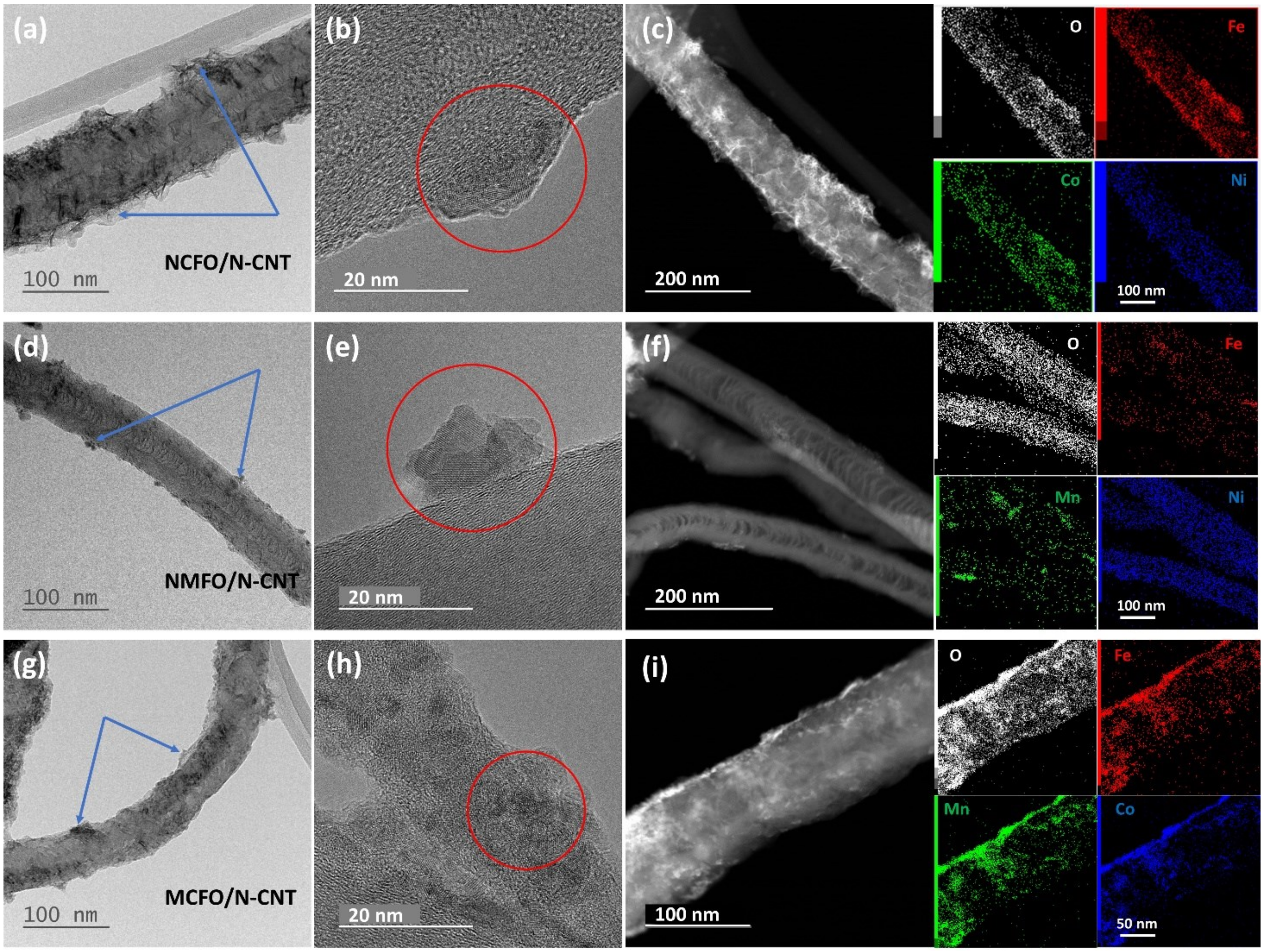

Figure 5.5 – TEM BF and high-resolution images, STEM ADF images, and STEM EDX elemental mapping of a-c) NCFO/N-CNT, d-f) NMFO/N-CNT and g-h) MCFO/N-CNT samples. Blue arrows are used to indicate the trimetallic oxide particles on the N-CNT surface.

Figure 5.5 shows TEM BF and STEM ADF images for the trimetallic oxides on N-CNTs. The morphology of the trimetallic oxides on the N-CNTs varies from sample to sample. NCFO/N-CNT catalysts have a sheet like structure of oxide on the nanotube surface (Figure 5.5a). Clusters of nanoparticles are also present; these are crystalline as evident from the lattice fringes within the particles (Figure 5.5b). Ni, Fe, and Co signals overlap within the oxide particles and sheets (Figure

5.5c). The O map overlaps with the metal concentrated areas, which suggests that a trimetallic oxide forms on the N-CNTs. As with the bimetallic oxides, Ni is present on the N-CNTs surfaces.

NMFO/N-CNT catalysts had regions with nanoparticles on the N-CNT surfaces and larger particles formed around nanotube bundles (Figure 5.5d and Figure S5.16, respectively). Lattice fringes are present in the HRTEM image (Figure 5.5e), which indicates crystallinity. The particle clusters on the N-CNT surfaces of both NMFO/N-CNT and NCFO/N-CNT samples range from approximately 5 nm to 30 nm in size. The Ni trend for NMFO/N-CNT is consistent with that for NCFO/N-CNT (Figure 5.5f). Mn and Fe are limited to oxide particles along the surface. The nanoparticles are Mn-rich, with lower amounts of Fe and Ni; some particles contained little or no Ni. The O map shows good overlap with the transition metal maps, indicating the formation of bimetallic (Mn-Fe) and trimetallic oxides. A STEM ADF image and elemental mapping of a NMFO/N-CNT bundle show distinct Ni particles (Figure S5.16). These particles are catalysts from N-CNT synthesis. X-ray mapping of the bundle illustrates the distribution of Mn, Fe, and Ni within the oxide particles. Towards the bottom of the bundle, there is clear overlap between all three transition metals. However, near the top of the bundle there is a clear Mn-rich area with some Fe and a small amount of Ni. This is in good agreement with the observations from the maps of individual nanotubes. As with the bimetallic oxide catalysts, most of the added Ni is present within the particles and particle clusters. The Ni along the N-CNT surfaces is the same Ni present on the as-purchased N-CNTs.

Some clustering of particles in MCFO/N-CNT samples is also observed (Figure 5.5g). However, clustering is less pronounced than for the Ni-based oxide samples. The HRTEM image of MCFO/N-CNT shows nanocrystalline areas which correspond to the MCFO particles (Figure 5.5h). The size of the particles is consistent with those of the other trimetallic oxides. STEM EDX elemental maps show overlap of the Mn, Co, Fe, and O signals, confirming the presence of trimetallic oxides (Figure 5.5i). It should be noted that Ni is also detected along the N-CNT surfaces (Ni X-ray map not shown here), as with the other samples. This observation confirms that the Ni on the as-purchased N-CNTs is unchanged during synthesis of MCFO/N-CNT. Furthermore, Ni is detected in the STEM EDX analysis, but not in the SEM EDX analysis. The discrepancy suggests that the amount of Ni on the N-CNT surface is very low. The elemental maps for Mn and Co in MCFO/N-CNT show higher intensities relative to Fe, indicating that the trimetallic oxide is Mn and Co rich, which is in good agreement with the SEM EDX analysis.

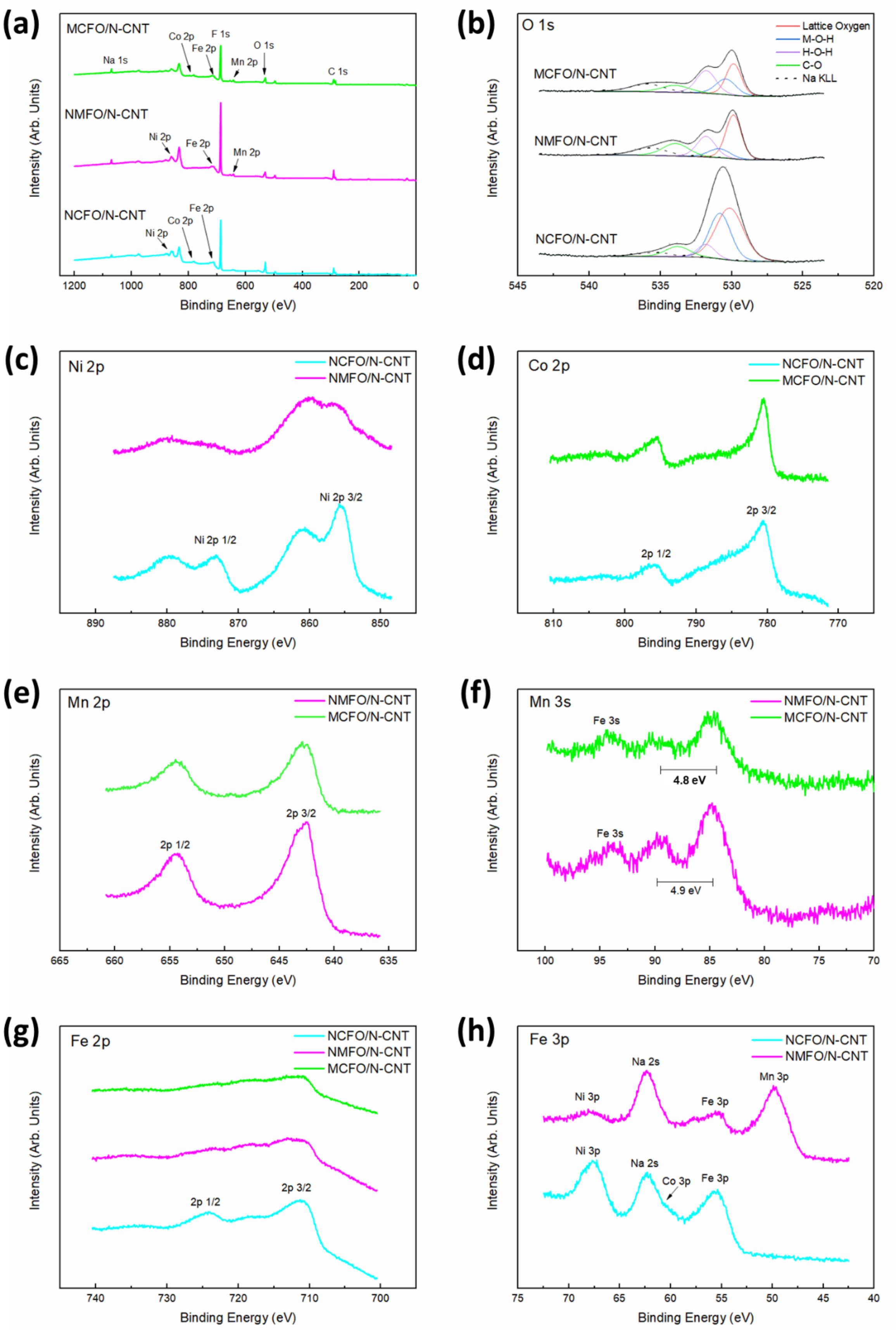
(a)
MCFO/N-CNT
Na 1s
Co 2p
Fe 2p
F 1s
Mn 2p
O 1s
C 1s
NMFO/N-CNT
Ni 2p
Fe 2p
Mn 2p
NCFO/N-CNT
Fe 2p
Co 2p
Ni 2p
Intensity (Arb. Units)
Binding Energy (eV)
1200 1000 800 600 400 200 0
(b)
O 1s
Lattice Oxygen
M-O-H
H-O-H
C-O
Na KLL
MCFO/N-CNT
NMFO/N-CNT
NCFO/N-CNT
Intensity (Arb. Units)
Binding Energy (eV)
545 540 535 530 525 520
(c)
Ni 2p
NCFO/N-CNT
NMFO/N-CNT
Ni 2p 3/2
Ni 2p 1/2
Intensity (Arb. Units)
Binding Energy (eV)
890 880 870 860 850
(d)
Co 2p
NCFO/N-CNT
MCFO/N-CNT
2p 3/2
2p 1/2
Intensity (Arb. Units)
Binding Energy (eV)
810 800 790 780 770
(e)
Mn 2p
NMFO/N-CNT
MCFO/N-CNT
2p 3/2
2p 1/2
Intensity (Arb. Units)
Binding Energy (eV)
665 660 655 650 645 640 635
(f)
Mn 3s
NMFO/N-CNT
MCFO/N-CNT
Fe 3s
4.8 eV
Fe 3s
4.9 eV
Intensity (Arb. Units)
Binding Energy (eV)
100 95 90 85 80 75 70
(g)
Fe 2p
NCFO/N-CNT
NMFO/N-CNT
MCFO/N-CNT
2p 3/2
2p 1/2
Intensity (Arb. Units)
Binding Energy (eV)
740 730 720 710 700
(h)
Fe 3p
NCFO/N-CNT
NMFO/N-CNT
Na 2s
Mn 3p
Ni 3p
Fe 3p
Ni 3p
Na 2s
Co 3p
Fe 3p
Intensity (Arb. Units)
Binding Energy (eV)
75 70 65 60 55 50 45 40

Figure 5.6 - XPS Spectra for NCFO/N-CNT, NMFO/N-CNT and MCFO/N-CNT samples; a) survey spectra, b) O 1s, c) Ni 2p, d) Co 2p, e) Mn 2p, f) Mn 3s, g) Fe 2p, and h) Fe 3p high resolution spectra. Fe 3p spectra are given for samples containing Ni as there is possible overlap between Ni LMM Auger and Fe 2p spectra [101]. Deconvolution and peak fitting for the 2p and 3p spectra are presented in Figure S5.4 to improve the presentation of data.

Samples were further studied through XPS analysis (Figure 5.6, Table 5.1). From the survey spectra, all three samples show peaks corresponding to C, O, F, and Na (Figure 5.6a). Fluorine is from the PTFE within the GDL, while Na is likely left over from NaOH used in the synthesis of the trimetallic oxide catalysts. The metals have lower intensities relative to peaks from the GDL (C, O and F). It should also be noted that the Fe 2p peak is particularly weak in all samples, while the Ni 2p peak intensity is quite low for NMFO/N-CNT. The O 1s high resolution spectra for all samples is presented in Figure 5.6b. Deconvolution of O 1s spectra can be fit to 5 peaks at approximately 529 eV, 531 eV, 532 eV, 533 eV and 535 eV. The binding energies at 529 eV, 531 eV and 532 eV are attributed to lattice oxygen (M-O-M bonds), M-O-H bonds, and H-O-H bonds, respectively.[104] Lattice oxygen has the highest relative contribution for all samples. The M-O-H peak for NCFO/N-CNT is larger relative to those in the other trimetallic oxide samples, as NCFO/N-CNT samples were not annealed after synthesis. It is assumed that annealing oxidizes most of the metal hydroxides which may be present, resulting in a reduction in the M-O-H peak. C-O-C bonds on the N-CNT surface and in the GDL are characterized by the peak at ~533 eV.[136] Finally, the peak at ~535 eV is attributed to the Na KLL Auger peak.[101]

The Ni 2p high-resolution spectra for NCFO/N-CNT and NMFO/N-CNT are shown in Figure 5.6c. Because of the low intensity of the Ni peaks in the NMFO/N-CNT samples, contributions from the F KLL Auger peaks (558 and 577 eV) and Mn LMM Auger peak (552 eV) interfere with the Ni 2p 3/2 and 2p 1/2 satellite peaks causing them to appear more intense.[101] As a result, deconvolution of the Ni 2p spectra for NMFO/N-CNT yields a degree of uncertainty, although Ni^{2+} multiplet splitting results in the best fit (Figure S5.17, Table 1).[105] Ni 2p deconvolution for NCFO/N-CNT achieves the best fit when Ni^{2+} and Ni^{3+} multiplets are used.[105], [153] The average Ni valence for NCFO/N-CNT and NMFO/N-CNT samples was estimated to be 2.4 and 2.0, respectively (Table 5.1). Similarly, Co 2p high-resolution spectra are presented for NCFO/N-CNT and MCFO/N-CNT samples in Figure 5.6d. The Co 2p 3/2 and 2p 1/2 peaks show similar behavior for both samples and can be fit using both Co^{2+} and Co^{3+} multiplet peaks, suggesting mixed Co valence in both samples (Figure S5.17, Table 5.1).[105] However, the fitting indicates that Co exists primarily as Co^{2+} in the NCFO/N-CNT samples, while Co exists primarily as Co^{3+} in the MCFO/N-CNT samples (Table 5.1). Furthermore, the shape of the Co 2p 1/2 peak is similar to that reported in the literature for samples containing mixed Co valence (Figure 5.6d, Figure S5.17).[39], [40], [105] The average Co valence for NCFO/N-CNT and MCFO/N-CNT was estimated to be 2.2 and 2.6, respectively (Table 5.1).

Mn valence for NMFO/N-CNT and MCFO/N-CNT samples can be determined using both the Mn 2p and Mn 3s high-resolution spectra (Figure 5.6e and 5.6f). Deconvolution and multiplet splitting of the Mn 2p 3/2 peak for both samples suggest the presence of Mn^{2+}, Mn^{3+}, and Mn^{4+} components (Figure S5.17, Table 5.1).[104]–[106] However, Mn^{2+} contribution is minor for both samples. Therefore, the average Mn valence from Mn 2p spectra can be estimated to be 3.6 and 3.7 for NMFO/N-CNT and MCFO/N-CNT samples respectively. The Mn valence is confirmed by peak splitting of the Mn 3s high-resolution spectra (Figure S5.17, Table 5.1).[103], [104] Mn 3s spectra are deconvoluted into three peaks at about 84 eV, 89 eV, and 94 eV; the latter corresponds to the Fe 3s peak, while the others correspond to Mn 3s. The Mn 3s peak positions for NMFO/N-CNT samples were determined to be 84.7 eV and 89.6 eV, while peak positions of MCFO/N-CNT samples were 84.5 eV and 89.3 eV. The difference between the peaks is thus 4.9 eV and 4.8 eV for the respective samples. From the peak splitting reported in the literature, the Mn valence from Mn 3s peak splitting was estimated to be 3.5 and 3.6 for NMFO/N-CNT and MCFO/N-CNT samples, respectively.[103], [104], [106] Thus, Mn 2p multiplet splitting and Mn 3s peak splitting are in good agreement.

Finally, Fe valence was determined through the combined use of Fe 2p and Fe 3p high-resolution spectra (Figure 5.6g and 5.6h, Figure S5.17, Table 5.1). Fe 2p spectra are presented for all samples and are fit using Fe^{2+} and Fe^{3+} multiplet splitting (Figure S5.4) [105]. The Fe 2p 3/2 peak shows abnormal features which are likely a result of weak Fe 2p intensity, in addition to overlap with Co LMM (peak at 714 eV) and Ni LMM Auger peaks (peak at 712 eV).[101] Fitting suggests the presence of Fe^{2+} and Fe^{3+} components in all three trimetallic oxides with a Fe^{3+} majority (Figure S5.17, Table 5.1). From the Fe 2p spectra, Fe valence is estimated to be 2.6, 2.6, and 2.7 for NCFO/N-CNT, NMFO/N-CNT, and MCFO/N-CNT samples, respectively. However, the overlap with the Auger peaks (particularly the Ni LMM Auger peak at 712 eV) raises uncertainty with the Fe 2p fitting.[101] Therefore, Fe 3p high-resolution spectra were acquired for Ni-containing samples to confirm the Fe valence (Figure 5.6h, Figure S5.17). The Fe 3p peak is situated at ~56 eV, near Co 3p and Na 2s (overlap, ~64 eV), as well as Ni 3p (~69 eV) and Mn 3p (~50 eV) peaks. Fe 3p peaks for NCFO/N-CNTs and NMFO/N-CNTs were fit in addition to the neighboring peaks and were deconvoluted into Fe^{2+} (~54.5 eV) and Fe^{3+} (~56.5 eV) components.[102], [154] From the Fe 3p spectra, Fe valence was estimated to be 2.5 and 2.6 for NCFO/N-CNT and NMFO/N-CNT samples, respectively. The Fe 3p analysis corroborates the results from the Fe 2p analysis.

Based on the combined XPS and TEM/STEM, the oxides are likely XY_2O_4 spinel-like phases with partial substitution in X (tetrahedral) lattice sites, Y (octahedral) lattice sites, or both.[155], [156] Tetrahedral site cations are most commonly 2+ species, while octahedral site cations are most commonly 3+ species, although other combinations of cation valences have been reported.[155], [156] NCFO/N-CNT samples have mixed Ni, Co, and Fe valences, allowing all metals to substitute for each other. Ni exists primarily as Ni^{2+}, and likely occupies the tetrahedral lattice sites with partial substitution by Co^{2+} and Fe^{2+}. Due to the relative peak intensity of Fe to Ni and Co in SEM EDX (Figure 5.4a), the octahedral sites are likely occupied predominantly by Fe^{3+} with some substitution by Co^{3+} and Ni^{3+}. Fe^{3+} is also the dominant Fe species determined from XPS analysis, which provides further evidence that Fe^{3+} is the primary species in the octahedral sites (Table 5.1). The high amounts of Ni^{2+}, Co^{2+}, and Fe^{3+} indicate that the spinel has a base structure similar to $(Ni,Co)Fe_2O_4$ with some substitution in both tetrahedral and octahedral sites by Ni, Co, and Fe ions. As such, the trimetallic spinel phase is denoted as $(Ni,Co,Fe)_3O_4$.

Similarly, NMFO/N-CNT and MCFO/N-CNT samples are likely spinel phases. Ni exists solely as Ni^{2+} in NMFO/N-CNT samples and occupies the tetrahedral lattice sites with partial substitution by Fe^{2+} (majority) and Mn^{2+} (minority) (Table 5.1). The octahedral sites are, therefore, occupied by Fe^{3+} and Mn^{3+} species. MCFO/N-CNT samples likely have Co^{2+} and Fe^{2+} in tetrahedral sites with small amounts of Mn^{2+} substitution, while the octahedral sites are occupied by Mn^{3+}, Co^{3+}, and Fe^{3+}. Therefore, it is proposed that $Ni(Mn,Fe)_2O_4$ and $(Mn,Co,Fe)_3O_4$ spinel phases are present in the NMFO/N-CNT and MCFO/N-CNT samples, respectively. However, Mn is mostly present as Mn^{4+} in both NMFO/N-CNT and MCFO/N-CNT samples (Table 5.1). From STEM elemental mapping, Mn-rich areas were observed with little or no presence of the other transition metals (Figure 5.5, Figure S5.16). The presence of Mn^{4+} may point to MnO_2 in some areas on the N-CNT surface, which agrees with the observations from Figure S5.16. Alternatively, Mn^{4+} may exist with Ni^{2+}/Co^{2+}/Fe^{2+} as $Mn(Ni,Fe)_2O_4$ or $Mn(Co,Fe)_2O_4$ spinels for NMFO/N-CNT and MCFO/N-CNT samples, respectively.[155], [156] The exact identity of the oxides cannot be specified as TEM electron diffraction analysis was inconclusive.

Table 5.1 - XPS Analysis of High-Resolution Spectra for the Trimetallic Oxide on N-CNT Catalysts

Sample	**Ni 2p 3/2**			**Co 2p 3/2**			**Mn 2p 3/2**			
	2+ (%)	3+ (%)	Valence	2+ (%)	3+ (%)	Valence	2+ (%)	3+ (%)	4+ (%)	Valence
NCFO/N-CNT	62.2	37.8	**2.4**	84.7	15.3	**2.2**	-	-	-	**-**
NMFO/N-CNT	100	0	**2.0**	-	-	**-**	7.1	15.5	77.5	**3.7**
MCFO/N-CNT	-	-	**-**	42.3	57.7	**2.6**	1.3	39.4	59.3	**3.6**

Sample	**Fe 2p 3/2**			**Fe 3p**			**Mn 3s**	
	2+ (%)	3+ (%)	Valence	2+ (%)	3+ (%)	Valence	Δ3s (eV)	Valence
NCFO/N-CNT	43.4	56.6	**2.6**	45.1	54.9	**2.5**	-	**-**
NMFO/N-CNT	35.7	64.3	**2.6**	38.4	61.6	**2.6**	4.8	**3.6**
MCFO/N-CNT	32.6	67.4	**2.7**	-	-	**-**	4.9	**3.5**

Values are determined from Figure 5.6 and Figure S5.17.

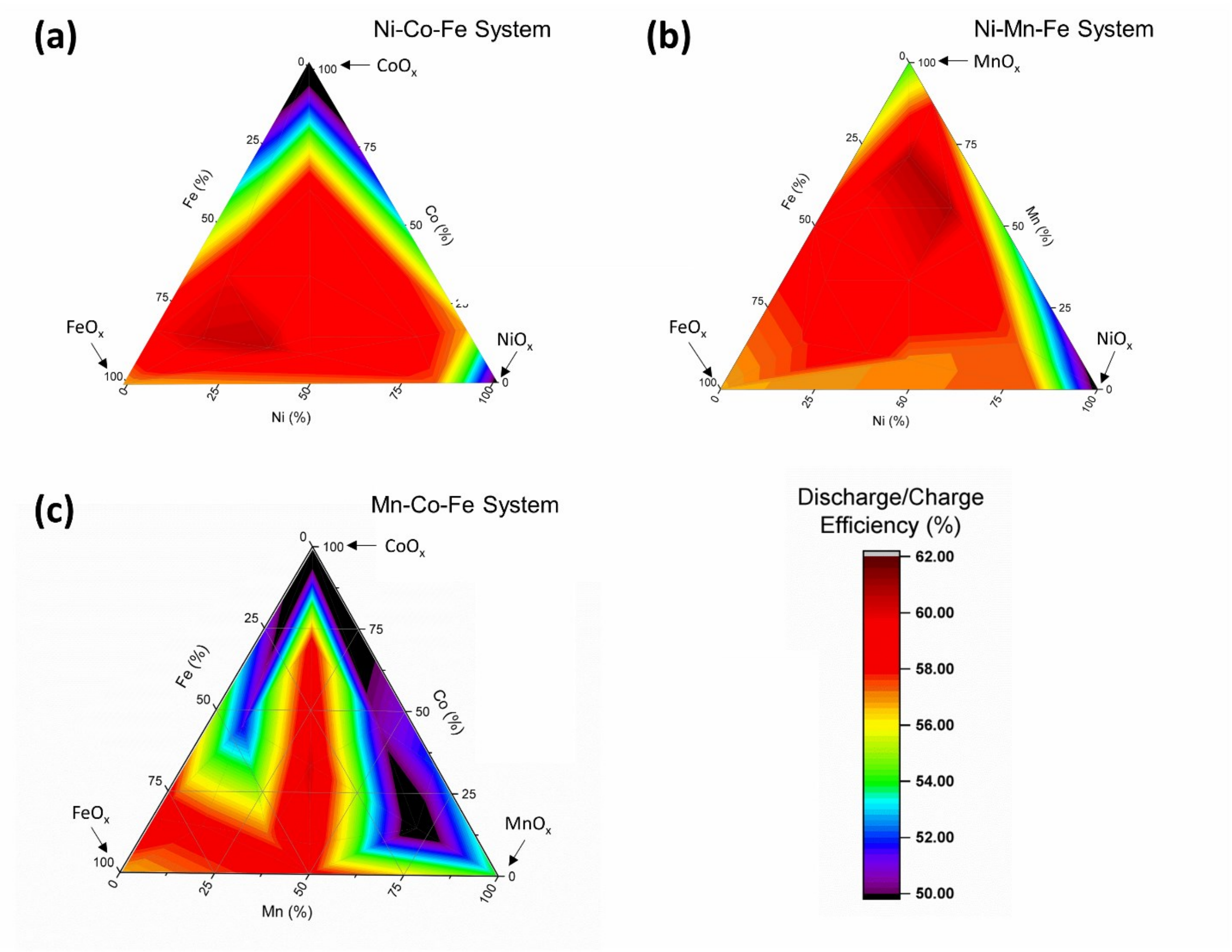

Figure 5.7 – Discharge/charge efficiency of tri-metallic oxides on N-CNTs as a function of metal salt composition for the synthesis of a) NCFO/N-CNT, b) NMFO/N-CNT and c) MCFO/N-CNT systems. Efficiencies are calculated using battery rate test data at a current density of 20 mA cm^{-2}.

Optimal ratios of the metal salts for synthesis of NCFO/N-CNT, NMFO/N-CNT, and MCFO/N-CNT catalysts were determined by using the discharge/charge efficiency results from the battery rate tests at a current density of 20 mA cm^{-2}. Figure 5.7 shows colormaps for each trimetallic system and illustrates the discharge/charge efficiency as a function of metal salt composition. The maps were created using the data acquired from synthesis and testing of over 30 trimetallic oxide on N-CNT samples and monometallic oxide samples (MO$_x$/N-CNTs where M = Mn, Co, Ni, or Fe, Figure S5.18). The optimal ratios of metal salts for synthesis are 3:1:5 (Ni:Co:Fe), 3:5:1 (Ni:Mn:Fe) and 1:1:1 (Mn:Co:Fe) for NCFO/N-CNT, NMFO/N-CNT, and MCFO/N-CNT samples, respectively. It should be noted that Figure 5.7 does not show the actual composition of the metal oxide nanoparticles and should only be used as a reference for optimizing synthesis conditions. The effect of annealing on sample performance was also investigated using battery rate tests (Figure S5.19). Annealing had mixed results; the efficiency of NMFO/N-CNT and MCFO/N-CNT samples improved, but the efficiency of NCFO/N-CNT samples decreased. Trimetallic oxides containing Mn benefitted from annealing with significant increases in discharge potential (up to 100 mV at 20 mA cm^{-2} for MCFO/N-CNT). NMFO/N-CNT samples also benefitted from annealing with a reduction of 40 mV in charge potential (Figure S5.19). However, NCFO/N-CNT samples suffered a slight decrease of 40 mV in discharge potential as well as an increase in charge potential of 30 mV when annealed.

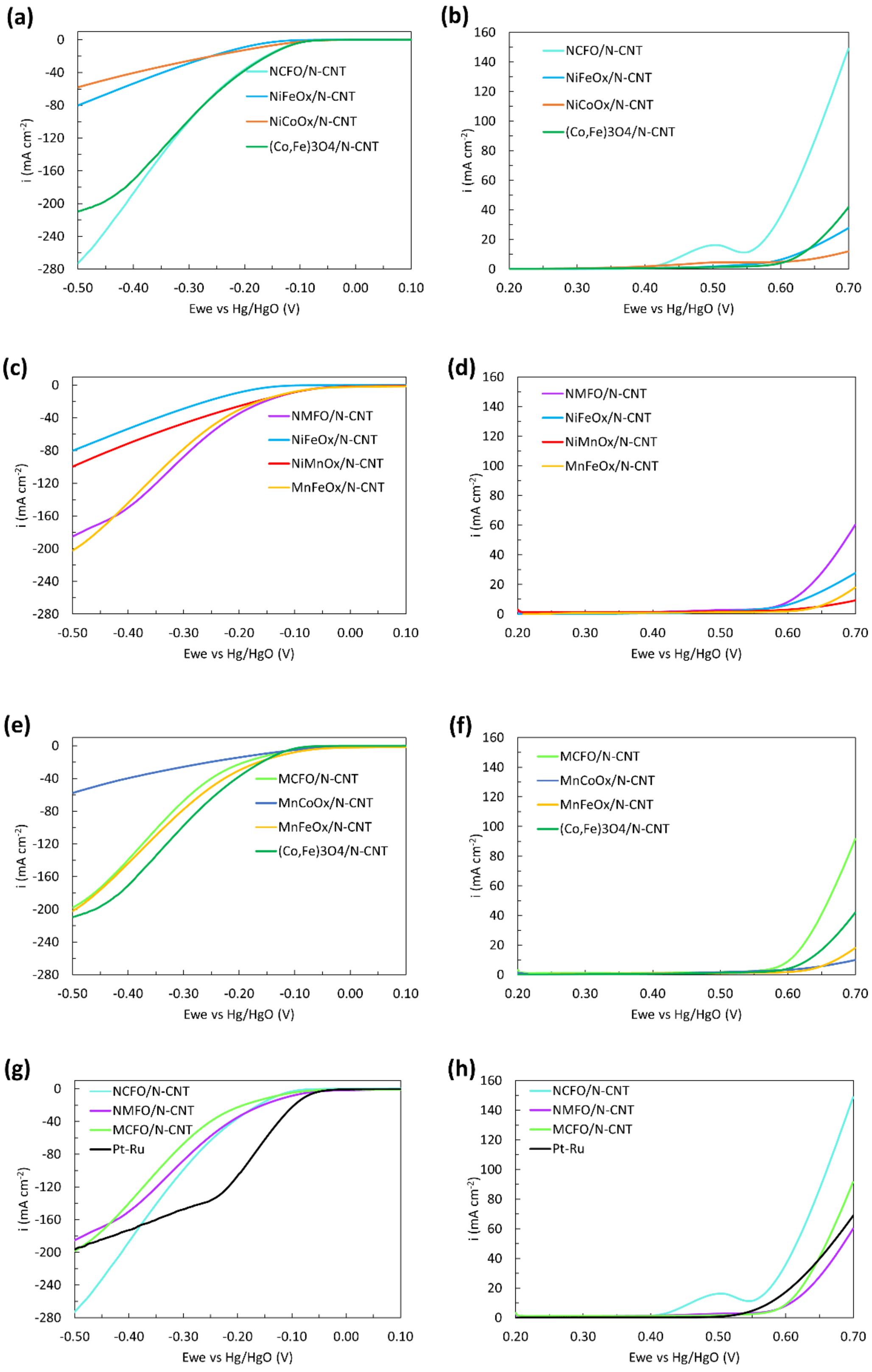

Figure 5.8 - ORR and OER LSV plot comparisons. a,b) Ni-Co-Fe system, c,d) Ni-Mn-Fe system, e,f) Mn-Co-Fe system, and g,h) trimetallic oxides vs Pt-Ru/C.

Half-cell ORR and OER LSV comparisons between the trimetallic oxides and their corresponding bimetallic systems are presented in Figure 5.8a-5.8f. For simplicity, the onset potential for either oxygen reaction is taken to be the potential corresponding to a current density of ±10 mA cm^{-2}. NCFO/N-CNT shows comparable ORR behavior to (Co,Fe)$_3$O$_4$/N-CNT with an onset potential of approximately -0.13V vs Hg/HgO (Figure 5.8a). The ORR behavior of NCFO/N-CNT is superior to that of NiFeO$_x$/N-CNT and NiCoO$_x$/N-CNT and reaches the largest current density for this system at higher overpotentials. NCFO/N-CNT also shows superior OER activity to (Co,Fe)$_3$O$_4$/N-CNT, NiFeO$_x$/N-CNT, and NiCoO$_x$/N-CNT in terms of both onset potential and maximum current density (Figure 5.8b). NCFO/N-CNT exhibits a two-step OER behavior due to the peak at 0.5 V vs Hg/HgO. The peak is likely due to a redox reaction involving Ni within the oxide structure. The onset potential of the first step is 0.46 V vs Hg/HgO and the second step has an onset of 0.54 V vs Hg/HgO (after redox). The first onset potential is likely for the Faradaic reaction of Ni, as it is oxidized from Ni^{2+} to Ni^{3+}; therefore, 0.54 V is assumed to be the onset potential for OER.[147] The Faradaic behavior of Ni was investigated through CV tests for NiO$_x$/N-CNT catalysts (Figure S5.20). NiO$_x$/N-CNT catalysts were synthesized via the same impregnation process as the other catalysts. The CV results show a redox couple with oxidation and reduction peaks at 0.52 V vs Hg/HgO and 0.34 V vs Hg/HgO, respectively. The peak positions are comparable to Ni^{2+}/Ni^{3+} redox couples reported in the literature.[157], [158] The ORR and OER comparisons for the Ni-Fe-Mn system are shown in Figure 5.8c and 5.8d, respectively. NMFO/N-CNT has an ORR onset potential comparable to that for NiMnO$_x$/N-CNT and MnFeO$_x$/N-CNT and superior to that for NiFeO$_x$/N-CNT (-0.11V vs Hg/HgO). However, NMFO/N-CNT clearly has a higher maximum current density than all bimetallic oxides of its system. The improvements achieved through the combination of Ni, Mn, and Fe are more apparent in OER activity. NMFO/N-CNT shows clear improvement in OER onset potential and maximum current compared with the bimetallic oxides, with an onset potential of 0.61 V vs Hg/HgO. It is noted that no Ni redox peak was observed in the OER LSV curve for NMFO/N-CNT. A similar trend is observed in the Mn-Co-Fe system (Figure 5.8e and 5.8f). ORR activity of MCFO/N-CNT is comparable to that for MnFeO$_x$/N-CNT, with an earlier onset potential to that of (Co,Fe)$_3$O$_4$/N-CNT (-0.12 V vs Hg/HgO) but a lower maximum current. The improvements are again most clearly illustrated by the OER activity, where MCFO/N-CNT has the earliest onset for OER at 0.60 V vs Hg/HgO (Figure 5.8f). The LSV comparisons suggest that the trimetallic oxide catalysts have increased

OER active sites, while the ORR activity resembles that of the most ORR active bimetallic combinations in the respective system.

Figure 5.8g and 5.8h show comparisons between NCFO/N-CNT, NMFO/N-CNT, and MCFO/N-CNT samples with commercially used Pt-Ru/C. Although the ORR activity of NMFO/N-CNT surpasses that of the other two trimetallic oxides, it is slightly less active than Pt-Ru/C (Figure 5.8g). Surprisingly, NCFO/N-CNT has the highest maximum current density even when compared against Pt-Ru/C. The OER activity of NCFO/N-CNT is also clearly superior to that of Pt-Ru/C, as well as the other trimetallic oxides in both onset potential and maximum current (Figure 5.8h). Despite having a larger onset potential than Pt-Ru/C, MCFO/N-CNT catalysts also have a higher maximum current density for OER at 0.7 V vs Hg/HgO, while NMFO/N-CNT catalysts have comparable OER performance to Pt-Ru/C. The onset potentials for ORR and OER for all catalysts are summarized in Table 5.2. Comparison of the potential window between onset potentials (ΔE_{onset}) indicates superior bifunctional activity of the trimetallic oxide catalysts over the bimetallic oxide catalysts. It should also be noted that NCFO/N-CNT has a potential window comparable to Pt-Ru/C.

Table 5.2 - ORR and OER LSV Data for the Prepared Catalysts in Oxygen Saturated 0.1 M KOH

	ORR LSV		OER LSV		
Sample	E_{onset} (V vs Hg/HgO)	Maximum |i| (mA cm^{-2})	E_{onset} (V vs Hg/HgO)	Maximum |i| (mA cm^{-2})	ΔE_{onset} (V vs Hg/HgO)
$(Co,Fe)_3O_4$/N-CNT	-0.13	208.9	0.63	41.1	0.76
$MnCoO_x$/N-CNT	-0.16	57.9	0.69	10.0	0.85
$MnFeO_x$/N-CNT	-0.11	202.4	0.67	18.1	0.78
$NiFeO_x$/N-CNT	-0.21	80.4	0.62	26.4	0.83
$NiMnO_x$/N-CNT	-0.11	99.9	0.70	9.2	0.81
$NiCoO_x$/N-CNT	-0.18	58.1	0.68	11.9	0.86
NCFO/N-CNT	-0.13	273.2	0.54	148.9	0.68
NMFO/N-CNT	-0.11	185.2	0.61	60.2	0.72
MCFO/N-CNT	-0.14	198.5	0.60	91.2	0.74
Pt-Ru/C	**-0.08**	**196.4**	**0.58**	**69.1**	**0.66**

*$\Delta E_{onset} = E_{onset}$ (OER) – E_{onset} (ORR)

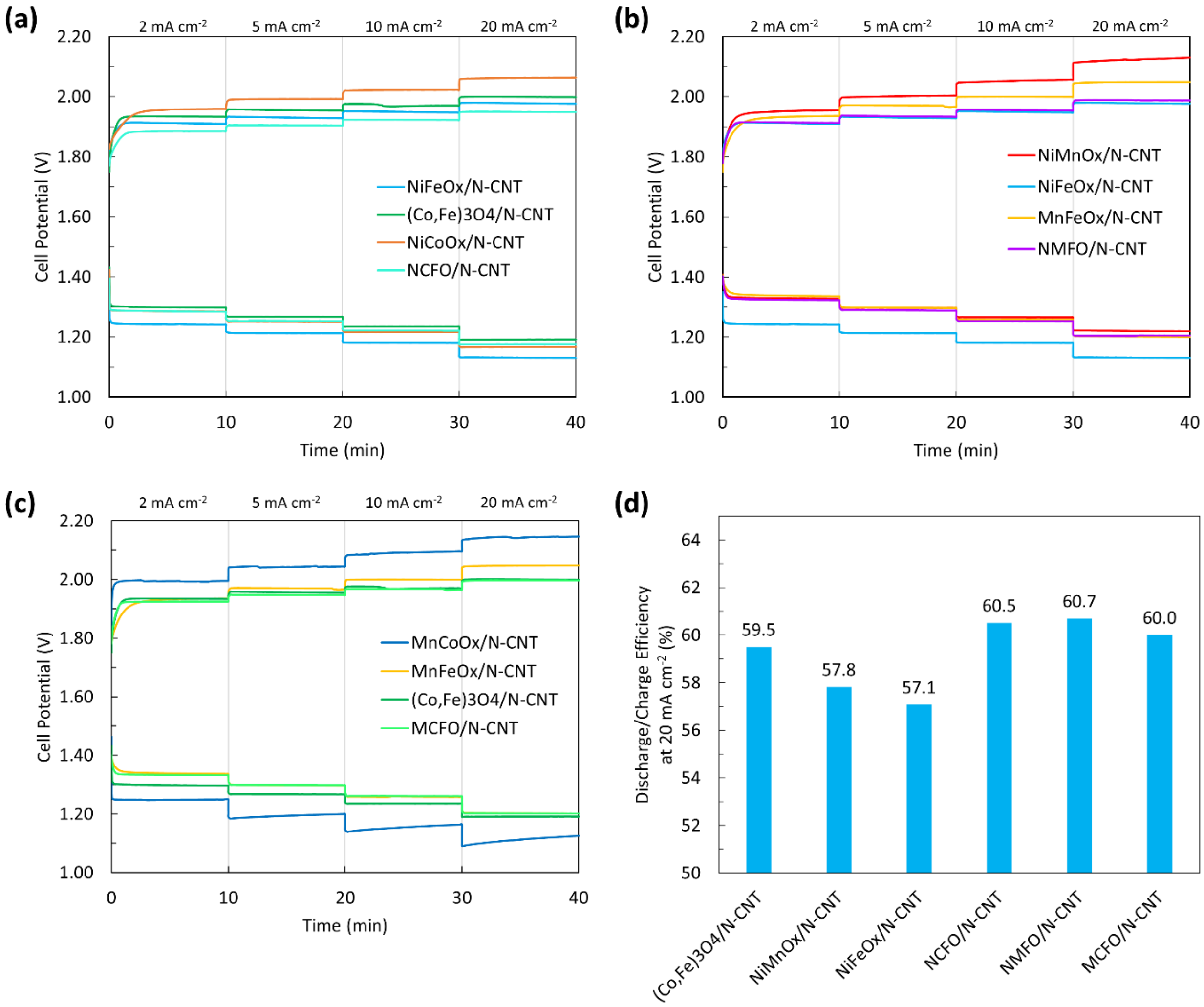

Figure 5.9 - Rate test comparisons for a) Ni-Co-Fe, b) Ni-Mn-Fe, and c) Mn-Co-Fe systems. d) Discharge/charge efficiency comparison of catalysts at a current density of 20 mA cm^{-2}.

Figure 5.9 shows battery rate test comparisons between bimetallic and trimetallic oxides of each system. NCFO/N-CNT samples have comparable ORR performance to $CoFe_2O_4$/N-CNT samples and superior OER performance to all bimetallic oxides in the Ni-Co-Fe system (1.95 V at 20 mA cm^{-2}), resulting in a discharge/charge efficiency of 60.5% at 20 mA cm^{-2} (Figure 5.9a and 5.9d). Similarly, NMFO/N-CNT samples have comparable ORR performance to $MnFeO_x$/N-CNT samples (1.20 V at 20 mA cm^{-2}) in addition to OER performance comparable to $NiFeO_x$/N-CNT (1.98 V at 20 mA cm^{-2}). Therefore, NMFO/N-CNT samples yield a discharge/charge efficiency of 60.7% at 20 mA cm^{-2} (Figure 5.9b and 5.9d). Finally, MCFO/N-CNT samples also have comparable ORR performance to $MnFeO_x$/N-CNTs while matching the OER performance of $(Co,Fe)_3O_4$/N-CNTs, which results in a discharge/charge efficiency of 60.0% at 20 mA cm^{-2}. From the rate test results and calculated discharge/charge efficiencies, trimetallic oxides on N-CNTs exhibited superior bifunctional performance compared with the bimetallic oxides on N-CNTs (Figure 5.9d).

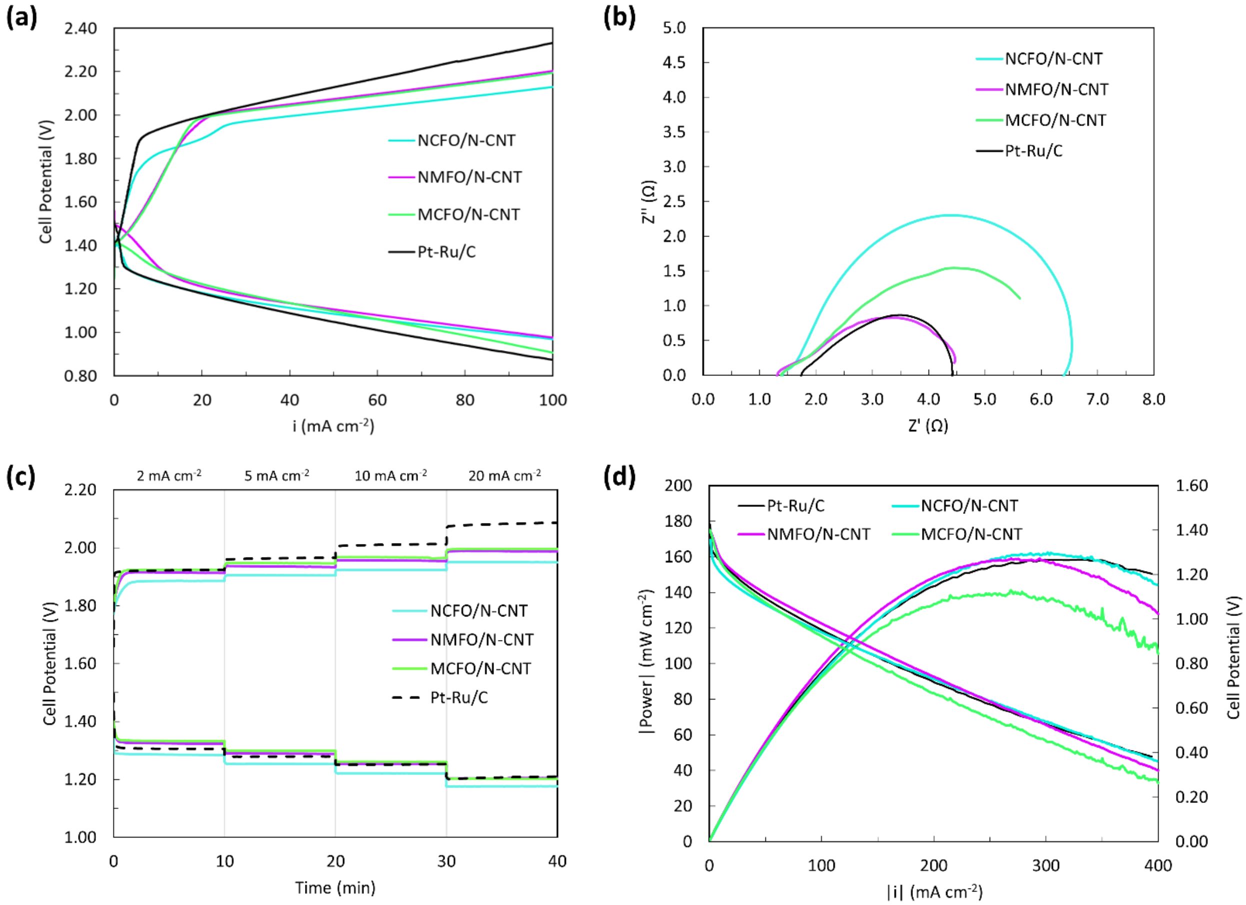

Figure 5.10 - Battery testing comparison between trimetallic oxide on N-CNT catalysts and Pt-Ru/C. a) ORR and OER polarization results, b) EIS Nyquist plots, c) discharge and charge rate tests at different current densities, and d) maximum power curves.

Although valuable information regarding catalytic activity can be obtained from LSV tests, the results do not always correlate with battery performance. The discrepancy is due to the difference in three phase-boundary conditions between configurations and has been reported in our previous work.[134], [151] The oxygen saturated electrolyte used in half-cell LSV measurements preserves the three-phase boundary at the surface of the electrode. In battery configurations, the three-phase boundary size can be increased by better catalyst distribution throughout the electrode porosity.[79] Therefore, the impregnation technique and higher surface area of the N-CNT structures may show superior battery performance. This phenomenon is observed in Figure 5.10, where battery testing results for the trimetallic oxide catalysts are compared with those of Pt-Ru/C. Polarization and rate test comparisons between catalysts show that the trimetallic oxides yield superior OER performance and comparable ORR performance to Pt-Ru/C in a battery configuration (Figure 5.10a and 5.10c). Superior OER performance for NCFO/N-CNT samples was expected from the LSV results; however, improvements in ORR performance corroborate the benefits of impregnation reported in previous work.[134], [151] The discharge/charge efficiencies for the trimetallic oxide on N-CNT catalysts calculated from the rate tests at 20 mA cm^{-2} are superior to that of Pt-Ru/C (57.9%). Charge transfer resistance is evaluated based on the size of the semi-circular region of the Nyquist plot (Figure 5.10b). Pt-Ru/C and NMFO/N-CNT share a similar semi-circular region, indicating similar charge transfer resistances for the two catalysts. However, charge transfer resistance for NCFO/N-CNT and MCFO/N-CNT is much higher. The charge transfer resistances for the trimetallic oxide catalysts decrease in the following order: NCFO/N-CNT > MCFO/N-CNT > NMFO/N-CNT. The power density of the catalysts was also compared (Figure 5.10d). NCFO/N-CNT samples have the highest power density among all catalysts (including Pt-Ru/C) with a maximum power density of 161 mW cm^{-2}. NMFO/N-CNT samples have a comparable maximum power density to Pt-Ru/C (158 mW cm^{-2}), while MCFO/N-CNT samples have the lowest maximum power density of 133 mW cm^{-2}. Maximum power densities and corresponding current densities are summarized in Table 5.3.

Table 5.3 - Summary of Power Curve Comparison for Trimetallic Oxide on N-CNT Catalysts

Catalyst	Maximum Power (mW cm^{-2})	Current Density at Maximum (mA cm^{-2})
NCFO/N-CNT	161.2	287.5
NMFO/N-CNT	158.8	267.4
MCFO/N-CNT	138.7	265.2
Pt-Ru/C	158.1	348.9

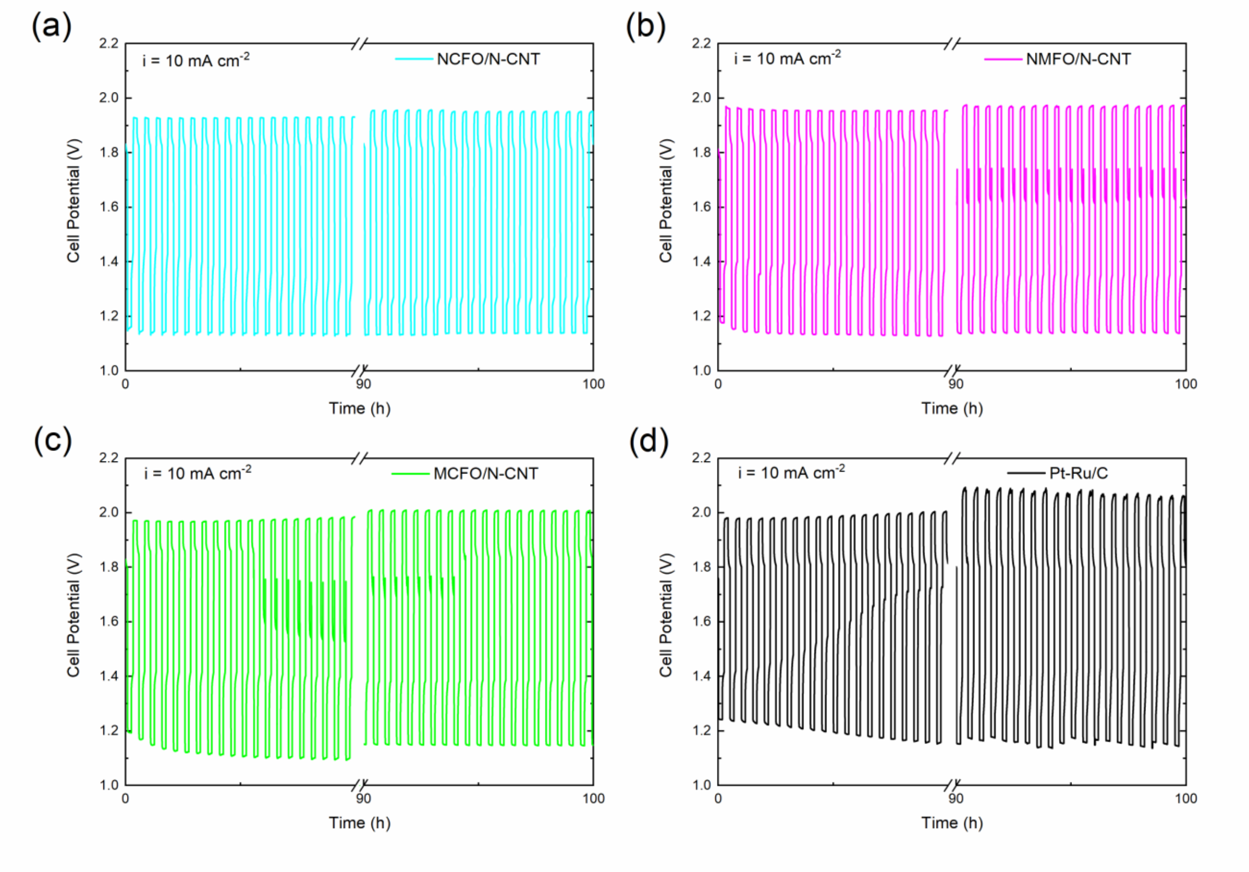

Figure 5.11 - Bifunctional cycling of a) NCFO/N-CNT, b) NMFO/N-CNT, c) MCFO/N-CNT, and d) Pt-Ru/C catalysts. Cycling tests were conducted in a horizontal Zn-air battery configuration with 6 M KOH as the electrolyte, at a current density of 10 mA cm^{-2} for 200 cycles with 30 min per cycle.

Trimetallic oxides were cycled bifunctionally in a homemade Zn-air battery for 200 cycles (100 hours) at 10 mA cm^{-2} and were compared with Pt-Ru/C cycled under the same conditions (Figure 5.11). NCFO/N-CNT samples showed excellent stability over 200 cycles (Figure 5.11a). A slight drop of 30 mV in discharge potential was observed within the first 5 cycles before stabilizing for the remainder of the cycles. Charge potentials increased by 20 mV over the course of the cycling test, which is attributed to the formation of oxygen bubbles within the pores of the impregnated electrode. The initial discharge/charge efficiency for NCFO/N-CNT samples was 60.1%, dropping to 58.5% by the end of the cycling test (Table 5.4). Similar cycling behavior was observed for NMFO/N-CNT and MCFO/N-CNT samples (Figure 5.11b and 5.11c). Initial drops in discharge potential over the first 5 cycles were more pronounced and resulted in decreases of 40 mV and 60 mV for NMFO/N-CNT and MCFO/N-CNT samples, respectively. However, unlike NCFO/N-CNT samples, NMFO/N-CNT and MCFO/N-CNT exhibited a slight recovery of discharge performance with cycling (10 – 20 mV recovery). The recovery in potential is attributed to improved wettability of the electrode during cycling, enabling access to the catalysts within the GDL porosity. OER behavior for NMFO/N-CNT and MCFO/N-CNT is comparable to NCFO/N-CNT, although the charge potentials are slightly higher (Table 5.4). Again, slight increases of 10 – 40 mV are gradually accumulated with cycling, which is also presumed to be a result of trapped oxygen bubbles within the electrode. Initial efficiencies were 60.2% and 60.4%, dropping to 57.9% and 57.2%, respectively, for NMFO/N-CNT and MCFO/N-CNT samples, (Table 5.4). Pt-Ru/C exhibits the best initial efficiency (62.6%, Table 5.4), but shows the largest degradation of performance during cycling. The degradation and poor cyclability of Pt-Ru/C is likely a result of catalyst degradation and issues of flooding due to the nature of the spray coating. The final efficiency of Pt-Ru/C was the lowest of the four catalysts at 55.3% (Table 5.4). Trimetallic oxides on N-CNT catalysts had superior cyclability and stability. Cycling stability and final efficiency follow the trend of NCFO/N-CNT > NMFO/N-CNT > MCFO/N-CNT.

Table 5.4 - Bifunctional Cycling Data of Trimetallic Oxide on N-CNT Catalysts at 10 mA cm^{-2} for 200 Cycles (100 h)

	Initial				Final			
Catalysts	E_{ORR} (V)	E_{OER} (V)	ΔE (V)	Efficiency (%)	E_{ORR} (V)	E_{OER} (V)	ΔE (V)	Efficiency (%)
NCFO/N-CNT	1.16	1.93	0.77	60.1	1.14	1.95	0.81	58.5
NMFO/N-CNT	1.18	1.96	0.78	60.2	1.14	1.97	0.83	57.9
MCFO/N-CNT	1.19	1.97	0.78	60.4	1.15	2.01	0.86	57.2
Pt-Ru/C	1.24	1.98	0.74	62.6	1.15	2.08	0.93	55.3

The effects of cycling on the impregnated electrodes was investigated through SEM and EDX analysis (Figure 5.12). NCFO/N-CNT samples showed a morphology change after cycling (Figure 5.12a). Prior to cycling, the N-CNT surface appears smooth with clusters of particles, whereas the surface is rough after cycling. Additionally, the Ni-Co-Fe peak intensity ratio from SEM EDX area analysis changes during cycling. Specifically, the Fe and Co peak intensities decrease relative to that for Ni, indicating that Fe and Co may dissolve to some degree during cycling. The change in relative amounts of Ni, Co, and Fe may contribute to the morphology change on the N-CNT surface. NMFO/N-CNT samples show virtually no change after cycling (Figure 5.12b). The surface of the N-CNTs remains relatively smooth with some visible clusters of NMFO nanoparticles before and after cycling. SEM EDX area analysis confirms the SEM imaging observations, as the relative intensities of Ni, Mn and Fe remain roughly the same before and after cycling. MCFO/N-CNT samples show minor differences before and after cycling (Figure 5.12c). SEM images have similar N-CNT surface morphologies, although SEM EDX area analysis shows slight variations in the relative peak intensities for Mn, Co, and Fe. The intensity of the Fe peak decreases relative to the intensities for the Mn and Co peaks after cycling, which indicates some Fe dissolution. For all three trimetallic systems, K and Zn peaks are present after cycling in the SEM EDX spectra. The K peak is quite intense and is due to residual KOH from the electrolyte drying on the electrode. It is possible that K_2CO_3 precipitates from KOH reacting with CO_2 (from air or oxidation of the GDL).[5], [27] The Zn peak (at ~8.6 keV) is weaker and is may be due to ZnO precipitating from the electrolyte.

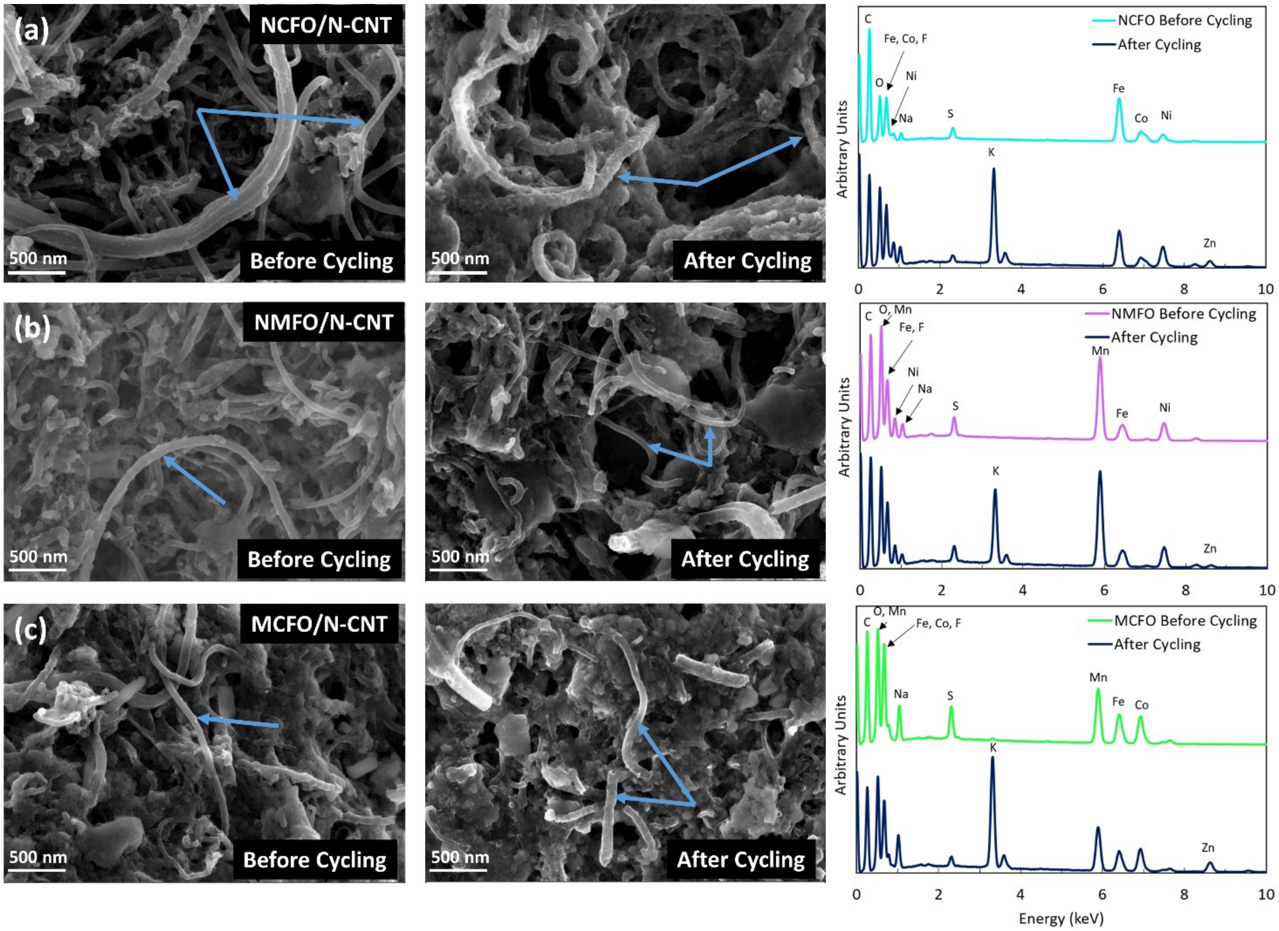

Figure 5.12 - SEM SE images and SEM EDX area analyses before and after cycling at 10 mA cm^{-2} for a) NCFO/N-CNT, b) NMFO/N-CNT, and c) MCFO/N-CNT impregnated electrodes. Blue arrows are used to indicate the catalysts on the GDL surface.

NCFO/N-CNT was determined as the most promising of the trimetallic oxide on N-CNT catalysts and was selected for bifunctional cycling at 20 mA cm^{-2} (Figure 5.13). Both NCFO/N-CNT and Pt-Ru/C were cycled at 20 mA cm^{-2} for 100 cycles, at 30 min/cycle. NCFO/N-CNT samples had good stability even at the higher current density with an initial efficiency of 55.8% and a final efficiency of 53.2%. This compares favorably with Pt-Ru/C cycled bifunctionally under the same conditions. Pt-Ru/C has a higher initial efficiency (57.3%), but there is significant performance loss during cycling resulting in a final efficiency of only 41.3%. Despite its good stability, the performance of NCFO/N-CNT samples is limited by its relatively low discharge potential. Similar to the results at 10 mA cm^{-2}, the discharge potential decreases by 40 mV over the first few cycles before stabilizing at a value of approximately 1.07 V. An increase of 30 mV in charge potential also occurs over the course of 100 cycles which results in a final charge potential of approximately 2.01 V. The gradual increase is again assumed to be due to bubble accumulation within the GDL porosity. A sudden increase in discharge potential occurs for NCFO/N-CNT samples during the 46th h of cycling. This is due to a bubble that has accumulated on the surface of the GDL being released. Similar behavior is shown by Pt-Ru/C after 48 h.

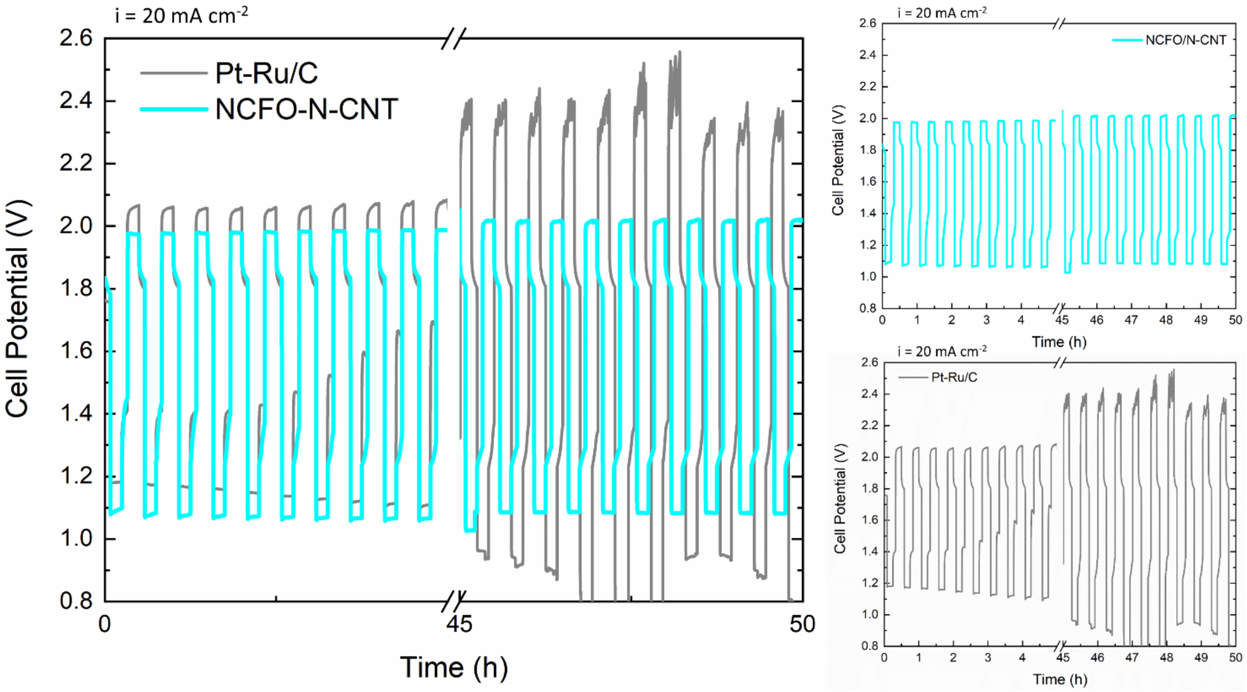

Figure 5.13 - Battery cycling comparison of NCFO/N-CNT impregnated electrodes and Pt-Ru/C loaded electrodes. Cycling was performed in a horizontal Zn-air battery at a current density of 20 mA cm^{-2} for 50 h (100 cycles); 6 M KOH + 0.25 M ZnO was used as the electrolyte and the battery was operated under ambient air conditions. The cycling data for NCFO/N-CNT and Pt-Ru/C is also shown separately for clarity.

5.4 Summary

Various bimetallic and trimetallic transition metal-based oxide nanoparticles were successfully synthesized on N-CNTs and used in impregnated air electrodes for Zn-air batteries (ZABs). Synthesis and electrode preparation were achieved simultaneously for all samples via a simple one-pot process. $NiMnO_x$/N-CNT, $NiFeO_x$/N-CNT, and $(Co,Fe)_3O_4$/N-CNT were the most promising bimetallic catalysts for ORR, OER, and bifunctional performance, respectively, of the combinations tested. $NiMnO_x$/N-CNT samples had an impressive maximum discharge potential of 1.22 V at 20 mA cm^{-2}, while $NiFeO_x$/N-CNT samples had a charge potential of 1.97 V at 20 mA cm^{-2}. $CoFe_2O_4$/N-CNT samples had the highest bimetallic discharge/charge efficiency of 59.5% at 20 mA cm^{-2}.

Based on the bimetallic oxide on N-CNT catalyst results, $NiCoFeO_x$ on N-CNT (NCFO/N-CNT), $NiMnFeO_x$ on N-CNT (NMFO/N-CNT), and $MnCoFeO_x$ on N-CNT (MCFO/N-CNT) catalysts were prepared. All trimetallic oxides showed improved performance towards OER while maintaining good ORR performance compared with the bimetallic oxide catalysts. NCFO/N-CNT catalysts had the best charge potential at 20 mA cm^{-2} of 1.95 V, which was 140 mV lower than that of Pt-Ru/C (2.09 V). NMFO/N-CNT and MCFO/N-CNT catalysts shared the highest discharge potential of the trimetallic oxide catalysts with a potential of 1.20 V at 20 mA cm^{-2}, which is comparable to that for Pt-Ru/C. In battery testing, the trimetallic oxides showed high initial maximum discharge/charge efficiencies of 60.5%, 60.7%, and 60.0% at 20 mA cm^{-2} for NCFO/N-CNT, NMFO/N-CNT, and MCFO/N-CNT catalysts, respectively. These efficiencies compare favorably with that of commercial Pt-Ru/C (57.9%). The trimetallic oxide catalysts performed well in bifunctional cycling tests at 10 mA cm^{-2} for 200 cycles, with excellent stability relative to that for Pt-Ru/C. The final discharge/charge efficiencies of the catalysts after cycling were 58.5%, 57.9%, and 57.2% for NCFO/N-CNT, NMFO/N-CNT, and MCFO/N-CNT samples, respectively. All trimetallic oxides exhibited higher final efficiencies than Pt-Ru/C (55.3%). The NCFO/N-CNT catalyst showed the most promise of the trimetallic oxide catalysts and was selected for cycling at 20 mA cm^{-2} for 200 cycles. NCFO/N-CNT catalysts had good stability and superior discharge/charge efficiency when compared with Pt-Ru/C (53.2% vs 41.3%, respectively). Trimetallic oxides coupled with N-CNTs proved to be excellent bifunctional (ORR/OER) catalysts and should be investigated further in catalyst design for ZABs. Furthermore, the simple and scalable process for producing the composite electrodes provides a low-cost and high performing alternative to noble metal catalysts.

5.5 Supporting Information

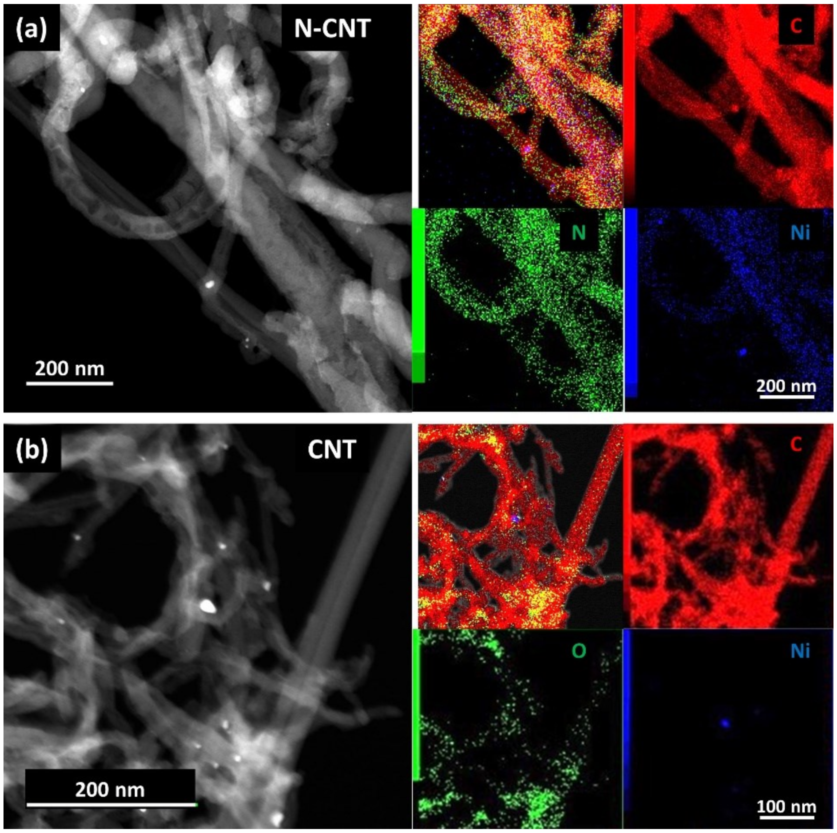

Figure S5.14 - STEM ADF and STEM EDX elemental maps for a) as-purchased N-CNTs and b) as-purchased CNTs. Bright spots in the ADF micrographs are Ni catalysts used in CVD of CNTs and N-CNTs.

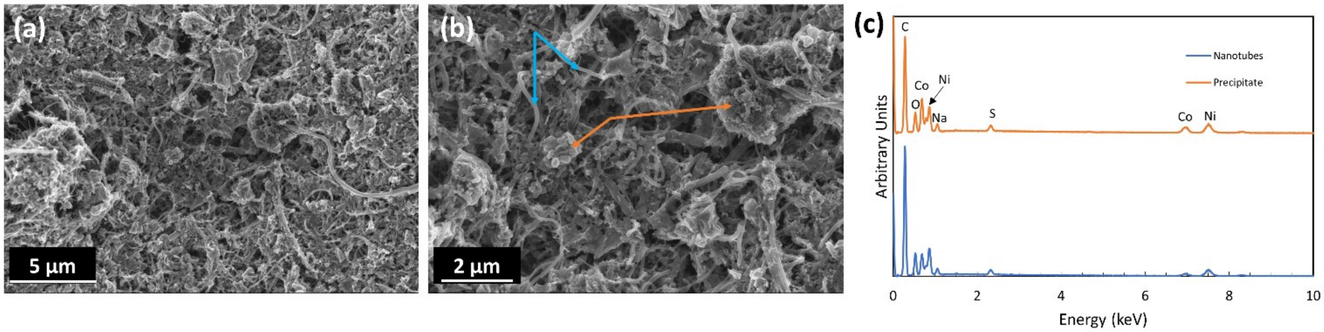

Figure 5.15 – Example of SEM and EDX analyses of bimetallic oxide on N-CNT catalysts: a) Low magnification SEM SE image of the GDL surface, b) higher magnification SEM SE image of the GDL surface with visible nanotubes and precipitates, and c) EDX spectra for nanotubes and precipitate clusters for $NiCoO_x$/N-CNT. Blue arrows are used to identify the nanotube catalysts and orange arrows are used to identify the precipitates. The results shown for $NiCoO_x$/N-CNTs are analogous to those observed for other bimetallic oxides on N-CNTs.

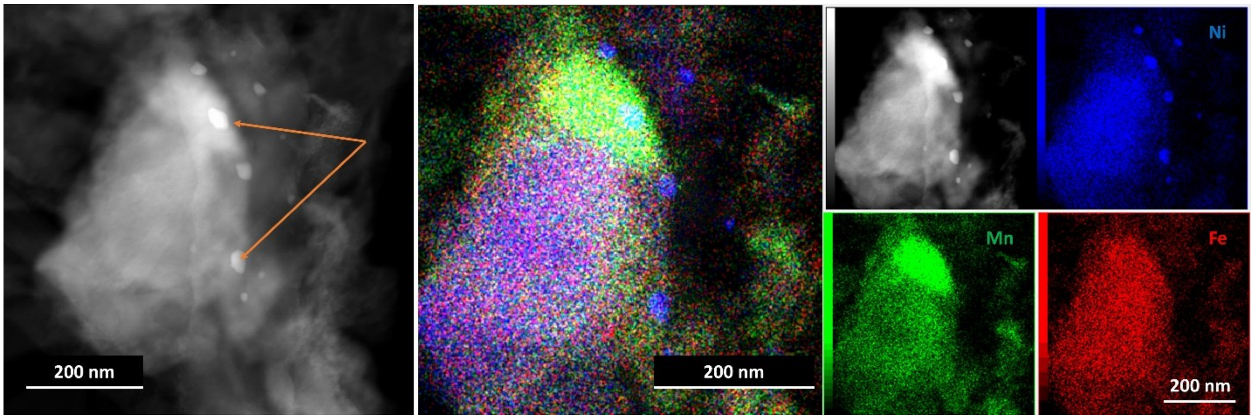

Figure S5.16 - TEM DF and EDX elemental maps for NMFO/N-CNT precipitates. Orange arrows are used to identify the presence of Ni catalysts remaining from CVD of N-CNTs, which suggest the presence of N-CNTs within the precipitate.

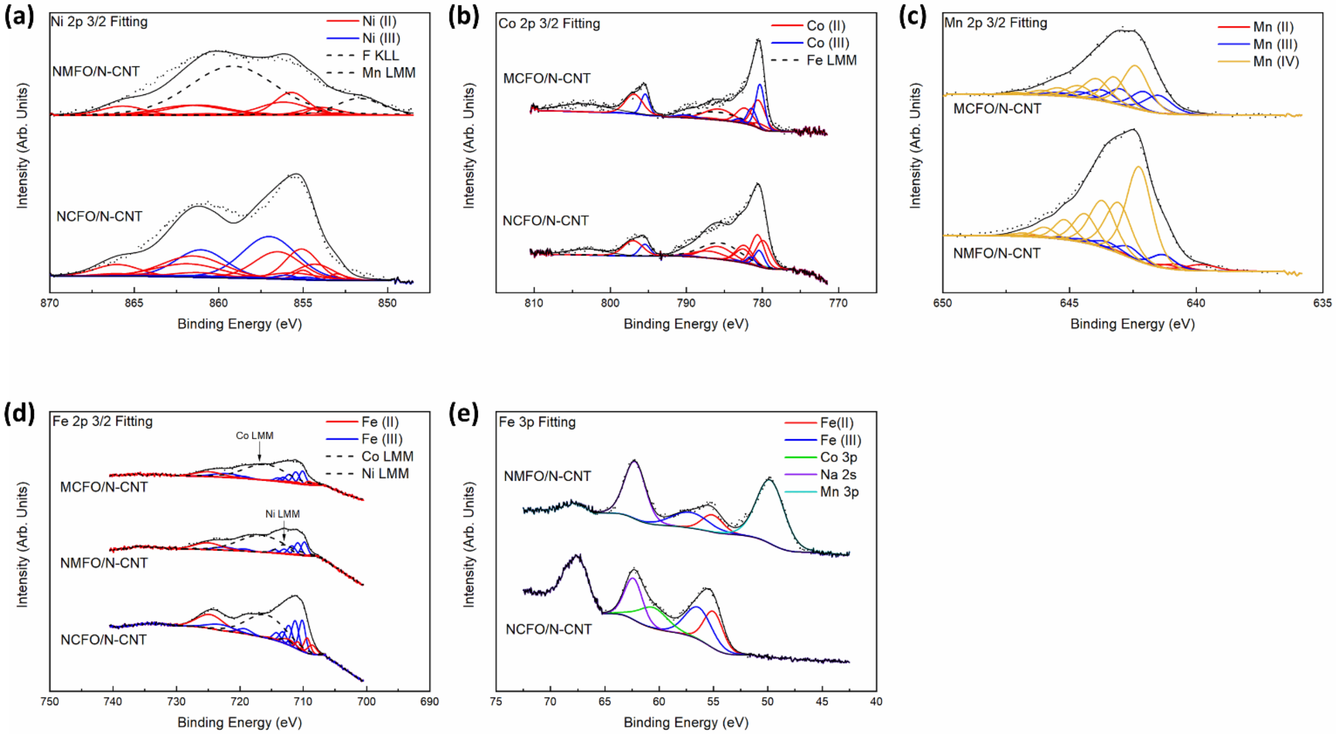

Figure S5.17 – XPS fitting of a) Ni 2p 3/2, b) Co 2p 3/2, c) Mn 2p 3/2, d) Fe 2p 3/2, and e) Fe 3p high resolution spectra. High resolution metal 2p spectra were fit using multiplet splitting for different oxidation states.[105], [106], [154]

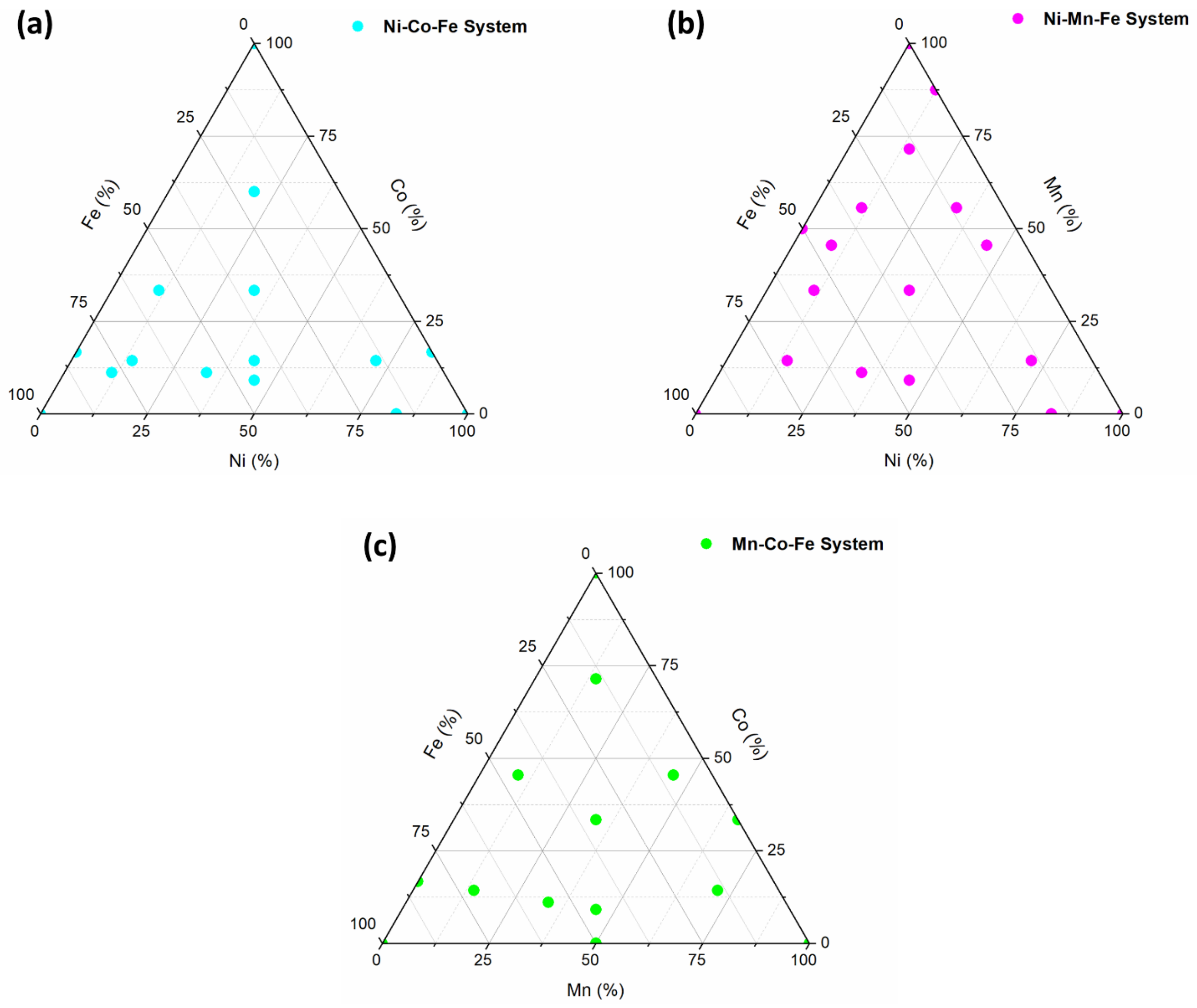

Figure S5.18 - Representation of the 40 samples synthesized using different metal salt ratios for the a) Ni-Co-Fe system, b) Ni-Mn-Fe system, and c) Mn-Co-Fe system. It should be noted that the corners of each ternary system were also synthesized and tested.

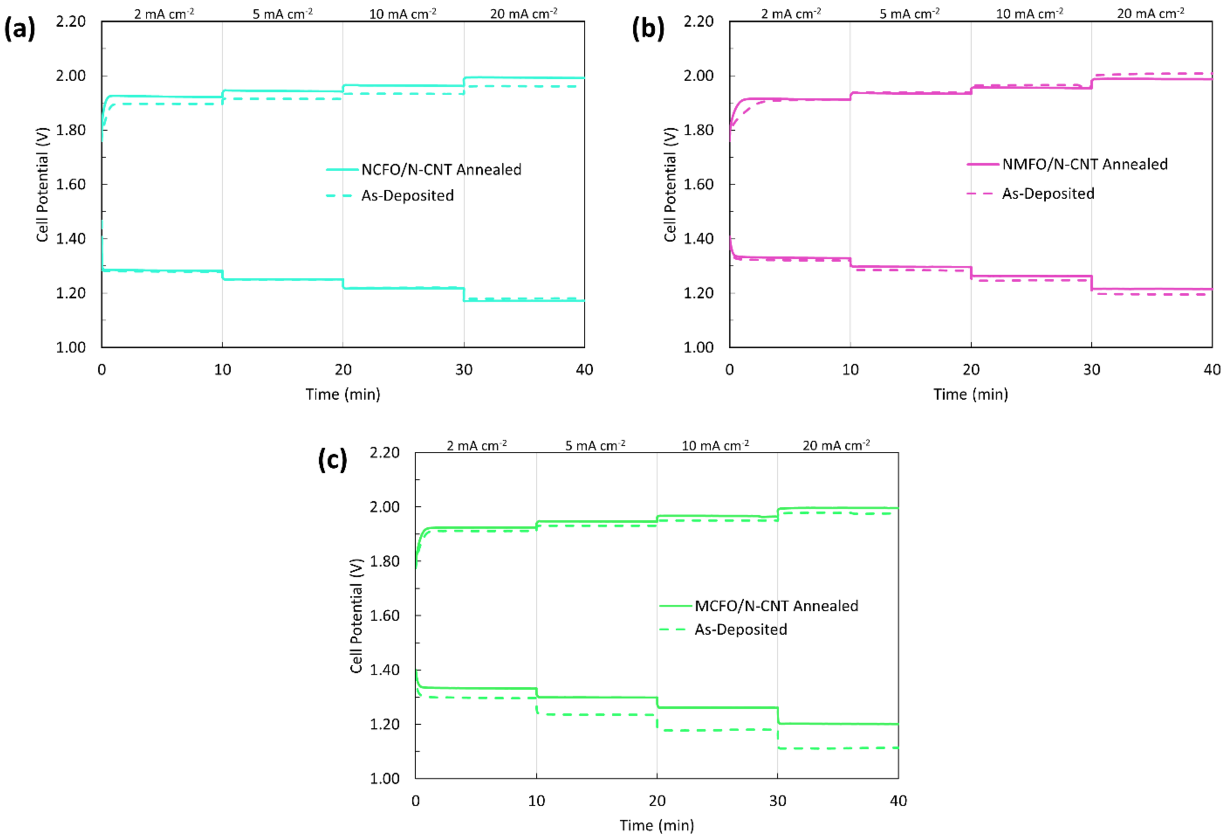

Figure S5.19 - Effect of annealing on rate test results for a) NCFO/N-CNT, b) NMFO/N-CNT, and c) MCFO/N-CNT impregnated electrodes.

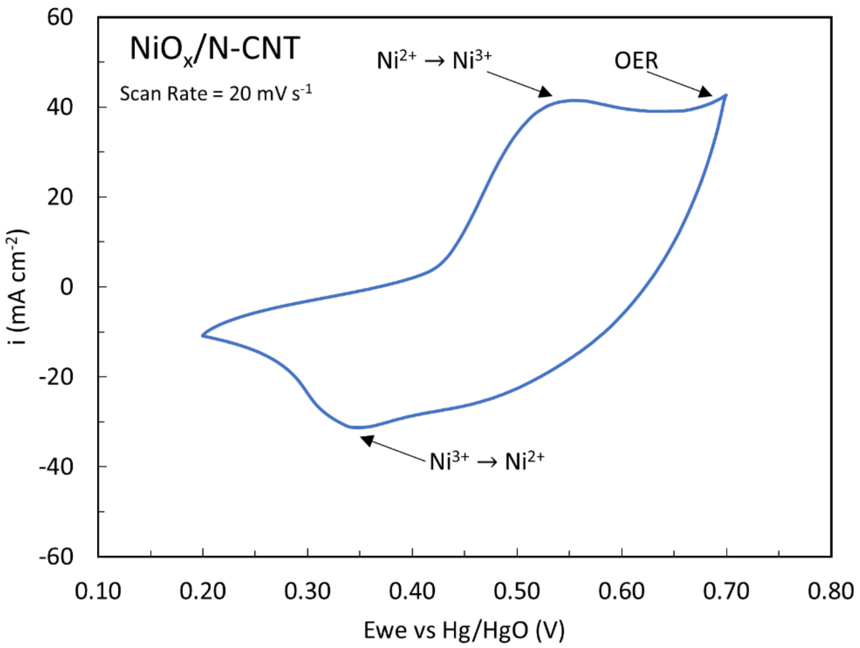

Figure S5.20 - CV results for NiO$_x$/N-CNTs in O_2 saturated 1 M KOH at a scan rate of 20 mV s^{-1}.

6 Conclusions and Future Work

6.1 Conclusions

Efforts to develop air-electrodes with resilience to flooding and good cycling stability for Zn-air batteries have been presented. Mn_3O_4 decorated N-CNTs were prepared in a simple one-pot process and simultaneously deposited into the gas diffusion layer (GDL). The influence of mass ratio between Mn precursor and N-CNTs, as well as other synthesis parameters, were systematically examined. The impregnated electrode showed improved catalyst distribution throughout the porosity of the GDL and exhibited better oxygen reduction reaction (ORR) performance than other Mn_3O_4 catalysts in the literature. Next, $(Co,Fe)_3O_4$/N-CNT catalysts were prepared based on the success of previous work within our group. The bimetallic spinel was realized using the same simple synthesis and impregnation procedure as Mn_3O_4/N-CNT and showed remarkable bifunctional capabilities for ORR and oxygen evolution reaction (OER), superior to that of the benchmark catalyst Pt-Ru/C. $(Co,Fe)_3O_4$/N-CNT showed excellent stability during 200 charge-discharge cycles. The versatility of the synthesis and impregnation procedure was investigated through the study of trimetallic oxide catalysts on N-CNTs. Six bimetallic combinations were successfully synthesized and were used to select promising trimetallic combinations. NiCoFe oxide, NiMnFe oxide, and MnCoFe oxide particles were successfully anchored onto N-CNTs. The trimetallic oxides showed improved catalytic activity when compared with the bimetallic catalysts. Furthermore, each trimetallic oxide demonstrated good cycling stability for 100 h (200 cycles) of cycling tests. The results of this study demonstrate a simple, reproducible, and commercially scalable means to produce high performing air electrodes for Zn-air batteries without the use of noble metal catalysts.

Impregnated Gas Diffusion Layers with Mn_3O_4/N-CNTs

Mn_3O_4 particles anchored to N-CNTs were synthesized by a simple precipitation method at room temperature. The GDL was immersed in the catalyst solution during synthesis, removed, and then was used like filter paper as the catalyst solution passed through during vacuum filtration. The result was GDL impregnated with Mn_3O_4/N-CNT catalysts. The GDL was examined through cross-sectional SEM to confirm that the catalysts had infiltrated the porosity of the electrode and were not solely present on the surface. Mn_3O_4 was identified through a combination of TEM selected area diffraction and XPS analysis. Electrochemical analysis compared various electrode preparation techniques to highlight the influence of impregnation during battery testing. The impregnated GDL had superior ORR rate test results over conventional spray coating techniques. Next, the impregnated electrode was compared with commercially used Pt-Ru/C. Mn_3O_4/N-CNT impregnated GDL samples showed superior ORR performance compared with Pt-Ru/C at current densities lower than 20 mA cm^{-2} and comparable performance at 20 mA cm^{-2} (1.21 V at 20 mA cm^{-2}). The impregnated GDL was combined with electrodeposited Co-Fe/Ni foam OER catalysts (reported previously by our group) and cycled in a tri-electrode cell configuration. When combined with Co-Fe/Ni foam, the Mn_3O_4/N-CNT impregnated GDL had comparable cycling performance to Pt-Ru/C (cycled under the same tri-electrode conditions) with a discharge/charge efficiency of 59%.

$(Co,Fe)_3O_4$/N-CNT Bifunctional Catalysts

Following the development of the impregnation technique and based on the good performance previously reported for electrodeposited Co-Fe on Ni foam, Co and Fe were selected to form a bimetallic oxide on N-CNTs. $(Co,Fe)_3O_4$/N-CNT catalysts were realized using a 5:1 ratio of Fe salt to Co salt in the synthesis solution. The XPS analysis indicated that Fe in the oxide promotes higher oxidation states of Co which increased the activity towards OER; this was confirmed by reports in literature. The combination of the oxide with N-CNTs also improved the catalyst activity towards ORR. ORR and OER performance of these catalysts were compared with Pt-Ru/C in battery rate tests. $(Co,Fe)_3O_4$/N-CNT samples showed comparable ORR performance to Pt-Ru/C (1.19 V vs 1.21 V, respectively) and superior OER performance (2.00 V vs 2.06 V, respectively) when tested at a current density of 20 mA cm^{-2}. Cycling of the catalysts at 10 mA cm^{-2} for 200 cycles (100 h) revealed exceptional stability of $(Co,Fe)_3O_4$/N-CNT impregnated electrodes; less than 1% drop in efficiency over 100 h was observed. The stability of $(Co,Fe)_3O_4$/N-CNT electrodes was superior to that of Pt-Ru/C.

Trimetallic Oxide Decorated N-CNT Catalysts

Various bimetallic oxides were prepared on N-CNTs using the developed synthesis and impregnation technique. $NiMnO_x$/N-CNT, $(Co,Fe)_3O_4$/N-CNT, and $NiFeO_x$/N-CNT catalysts showed the most promise of the bimetallic oxides in terms of ORR performance, bifunctional performance, and OER performance, respectfully. Trimetallic oxides based on the best performing bimetallic combinations were then synthesized and investigated as catalysts for Zn-air batteries. NiCoFe oxide on N-CNT (NCFO/N-CNT), NiMnFe oxide on N-CNT (NMFO/N-CNT), and MnCoFe oxide on N-CNT (MCFO/N-CNT) were fabricated. The ratios between the metal salts for synthesis were 3:1:5 (Ni:Co:Fe) for NCFO/N-CNT, 3:5:1 (Ni:Mn:Fe) for NMFO/N-CNT, and 1:1:1 (Mn:Co:Fe) for MCFO/N-CNT. The effect of metal salt ratio was studied using battery rate tests in order to determine the optimal ratios for synthesis. The trimetallic oxides were studied using EDX analysis (both SEM and TEM), as well as XPS analysis. Through the characterization work, it is proposed that the trimetallic oxides form spinel structures with substitution in both tetrahedral and octahedral lattice sites. The trimetallic oxide catalysts had superior OER performance and comparable ORR performance to bimetallic oxides. ORR performance of trimetallic oxides followed the trend of NMFO/N-CNT, MCFO/N-CNT > NCFO/N-CNT. OER performance followed the opposite trend. The trimetallic oxide catalysts exhibited discharge/charge efficiencies above 60% at current densities of 20 mA cm^{-2} in battery rate tests. All trimetallic oxides were cycled bifunctionally at 10 mA cm^{-2} for 200 cycles (100 h) and were compared with Pt-Ru/C. All three catalysts showed superior cycling stability to that of Pt-Ru/C, most notably NCFO/N-CNT. Bifunctional cycling of NCFO/N-CNT at 20 mA cm^{-2} further confirmed the stability of the catalyst, as it outperformed Pt-Ru/C after 50 h of cycling (100 cycles) with a final efficiency of 55.3%.

6.2 Future Work

Impregnation and Synthesis

This study only investigated impregnation of N-CNT supported catalysts. However, the impregnation technique could be applied to a wide range of catalysts and electrode materials. For instance, sequential impregnation of the electrode with two different catalysts may be beneficial as a bifunctional electrode. Sequential impregnation could be achieved by soaking the GDL in the ORR catalyst suspension, followed by passing of the OER catalyst suspension through the electrode via vacuum filtration. Preliminary results for sequentially impregnated Mn_3O_4/N-CNT and $(Co,Fe)_3O_4$/N-CNT electrodes showed promising cycling efficiency at 10 mA cm^{-2} (58.6% after 100 cycles). Additionally, investigation into electrodes impregnated with noble metal catalysts would be useful to further confirm the benefits of the preparation technique.

The mechanism for the synthesis technique should be further explored. It was shown in this study that the catalysts do not form without the presence of N in the CNTs, but other dopants and graphene structures were not explored. More understanding of the precipitation mechanism may allow for more sophisticated designs of bifunctional catalysts for Zn-air batteries. Additionally, the influence of temperature on synthesis may allow for more tunable oxide particle size and morphology and should be considered going forward. Finally, a scalability analysis on the impregnation technique would be useful for applying the method in commercial battery manufacturing. The impregnation technique is simple, reproducible, and requires little specialized equipment; however, it is not clear as to how the technique could be scaled up for a continuous manufacturing process.

Transition Metal Oxide Catalysts

Several metal oxides using various combinations of transition metals were synthesized in this work. However, further investigation into trimetallic combinations may yield improved stability and catalytic activity compared with the results presented herein. The Ni-Mn-Co system was not investigated and may provide further insight into the design of trimetallic oxide catalysts and possible tetra-metallic oxide catalysts. Furthermore, Zn appears on all electrodes after cycling. The role of Zn in the cycling performance should be explored. For example, is Zn incorporated into the metal oxide and does this influence the stability or performance of the catalyst? ZnCo oxide, ZnMn oxide, and ZnMnCo oxide (ZMCO) on N-CNT catalysts have been prepared to develop a foundation for future work. Preliminary results for Zn-based oxides show exceptional ORR performance (1.23 V at 20 mA cm^{-2} for $ZnMnO_x$/N-CNT), good bifunctional performance (58.7% discharge/charge efficiency at 20 mA cm^{-2} for ZMCO/N-CNT), and good cycling performance (56.8% and 57.7% efficiencies at 10 mA cm^{-2} after 200 cycles for $ZnCoO_x$/N-CNT and

$ZnMnO_x$/N-CNT, respectively). The addition of Zn improved the performance of the catalysts compared with their non-Zn counterparts (Mn_3O_4/N-CNT, Co_3O_4/N-CNT, and $MnCoO_x$/N-CNT). Other Zn based oxides may also provide improvements in terms of catalyst activity and cycling stability. Therefore, Zn-based catalysts should be investigated further as bimetallic and trimetallic oxides as candidates for air electrodes in secondary Zn-air batteries.

References:

[1] J. Fu, Z. P. Cano, M. G. Park, A. Yu, M. Fowler, and Z. Chen, *Adv. Mater.*, **2017**, 29, 1604685.

[2] A. Eitan, L. Herman, I. Fischhendler, and G. Rosen, *Renew. Sustain. Energy Rev.*, **2019**, 105, November 2018, 95–104.

[3] S. G. Azevedo, M. Santos, and J. R. Antón, *Biomass and Bioenergy*, **2019**, 126, May, 70–83.

[4] J. Zhu, T. Wierzbicki, and W. Li, *J. Power Sources*, **2018**, 378, November 2017, 153–168.

[5] E. Davari and D. G. Ivey, *Sustain. Energy Fuels*, **2017**, 2, 39–67.

[6] N. Chawla, *Mater. Today Chem.*, **2019**, 12, 324–331.

[7] H. D. Yoo, E. Markevich, G. Salitra, D. Sharon, and D. Aurbach, *Biochem. Pharmacol.*, **2014**, 17, 3, 110–121.

[8] G. Girishkumar, B. McCloskey, A. C. Luntz, S. Swanson, and W. Wilcke, *J. Phys. Chem. Lett.*, **2010**, 1, 14, 2193–2203.

[9] A. L. Zhu, D. P. Wilkinson, X. Zhang, Y. Xing, A. G. Rozhin, and S. A. Kulinich, *J. Energy Storage*, **2016**, 8, 35–50.

[10] T. Reier, M. Oezaslan, and P. Strasser, *ACS Catal.*, **2012**, 2, 8, 1765–1772.

[11] Y. J. Wang, N. Zhao, B. Fang, H. Li, X. T. Bi, and H. Wang, *Chem. Rev.*, **2015**, 115, 9, 3433–3467.

[12] S. R. Stoyanov, A. V. Titov, and P. Král, *Coord. Chem. Rev.*, **2009**, 253, 23–24, 2852–2871.

[13] Q. Wang, K. Dastafkan, and C. Zhao, *Curr. Opin. Electrochem.*, **2018**, 1–8.

[14] W. Lv, Z. Li, Y. Deng, Q. H. Yang, and F. Kang, *Energy Storage Mater.*, **2016**, 2, 107–138.

[15] S. Zhao, L. Yan, H. Luo, W. Mustain, and H. Xu, *Nano Energy*, **2018**, 47, February, 172–198.

[16] S. Qu, Z. Song, J. Liu, Y. Li, Y. Kou, C. Ma, and X. Han, *Nano Energy*, **2017**, 39, June, 101–110.

[17] V. Neburchilov, H. Wang, J. J. Martin, and W. Qu, *J. Power Sources*, **2010**, 195, 5, 1271–1291.

[18] P. C. Li, C. C. Hu, T. H. You, and P. Y. Chen, *Carbon N. Y.*, **2017**, 111, 813–821.

[19] L. Li, J. Yang, H. Yang, L. Zhang, J. Shao, W. Huang, B. Liu, and X. Dong, *ACS Appl. Energy Mater.*, **2018**, 1, 963–969.

[20] P. Pei, K. Wang, and Z. Ma, **2014**, 128, 315–324.

[21] X. Zhang, X. Wang, Z. Xie, and Z. Zhou, *Green Energy Environ.*, **2016**, 1, 1, 4–17.

[22] B. Pichler, S. Weinberger, L. Re, F. Gebetsroither, B. Bitschnau, and V. Hacker, *Electrochim. Acta*, **2017**, 251, 488–497.

[23] M. Kim, H. M. Hwang, G. H. Park, and H. Lee, *FlatChem*, **2017**, 6, 48–76.

[24] C. Moreno-Castilla and F. J. Maldonado-Hódar, *Carbon N. Y.*, **2005**, 43, 3, 455–465.

[25] Y. H. Kwok, Y. F. Wang, A. C. H. Tsang, and D. Y. C. Leung, *Appl. Energy*, **2018**, 217, February, 258–265.

[26] S. A. Baskakov, R. A. Manzhos, A. S. Lobach, Y. V. Baskakova, A. V. Kulikov, V. M. Martynenko, F. O. Milovich, Y. Kumar, A. Michtchenko, E. N. Kabachkov, A. G. Krivenko, and Y. M. Shulga, *J. Non. Cryst. Solids*, **2018**, 498, May, 236–243.

[27] A. R. Mainar, E. Iruin, L. C. Colmenares, A. Kvasha, I. De Meatza, M. Bengoechea, O. Leonet, I. Boyano, Z. Zhang, and J. A. Blazquez, *J. Energy Storage*, **2018**, 15, 304–328.

[28] S. Liu, W. Han, B. Cui, X. Liu, F. Zhao, J. Stuart, and S. Licht, *J. Power Sources*, **2017**, 342, 435–441.

[29] G. Zhang, X. Zhang, and Y. Wang, **2004**, 42, 3097–3102.

[30] Z. Li and L. Liu, *Chinese J. Catal.*, **2015**, 36, 1, 3–14.

[31] H. Osgood, S. V. Devaguptapu, H. Xu, J. Cho, and G. Wu, *Nano Today*, **2016**, 11, 5, 601–625.

[32] Y. Gao, L. Wang, G. Li, Z. Xiao, Q. Wang, and X. Zhang, *Int. J. Hydrogen Energy*, **2018**, 43, 16, 7893–7902.

[33] L. Hadidi, E. Davari, M. Iqbal, T. K. Purkait, D. G. Ivey, and J. G. C. Veinot, *Nanoscale*, **2015**, 7, 48, 20547–20556.

[34] H. Li, Y. Huang, H. Zhou, W. Yang, M. Li, Z. Huang, C. Fu, and Y. Kuang, *Electrochim. Acta*, **2017**, 247, 736–744.

[35] Y. R. Liu, W. H. Hu, X. Li, B. Dong, X. Shang, G. Q. Han, Y. M. Chai, Y. Q. Liu, and C. G. Liu,

Appl. Surf. Sci., **2016**, 384, 51–57.

[36] Z. Yang, H. Nie, X. Chen, X. Chen, and S. Huang, *J. Power Sources*, **2013**, 236, 238–249.

[37] M. Gong and H. Dai, *Nano Res.*, **2014**, 8, 1, 23–39.

[38] R. D. L. Smith, M. S. Pre, R. D. Fagan, and S. Trudel, *J. Am. Chem. Soc.*, **2013**, 135, 11580–11586.

[39] N. Xu, J. Qiao, Q. Nie, M. Wang, H. Xu, Y. Wang, and X. Zhou, *Catal. Today*, **2018**, 318, 144–149.

[40] W. Bian, Z. Yang, P. Strasser, and R. Yang, *J. Power Sources*, **2014**, 250, 196–203.

[41] Y. Li, S. Yang, H. Li, G. Li, M. Li, L. Shen, Z. Yang, and A. Zhou, *Colloids Surfaces A Physicochem. Eng. Asp.*, **2016**, 506, 694–702.

[42] W. Yan, Z. Yang, W. Bian, and R. Yang, *Carbon N. Y.*, **2015**, 92, 74–83.

[43] L. Wei, H. E. Karahan, S. Zhai, H. Liu, X. Chen, Z. Zhou, Y. Lei, Z. Liu, and Y. Chen, *Adv. Mater.*, **2017**, 29, 38, 1–10.

[44] T. Gao, Z. Jin, Y. Zhang, G. Tan, H. Yuan, and D. Xiao, *Electrochim. Acta*, **2017**, 258, 51–60.

[45] S. Zhu, Z. Chen, B. Li, D. Higgins, H. Wang, H. Li, and Z. Chen, *Electrochim. Acta*, **2011**, 56, 14, 5080–5084.

[46] K. Mamtani, D. Jain, D. Dogu, V. Gustin, S. Gunduz, A. C. Co, and U. S. Ozkan, *Appl. Catal. B Environ.*, **2018**, 220, 88–97.

[47] Y. Qian, Z. Hu, X. Ge, S. Yang, Y. Peng, Z. Kang, Z. Liu, J. Y. Lee, and D. Zhao, *Carbon N. Y.*, **2017**, 111, 641–650.

[48] S. U. Dar, M. A. Ud Din, M. U. Hameed, S. Ali, R. Akram, Z. Wu, and D. Wu, *J. Power Sources*, **2018**, 373, November 2017, 61–69.

[49] H. Lin, D. Chen, C. Lu, C. Zhang, F. Qiu, S. Han, and X. Zhuang, *Electrochim. Acta*, **2018**, 266, 17–26.

[50] X. Zhang, Z. Yang, Z. Lu, and W. Wang, *Carbon N. Y.*, **2018**, 130, 112–119.

[51] Y. Wang, H. Fan, A. Ignaszak, L. Zhang, S. Shao, and P. David, *Chem. Eng. J.*, **2018**, 348, 1, 416–437.

[52] M. Wang, T. Qian, S. Liu, J. Zhou, and C. Yan, *ACS Appl. Mater. Interfaces*, **2017**, 9, 25, 21216–21224.

[53] Z. Zhang, Z. Li, C. Sun, T. Zhang, and S. Wang, *Catal. Today*, **2017**, 298, October 2016, 241–249.

[54] Z. Yang, X. Zhou, H. Nie, Z. Yao, and S. Huang, *ACS Appl. Mater. Interfaces*, **2011**, 3, 7, 2601–2606.

[55] N. T. Alvarez, V. N. Shanov, T. Ochmann, and B. Ruff, Elsevier, **2013**.

[56] S. L. Candelaria, Y. Shao, W. Zhou, X. Li, J. Xiao, J. G. Zhang, Y. Wang, J. Liu, J. Li, and G. Cao, *Nano Energy*, **2012**, 1, 2, 195–220.

[57] C. Hu, D. Liu, Y. Xiao, and L. Dai, *Prog. Nat. Sci. Mater. Int.*, **2018**, 28, 2, 121–132.

[58] J. Albero and H. Garcia, *J. Mol. Catal. A Chem.*, **2014**, 408, 296–309.

[59] M. Inagaki, M. Toyoda, Y. Soneda, and T. Morishita, *Carbon N. Y.*, **2018**, 132, 104–140.

[60] W. H. Shin, H. M. Jeong, B. G. Kim, J. K. Kang, and J. W. Choi, *Nano Lett.*, **2012**, 12, 5, 2283–2288.

[61] R. Ma, Y. Zhou, F. Wang, K. Yan, Q. Liu, and J. Wang, *Mater. Today Energy*, **2017**, 6, 173–180.

[62] Z. Chen, Z. Chen, and D. Higgins, *Carbon N. Y.*, **2010**, 48, 11, 3057–3065.

[63] R. Ghasempour and H. Narei, Elsevier Inc., **2018**.

[64] P. Guo, Y. X. Wu, W. M. Lau, H. Liu, and L. M. Liu, *J. Alloys Compd.*, **2017**, 723, 772–778.

[65] J. Fang, L. Hu, M. Wang, L. Gan, C. Chen, Y. Jiang, B. Xiao, Y. Lai, and J. Li, *Mater. Lett.*, **2018**, 218, 36–39.

[66] J. Zhu, youlong Xu, J. Hu, L. P. Wei, J. Liu, and M. Zheng, *J. Power Sources*, **2018**, 393, April, 135–144.

[67] S. Rout, A. K. Nayak, J. L. Varanasi, D. Pradhan, and D. Das, *J. Electroanal. Chem.*, **2018**, 815, January, 1–7.

[68] A. Muhulet, F. Miculescu, S. I. Voicu, F. Schütt, V. K. Thakur, and Y. K. Mishra, *Mater. Today Energy*, **2018**, 9, 154–186.

[69] M. Zhang, J. Shi, Y. Sun, W. Ning, and Z. Hou, *Catal. Commun.*, **2015**, 70, 72–76.

[70] Y. Liu, K. Ai, and L. Lu, *Chem. Rev.*, **2014**, 114, 9, 5057–5115.

[71] K. Qu, Y. Zheng, Y. Jiao, X. Zhang, S. Dai, and S. Z. Qiao, *Adv. Energy Mater.*, **2017**, 7, 9.

[72] J. Yue, X. Gu, X. Jiang, L. Chen, N. Wang, J. Yang, and X. Ma, *Electrochim. Acta*, **2015**, 182, 676–681.

[73] Y. Liu, H. Jiang, Y. Zhu, X. Yang, and C. Li, *J. Mater. Chem. A*, **2016**, 4, 5, 1694–1701.

[74] L. Ma, H. Zhou, Y. Sun, S. Xin, C. Xiao, A. Kumatani, T. Matsue, P. Zhang, S. Ding, and F. Li, *Electrochim. Acta*, **2017**, 252, 338–349.

[75] M. Xiong and D. G. Ivey, *Electrochem. commun.*, **2017**, 75, 73–77.

[76] M. Xiong and D. G. Ivey, *J. Electrochem. Soc.*, **2017**, 164, 6, A1012–A1021.

[77] P. Gu, M. Zheng, Q. Zhao, X. Xiao, H. Xue, and H. Pang, *J. Mater. Chem. A*, **2017**, 5, 17, 7651–7666.

[78] Y. Wang, S. Wang, T. Zhao, Y. Chen, Z. Li, W. Wu, and M. Wu, *Chem. Eng. J.*, **2016**, 306, 336–343.

[79] A. Sumboja, F. Wei, T. Goh, B. Li, and D. Geng, *Chempluschem*, **2015**, 80.

[80] I. Gurrappa and L. Binder, *Sci. Technol. Adv. Mater.*, **2008**, 9, 4.

[81] K. Kordesch and G. Simader, Elsevier Inc., **1996**.

[82] G. H. A. Therese and P. V. Kamath, *Chem. Mater.*, **2000**, 12, 5, 1195–1204.

[83] Z. Wang, X. Cai, C. Yang, L. Zhou, and C. Hu, *J. Alloys Compd.*, **2018**, 735, 1357–1362.

[84] Y. Jin, L. Zhu, W. D. Xue, and W. Z. Li, *Trans. Nonferrous Met. Soc. China (English Ed.*, **2015**, 25, 9, 2994–3001.

[85] L. Besra and M. Liu, *Prog. Mater. Sci.*, **2007**, 52, 1, 1–61.

[86] G. A. M. Ali, M. M. Yusoff, Y. H. Ng, H. N. Lim, and K. F. Chong, *Curr. Appl. Phys.*, **2015**, 15, 10, 1143–1147.

[87] Suhasini, *J. Electroanal. Chem.*, **2013**, 690, 13–18.

[88] S. Banbur-Pawlowska, K. Mech, R. Kowalik, and P. Zabinski, *Appl. Surf. Sci.*, **2016**, 388, 805–808.

[89] L. Jiang, Y. Ding, F. Jiang, L. Li, and F. Mo, *Anal. Chim. Acta*, **2014**, 833, 22–28.

[90] Y. Ma, J. Han, M. Wang, X. Chen, and S. Jia, *J. Mater.*, **2018**, 4, 2, 108–120.

[91] P. M. Hannula, A. Peltonen, J. Aromaa, D. Janas, M. Lundström, B. P. Wilson, K. Koziol, and O. Forsén, *Carbon N. Y.*, **2016**, 107, 281–287.

[92] S. K. Kim and T. S. Oh, *Trans. Nonferrous Met. Soc. China (English Ed.*, **2011**, 21, SUPPL. 1, s68–s72.

[93] M. Abd Mutalib, M. A. Rahman, M. H. D. Othman, A. F. Ismail, and J. Jaafar, Elsevier B.V., **2017**.

[94] C. Cardell and I. Guerra, *TrAC - Trends Anal. Chem.*, **2016**, 77, 156–166.

[95] B. J. Inkson, Elsevier Ltd, **2016**.

[96] A. Mayeen, L. K. Shaji, and A. K. Nair, Elsevier Ltd., **2018**.

[97] L. Faulkner and A. Bard, 2nd ed. John Wiley & Sons, Inc., **2001**.

[98] H. Seyama, M. Soma, and B. K. G. Theng, 1st ed., 5, C. Elsevier Inc., **2013**.

[99] H. Konno, Tsinghua University Press Limited, **2016**.

[100] M. Aziz and A. F. Ismail, Elsevier B.V., **2017**.

[101] J. F. Moulder, W. F. Stickle, P. E. Sobol, and K. D. Bomben, 6509 Flying Cloud Drive Eden Prairie, Minnesota 55344 United Stales of America: Perkin-Elmer Corporation Physical Electronics Division, **1992**.

[102] A. P. Grosvenor, B. A. Kobe, M. C. Biesinger, and N. S. McIntyre, *Surf. Interface Anal.*, **2004**, 36, 12, 1564–1574.

[103] M. P. Clark, T. Muneshwar, M. Xiong, K. Cadien, and D. G. Ivey, *ACS Appl. Nano Mater.*, **2018**, 2, 267–277.

[104] M. Chigane, M. Ishikawa, and M. Izaki, *J. Electrochem. Soc.*, **2001**, 148, 7, 96–101.

[105] M. C. Biesinger, B. P. Payne, A. P. Grosvenor, L. W. M. Lau, A. R. Gerson, and R. S. C. Smart, *Appl. Surf. Sci.*, **2011**, 257, 7, 2717–2730.

[106] E. S. Ilton, J. E. Post, P. J. Heaney, F. T. Ling, and S. N. Kerisit, *Appl. Surf. Sci.*, **2016**, 366, 475–485.

[107] J. Epp, Elsevier Ltd, **2016**.

[108] B. Ingham and M. F. Toney, Woodhead Publishing, **2014**.

[109] Y. S. Choudhary, L. Jothi, and G. Nageswaran, Elsevier Inc., **2017**.

[110] G. M. Ehrlich, McGraw-Hill Companies Inc., **2002**.

[111] S. R. Taylor and E. Gileadi, *Corrosion*, **1995**, 51, 9, 664–671.

[112] D. Pletcher, R. Greff, R. Peat, L. M. Peter, and J. Robinson, *Instrum. Methods Electrochem.*, **2010**, 178–228.

[113] C. Du, Y. Sun, T. Shen, G. Yin, and J. Zhang, Elsevier B.V., **2014**.

[114] M. Xiong, M. P. Clark, M. Labbe, and D. G. Ivey, *J. Power Sources*, **2018**, 393, May, 108–118.

[115] A. R. Mainar, L. C. Colmenares, O. Leonet, F. Alcaide, J. J. Iruin, S. Weinberger, V. Hacker, E. Iruin, I. Urdanpilleta, and J. A. Blazquez, *Electrochim. Acta*, **2016**, 217, 80–91.

[116] G. Wu, A. Santandreu, W. Kellogg, S. Gupta, O. Ogoke, H. Zhang, H. L. Wang, and L. Dai, *Nano Energy*, **2016**, 29, 83–110.

[117] Z. Huang, X. Qin, X. Gu, G. Li, Y. Mu, N. Wang, K. Ithisuphalap, H. Wang, Z. Guo, Z. Shi, G. Wu, and M. Shao, *ACS Appl. Mater. Interfaces*, **2018**, 10, 28, 23900–23909.

[118] C. Tang, M. M. Titirici, and Q. Zhang, *J. Energy Chem.*, **2017**, 26, 6, 1077–1093.

[119] M. Chigane and M. Ishikawa, *J. Electrochem. Soc.*, **2000**, 147, 6, 2246–2251.

[120] Y. Gorlin, B. Lassalle-kaiser, J. D. Benck, S. Gul, S. M. Webb, V. K. Yachandra, J. Yano, and T. F. Jaramillo, *J. Am. Chem. Soc.*, **2013**, 135, 8525–8534.

[121] X. Chen, Z. Zhou, H. E. Karahan, Q. Shao, L. Wei, and Y. Chen, *Small*, **2018**, 1801929, 1–29.

[122] G. Du, X. Liu, Y. Zong, T. S. A. Hor, A. Yu, and Z. Liu, *Nanoscale*, **2013**, 5, 11, 4657–4661.

[123] J. Fu, F. M. Hassan, J. Li, D. U. Lee, A. R. Ghannoum, G. Lui, A. Hoque, and Z. Chen, *Adv. Mater.*, **2016**, 28, 6421–6428.

[124] F. Li, H. Li, X. Liu, L. Wang, Y. Lu, and X. Hu, *Chemistry (Easton).*, **2019**.

[125] Z. Zhang, S. H. Lim, B. Li, X. Wang, and Z. Liu, **2014**, 4–11.

[126] F. Meng, H. Zhong, D. Bao, J. Yan, and X. Zhang, *J. Am. Chem. Soc.*, **2016**, 138, 32, 10226–

10231.

[127] J. Wang, H. Wu, D. Gao, S. Miao, G. Wang, and X. Bao, *Nano Energy*, **2015**, 13, 387–396.

[128] Y. Niu, X. Huang, L. Zhao, W. Hu, and C. M. Li, *ACS Sustain. Chem. Eng.*, **2018**, 6, 3556–3564.

[129] T. Li, Y. Lv, J. Su, Y. Wang, Q. Yang, Y. Zhang, and J. Zhou, *Adv. Sci.*, **2017**, 4, 1700226.

[130] C. Si, Y. Zhang, C. Zhang, H. Gao, W. Ma, L. Lv, and Z. Zhang, *Electrochim. Acta*, **2017**, 245, 829–838.

[131] T. Zhang, Z. Li, L. Wang, P. Sun, Z. Zhang, and S. Wang, *ChemSusChem*, **2018**, 11, 16, 2730–2736.

[132] X. Lu, L. Gu, J. Wang, J. Wu, P. Liao, and G. Li, *Adv. Mater.*, **2017**, 29, 1604437.

[133] W. Yan, X. Cao, J. Tian, C. Jin, K. Ke, and R. Yang, *Carbon N. Y.*, **2016**, 99, 195–202.

[134] D. Aasen, M. Clark, and D. G. Ivey, *Batter. Supercaps*, **2019**, 2, 882–893.

[135] T. Zhang, Z. Li, L. Wang, Z. Zhang, and S. Wang, *Int. J. Hydrogen Energy*, **2019**, 44, 1610–1619.

[136] Y. C. G. Kwan, G. M. Ng, and C. H. A. Huan, *Thin Solid Films*, **2015**, 590, 40–48.

[137] W. Yan, W. Bian, C. Jin, J.-H. Tian, and R. Yang, *Electrochim. Acta*, **2015**, 177, 65–72.

[138] D. Wilson and M. A. Langell, *Appl. Surf. Sci.*, **2014**, 303, 6–13.

[139] Z. P. Cano, M. G. Park, D. U. Lee, J. Fu, H. Liu, M. Fowler, and Z. Chen, *J. Phys. Chem. C*, **2018**, 122, 35, 20153–20166.

[140] C. Wang, Z. Li, L. Wang, X. Niu, and S. Wang, *ACS Sustain. Chem. Eng.*, **2019**, 7, 16, 13873–13885.

[141] E. Davari, A. D. Johnson, A. Mittal, M. Xiong, and D. G. Ivey, *Electrochim. Acta*, **2016**, 211, 735–743.

[142] S. Zhang, Y. Zhang, W. Jiang, X. Liu, S. Xu, R. Huo, F. Zhang, and J. S. Hu, *Carbon N. Y.*, **2016**, 107, 162–170.

[143] Z. Lu, L. Qian, Y. Tian, Y. Li, X. Sun, and X. Duan, *Chem. Commun.*, **2016**, 52, 5, 908–911.

[144] J. Zhang, Z. Zhao, Z. Xia, and L. Dai, *Nat. Nanotechnol.*, **2015**, 10, 5, 444–452.

[145] B. Li and S. H. Chan, *Int. J. Hydrogen Energy*, **2013**, 38, 8, 3338–3345.

[146] E. Detsi, J. B. Cook, B. K. Lesel, C. L. Turner, Y. L. Liang, S. Robbennolt, and S. H. Tolbert, *Energy Environ. Sci.*, **2016**, 9, 2, 540–549.

[147] R. D. L. Smith, M. S. Prevot, R. D. Fagan, Z. Zhang, P. A. Sedach, M. K. J. Siu, S. Trudel, and C. P. Berlinguette, *Science*, **2013**, 340, April, 60–63.

[148] X. Jia, S. Gao, T. Liu, D. Li, P. Tang, and Y. Feng, *Electrochim. Acta*, **2017**, 245, 59–68.

[149] M. Wu, G. Zhang, J. Qiao, N. Chen, W. Chen, and S. Sun, *Nano Energy*, **2019**, 61, April, 86–95.

[150] Y.-T. Lu, Y.-J. Chien, C.-F. Liu, T.-H. You, and C.-C. Hu, *J. Mater. Chem. A*, **2017**, 5, 39, 21016–21026.

[151] D. Aasen, M. P. Clark, and D. G. Ivey, *Batter. Supercaps*, **2019**.

[152] P. C. Philippi, **2016**.

[153] J. F. Marco, J. R. Gancedo, M. Gracia, J. L. Gautier, E. Ríos, and F. J. Berry, *J. Solid State Chem.*, **2000**, 153, 1, 74–81.

[154] T. Yamashita and P. Hayes, *Appl. Surf. Sci.*, **2008**, 254, 8, 2441–2449.

[155] K. E. Sickafus, J. M. Wills, and N. W. Grimes, *J. Am. Ceram. Soc.*, **2004**, 82, 12, 3279–3292.

[156] E. J. Verwey, P. W. Haayman, and F. C. Romeijn, *J. Chem. Phys.*, **1947**, 15, 4, 181–187.

[157] D. A. Corrigan, *J. Electrochem. Soc.*, **2006**, 136, 3, 613.

[158] D. A. Corrigan, *J. Electrochem. Soc.*, **1989**, 136, 3, 723.